

# **Comparing magnetic pore fabrics, pore fabrics and permeability anisotropy in synthetic and natural sedimentary rocks**

Inaugural dissertation  
of the Faculty of Science,  
University of Bern

presented by

Yi, Zhou

from China

Supervisor of the doctoral thesis:

Prof. Dr. Andrea R. Biedermann

Institute of Geological Sciences, University of Bern, Baltzerstrasse 1+3, CH-3012  
Bern, Switzerland.

Co-supervisor of the doctoral thesis:

Prof. Dr. Anneleen Foubert

Department of Geosciences, University of Fribourg, Chemin du Musée 6, CH-  
1700 Fribourg, Switzerland.

This thesis is licensed under a Creative Commons Attribution 4.0 International License  
(CC BY 4.0 DEED): <https://creativecommons.org/licenses/by/4.0>

**Comparing magnetic pore fabrics, pore fabrics and permeability  
anisotropy in synthetic and natural sedimentary rocks**

Inaugural dissertation  
of the Faculty of Science,  
University of Bern

presented by

Yi, Zhou

from China

Supervisor of the doctoral thesis:

Prof. Dr. Andrea R. Biedermann

Institute of Geological Sciences, University of Bern, Baltzerstrasse 1+3, CH-3012  
Bern, Switzerland.

Co-supervisor of the doctoral thesis:

Prof. Dr. Anneleen Foubert

Department of Geosciences, University of Fribourg, Chemin du Musée 6, CH-  
1700 Fribourg, Switzerland.

Accepted by the Faculty of Science.

Bern, 30th April, 2025

The Dean  
Prof. Dr. Jean-Louis Reymond

## Abstract

Pore fabrics represent the geometric arrangement and network of pores in rocks, with a particular focus on the pore connectivity and orientation, which have a significant impact on the fluid flow within the pores. Accurately describing the pore fabric characteristics is critical in assessing the flow behaviour (connectivity, permeability) of underground fluid resources such as geothermal fluids, groundwater, and hydrocarbons. Thin section analysis is the most direct and fundamental method for observing and describing pore fabrics, but it usually only presents two-dimensional features. X-ray computed microtomography (XRCT) is certainly an effective way to non-destructively observe samples and describe their three-dimensional features, but it is constrained by the trade-off between resolution and sample size. The magnetic pore fabric (MPF) method theoretically can detect pore sizes as small as 10 nm, but MPF is only empirically associated with pore fabrics and permeability characteristics, leading to potential biases in practical applications. Direct measurement of permeability anisotropy on samples is indeed a relevant method for determining the optimal flow direction of fluids, but the determination of measurement direction often requires prior knowledge of the fabric characteristics. If MPF can establish a more quantitative relationship with pore fabrics and permeability anisotropy, considering that impregnated samples can be prepared in large quantities at once and that MPF measurements are relatively simple and efficient, the MPF method is expected to provide a more accurate and efficient quantitative prediction of fluid flow direction in porous rocks. In this study, typical sandstones (Berea, Berea Spider, Bentheimer, Castlegate, Molasse, Salt Wash North) and carbonates (Calcarenite, Indiana limestone), as well as artificial rocks (quartz sandstone bonded by liquid glass, and hot isostatically pressed (HIP) calcite-muscovite mixture) with various porosities and pore fabrics were selected. For HIP samples, calcite and muscovite were mixed to simulate impure carbonate rocks. Irregular calcite and sheet-like muscovite grains were combined in ratios of 3:7, 5:5, and 7:3 to produce pore fabrics with different anisotropies. The grains were uniformly mixed and subjected to 20 MPa cold pressing, followed by 160 MPa and 670 °C hot isostatic pressing for 3 hours, resulting in a homogeneous structure. Pore fabrics were extracted using a combination of three mutually perpendicular thin sections. XRCT scans of samples were conducted to establish digital rock models, obtain pore fabrics, and simulate permeability anisotropy and MPF. Multiple sets of cores were sampled in various directions to form multiple sets of full tensor permeability anisotropy measurements for cross-comparison. The appropriate ferrofluids were selected based on the surface wettability and charge properties of the mineral grains, and then impregnated into the rock samples. Afterward, the MPF of each sample was measured. The research results demonstrate that pore fabrics, permeability anisotropy, and MPF generally exhibit consistent orientations for most samples. However, there are significant differences in the anisotropy degree and anisotropy shape. Simulated permeability anisotropy and MPF model show more similarity with XRCT-derived digital pore fabrics which they are based on, compared to directly measured permeability anisotropy and MPF, which exhibit differences in some samples. For HIP samples, MPF maintains consistent orientations with permeability anisotropy. The MPF and permeability anisotropy also exhibit similar changes in anisotropy degree with varying muscovite ratios. This is because the shape of flaky muscovite has a higher anisotropy degree compared to irregular calcite. As the muscovite content in the sample increases, the anisotropy degree of both MPF and permeability also increases. Overall, MPF and permeability anisotropy show a strong correlation in terms of orientation and anisotropy degree. Therefore, the MPF method can serve as an effective prior method for assessing the sample heterogeneity and pore fabrics, providing a robust tool for predicting optimal flow directions in the exploration of underground liquid resources, including geothermal energy and hydrocarbons.

## **Acknowledgments**

I would like to express my gratitude to Prof. Dr. Andrea R. Biederman for her guidance and support throughout this doctoral project. Special thanks to Prof. Dr. Anneleen Foubert for her collaborative guidance on the doctoral project and for providing the XRCT scanning equipment Bruker SkyScan 2211 and processing software Avizo. I also acknowledge Prof. Dr. Pierre Lanari for his generous support, valuable insights, and suggestions on the research, as well as for providing the XRCT scanning equipment Bruker SkyScan 1273 and valuable guidance on image processing. My sincere appreciation goes to Michele Pugnetti for his in-depth research on the MPF method and valuable input. I am thankful to Christoph Neururer for his guidance on the use of the XRCT scanning equipment Bruker SkyScan 2211 as the Technical Officer in Prof. Dr. Anneleen Foubert's laboratory. I am also grateful for the support from technician Sandro Bula. Thank you to my colleague Philip Hartmeier for the discussions on XRCT image processing, and to my colleague Alejandro Prieto for his help with the experiments. Special thanks to R. Castellanza from the Università degli Studi Milano Bicocca (Milano, Italy) for providing the calcarenites. Thank you to Claudio Madonna for providing marble materials and laboratory for us to crush and grind samples, as well as for his assistance in preparing HIP samples. Thanks to Stephan Brechbühl, Nadine Lötscher, and Thomas Aebi for helping prepare thin sections and providing their studio for drilling and cutting samples. Appreciation goes to Thomas Siegenthaler for assisting in the preparation of relevant molds for experiments. Thank you to Ferrotec company for selling us the ferrofluid, to Cleveland Quarries for selling us Berea sandstones, and to Kocurek Industries for selling us various benchmark samples. Special thanks to Alberto Luisoni AG for generously providing a large quantity of calcite and muscovite powder for our research at no cost. The XRCT analysis in Bern was supported by the European Research Council (ERC) under the European Union's Horizon 2020 research and innovation program (grant agreement No. 850530 to PL). The Bruker Skyscan 2211 at the University of Fribourg was funded by R'Equip Swiss National Science Foundation grant 206021\_150731. This study was funded by the Swiss National Science Foundation, project 176917 (to ARB).

## Contents

Abstract.....	1
Acknowledgments .....	2
Contents .....	3
1. Introduction .....	6
1.1 Background.....	6
1.2 Research hypothesis and objectives.....	7
2. Theory and organization of the thesis.....	8
2.1 Central concepts.....	8
2.2 Organization of the thesis .....	10
3. Article I: Quantitative comparison of 3D pore space properties with magnetic pore fabrics— testing the ability of magnetic methods to predict pore fabrics in rocks.....	11
3.1. Introduction.....	12
3.2. Materials and Methods.....	14
3.2.1 Sample description .....	14
3.2.2 XRCT data acquisition and processing .....	15
3.2.3 Magnetic pore fabric measurements .....	21
3.2.4 Correlation of XRCT and MPF data .....	22
3.3. Results.....	22
3.3.1 XRCT results.....	22
3.3.1.1 3D reconstructions and porosity .....	22
3.3.1.2 Pore size distributions.....	22
3.3.1.3 Pore orientation .....	22
3.3.1.4 Pore shape and anisotropy degree .....	27
3.3.2 MPF results .....	28
3.3.2.1 Magnetic fabric orientation .....	28
3.3.2.2 Anisotropy degree and shape of the magnetic fabric .....	28
3.3.3 Comparison of XRCT and MPF data.....	30
3.3.3.1 Porosities .....	30
3.3.3.2 Directional comparison.....	31
3.3.3.3 Comparison of anisotropy degree and shape.....	31
3.4. Discussion.....	31
3.5. Conclusions.....	33
Acknowledgments .....	34
4. Article II: Quantitative assessment of direct and indirect measures of 3D pore fabrics and permeability anisotropy in sedimentary rocks.....	35
4.1. Introduction.....	36
4.2. Materials and Methods.....	40

4.2.1 Sample description and characterization.....	40
4.2.2 Direct and indirect pore fabric determination .....	56
4.2.2.1 Thin section analysis .....	56
4.2.2.2 XRCT data acquisition and processing .....	56
4.2.2.3 Permeability anisotropy measurements .....	57
4.2.2.4 Magnetic pore fabric measurements.....	57
4.2.3 Correlation of thin section, XRCT, permeability anisotropy and MPF data.....	59
4.3. Results.....	59
4.3.1 Thin section .....	60
4.3.2 XRCT data.....	61
4.3.3 Permeability anisotropy.....	65
4.3.4 AMS and MPF .....	66
4.3.5 Comparison .....	68
4.4. Discussion.....	68
4.5. Conclusions.....	70
Acknowledgment .....	70
5. Article III: Comparing thin-section-derived and X-ray tomography-derived pore fabrics, permeability anisotropy and magnetic pore fabrics in hot isostatically pressed calcite-muscovite rocks .....	71
5.1. Introduction.....	72
5.2. Materials and Methods.....	77
5.2.1 Sample description .....	77
5.2.2 Direct and indirect pore fabric determination .....	91
5.2.2.1 Thin section analysis .....	91
5.2.2.2 XRCT data acquisition and processing .....	92
5.2.2.3 Permeability anisotropy measurements .....	92
5.2.2.4 Magnetic pore fabric measurements.....	92
5.2.3 Correlation of thin section, XRCT, permeability anisotropy and MPF data.....	93
5.3. Results.....	94
5.3.1 Thin section .....	99
5.3.2 XRCT data.....	99
5.3.3 Measured permeability anisotropy .....	99
5.3.4 AMS and MPF .....	101
5.3.5 Comparison .....	101
5.4. Discussion.....	102
5.5. Conclusions.....	105
Acknowledgment .....	105
6. Conclusion and outlook.....	106

7. Supplementary material .....	108
Supplementary material for Article I: Quantitative comparison of 3D pore space properties with magnetic pore fabrics—testing the ability of magnetic methods to predict pore fabrics in rocks .....	108
References .....	113
Appendix .....	129
Appendix for Article I: Quantitative comparison of 3D pore space properties with magnetic pore fabrics—testing the ability of magnetic methods to predict pore fabrics in rocks .....	129
Appendix for Article II: Quantitative assessment of direct and indirect measures of 3D pore fabrics and permeability anisotropy in sedimentary rocks .....	129
Appendix for Article III: Comparing thin-section-derived and X-ray tomography-derived pore fabrics, permeability anisotropy and magnetic pore fabrics in hot isostatically pressed calcite-muscovite rocks .....	129

# 1. Introduction

## 1.1 Background

Pore fabrics focus on the spatial arrangement and orientation of pores in rocks, describing the connectivity, distribution and anisotropy of the pore network. The fluid flow within pores is naturally constrained by the pore fabrics, thus characterizing the pore fabrics plays a pivotal role in the exploration and exploitation of fluid resources such as geothermal energy, hydrocarbons, and groundwater (Aliyu & Chen, 2018; Chen et al., 2020; Frosch et al., 2000; Gao & Hu, 2018; Kibria et al., 2018; Sun et al., 2021; Wagner et al., 2005; Yang et al., 2017, 2018; Zhang et al., 2020). Despite the recognized importance, characterizing pore fabrics with sufficient accuracy and efficiency remains a significant challenge, hindering the ability to fully predict and manage fluid flow in complex geological formations. Currently, there are various direct and indirect methods for studying the pore fabrics and fluid flow characteristics of reservoir rocks, each with its own advantages and disadvantages.

The utilization of optical microscopy to observe thin sections of rocks and the combination with image analysis remains a cornerstone technique for studying pore fabrics (Chen et al., 1999; Nishiyama & Kusuda, 1994, 1996; Prikryl, 2015). Its advantages lie in its relatively simple preparation process, and the contrast of the pore portions can be effectively enhanced by injecting fluorescent resin into the thin sections. When observed under a microscope equipped with UV light, the pore fabrics injected with fluorescent resin exhibit significant luminescent characteristics, facilitating easy characterization (Anselmetti et al., 1998; Chen et al., 1999, 2000; Hakami, 1995; Montoto et al., 1981; Nishiyama & Kusuda, 1994, 1996; Persson, 1998; Prévosteau et al., 1970; Prikryl, 2015; Prikryl & Kou, 1996). By increasing the magnification of the microscope, images with submicron resolution can be obtained, and observations of larger areas can be achieved through multiple scans and image stitching (Andriani & Walsh, 2002; Gustafsson, 2000; Heintzmann & Ficz, 2013; Ingham, 2010). However, the inherent limitation of thin sections is their two-dimensional nature. This 2D representation presents a significant challenge because the complex and three-dimensional connectivity of pore networks, which is critical for fluid flow, cannot be fully captured. A key gap remains in developing robust methods to accurately extrapolate 2D thin section observations to represent the true 3D pore fabric, and to quantify the uncertainties associated with this extrapolation. Additionally, there is a risk of damaging the pore fabrics during the process of polishing the mineral specimen (Heilbronner & Barrett, 2013).

Another approach to obtaining pore fabrics is through X-ray computed microtomography (XRCT), a widely used method for acquiring three-dimensional structures within objects. By continuously scanning the sample laterally and combining the scans to generate a three-dimensional image of the sample, a digital model of the rock sample is established. Based on the digital rock model, the pore fabrics can be extracted for various types of analysis, such as pore shape, size, and distribution. Physical simulation experiments, such as simulating fluid permeation within pores, can also be conducted based on such digital pore fabrics (Andrä et al., 2013a; Holzer et al., 2011; Madadi & Varslot, 2009; Madonna et al., 2012; Pini & Madonna, 2016). Compared to two-dimensional images, acquiring and processing three-dimensional data requires more computational power. Using higher resolution and larger sample sizes significantly increases the data volume. Therefore, a persistent gap is the need for optimized XRCT workflows to efficiently process large datasets and extract representative pore fabric information across varying scales (Chen et al., 2020; Lai et al., 2018; Sun et al., 2021; Zhan et al., 2009; Zhang et al., 2020). This pore fabric information also should be representative of the overall sample characteristics and not simply a collection of individual pores.

Assessing the fluid connectivity within rock pores in various directions is most directly done by measuring the permeability anisotropy of samples. However, this method typically requires prior

knowledge of the fabric orientation of the rock sample, such as bedding planes, paleoflow directions, etc., to determine the optimal direction of fluid migration. Then, at least two measurements are taken parallel and perpendicular to the structural orientation to calculate their anisotropy (Adams et al., 2013, 2016; Benson et al., 2003, 2005; Nabawy, 2018). However, relying solely on qualitative observation of fabric information from samples is not accurate enough and lacks quantification, potentially leading to misjudgement of the preferred flow direction. Without prior information about fabric, at least six measurements are needed to calculate the anisotropy characteristics of permeability, a second-order tensor (Coulson & Nye, 1958). Additional measurements in more directions can help assess the confidence of the results (Jelinek, 1977). However, full tensor measurements are too costly. Therefore, a gap exists for a stable, efficient, and convenient method to acquire prior information, thereby reducing the need for extensive measurements.

Another indirect method for measuring pore fabrics and predicting permeability anisotropy is called magnetic pore fabric (MPF) (Pfleiderer & Halls, 1990, 1994). This involves injecting a highly magnetic ferrofluid into the sample and measuring the magnetic susceptibility in various directions by rotating the sample. The magnetic anisotropy of the impregnated sample reflects the overall magnetic anisotropy of the pores injected by ferrofluid, hence termed magnetic pore fabric. MPF provides a three-dimensional overall characterization of the sample without requiring a trade-off between sample size and resolution, and also without requiring prior information about the fabric. Additionally, impregnated samples can be mass-produced at once, and MPF measurements are relatively simple and efficient. Most studies have shown that MPF exhibits relative consistent orientations with pore fabrics and permeability anisotropy (Benson et al., 2003; Louis et al., 2005; Pfleiderer & Halls, 1990, 1994). However, its anisotropy degree generally appears lower than that of pore fabrics and permeability anisotropy (Benson et al., 2003; Jones et al., 2006; Louis et al., 2005; Nabawy et al., 2009; Pfleiderer & Halls, 1994). The results of MPF are influenced by various factors such as pore distribution, ferrofluid magnetism, and even measurement frequency (Biedermann, 2019; Biedermann et al., 2021). Further validation is needed to confirm the ability of the MPF method to predict the pore fabrics and permeation characteristics of rock samples.

## **1.2 Research hypothesis and objectives**

The research hypothesis is to what extent can this study establish robust quantitative relationships among pore fabrics characterized by thin section and XRCT methods, permeability anisotropy, and magnetic pore fabric, and how robust are these relationships across diverse rock types, thereby providing a more integrated and efficient approach for porous media characterization and preferred flow direction prediction?

To address the research question, the objectives are:

- To quantify geometric characteristics of individual pores using thin section and XRCT methods and develop a mathematical framework to integrate these individual pore features to derive overall pore fabric characteristics for direct comparison with other methods (addressing the gaps in 2D to 3D extrapolation and multi-method comparison)
- To establish quantitative relationships between pore fabrics (from thin section and XRCT), permeability anisotropy, and MPF, utilizing tensor representations to enable direct comparison and analysis of anisotropy degrees and orientations (addressing the gap in linking different methods and quantifying anisotropy relationships).
- To validate the robustness of these quantitative relationships across a diverse suite of sedimentary and artificial rock samples, assessing the generalizability of the integrated approach to various porous media (addressing the gap in validation and general applicability).

- To evaluate the potential of MPF as a predictive tool for pore fabrics and permeability anisotropy, aiming to reduce the measurement burden and enhance the efficiency of porous media characterization (addressing the gap in efficiency and MPF validation).

## 2. Theory and organization of the thesis

### 2.1 Central concepts

This chapter provides a theoretical foundation for understanding anisotropy in sedimentary rocks and the methods employed in this study to characterize pore fabrics and permeability anisotropy. To provide a robust theoretical framework for this thesis, it is essential to define and elaborate upon the concept of anisotropy within the context of rock properties. In geological materials, anisotropy refers to the directional dependence of physical properties. Sedimentary rocks, in particular, exhibit inherent anisotropy due to their formation processes, including depositional environment, compaction, and diagenesis. This intrinsic anisotropy significantly influences various rock characteristics, most notably permeability and pore fabrics, thereby critically affecting fluid flow behaviour within subsurface reservoirs. Understanding and quantifying anisotropy is therefore important for accurate reservoir characterization and the optimization of fluid resource exploration and development (Aliyu & Chen, 2018; Chen et al., 2020; Gao & Hu, 2018; Kibria et al., 2018; Sun et al., 2021; Yang et al., 2017, 2018; Zhang et al., 2020).

Mathematically, second-order tensors provide a powerful tool for representing and analysing anisotropic properties. A second-order tensor is a linear transformation that can be represented by a matrix, capturing directional variations in a property within a three-dimensional space. In the context of rock anisotropy, tensors can effectively describe properties such as permeability, magnetic susceptibility, and pore fabric. For a symmetric second-order tensor, diagonalization yields a set of orthogonal eigenvectors and corresponding eigenvalues. The eigenvectors ( $V_1$ ,  $V_2$ , and  $V_3$ ) define the principal axes of the anisotropic property, indicating the directions of maximum, intermediate, and minimum magnitudes. The eigenvalues (typically denoted as  $a \geq b \geq c$ ) quantify the magnitude of the property along these principal axes, with  $a$  representing the maximum,  $b$  the intermediate, and  $c$  the minimum. These eigenvalues and eigenvectors provide a complete quantitative description of the anisotropy, enabling the calculation of anisotropy degree ( $P = a/c$ ,  $[1, \infty]$ ) and anisotropy shape ( $U = (2*b - a - c)/(a - c)$ ,  $[-1, 1]$ ) (Coulson & Nye, 1958; Jelinek, 1981; Strang, 2022).

Characterizing pore fabrics and permeability anisotropy in rocks necessitates a range of experimental and analytical techniques. Beyond the methods employed in this study, a broader spectrum of approaches exists, each with its own strengths and limitations. These methods can be categorized as follows:

- Pore fabric characterization techniques: In addition to thin section analysis and X-ray computed tomography, other advanced imaging techniques like micro-computed tomography (micro-CT) (Garum et al., 2020), focused ion beam scanning electron microscopy (FIB-SEM) (Devarapalli et al., 2017; Garum et al., 2020; Liang et al., 2024; Zhao et al., 2022), and transmission electron microscopy (TEM) (Bernard et al., 2013) offer higher resolution imaging of pore fabrics. Statistical methods such as mercury intrusion porosimeter (MIP) (Zhang et al., 2018) and Nitrogen gas adsorption (Kuila & Prasad, 2013; Schmitt et al., 2013) provide quantitative information on pore size distribution and surface area. Nevertheless, MIP and Nitrogen gas adsorption are limited in their ability to comprehensively characterize pore fabrics, especially regarding anisotropy. Although micro-CT, FIB-SEM, and TEM can achieve higher resolution images, their application is often restricted by smaller sample sizes that may not be representative, as well as complex and expensive experimental procedures.

Conversely, thin section method is advantageous due to its simplicity, efficiency, and low cost. XRCT method offers a more favourable trade-off between resolution and representative sample volume.

- Permeability measurement techniques: While this study utilizes steady-state gas permeameter with Klinkenberg correction, other methods exist, including the pressure pulse decay method (Dicker & Smits, 1988; Jones, 1997; Zhao et al., 2022) for low permeability rocks and oscillatory pressure method (Bernabe et al., 2006; Elkhoury et al., 2011) for dynamic permeability characterization. However, both latter methods are unsteady-state permeability measurements. The unstable fluid pressure inherent in these techniques can potentially induce greater damage to the rock pores, especially those exhibiting pressure sensitivity.
- Indirect anisotropy characterization methods: Besides MPF, elastic anisotropy offers another indirect description of pore fabrics. However, given that elasticity is a fourth-order tensor, its characterization demands extensive directional measurements or symmetry assumptions. In parallel with permeability anisotropy assessments, directional velocity measurements necessitate oriented core samples. Furthermore, seismic velocities are influenced by factors beyond pore fabrics, including microcracks, grain boundaries, and the intrinsic elastic anisotropy of individual grains. Consequently, seismic-based pore fabric characterization remains a challenge (Almqvist et al., 2011; Benson et al., 2003; David et al., 2017; Laurent Louis et al., 2004; Robion et al., 2014). Conversely, the MPF method used in this study establishes a relationship with pore fabrics without extensive measurements and is less susceptible to extra factors.

In geology, the term "fabric" emphasizes the geometric arrangement and orientation of components within a rock, serving as a description of anisotropy that varies with direction. In contrast, "structure" refers to more general features. It is important to note that the terms "pore fabrics" and "pore structures" are both used to describe the arrangement and characteristics of pores. But pore fabric is a component of pore structure. Pore structure is the overarching term describing the complete characterization of the pore space, while pore fabric specifically focuses on the geometric arrangement of the pores and network of pores. Pore fabric examines how pores are interconnected and oriented, which can significantly affect the permeability. In this study, the primary focus is on any characteristics of pores related to the preferred flow direction. Therefore, pore fabrics are the main focus of the research, utilizing methods such as thin section analysis, XRCT, and MPF techniques.

Here are some other terms related to fabric and structure, such as sedimentary structures which are characteristics formed during or shortly after the deposition of sediment. These structures provide valuable information about the depositional environment and processes. For example, common sedimentary structures include bedding, cross-bedding, ripple marks, mud cracks, and graded bedding (Nichols, 2009).

Macroscopic fabric and block fabric both refer to the fabric of a rock or sediment as observed at a hand-sample or outcrop scale. This fabric is visible to the naked eye or with minimal magnification and can include features such as visible grain alignment, layering or banding, vesicles, amygdules, and vugs (Blatt et al., 2006).

Magnetic fabric describes the preferred orientation of magnetic minerals within a rock and is typically analyzed using anisotropy of magnetic susceptibility (AMS) measurements. Key aspects of magnetic fabric include magnetic lineation and magnetic foliation (Jelinek, 1977).

Grain fabric specifically refers to the arrangement and orientation of grains within a rock or sediment, typically observed at a microscopic to mesoscopic scale. It reflects the rock's depositional processes and deformation history. Packing and grain shape directly affect the amount of pore space and how easily fluids can flow through the rock. Preferred grain orientation can lead to anisotropic properties, meaning the rock's properties, such as strength or permeability, vary depending on the preferred grain orientation (Blatt et al., 2006).

Based on the above central concepts and important criteria, this study can establish a quantitative comparison between pore fabrics, permeability anisotropy, and MPF. This enables MPF to serve as an efficient prior method for predicting the optimal direction of fluid flow, thereby benefiting the exploration and development of fluid resources, such as geothermal energy and hydrocarbon, and underground CO<sup>2</sup> storage.

## **2.2 Organization of the thesis**

Based on the research objectives and central concepts, the specific research content was presented in Chapters 3 to 5, with each chapter structured as a self-contained academic article. The article in Chapter 3 has been published in *Geochemistry, Geophysics, Geosystems*, while the content of the other chapters may be prepared for potential submission to peer-reviewed journals.

In Chapter 3, two rocks with significantly different porosity and pore structure, calcarenite and molasse sandstone, were selected as research samples. MPF at three measurement frequencies and XRCT-derived pore fabrics at two resolutions were compared and analyzed. To generate effective comparative results, the study also utilized techniques such as total shape ellipsoid and representative elementary volume (REV) to process relevant data, forming a systematic and effective technical workflow for acquiring sample MPF and pore fabrics data and conducting comparative analysis.

In Chapter 4, the focus was on investigating the measurement of permeability anisotropy using different numbers of directional cores and comparing MPF, pore fabrics, and permeability anisotropy. A wider variety of rock samples were employed in the study, including six sandstones, two carbonates, and one artificial quartz sandstone, to promote the broader applicability of the MPF method. In addition to the XRCT and MPF methods, three-dimensional pore structures obtained from thin sections analysis and full-tensor permeability anisotropy measured from 7 or 14 directional cores were also included, along with data confidence analysis and sample heterogeneity assessment. For the MPF method, discussions were held on the selection of ferrofluid and measurement frequency, as well as issues such as frequency dependence and self-demagnetization. The aim was to achieve a comprehensive and accurate quantitative relationship between pore fabrics, permeability anisotropy, and MPF based on comparisons across multiple samples.

In Chapter 5, given the inherent heterogeneity characteristics of natural samples, the focus shifted to experimental studies using synthetic samples. The hot isostatic pressing method was employed to simulate the high-temperature and high-pressure environment of rock formation, using calcite and muscovite minerals with different grain geometries for mixing, to create rock samples with relative homogeneity yet significant anisotropy. The goal was to further investigate the relationship between MPF, pore fabrics, permeability anisotropy, and promote the MPF method as an effective and prior means to indicate fabric anisotropy and the optimal direction of fluid permeation.

### **3. Article I: Quantitative comparison of 3D pore space properties with magnetic pore fabrics—testing the ability of magnetic methods to predict pore fabrics in rocks**

**(Published in *Geochemistry, Geophysics, Geosystems* (doi.org/10.1029/2022GC010403))**

**Y. Zhou<sup>1</sup>, M. Puggetti<sup>1</sup>, A. Foubert<sup>2</sup>, P. Lanari<sup>1</sup>, C. Neururer<sup>2</sup> & A. R. Biedermann<sup>1</sup>**

<sup>1</sup>Institute of Geological Sciences, University of Bern, Baltzerstrasse 1+3, CH-3012 Bern, Switzerland.

<sup>2</sup>Department of Geosciences, University of Fribourg, Chemin du Musée 6, CH-1700 Fribourg, Switzerland.

Corresponding author: Yi Zhou (yi.zhou@geo.unibe.ch)

#### **Key Points:**

- Magnetic pore fabrics can complement X-ray tomography, to capture small pores, and assess field-scale variations in pore fabrics
- A total shape ellipsoid is derived from X-ray tomography data, to represent average pore orientation and shape, and minimize artefacts
- The principal directions of magnetic pore fabrics and total shape ellipsoids are generally coaxial in most samples

#### **Abstract**

Pore fabrics characterize the anisotropy of pore space in rocks and influence the direction of fluid flow. This is important in reservoir characterization, and petroleum and geothermal energy exploitation. X-ray computed micro-tomography (XRCT) is commonly used to analyze pore fabrics, but limited by the micron-scale resolution for representative 1-inch rock cores. The magnetic pore fabric (MPF) method has been proposed to capture pores down to 10 nm. Although empirical relationships between MPF and pore space properties or permeability anisotropy are available, their application is compromised by large variability. This study integrates He pycnometry and XRCT-derived pore space models with MPFs, and provides a quantitative comparison for calcarenite (~50 vol% porosity and complex pore structure), and molasse sandstone (10-30% porosity and relatively homogeneous pore fabrics). The preferred orientation of pores obtained from XRCT is described by a total shape ellipsoid, calculated by summing the second-order tensors reflecting the best-fit ellipsoids of individual pores. This ellipsoid is then compared to the MPF magnitude ellipsoid in terms of fabric orientation, degree and shape of anisotropy. The MPF and total shape ellipsoids are generally coaxial. The MPF has a smaller anisotropy degree than the total shape ellipsoid, and their relationship depends on the ferrofluid properties. The anisotropy shapes show large variability. Nevertheless, the good agreement of principal directions in most samples makes MPFs a valuable and efficient complementary tool to analyze a large number of samples, in combination with XRCT on selected samples, for a field-scale pore space characterization.

#### **Plain Language Summary**

Understanding underground fluid flow is a major goal when exploring geothermal energy and the migration of petroleum. These fluids transfer between pores at multiple scales. When the pores are

flattened or elongated and display a preferred orientation, fluids will flow more readily in some directions compared to others. This results in preferred flow directions and flow paths. In this study, a fast way of determining pore geometry based on magnetic measurements is compared to traditional characterization methods. The good agreement between results suggests that magnetic methods can be applied as a complementary tool to include larger numbers of samples and potentially capture pores not resolved by traditional methods, with important implications for studies in geology and geological engineering.

### 3.1. Introduction

The fabric of connected pores, i.e., their shape, orientation, and connectivity, largely controls rock properties such as permeability. An accurate 3D description of pore fabrics has therefore many applications, including geothermal energy usage (Aliyu & Chen, 2018; Frosch et al., 2000; Wagner et al., 2005; Zhang et al., 2020), hydrocarbon exploitation, especially in tight rock (Chen et al., 2020; Gao & Hu, 2018; Kibria et al., 2018; Lai et al., 2018; Sun et al., 2021; Yang et al., 2017, 2018; Zhang et al., 2020), and numerical simulations of fluid flow in reservoirs (Mehmani et al., 2020; Wang et al., 2009; Yang et al., 2019; Zhang et al., 2015). Pore fabrics can be characterized directly or indirectly, as defined below.

Direct methods provide maps or grids of the pore network: (1) Image analysis of optical microscopy thin sections has a resolution of  $\sim 0.23 \mu\text{m}$  at best for 2D observations (Andriani & Walsh, 2002; Gustafsson, 2000; Heintzmann & Ficz, 2013; Ingham, 2010). Sample preparation may destroy or alter pores or create pseudo-pores if grains are detached during polishing (Heilbronner & Barrett, 2013). (2) Scanning electron microscopy (SEM) is a 2D mapping technique that can image pores down to 1-10 nm (Bultreys et al., 2016; Reed, 2005), characterizing a limited number of micropores within a single plane (De Boever et al., 2015; Marszałek et al., 2014; Mavris et al., 2012; Vázquez et al., 2013). (3) X-ray computed micro-tomography (XRCT) has emerged as a 3D technique to characterize the internal structure of rocks including their pore fabric, and provides the basis for digital rock physics (DRP) models that predict physical properties of rocks, especially acoustic and flow properties (Andrä et al., 2013; Holzer et al., 2011; Madadi & Varslot, 2009; Madonna et al., 2012; Pini & Madonna, 2016). Zhan et al. (2009) and Zubair (2012) reported a good fit between numerical calculation and direct porosity and permeability measurements using Berea sandstone and carbonate rocks. A crucial prerequisite for meaningful comparisons between model and measurement is that both are conducted on representative sample volumes. Sample sizes ranging from sub-micrometers to a few centimeters are commonly used for XRCT (Cnudde & Boone, 2013; Gelb et al., 2009; Landis & Keane, 2010; da Silva, 2018; Zubair, 2012). Larger samples may be more representative of the investigated rock, but suffer from lower spatial resolution (Figure 3.1). Unresolved pores can result in up to 32% difference between modelled and measured data (Zhan et al., 2009).

Indirect methods characterize pore fabrics by measuring the anisotropy of specific physical properties influenced by pore fabrics, e.g., permeability and seismic anisotropy and magnetic anisotropy of samples impregnated by ferrofluid. They provide average information on pore space properties, which is sufficient for many applications (e.g. Almqvist et al., 2011). Note that although permeability anisotropy is considered an indirect measurement of pore fabric, it is the most direct assessment of a rock's fluid transport properties. Permeability anisotropy is a symmetric second-order tensor, requiring at least six independent directional measurements for full description (Coulson & Nye, 1958). Otherwise, a priori information on the fabric orientation is needed, e.g., lineation and foliation directions, in case that measured directions disagree with the principal permeability directions, thus underestimating permeability anisotropy. Another indirect description for pore fabric is elastic anisotropy. However, elasticity is a fourth-order tensor, thus requiring a large number of directional measurements or symmetry assumptions. Analogously

to permeability anisotropy, each directional velocity is generally measured along a separate oriented core. Moreover, seismic velocities are affected by microcracks, grain boundaries and intrinsic elastic anisotropy of each grain in addition to pore fabrics, so seismic-based pore space characterization is challenging (Benson et al., 2003; David et al., 2017; Laurent Louis et al., 2004; Robion et al., 2014).

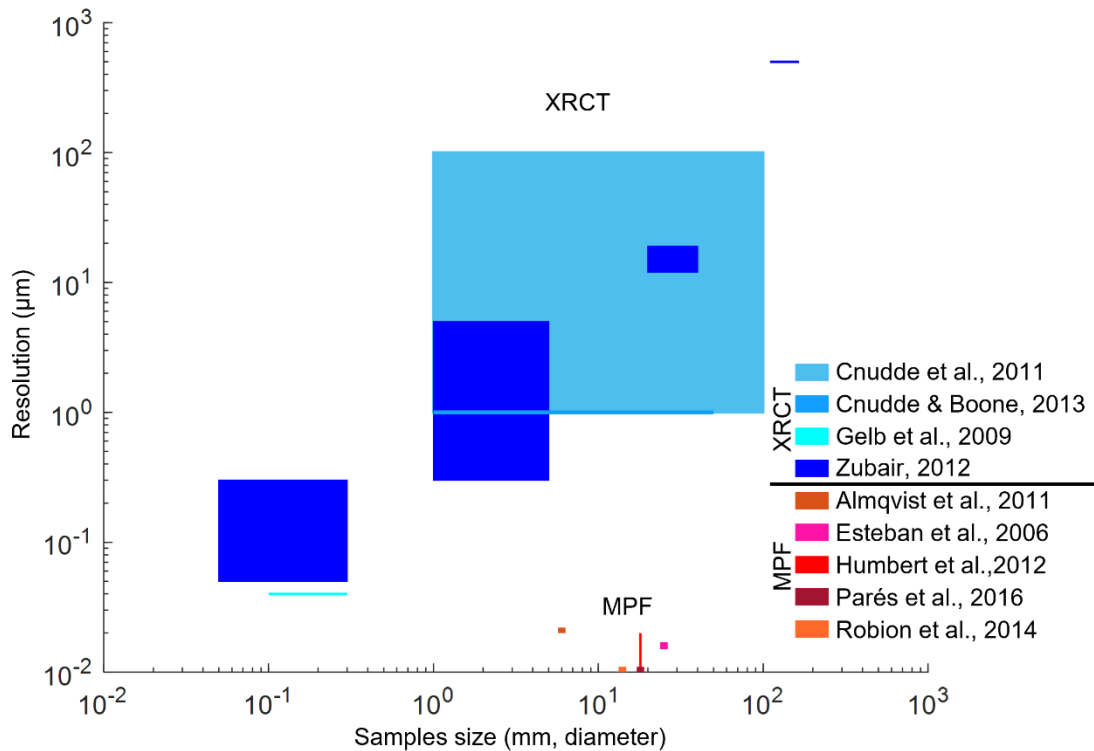


**Figure 3.1.** Sample size (diameter of the cylindrical core) vs resolution for XRCT and MPF methods (XRCT modified from Cnudde et al., 2011; Cnudde & Boone, 2013; Gelb et al., 2009; Zubair, 2012). The MPF resolution is 10-20 nm for sample sizes ranging from 6 mm to 25.4 mm diameter (Almqvist et al., 2011; Esteban et al., 2006; Humbert et al., 2012; Parés et al., 2016; Robion et al., 2014).

Magnetic pore fabrics (MPFs) provide a fast and efficient tool for pore fabric characterization. The samples' pore space is impregnated with ferrofluid, followed by measuring the anisotropy of magnetic susceptibility (AMS) (Pfleiderer & Halls, 1990), and thus only connected pores, which contribute to flow, are targeted by MPFs. MPFs can be applied on a single sample, without any priori information on the fabric, thus avoiding underestimating anisotropy by heterogeneity. Additionally, the method has been ascribed the ability to capture pores and pore throats down to 10-20 nm (Figure 3.1) (Almqvist et al., 2011; Esteban et al., 2006; Humbert et al., 2012; Parés et al., 2016; Robion et al., 2014). Pores and throats smaller than magnetic nanoparticles (10-20 nm diameter) are not captured by MPF. In practice, the threshold of pores that are impregnated depends on pore throat geometry and wettability (Robion et al., 2014), and 100 nm has been put forward as a more realistic threshold (Pugnetti et al., 2022). Empirical relationships have been established between MPFs and pore fabrics: (1) the maximum and minimum principal susceptibility axes are sub-parallel to the average orientations of major and minor pore axes (Hrouda et al., 2000; Jezek & Hrouda, 2007; Jones et al., 2006; Pfleiderer & Halls, 1990, 1994), (2) the degree of magnetic anisotropy increases when pore shapes become more anisotropic (Jones et al., 2006; Pfleiderer & Halls, 1990, 1993; Robion et al., 2014), and (3) oblate or prolate MPFs

are related to flattened or elongated pore shapes (Jones et al., 2006; Pfeleiderer & Halls, 1990). MPFs have been compared to permeability anisotropy (Benson et al., 2003; Hailwood et al., 1999; Louis et al., 2005; Nabawy et al., 2009; Pfeleiderer & Halls, 1994), and used to predict anisotropy of elastic properties (Almqvist et al., 2011). Unfortunately, empirical relationships vary largely between different studies, making the results hard to interpret (Almqvist et al., 2011; Benson et al., 2003; Jones et al., 2006; Louis et al., 2005; Nabawy et al., 2009; Pfeleiderer & Halls, 1990, 1993, 1994; Robion et al., 2014). The variability may be explained partly by that large pores contain large volumes of ferrofluid, whereas the preferred orientation of pore connections is more relevant for permeability anisotropy (Pfeleiderer & Halls, 1994). Pore shape, orientation and arrangement control MPFs, and ferrofluid susceptibility and measurement conditions largely influence MPF – pore fabric relationships (Biedermann, 2019; Biedermann et al., 2021). Many MPF studies focused on simplified samples (Biedermann, 2019; Jones et al., 2006; Pfeleiderer & Halls, 1990), and factors affecting the relationships between MPFs and pore space in natural samples are not yet fully understood.

Two complementary pore fabric characterization methods are investigated and correlated quantitatively in terms of the portion of pore space they characterize, and obtained fabric orientation, degree and shape: XRCT as a standard method, and MPF which has great potential but is rarely used. Two sedimentary rocks, calcarenite and molasse, were included with variability in porosity and pore complexity. A new second-order tensor quantity, the total shape ellipsoid, is derived from XRCT data, for direct comparison with MPF in terms of fabric orientation, anisotropy degree and shape.

## **3.2. Materials and Methods**

### **3.2.1 Sample description**

Samples with porosity of 10-55 % were chosen, molasse and calcarenite, applying for typical porosity of reservoir rocks varying between 5-40 % (Guo, 2019; Monicard, 1980). Ideally, a single rock type would have been used for all porosities to minimize the number of variables. Because the collected molasse samples have 10-30 % porosity with micropores, calcarenite with large pores was included, extending the porosity range to ~50 %.

The studied calcarenites are Plio-Pleistocene in age and recovered from the Gravina Formation in Apulia, Italy (Figure 3.2a) (Oryem et al., 2015). They possess high porosity (16–60 %) and a large proportion of interconnected pores (>99.5 % of pore space on average) (Ciantia et al., 2015). Different pore types are identified in BSE images, such as inter- and intragranular porosity, microporosity, and moldic porosity (Figure 3.2b). Calcarenite cores MI-1-Z3, MI-2-Y3, MI-2-Y8, MI-2-Y10, MI-3-X15, MI-3-X11 were drilled from the same block along three perpendicular directions, indicated by X, Y and Z in the sample names. Samples MI-5-Z21 and MI-5-X22 were drilled from another block. Molasse sandstone was collected in four areas from the Upper Marine Molasse (OMM) in the Swiss molasse basin (SMB): (1) Rüeggisberg, BE, samples D1121Z, D1112Y, D1263Y2, D1234X, D1221X, D1261X, (2) Entlebuch, LU, samples C43Y, C334Y, BE42AY, (3) Düringen, FR, Switzerland, sample 5256X, and (4) Tifers, FR, Switzerland, sample F31Z1 (Figure 3.2c). The molasse samples are characterized by cross and parallel bedding (Figure 3.2d). OMM consists mainly of shallow marine and tidal-influenced sandstones and mudstones, deposited in a shallow seaway from 20 to 17 Ma (Chevalier et al., 2010; Garefalakis & Schlunegger, 2019). The OMM sandstone displays porosities from 5 to 20 % (Chevalier et al., 2010; Schegg et al., 1997), mainly including intergranular porosity and microporosity (Figure 3.2d). Being an important aquifer in the SMB, OMM may provide pore space to store and transfer CO<sub>2</sub> and geothermal fluids (Chelle-Michou et al., 2017; Chevalier et al., 2010; Kohl et al., 2010; Rybach, 2019). All rocks were drilled and cut to obtain standard-sized cores of 25.4 mm diameter and 22 mm length. Initial sample characterization involved porosity measurements by comparing

grain volume (obtained from a Micromeritics AccuPyc 1340 Automatic Gas (He) Pycnometer system in the Petrophysics Laboratory at the University of Bern) with bulk volume (calculated by core diameter and length).

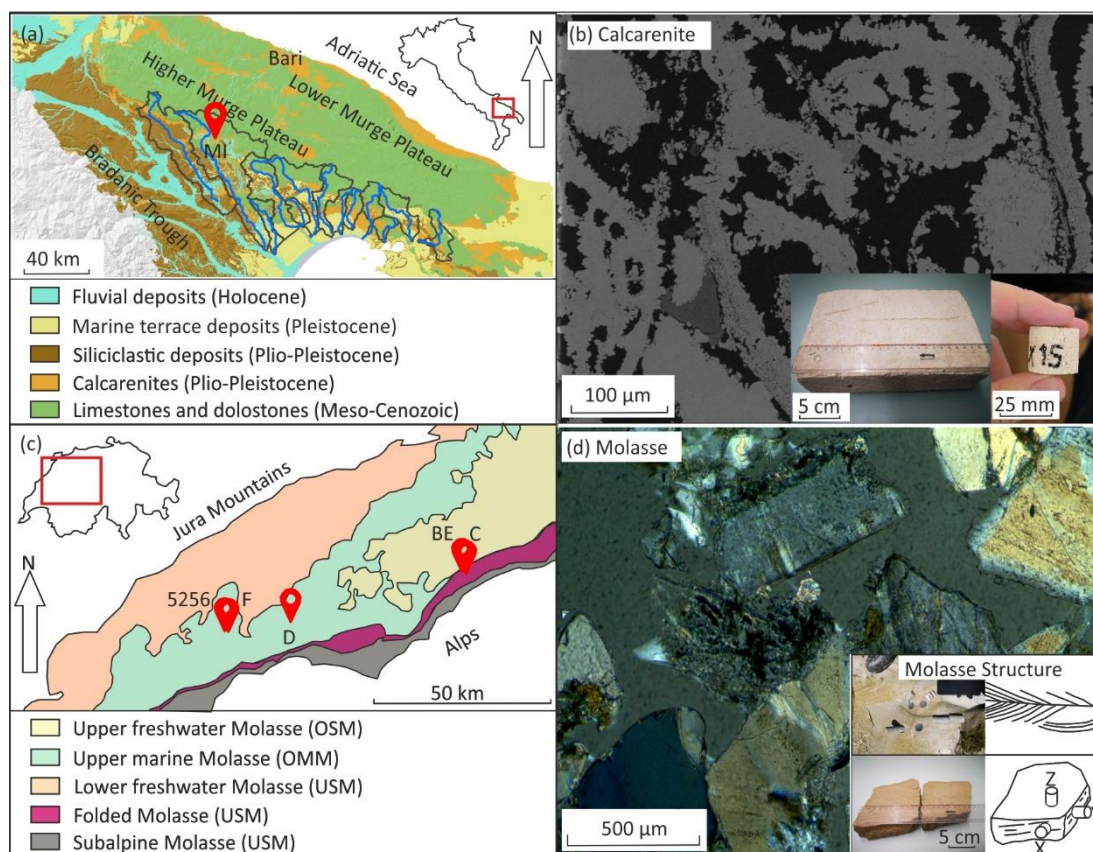


**Figure 3.2.** (a) Location of calcarenite samples, (b) Backscattered electron (BSE) image of calcarenite sample and photograph of calcarenite sample and core, (c) location of molasse samples, (d) thin section image and photograph of molasse sandstone with sketch on internal structure and drilling directions. Note the cross-stratification in the molasse sandstone. The core axis was generally oriented parallel or perpendicular to lamination, provided that lamination could be clearly identified. Coordinates of MI are  $40^{\circ}49'14.5''\text{N}$ ,  $16^{\circ}25'25.0''\text{E}$ ; for D  $46^{\circ}49'45.6''\text{N}$ ,  $7^{\circ}24'04.4''\text{E}$ ; for C  $46^{\circ}58'52.4''\text{N}$ ,  $8^{\circ}03'48.3''\text{E}$ ; for BE  $46^{\circ}58'54.3''\text{N}$   $8^{\circ}03'47.7''\text{E}$ ; for 5256  $46^{\circ}48'11.2''\text{N}$ ,  $7^{\circ}10'51.2''\text{E}$ , and for F  $46^{\circ}48'09.8''\text{N}$ ,  $7^{\circ}11'00.9''\text{E}$ . All molasse samples are OMM, even though mainly USM is present in the area where samples C and BE were obtained. Geological maps are modified after Donnalioia et al., 2019 (a), Sommaruga et al., 2012 and Wirth et al., 2020 (c).

### 3.2.2 XRCT data acquisition and processing

The Bruker SkyScan 2211 3D X-ray micro-tomography scanner perform initial scans at the University of Fribourg (15  $\mu\text{m}$  pixel size), and a Bruker SkyScan 1273 obtain later measurements at the University of Bern (9  $\mu\text{m}$  or 5.5  $\mu\text{m}$  pixel size). Samples D1112Y and C334Y were measured on both systems for different resolution (Table S3.1). However, the direct comparison between both systems was not performed for all samples, as part of them (MI-1-Z3, MI-2-Y3, MI-2-Y10, MI-3-X15, MI-3-X11, D1121Z, D1234X, D1221X, D1261X, C43Y and BE42AY) were impregnated or destructively analyzed after initial scanning with the Bruker Skyscan 2211, while others (MI-2-Y8, MI-5-Z21, MI-5-X22, D1263Y2 and 5256X, F31Z1) were measured only on the SkyScan 1273 for later analysis. XRCT data of impregnated samples were not further analyzed due to impregnation rendering the segmentation between ferrofluid/resin and solid fraction difficult. Rather, additional cores, so-called sister samples, were drilled from the original block in close proximity, assuming that both cores represent the same pore fabric. Pairs of sister samples

are given as Core1/Core2, where XRCT data were obtained on the first core, and MPF on the second, e.g., MI-3-X15/MI-3-X11. Where possible, XRCT data were obtained on Core1, and MPF data were obtained on both sister samples, allowing to test between-sample heterogeneity, e.g., MI-2-Y8/MI-2-Y10 and D1234X/D1221X. Sample MI-2-Y3 was drilled along the same direction as MI-2-Y8/MI-2-Y10 but further away, and similar situation for D1261X with D1234X/D1221X. The D12 block has a visible macroscopic fabric, parallel bedding, and thus similar pore fabrics are expected for samples along the same orientation.

Initially, different filters, voltage, current, and exposure time were used on each sample, in accordance with minor changes in their physical properties. Conditions for the X-ray source on the Bruker Skyscan 2211 were 80 kV/230  $\mu$ A for the calcarenites, and 100-156 kV/200-445  $\mu$ A for the molasse sandstones. Filters of 0.5 mm Al, 0.5 mm Ti, 0.5 mm Mo and 0.5 mm Cu were chosen for different samples. Images were acquired at 220 ms exposure time for calcarenite, and 100 - 300 ms for the molasse sandstone (Table S3.1). Different settings resulted in different contrast and artefacts, which could be corrected and removed during the reconstruction. Then it became evident that one consistent set of settings was sufficient for all samples to obtain images with good contrast and reduced artefacts. Only resolution was decisive in defining image quality. Settings on the Bruker Skyscan 1273 were the same for all samples with 100 kV/80  $\mu$ A, 1 mm Al+0.038 mm Cu filter, and 275 ms exposure time (Table S3.1). Reconstructions were performed using NRecon, and images were compensated for misalignment, corrected for ring artefacts and beam hardening artefacts (Skyscan, 2011).

After reconstruction, the unsharp masking filter (Polesel et al., 2000; Strobel, 1996) was applied to noisy images, to sharpen and enhance image details in Avizo versions 2019.4 and 2020.1. Single thresholding segmentation was applied to differentiate pores from the solid fraction based on the attenuation coefficients, expressed as grayscale values (Figure 3.3). Because the determination of a threshold value is user-dependent and affects the segmentation of pixels with intermediate values (Andrä et al., 2013; Karimpouli & Tahmasebi, 2019; Sun et al., 2017; Thomson et al., 2018), a watershed segmentation was applied to assign intermediate grayscale values (Bieniek & Moga, 2000). The uncertainties in calculated porosity were estimated by testing different thresholds (Figure S3.1).

To ensure the representativeness of the volume for XRCT-derived calculations while minimizing computational cost, the representative elementary volume (REV) was determined, by calculating porosity (defined as relative abundance of pixels with grayscale values identified as pores) or pore size distributions as a function of included volume. Porosity and pore size distribution were calculated for cubes of increasing size, from 100 x 100 x 100 voxels ( $0.9 \times 0.9 \times 0.9 \text{ mm}^3$ ) to 500 x 500 x 500 voxels. For small volumes, XRCT-derived parameters vary largely with increasing volume, reaching a plateau as cube size increases above a critical threshold. This threshold volume is the REV, i.e., the smallest volume representing the entire sample. Note that the REV can vary depending on the property of interest. Here, the REV for determining porosity is 100 x 100 x 100 voxels (cf Figure 3.3), while for pore size distributions, the REV is 300 x 300 x 300 voxels (Figure 3.4a, b). To further estimate the uncertainty associated with sample heterogeneity, calculated porosities from five  $5 \times 5 \times 5 \text{ mm}^3$  cubes located at different positions within the sample were compared to calculate a mean porosity with deviation (Table 3.1). Then, one cube was chosen arbitrarily for pore shape analysis (Figure 3.3).

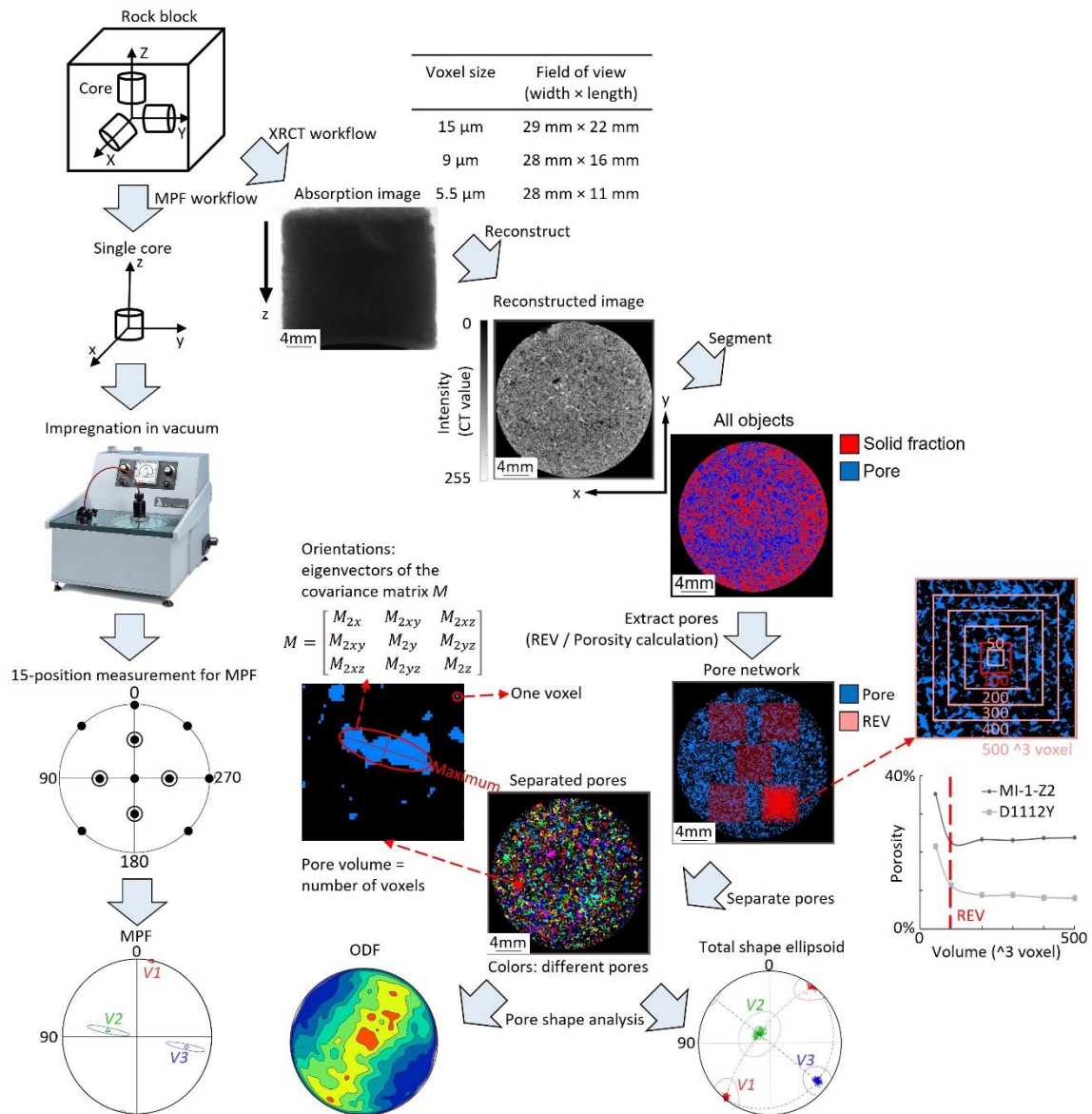


**Figure 3.3.** Workflow for XRCT image processing and MPF. The samples are scanned in field of view to obtain 28-29 mm width of images. Increasing voxel sizes are related to increasing fields of view. For 5.5 μm voxel size, results of two scans are stitched together after scanning in two horizontal positions. Absorption images are converted to cross-section images of greyscale CT intensity values during reconstruction. Hierarchical watershed segmentation divides the reconstructed volume into pores (blue) and solid fraction (red). Once the pore network is extracted from the segmented image, the bulk pore space is separated using the Skeleton-Aggressive algorithm which creates a connectivity network between the individual pores based on nodes and throats. The representative elementary volume (REV) is selected based the relationship between calculated porosity and sample size. The individual pore size is given as the equivalent diameter (EqDiameter) of a sphere that has the same volume as the pore, and the shape and orientation are defined by eigenvectors and eigenvalues of the covariance matrix  $M$  (a second-order tensor) (Text S3.1) (Avizo, 2020). The orientation density functions and total shape ellipsoids are derived from the matrices of single pores. The cores are impregnated by ferrofluid before measuring MPF.

Sample	Porosity (resolution: 15 µm / Skyscan 2211) (%) (threshold for pores, 0-255)	Porosity (resolution: 9 µm / Skyscan 1273) (%) (threshold for pores, 0-255)	Porosity (He pycnometry, AccuPyc 1340) (%)	Porosity (MPF) (%)
<b>Calcarenite</b>				
MI-1-Z3	43±4 (70)	▲	52±1	29.4
MI-2-Y3	36±4 (73)	▲	51.6±0.3	46.0
MI-2-Y8/MI-2-Y10	▲/▲	33±3 (74)/■	53.1±0.4/55.2±0.5	15.5/28.7
MI-3-X15/MI-3-X11	31±5 (65)/▲	▲/■	51.2±0.4/54.7±0.3	▲/28.9
MI-5-Z21	▲	35±3 (71)	55.2±0.2	17.5
MI-5-X22	▲	34±5 (68)	53.8±0.2	12.7
<b>Molasse (Rüeggisberg)</b>				
D1121Z	5±2 (45)	■	19.04±0.02	25.6
D1112Y	6±3 (45)	6±1 (45)	20.78±0.03	11.8
D1263Y2	▲	9±2 (55)	21.78±0.01	3.84
D1234X/D1221X	9±3 (55)/▲	■/■	19.01±0.01/20.29±0.01	10.7/9.26
D1261X	▲	▲	20.26±0.02	5.55
<b>Molasse (Entlebuch)</b>				
C43Y	4±4 (60)	■	16.0±0.2	7.63
C334Y	0.6±0.1 (55)	1.9±0.8 (60)	13.5±0.7	5.60
BE42AY	6.4±0.5 (65)	▲	12.05±0.01	6.69
<b>Molasse (Düdingen)</b>				
5256X	▲	4±1 (60)	11.13±0.01	▲
<b>Molasse (Tafers)</b>				
F31Z1	▲	16.4±1 (5.5 µm) (68)	30.78±0.07	9.22

**Table 3.1**

*Porosity comparison of numerical calculations based on XRCT data, laboratory measurements by He pycnometry and estimation from MPF*

*Note.* Uncertainty was estimated by calculating the standard deviation of five cube volumes (5 x 5 x 5 mm<sup>3</sup>) in five positions (XRCT) or the standard deviation of five measurements (He pycnometry). Triangle indicates data not measured and square indicates data not shown because they were measured after impregnation.

The segmented pore space was separated into individual pores to characterize pore shape and size distribution (Gostick, 2017; Soille, 2000). Pore size is given as equivalent diameter of a sphere with the same volume. Individual pores are approximated with best-fit ellipsoids, represented mathematically by symmetric second-order tensors whose eigenvalues  $a \geq b \geq c$  correspond to the lengths of the major, intermediate and minor ellipsoid axes, and the eigenvectors  $V1$ ,  $V2$  and  $V3$  describe their orientations (Figure 3.3 and Text S3.1) (Avizo, 2020). Pore fabrics are traditionally characterized by orientation density functions (ODFs) of the major and minor pore axes (Dullien, 1979). In the present study, ODFs are however strongly affected by artefacts arising from small pores whose geometry remained unresolved. A series of filters was applied to remove pores smaller than  $4 \times 4 \times 4$  voxels up to  $16 \times 16 \times 16$  voxels, to investigate related changes in the ODFs. Additional difficulties inherent to the characterization of major and minor axes by ODFs are that all pores contribute equally, independent of size, and the lack of information on pore shape. For example, in a strongly elongated pore, the minor and intermediate axes may be similar, so that the orientation of the minor axis is poorly defined.

An alternative approach to analyze the average pore fabric is introduced here to reduce these difficulties: the total shape ellipsoid, which is calculated by adding the unnormalized second-order tensors reflecting individual pores. Advantages of the total shape ellipsoid include: (1) The calculation was adapted from averaging normalized second-order tensors to compute a mean anisotropy of a group of samples (Jelínek & Kropáček, 1978). Normalized tensors ensure that each contribution has the same weight, so that the average is controlled by the most anisotropic item. Unnormalized tensors allow to give more weight to larger and better defined pores, and minimize resolution-related artefacts compared to ODFs; (2) the orientation distribution, pore shape distribution, and distribution of aspect ratios are integrated in one single measure; and (3) the total shape ellipsoid can be directly compared to other second-order tensor properties, including permeability and MPF. Finally, because the total shape ellipsoid is calculated from a large number of individual pores, its statistical robustness can be assessed by bootstrapping (Constable & Tauxe, 1990; Tauxe et al., 1998). Here, 500 total shape ellipsoids were calculated from randomly and repetitively choosing subsets including 579-14913 pores for different samples and resolutions (Hext, 1963; Jelínek & Kropáček, 1978; Owens, 2000). Finally, confidence ellipses were calculated based on those bootstrapped total shape ellipsoids and plotted by TomoFab (Petri et al., 2020).

The anisotropy of the individual pores as well as that of the total shape ellipsoid are described by the anisotropy degree  $P_s = a/c$ , and their shape by  $U_s = (2*b-a-c)/(a-c)$ . The definitions are analogous to standard parameters used for the characterization of magnetic anisotropy,  $P_m = k1/k3$  and  $U_m = (2*k2-k1-k3)/(k1-k3)$ , where  $k1 \geq k2 \geq k3$  are the principal susceptibilities (Jelinek, 1981).  $P_m$  and  $P_s$  range in the interval  $[1, \infty]$ , where 1 means isotropy and increasing values relate to increasing degrees of anisotropy. The values of  $U_m$  and  $U_s$  vary in the range  $[-1,1]$ , where -1 describes rotationally prolate ellipsoids and +1 indicates rotationally oblate ellipsoids. To investigate how different pore size windows affect pore fabrics, the fabrics of pores with  $EqDiameter \geq 100 \mu m$  and  $\leq 100 \mu m$  in sample MI-3-X15 were compared.

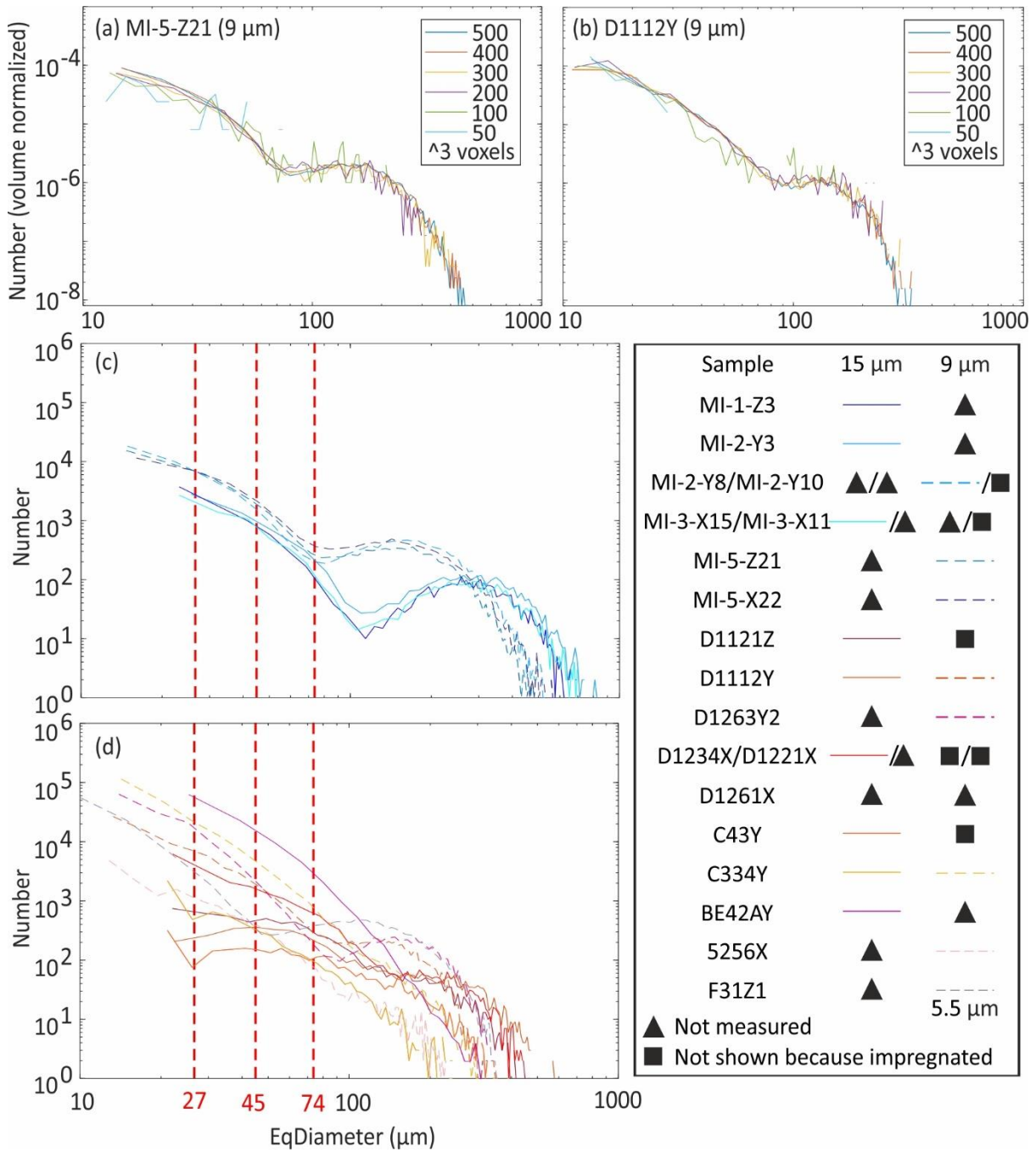


**Figure 3.4.** Results of pore size distribution for all XRCT scans. (a) and (b) present changes in pore size distribution associated with changing the included volume for calcarenite MI-5-Z21 and molasse D1112Y. The REV for pore size distribution is  $300^3$  voxels for both because the  $300^3$  voxels are the minimum volume to present similar pore size distribution. If the volume is smaller than  $300^3$  voxels, there are not enough pores to present the full range of distribution, and hence maxima and minima vary. (c) and (d) are pore size distributions for different calcarenites and molasse sandstones. The pore size is given as the equivalent diameter (EqDiameter) of a sphere that has the same volume as the pore. Only data obtained prior to impregnation are shown. The red vertical lines represent the threshold of  $4 \times 4 \times 4$  voxels (EqDiameter =  $27 \mu\text{m}$  for voxel size of  $5.5^3 \mu\text{m}^3$ , or  $45 \mu\text{m}$  for voxel size of  $9^3 \mu\text{m}^3$ , or  $74 \mu\text{m}$  for  $15^3 \mu\text{m}^3$  voxel size).

### 3.2.3 Magnetic pore fabric measurements

The AMS of the dry samples was measured using a 15 directions measurement scheme to determine the anisotropy of the rock itself (Jelinek, 1977). Two instruments were used, the magnetic susceptibility bridge SM150 from ZH instruments (Czech Republic) for initial measurements, followed by the MFK1-FA susceptibility bridge from AGICO (Czech Republic). The measurement frequencies were set to ~4 kHz, ~16 kHz, and ~512 kHz for the SM150, using a field of 80 A/m, the maximum available at all frequencies. On the MFK1-FA, frequencies of ~1 kHz, ~4 kHz, ~16 kHz were used with the standard field of 200 A/m. Five repeated measurements were obtained for every direction at each frequency, to increase data quality and assess the significance of anisotropy against the instrumental noise level (Biedermann et al., 2013). The noise level of the MFK1-FA is orders of magnitude lower than that of the SM150, so that the former is able to detect anisotropy where the latter cannot. Therefore, samples were remeasured on the MFK1-FA, except MI-1-Z3 and MI-2-Y3, which had been cut after impregnation to check the spatial variability of impregnation efficiency.

After characterizing their initial anisotropy, samples MI-1-Z3, MI-2-Y3 and MI-3-X15 were impregnated with oil-based ferrofluid (EMG 909 with an intrinsic susceptibility of 1.38 SI) diluted at 1:25 volume ratio of ferrofluid to light hydrocarbon carrier oil offered by Ferrotec. These samples were impregnated under vacuum for 24 hours at 100 kPa, following the technique outlined in Parés et al. (2016). After initial experiments had shown difficulties with impregnation efficiency, the remaining samples were impregnated with oil-based ferrofluid diluted by resin and hardener (hardener:resin = 1:4) under vacuum for 1 hour at 100 kPa. As the resin solidifies, it is thought to keep the magnetic nanoparticles immobile within the pores (Thorpe et al., 2016). Ferrofluid was diluted at volume ratio of 1:50 for molasse MI-2-Y10, MI-3-X11, D1121Z, D1112Y, D1234X, D1221X, C43Y, BE42AY, F31Z1 and 1:30 for the remaining molasse, and all calcarenite samples (Table S3.2). Any resin-ferrofluid mixture on the surface of the sample was cleaned before solidification to avoid artefacts. Unfortunately, the elimination was not thorough for samples MI-2-Y8, MI-5-X22, MI-5-Z21, D1263Y2, D1261X and C334Y, resulting in artefacts during MPF measurements. These samples were polished to remove leftover resin from the surface. Samples MI-3-X15 and 5256X broke during the impregnation experiment. New experiments will be performed once more sophisticated impregnation methods are available (Pugnetti et al., 2021).

To test which proportion of the pore space was impregnated, the susceptibility of impregnated samples was compared to the independently measured susceptibility of diluted ferrofluid and ferrofluid-resin mixtures. From this, the ferrofluid porosity, and susceptibility-based impregnation efficiencies were calculated (Parés et al., 2016). The susceptibility was divided by a coefficient 1-1.3 for 512-1 kHz to correct frequency dependence (Biedermann et al., 2021). The MPFs were measured as magnetic anisotropy after impregnation, following the same protocol as for AMS described above. Samples MI-1-Z3 and MI-2-Y3 were measured at 4 kHz, 16 kHz and 512 kHz on the SM150. Samples MI-3-X11, D1121Z, D1234X and C43Y were measured at 1 kHz, 4 kHz and 16 kHz on the MFK1-FA, and all remaining samples were measured at 1 kHz on the MFK1-FA, once it became clear that anisotropy is higher and better defined at lower frequency (Biedermann et al., 2021).

The data quality and statistical significance of the anisotropy compared to instrument noise for AMS and MPF are described by  $R1$  (Biedermann et al., 2013) as well as confidence angles  $E13$  ( $=E31$ ),  $E12$  ( $=E21$ ) and  $E23$  ( $=E32$ ) based on the 15 mean directional susceptibilities (Hext, 1963; Jelinek, 1977; Jelinek, 1981). Large  $R1$  values and small confidence angles indicate significant anisotropy and well-defined directions. Note that magnetic anisotropy measurements on dry samples are called AMS in this study, whereas the term MPF is used to indicate results on the impregnated samples. The susceptibility of the dry calcarenite samples is ~3 orders of magnitude

lower than that of the impregnated samples, and a factor of 4 to 10 lower for dry compared to impregnated molasse samples. Additionally, the AMS is not significant in many of the investigated rocks. Therefore, the AMS can be neglected, and only the MPF results will be discussed further.

### 3.2.4 Correlation of XRCT and MPF data

The size range of pores captured by XRCT or MPFs is different, and they yield different types of data: XRCT provides a grid of voxels identified as pores, whereas the MPF is an average representation of the overall pore fabric. Nevertheless, they can be compared when calculating a total shape ellipsoid, which represents the pore fabric of all pores larger than  $4 \times 4 \times 4$  voxels. Both total shape ellipsoids and MPFs are second-order tensors and represent the entire sample volume, which allows a direct comparison of fabric orientation, as well as the anisotropy degree and shape parameters. Abbreviations used as subscript are explained in Table S3.3. Note that the MPF  $P$ -value depends on the intrinsic susceptibility of the fluid used for impregnation in addition to the average pore shape (Biedermann, 2019; Jones et al., 2006). Therefore,  $P_m$  will always be lower than  $P_s$ , and it is also expected to be lower when the ferrofluid was more diluted. Nevertheless, an increase in  $P_m$  with increasing  $P_s$  is expected as long as the susceptibility of the fluid is constant.

## 3.3. Results

### 3.3.1 XRCT results

#### 3.3.1.1 3D reconstructions and porosity

The calcarenites present 31-43 % XRCT-derived porosities and 51.2-55.2 % He porosities, and molasse sandstones have 0.6-16.4 % XRCT-derived porosities and 11.13- 30.78 % He porosities (Table 3.1). There is no clear and uniquely defined limit in grey-scale values that distinguishes pores and solid fraction, due to averaging of the attenuation coefficients of pore and matrix in voxels containing a mix of both. Adjustment of the threshold value from 73 to 85 causes a change in calculated porosity for the calcarenite MI-2-Y3 of ~10 % (Figure S3.1). Additionally, pore throats are narrower than pores and thus harder to resolve by XRCT, leading to overestimating the isolated porosity and underestimating the connected porosity. The discrepancy between XRCT and He porosities is larger for molasse samples than calcarenites, due to the smaller pore size of molasse, resulting in a larger fraction of pores being below the spatial resolution of XRCT. These small pores are included in the He porosity, indicating that 46-95 % of the pore space in molasse sandstones and 17-43 % for calcarenites are not resolved by the XRCT data.

#### 3.3.1.2 Pore size distributions

The REV of pore size distribution was presented above (Figure 3.4a, b). Note that additional pores smaller than the voxel resolution ( $5.5^3 \mu\text{m}^3$ ,  $9^3 \mu\text{m}^3$  or  $15^3 \mu\text{m}^3$ ) may be presented. The different resolutions cause different datasets. Between 1 % and 22 % of the identified pores occupy a small number of voxels, generating unresolved shape and orientation. A lower threshold of  $4 \times 4 \times 4$  voxels was chosen for orientation and shape analyses, including 78–99 % of the XRCT-derived pore space and <83 % of the pore space defined by He pycnometry. Calcarenites display bimodal pore size distributions, with two maxima at ~20 and ~300  $\mu\text{m}$  equivalent pore diameter for samples measured with 15- $\mu\text{m}$  pixel size or at ~12 and ~150  $\mu\text{m}$  for samples with 9- $\mu\text{m}$  pixel size, as the range of pore sizes detected depends on the resolution. Molasse sandstones have a unimodal pore size distribution, where 95–99 % of micropores (1–22 % of the pore volume) have sizes below the threshold for shape/orientation resolution. For samples D1112Y and C334Y measured at both resolutions, additional micropores are identified at higher resolution, and C334Y also displays additional large pores at higher resolution (Figure 3.4).

#### 3.3.1.3 Pore orientation

As the orientation of pores below a certain size limit cannot be resolved, causing extreme maxima parallel to the sample  $x$ ,  $y$  and  $z$ -axes when including all identified pores for analysis. These

artefacts are reduced when increasing the lower threshold of analyzed pore sizes from 4 x 4 x 4 voxels to 16 x 16 x 16 voxels at the expense of diminishing the number of included pores. The total shape ellipsoids appear unaffected by these artefacts, and display similar orientations and anisotropy degrees, even when including the large number of small pores (66–84 % of the number of XRCT-derived pores but 1–5 % of XRCT-derived pore volume) (Figure 3.5a).

#### 3.3.1.3.1 Calcarenite

All samples whose names start with MI-1, MI-2 and MI-3 were drilled from the same block, in perpendicular directions. For MI-1-Z3,  $V1_{s\text{-individual}}$  group sub-parallel to the sample  $x$ -axis. The minor axes  $V3_{s\text{-individual}}$  form a girdle distribution in the  $yz$ -plane, with a sub-maximum parallel to  $z$ . The bootstrapped total shape ellipsoid displays a similar  $V1_{s\text{-total}}$  direction (at  $36^\circ$  from the sample  $x$ -axis), and the mean  $V3_{s\text{-total}}$  direction is at  $26^\circ$  to the sample  $y$ -axis (Figure 3.5a). A comparison of the total shape ellipsoid with individual pore orientations shows that  $V3_{s\text{-total}}$  is defined by the absence of  $V1_{s\text{-individual}}$  axes rather than a grouping of  $V3_{s\text{-individual}}$ . Sister samples MI-2-Y8/MI-2-Y10, and MI-2-Y3 were drilled in the same orientation, but display different fabric orientations. In MI-2-Y3,  $V1_{s\text{-individual}}$  show a girdle distribution in the  $yz$ -plane with three sub-maxima, and  $V3_{s\text{-individual}}$  group closely around  $z$ . The orientation of total shape ellipsoid, with  $V3_{s\text{-total}}$  at  $33^\circ$  to the  $x$ -axis and broad distributions of  $V1_{s\text{-total}}$  and  $V2_{s\text{-total}}$ , is dominantly controlled by the  $V1_{s\text{-individual}}$  distribution (Figure 3.5b). Conversely, the  $V1_{s\text{-individual}}$  axes of sample MI-2-Y8 show a girdle distribution within a plane rotated  $\sim 30^\circ$  from the  $xz$ -plane around the  $z$ -axis, and  $V3_{s\text{-individual}}$  axes are grouped at  $\sim 30^\circ$  to the  $y$ -axis in the  $xy$ -plane. The  $V1_{s\text{-total}}$  and  $V2_{s\text{-total}}$  axes show a broad distribution in the plane defined by the  $V1_{s\text{-individual}}$  girdle (Figure 3.5c). For MI-3-X15, both  $V1_{s\text{-individual}}$  and  $V1_{s\text{-total}}$  are sub-parallel to the  $z$ -axis. The  $V3_{s\text{-individual}}$  and  $V3_{s\text{-total}}$  directions group close to the  $y$ -axis. For  $\text{EqDiameter} \leq 100 \mu\text{m}$  and  $\geq 100 \mu\text{m}$  of pores,  $V3_{s\text{-total}}$  axes of both size windows are close to the  $y$ -axis and  $V1_{s\text{-total}}$  and  $V2_{s\text{-total}}$  are in the  $xz$ -plane (Figure 3.5d).

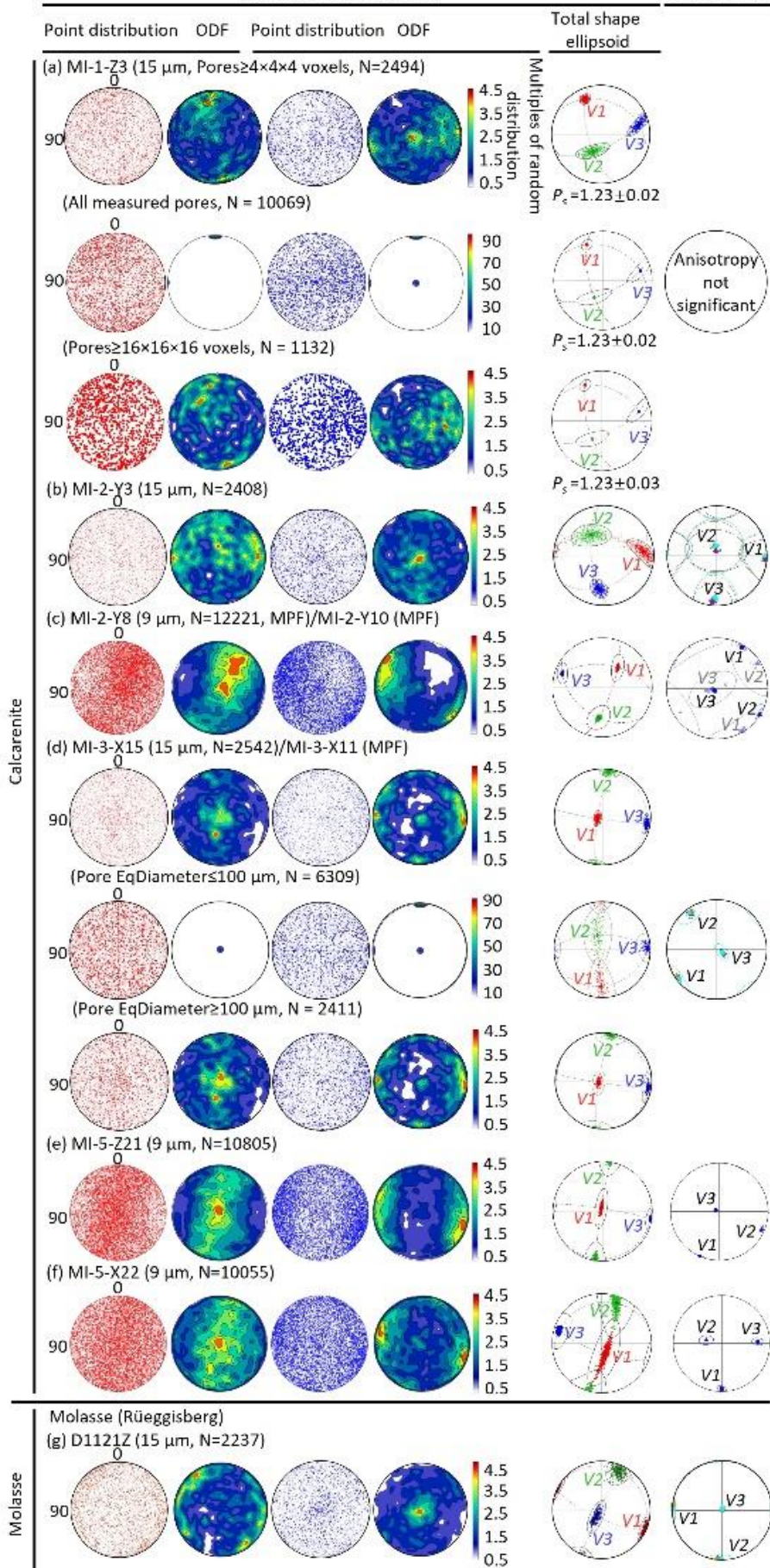
Samples MI-5-Z21 and MI-5-X22 were drilled from a second block, and their orientations are mutually perpendicular, but unrelated to previous calcarenite samples. Nevertheless, they show similar pore fabrics:  $V3_{s\text{-individual}}$  and  $V3_{s\text{-total}}$  group sub-parallel to  $y$ , and  $V1_{s\text{-individual}}$  groups sub-parallel to  $z$ , defining  $V1_{s\text{-total}}$  (Figure 3.5e, f).

The calcarenites MI-1-Z3, MI-2-Y3, MI-2-Y8 and MI-3-X15 are mutually perpendicular, and can be used to assess how representative fabrics on cores are for the entire block. If the block is perfectly homogeneous, the total shape ellipsoids should coincide once all datasets in a common coordinate system. After rotating all datasets to the sample coordinates of MI-1-Z3, the  $V1_{s\text{-total}}$  axes of MI-1-Z3, MI-2-Y3, MI-2-Y8 and MI-3-X15 are at  $9^\circ$ - $36^\circ$  to the  $x$ -axis, but are statistically distinct at 95 % confidence. The orientations of  $V2_{s\text{-total}}$  and  $V3_{s\text{-total}}$  axes are largely variable (Figure S3.2). Additionally, the type of grouping is different for each sample: in MI-1-Z3, the  $V1_{s\text{-total}}$  form a point distribution, whereas the  $V3_{s\text{-total}}$  form a point distribution in MI-3-X15. This indicates between-sample heterogeneity, and implies that a large number of standard-sized samples would need to be measured and averaged to obtain a pore fabric representative of this rock.

5a)

XRCT derived pore fabrics  
(Orientation of pore axes)

Magnetic  
pore fabrics



5b)

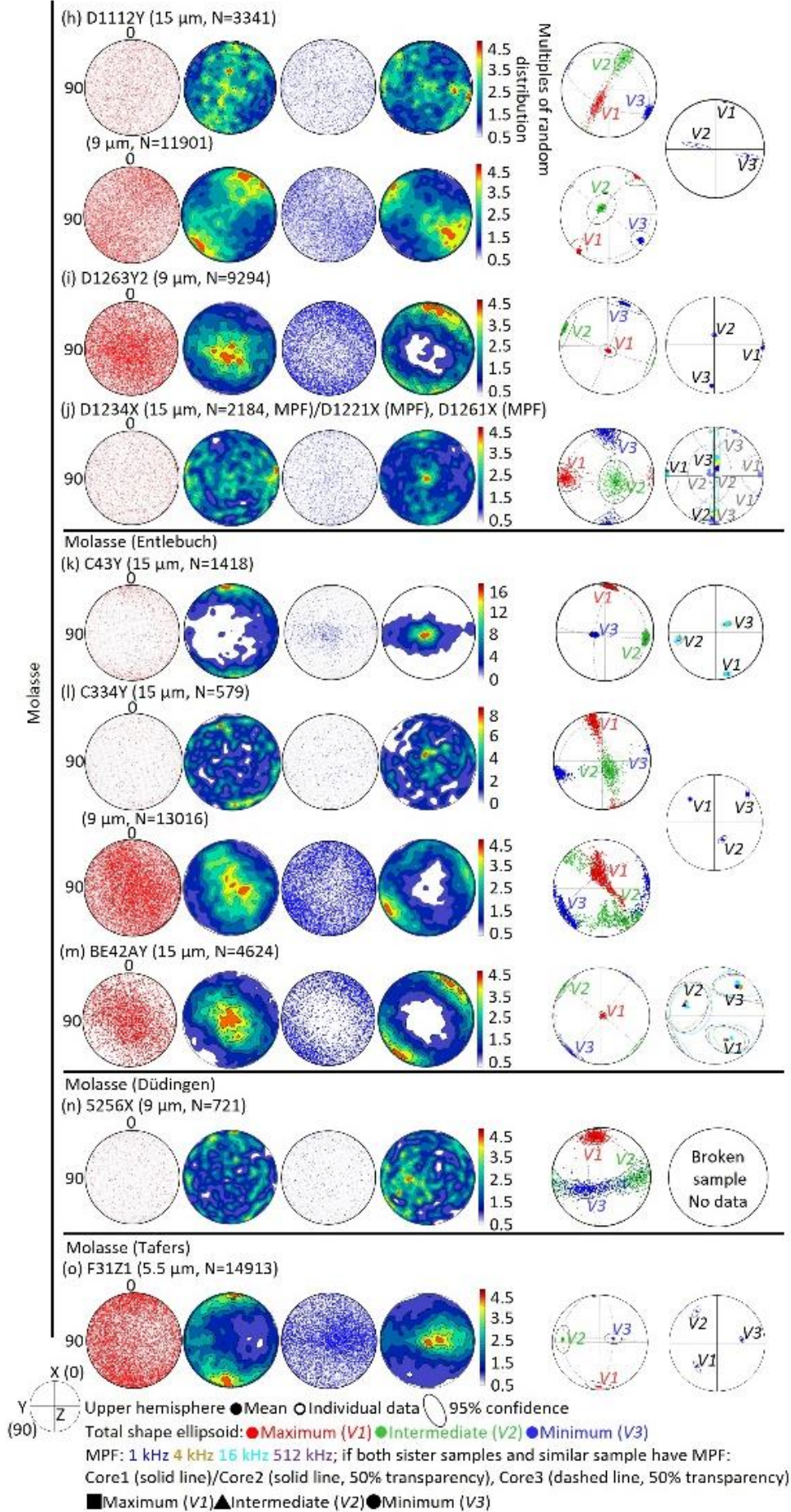


**Figure 3.5.** Comparison of point distribution and ODFs of pore axes, bootstrapped total shape ellipsoids, and MPFs for calcarenites and molasses. ODFs include pores larger than  $4 \times 4 \times 4$  voxels to reduce resolution artefacts. Pore orientation and MPF results are shown on upper hemisphere equal area stereonet.  $V1$ ,  $V2$  and  $V3$  indicate the maximum, intermediate and minimum axes of the total shape ellipsoid. The ellipses show the 95 % confidence based on bootstrapping (Constable & Tauxe, 1990; Hext, 1963; Jelínek & Kropáček, 1978; Owens, 2000; Tauxe et al., 1998). The total shape ellipsoid with confidence ellipses is drawn using the TomoFab MATLAB code, and the red dashed line highlights the  $V1$ – $V2$  plane, i.e., the foliation defined by the SPO; the lineation corresponds to the direction of  $V1$  (Petri et al., 2020). Principal susceptibility directions are shown for averaged (solid symbols), and individual datasets (open symbols). (a) presents the comparison of point distributions and orientation density functions of pore axes and total shape ellipsoids as a function of pore size threshold for MI-1-Z3.  $P_s$  is the anisotropy degree of total shape ellipsoid. (d) presents the comparison of point distributions and orientation density functions of pore axes and total shape ellipsoids with different pore size windows ( $EqDiameter \leq 100 \mu\text{m}$  and  $\geq 100 \mu\text{m}$ ) for MI-3-X15.

### 3.3.1.3.2 Molasse

Samples D11 and D12 were drilled from two different blocks collected at the same site. Samples C43Y and C334Y were also drilled from blocks from the same location, but with different orientations. Sample 5256X was from another block. For molasse D1121Z, the  $V3_{s\text{-individual}}$  and  $V3_{s\text{-total}}$  group around the  $z$  direction, and the  $V1_{s\text{-individual}}$  present a girdle distribution in the  $xy$  plane, which is also reflected by the total shape ellipsoid (Figure 3.5g). Sample D1112Y was measured at both resolutions, 15- $\mu\text{m}$  and 9- $\mu\text{m}$ , and both datasets show girdle distributions of  $V1_{s\text{-individual}}$ , and  $V1_{s\text{-total}}$  axes rotated  $\sim 30^\circ$  around the  $z$ -axis from the  $xz$ -plane. The directions for  $V3_{s\text{-individual}}$  and  $V3_{s\text{-total}}$  group at  $\sim 30^\circ$  from  $y$  in the  $xy$ -plane. Despite these similarities, the ODFs change significantly with resolution. For example, the grouping of  $V1_{s\text{-individual}}$  and  $V3_{s\text{-individual}}$  is more pronounced in the higher-resolution data. These differences are reflected by the total shape ellipsoids (Figure 3.5h), and may be a result of resolution artefacts, or indicate size-dependent pore orientation. For D1263Y2, the orientation of the total shape ellipsoid is controlled by the main groupings of  $V1_{s\text{-individual}}$  and  $V3_{s\text{-individual}}$  (Figure 3.5i). Conversely, for D1234X,  $V2_{s\text{-total}}$  is sub-parallel to the maximum grouping of  $V3_{s\text{-individual}}$ , while  $V1_{s\text{-total}}$  aligns with the maximum of a broad distribution of  $V1_{s\text{-individual}}$ . Thus, it is the absence of  $V1_{s\text{-individual}}$  rather than the presence of  $V3_{s\text{-individual}}$  that define the orientation of  $V3_{s\text{-total}}$  (Figure 3.5j).

For molasse sample C43Y, the  $V1_{s\text{-individual}}$  and  $V1_{s\text{-total}}$  axes are sub-parallel to  $x$ . The  $V3_{s\text{-individual}}$  and  $V3_{s\text{-total}}$  show a pronounced maximum along  $z$  (Figure 3.5k). Sample C334Y displays largely different ODFs for data obtained with 15  $\mu\text{m}$  and 9  $\mu\text{m}$  resolution. The 15  $\mu\text{m}$  data show the  $V1_{s\text{-individual}}$  sub-parallel to  $x$  and  $V3_{s\text{-individual}}$  along  $z$ . Conversely, the higher-resolution data shows a concentration of  $V1_{s\text{-individual}}$  parallel to  $z$ , i.e., along the preferred directions of  $V3_{s\text{-individual}}$  as identified by 15  $\mu\text{m}$  data. Also the orientation of the total shape ellipsoid is resolution-dependent, although the discrepancy is less than observed in the ODFs (Figure 3.5l). This observation highlights the importance of adequate resolution in XRCT studies. For sample BE42AY, the  $V1_{s\text{-individual}}$  and  $V1_{s\text{-total}}$  axes are along  $z$ . The  $V3_{s\text{-individual}}$  and  $V3_{s\text{-total}}$  are at  $\sim 30^\circ$  from  $x$  in the  $xy$ -plane (Figure 3.5m).

A relatively small number of pores was identified above the size threshold suitable for fabric analysis in 5256X, resulting in ODFs with many sub-maxima. As a consequence, the total shape ellipsoid is poorly defined, especially in the  $V2$ - $V3$  plane (Figure 3.5n). The confidence angles of the total shape ellipsoid may thus indicate the quality of the underlying XRCT data. Sample F31Z1 shows the  $V1_{s\text{-individual}}$  and  $V1_{s\text{-total}}$  axes along  $x$ . The directions for  $V3_{s\text{-individual}}$  and  $V3_{s\text{-total}}$  group at  $\sim 20^\circ$  from  $z$  in the  $yz$ -plane (Figure 3.5o).

### 3.3.1.4 Pore shape and anisotropy degree

For all samples, the individual pores present a large range of pore shapes ( $U_{s\text{-individual}}$  varies from -0.99 to +0.99) and anisotropy degrees ( $P_{s\text{-individual}}$  varies from 1.14 to 2826). The total shape ellipsoid shows a lower anisotropy degree than the individual pores ( $P_{s\text{-total}}$  of 1.07-2.41), and a slightly smaller range of  $U_{s\text{-total}}$  values from -0.99 to 0.98, which reflects the large variability in pore orientations (Figure 3.6).

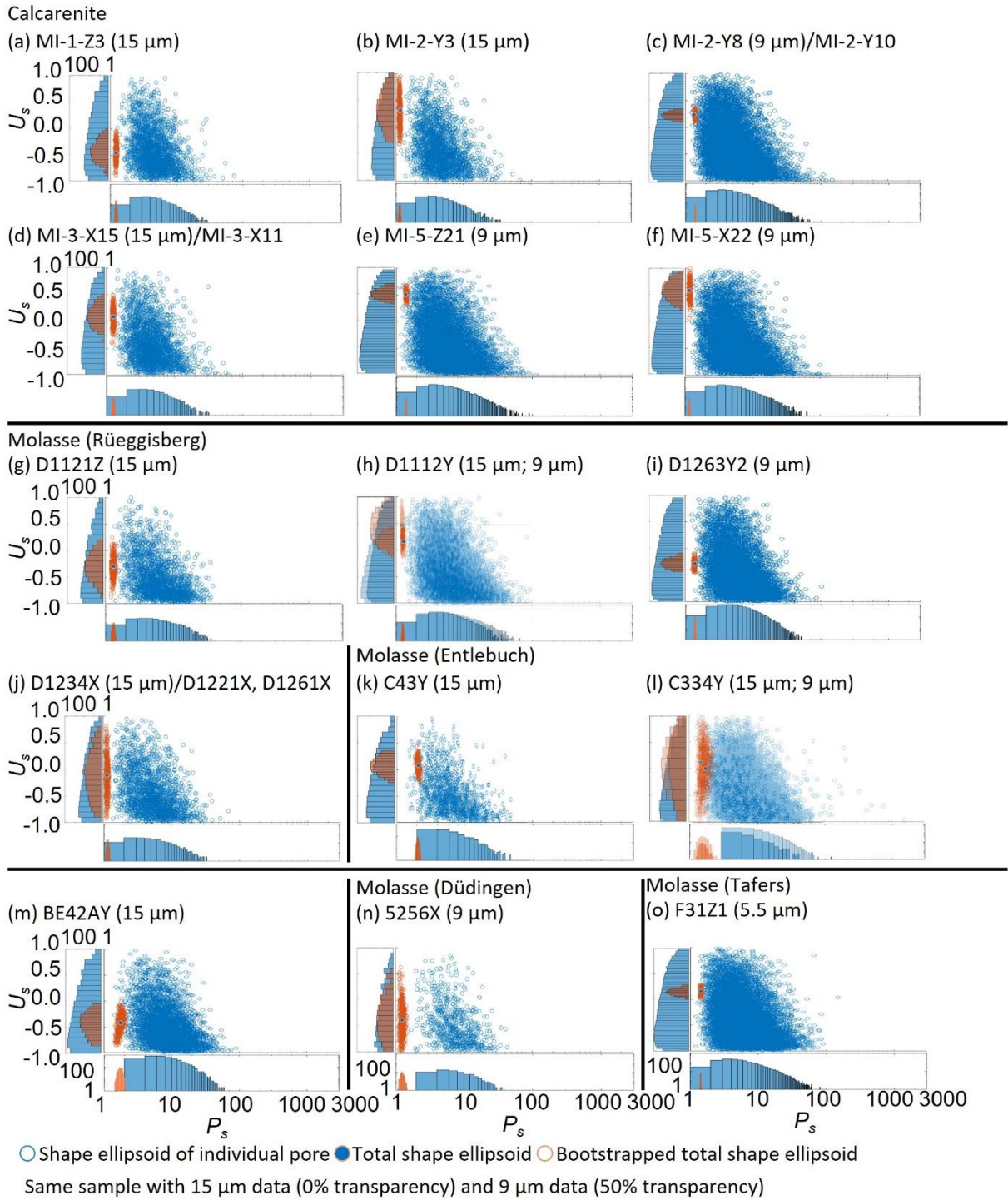


**Figure 3.6.** Anisotropy degree  $P_s$  ( $P_{s\text{-individual}}$ ,  $P_{s\text{-total}}$ ) and shape  $U_s$  ( $U_{s\text{-individual}}$ ,  $U_{s\text{-total}}$ ) of individual pore best-fit ellipsoids, total shape ellipsoid and bootstrapped total shape ellipsoid for all samples.

### 3.3.2 MPF results

After impregnation, the volume-normalized mean susceptibility is  $1.47\text{--}20.60 \times 10^{-3}$  SI for calcarenites and  $4.44\text{--}19.03 \times 10^{-4}$  SI for molasse sandstones (Table S3.4). The susceptibility of diluted ferrofluid is  $4.36\text{--}4.39 \times 10^{-2}$  SI (1:25 oil),  $1.16 \times 10^{-2}$  SI (1:30 resin) and  $7.11\text{--}7.39 \times 10^{-3}$  SI (1:50 resin). The MPF-derived porosity is 12.7–47.1% for calcarenites and 3.84–26.2% for molasse sandstones (Table 3.1), reflecting  $I.E.susc$  of 23.7–91.3% and 17.6–138%, respectively.  $I.E.susc$  with diluted oil (52–91.5%) is higher than one with resin mixture (23.7–53.0%) for calcarenites (Table S3.4).

#### 3.3.2.1 Magnetic fabric orientation

Not all calcarenites display well-defined MPFs; MI-1-Z3 shows no significant anisotropy (Figure 3.5a). Samples MI-2-Y3 (measured at 512 kHz) and MI-2-Y10 (1 kHz) display significant anisotropy, but their principal directions are poorly defined (Figure 3.5b, c). Samples MI-2-Y8, MI-3-X11, MI-5-Z21 and MI-5-X22 show significant anisotropy, and well-defined directions (Figure 3.5c, d, e, f, and Table S3.4). The  $V3_{m-MPF}$  of sample MI-2-Y8 is sub-parallel to the  $z$ -axis. The  $V1_{m-MPF}$  is at  $31^\circ$  to  $x$ -axis in the  $xy$ -plane (Figure 3.5c). For sample MI-3-X11, the MPFs measured at different frequencies are co-axial, with largest confidence angles at 16 kHz, and  $V1_{m-MPF}$  at  $36^\circ$  to the  $y$ -axis in the  $xy$ -plane,  $V3_{m-MPF}$  sub-parallel to the  $z$ -axis (Figure 3.5d). For sample MI-5-Z21, the  $V1_{m-MPF}$  deviates  $24^\circ$  from the  $x$ -axis, and  $V3_{m-MPF}$  is oriented along  $z$ -axis (Figure 3.5e). The  $V1_{m-MPF}$  of sample MI-5-X22 is parallel to the  $x$ -axis, and  $V2_{m-MPF}$  and  $V3_{m-MPF}$  lie within the  $yz$ -plane (Figure 3.5f).

Most molasse samples show significant anisotropy and well-defined directions. Sample D1221X possesses significant anisotropy but poorly defined directions, and samples D1234X and D1261X have a well-defined  $V1_{m-MPF}$ , but large confidence angles in the  $V2_{m-MPF} - V3_{m-MPF}$  plane (Figure 3.5). For sample D1121Z, the MPFs show similar orientation independent of frequency and the  $V1_{m-MPF}$ ,  $V2_{m-MPF}$  and  $V3_{m-MPF}$  are along to the  $y$ -,  $x$ - and  $z$ -axes, respectively. Largest confidence angles are observed at 16 kHz (Figure 3.5g). The  $V1_{m-MPF}$  of sample D1121Y is  $\sim 10^\circ$  from the  $x$ -axis, and  $V2_{m-MPF}$  and  $V3_{m-MPF}$  are in a plane that is rotated ca  $10^\circ$  around  $z$  from the  $yz$ -plane (Figure 3.5h). Both samples D1263Y2 and D1234X show well-defined  $V1_{m-MPF}$  sub-parallel to the  $y$ -axis, and  $V2_{m-MPF}$  and  $V3_{m-MPF}$  in the  $xz$ -plane (Figure 3.5i, j). Sample D1221X and BE42AY have significant anisotropy of MPFs but poorly defined directions. Sample D1261X shows well-defined  $V2_{m-MPF}$  along  $z$ -axis, and  $V1_{m-MPF}$  and  $V3_{m-MPF}$  rotated  $\sim 30^\circ$  around the  $z$ -axis in the  $xy$ -plane (Figure 3.5j, m). The MPFs of sample C43Y in different frequencies possess the same well-defined  $V1_{m-MPF}$ ,  $V2_{m-MPF}$  and  $V3_{m-MPF}$  at  $\sim 10^\circ$  to the  $x$ ,  $y$  and  $z$  directions, respectively (Figure 3.5k). Sample C334Y has well defined  $V1_{m-MPF}$  and  $V2_{m-MPF}$  in a plane rotated ca  $45^\circ$  around  $z$  from the  $xz$ -plane and  $V3_{m-MPF}$  at  $\sim 45^\circ$  to  $x$ -axis (Figure 3.5l). For sample F31Z1, MPF axes are well defined. The  $V1_{m-MPF}$  is at  $\sim 20^\circ$  from the  $xy$ -plane, and  $V3_{m-MPF}$  is at  $\sim 30^\circ$  to the  $z$ -axis (Figure 3.5o).

#### 3.3.2.2 Anisotropy degree and shape of the magnetic fabric

The MPF anisotropy degrees of calcarenites are 1.01–1.05, and the shape values  $U_{m-MPF}$  vary between -0.79 and 0.52 for samples with significant anisotropy. Note that the anisotropy shape is poorly defined for samples with low anisotropy and noisy data (Biedermann et al., 2013), which explains the large variability in these datasets. The molasse sandstones show higher anisotropy degrees, with  $P_{m-MPF}$  between 1.01 and 1.20, and the shape values  $U_{m-MPF}$  range from -0.86 to 0.37. The samples that were measured at several frequencies mostly show different  $U_{m-MPF}$  values and similar  $P_{m-MPF}$ . Conversely, sample D1121Z shows similar  $U_{m-MPF}$  values at all frequencies, but  $P_{m-MPF}$  appears to vary with measurement frequency, and is higher than for other molasse samples from the same block (Figure 3.7).

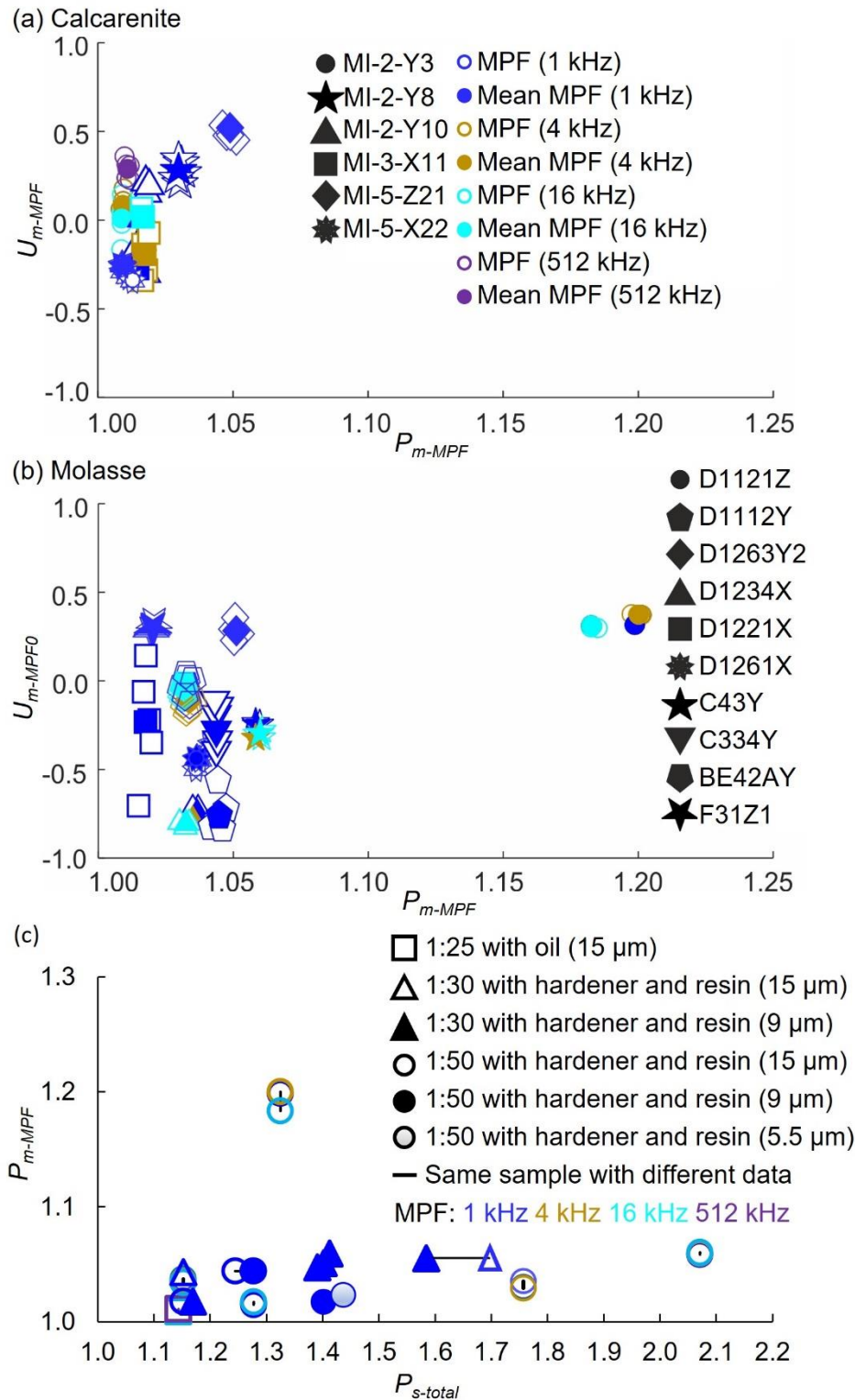


**Figure 3.7.** (a) and (b) Anisotropy degree and shape of the magnetic fabric. Sample MI-2-Y3 was measured at 4 kHz, 16 kHz and 512 kHz on the SM150. MI-3-X11, D1121Z, D1234X, C43Y and BE42AY were measured at 1 kHz, 4 kHz and 16 kHz on the MFK1-FA. Remaining samples were measured at 1 kHz on the MFK1-FA. (c) Degree of magnetic anisotropy ( $P_{m-MPF}$ ) against anisotropy degree of total shape ellipsoid ( $P_{s-total}$ ). All samples were measured in 15  $\mu\text{m}$ , 9  $\mu\text{m}$  or 5.5  $\mu\text{m}$  XRCT and impregnated by oil-based ferrofluid (EMG 909), using different concentrations.

### 3.3.3 Comparison of XRCT and MPF data

#### 3.3.3.1 Porosities

For calcarenite, XRCT-derived porosities are 13.6-21.3% higher than MPF-derived ones except MI-2-Y3 (10% lower), and molasse presents opposite results (0.3-20.0% lower) except D1263Y2 and F31Z1 (5.2-7.2% higher). MPF-derived porosities with diluted oil (29.4-46.0%) are higher than ones with resin mixture (12.7-28.9%) for calcarenites. For calcarenites, the XRCT-derived porosities (31-43%) have lower variability than MPF data (12.7-46.0%). For molasses, both methods have large variability (0.6-16.4% for XRCT and 3.8-25.6% for MPF) (Table 3.1).

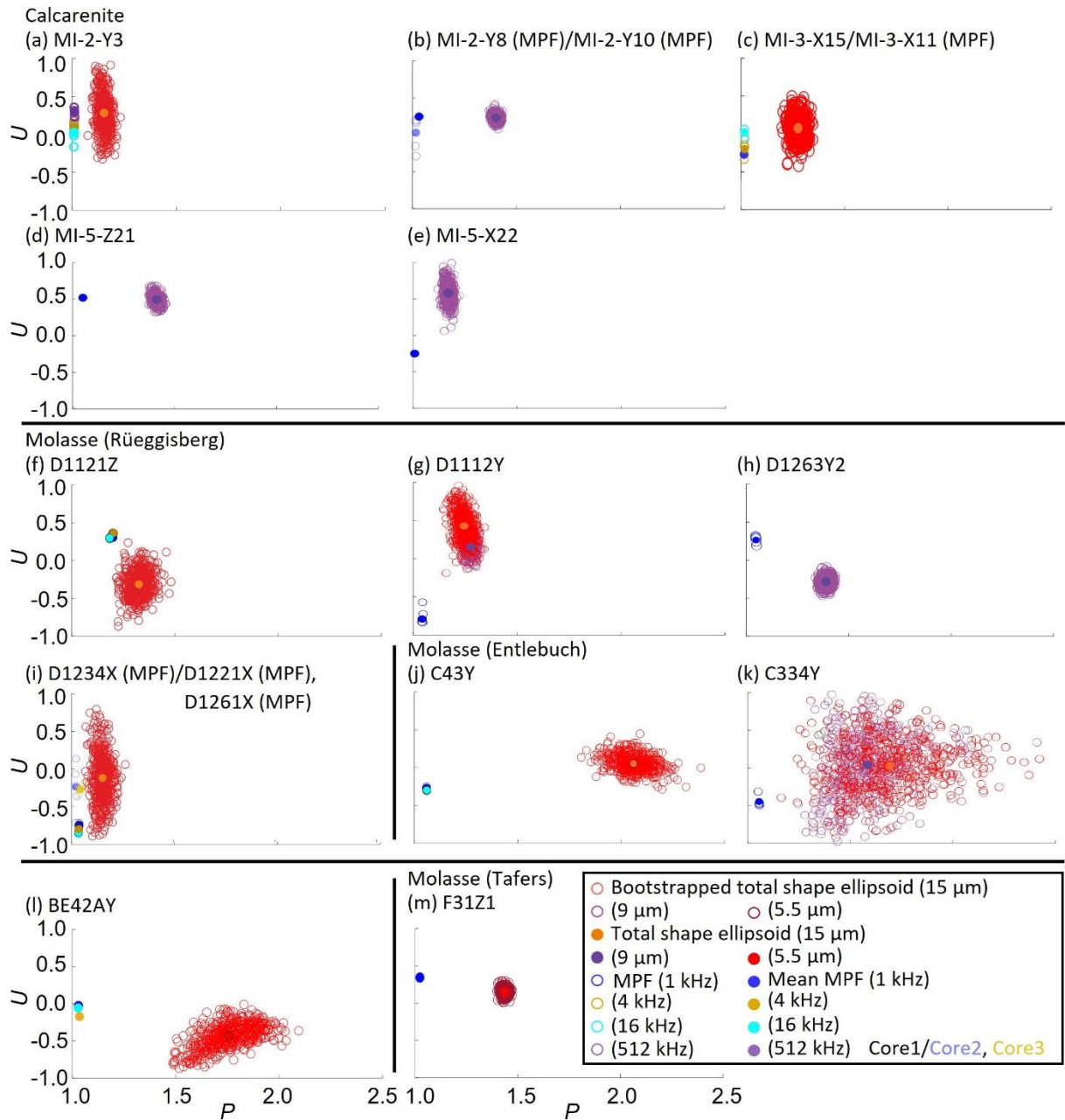


**Figure 3.8.** Comparison of anisotropy degree and shape derived from XRCT (total shape ellipsoid) and MPF datasets. Samples MI-1-Z3, MI-2-Y3 and MI-3-X15 were measured at 4 kHz, 16 kHz and 512 kHz on the SM150. MI-3-X11, D1121Z, D1234X, C43Y and BE42AY were measured at 1 kHz, 4 kHz and 16 kHz on the MFK1-FA. Remaining samples were measured at 1 kHz on the MFK1-FA.

### 3.3.3.2 Directional comparison

For MI-2-Y3,  $V1$  and  $V3$  directions of total shape ellipsoids and MPF at 512 kHz agree with each other at 95 % confidence level. Similarly, total shape ellipsoids and MPFs are generally coaxial in samples D1121Z, D1112Y, D1234X, D1261X and D1221X. The principal directions of the total shape ellipsoid and MPF are sub-parallel in C43Y, C334Y and BE42AY but distinct at 95 % confidence. For MI-5-X22, D1263Y2 and F31Z1,  $V3$  directions of total shape ellipsoid and MPF are similar but their  $V1$  and  $V2$  axes are distinct. Conversely, directions are statistically distinct at 95 % confidence in samples MI-2-Y8 and MI-5-Z21 (Figure 3.5).

### 3.3.3.3 Comparison of anisotropy degree and shape

The MPF anisotropy degree is lower than that of the total shape ellipsoid in all samples. It is expected that  $P_{m-MPF}$  increases with  $P_{s-total}$ , and a higher-susceptibility ferrofluid causes stronger increase. Inconsistent correlations are presented in our data, partly due to measurement uncertainty, and only few datasets existing with the same ferrofluid susceptibility and measurement frequency, hindering statistical analysis. For similar reasons, it is impossible to evaluate whether  $P_{m-MPF}$  displays a consistent frequency dependence (Figure 3.7). Anisotropy shapes agree within uncertainty for total shape ellipsoid and MPF in samples MI-2-Y3, MI-2-Y8, MI-5-Z21, D1234X, D1261X, D1221X, BE42AY and F31Z1, but are different for both fabric measurements in the remaining samples (Figure 3.8). Comparing higher and lower resolution XRCT data suggests that both D1112Y and C334Y show similar anisotropy degree and shape at both resolutions (Figure 3.8g, k).

## 3.4. Discussion

3D pore fabrics of calcarenite and molasse sandstone were investigated directly by XRCT, and indirectly by MPF. The XRCT technique is commonly used to characterize the internal structure of reservoir rocks because of non-destructiveness and 3D descriptions on pore fabrics (Cnudde & Boone, 2013; Landis & Keane, 2010; da Silva, 2018; Zeng et al., 2017). However, due to limited resolution and related artefacts, the smallest pores are unresolved by XRCT, and distinguishing isolated and connected pores is challenging because of narrow pore throats (Feser et al., 2008; Gelb et al., 2009; Zhan et al., 2009; Zubair, 2012). The voxel size is 5.5, 9 or 15  $\mu\text{m}$ , corresponding to a spatial resolution of  $10^3 \times 648$ ,  $46^3 \times 656$  or  $216^3 \times 000 \mu\text{m}^3$  ( $4 \times 4 \times 4$  voxels) for characterizing pore fabrics. Selecting  $4 \times 4 \times 4$  voxels as filter was a compromise between keeping as many pores as possible and reducing resolution-related artefacts that affect the ODFs of the major and minor pore axes at the expense of losing 1 % to 22 % of XRCT-derived pores (Table 3.1), decreasing the representativeness. Fabric orientations in different pore size windows show sub-parallel axes and different confidence angles, because window of smaller pores includes more unresolved micropores (Figure 3.5d). The comparisons of different resolutions (9  $\mu\text{m}$  and 15  $\mu\text{m}$ ) indicate higher resolution detects more micropores, and also more small grains decreasing pore volume. One sample presents additional pores in all sizes with higher resolutions, probably because changing XRCT threshold to segment pores caused more pores resolved in all sizes. For these, different fabric orientations are observed between two datasets (Figure 3.5h, l), indicating that different pore sizes display different pore fabrics. Conversely, anisotropy degrees and shapes appear independent of resolution (Figure 3.6h, l, and 3.8g, k). This suggests that the pore shapes and aspect ratios are similar across all pore sizes, while their orientations vary.

A total shape ellipsoid is introduced to minimize the effect of resolution-related artefacts without excluding small pores, providing a more stable measurement of pore fabric. In addition to reducing artefacts, the total shape ellipsoid can also derive an average pore fabric from a poorly defined and noisy ODF, and it allows a direct comparison of pore fabrics with second-order tensor properties, such as magnetic susceptibility, permeability or thermal diffusivity. We recommend this strategy for future analyses of pore or grain shape distributions in studies about average fabric

determination, or when modeling physical properties for reservoir evaluation and characterization. We expect that analyses based on total shape ellipsoids are particularly applicable to rocks with simple ellipsoidal pores. An alternative approach in need of further tests, is to use the best-fit ellipsoids of pores as input for a numerical model calculating MPFs for given pore assemblies and ferrofluid susceptibility (Biedermann, 2020). Complex pore shapes may need more sophisticated descriptions from further investigations.

The MPF method has been proposed as an efficient pore fabric characterization technique to capture pores down to 10 nm (Pfleiderer & Halls, 1993; Robion et al., 2014). If reaching this limit, it would provide insight into the fabric of small pores unresolved by XRCT. There is no linear trend between the concentration and fluid susceptibility because susceptibility is lower when using resin rather than oil for dilution (Pugnetti et al., 2021). Fluid susceptibility still varies (<4%) after correcting frequency dependence, possibly because of the discrepancy between this study and Biedermann et al. (2021), e.g., time dependence. If changing corrected coefficient, all derived quantities, e.g., impregnation efficiency will change. The impregnation efficiency varies largely for different samples when using the standard vacuum impregnation method commonly applied in MPF studies (Parés et al., 2016; Pugnetti et al., 2021) (Table S3.4).  $I.E._{susc}$  and MPF-derived porosities with diluted oil are higher than with resin mixture, due to higher viscosity of resin causing harder impregnation. He-pycnometer porosity is higher than MPF and XRCT-derived porosities. MPF presents higher porosity than XRCT for most molasses but opposite for most calcarenites, possibly because in the large pores, ferrofluid particles may aggregate and sediment (Figure 3.2b, d). XRCT-derived porosities for calcarenites present lower variability than ones for molasses, may due to large pores easily resolved by XRCT. Ferrofluid on the sample surface was not entirely eliminated, may causing  $I.E._{susc} > 100\%$  and MPF-derived porosity  $>$  He-pycnometer porosity in the corresponding samples and MPF-derived porosities varying for different samples and diluents. The anomalies may also result from inhomogeneous fluid, and the uncertainty in the determination of fluid susceptibility/frequency dependence, because of the time-dependent nature of fluid properties. Nevertheless, results presented here show a quantitative relationship between MPF and XRCT-derived pore fabric. Six out of 12 samples exhibit the same fabric orientation for XRCT and MPF data at 95 % confidence, including only one calcarenite, probably because very weak anisotropy of calcarenite makes it impossible to interpret orientation. With very large pores, ferrofluid sedimenting to the bottom of pore may cause changes to MPF, especially for an almost isotropic sample, e.g., calcarenite. The additional three samples show sub-parallel fabric orientations, though they are distinct at 95 % confidence. Three samples possess fabrics with minimum axes that are co-axial between XRCT and MPF data but one of them shows deviations in the other two axes. In the other, the orientations of  $V1$  and  $V2$  axes cannot be compared, as  $V1_{s-total}$  and  $V2_{s-total}$  directions are not statistically significant. Observed discrepancies in the XRCT and MPF fabric measures may be related to artefacts with either method, e.g., incomplete or inhomogeneous impregnation may affect MPF data, and resolution artefacts affect XRCT, as evidenced by differences in the fabric obtained on the same sample when measured at different resolutions and when considering different pore size windows in the same sample. Where XRCT data at 9 and 15  $\mu\text{m}$  resolution did not agree, the higher-resolution XRCT data was compared with the MPFs, as this captures more pores, and better reflects the pores targeted by MPFs. Related to the observation that XRCT scans at different resolutions produce different pore fabric orientations, MPFs may show different fabrics as they capture smaller pores than XRCT. In this case, the investigated methods target different parts of the pore space, and thus provide complementary information when used together. Thus, discrepancies between MPF and XRCT fabric orientations in some samples indicate a variation of pore fabric with pore size, provided that other sources such as measurement uncertainty and impregnation artefacts can be excluded. To investigate this further, a complete set of XRCT data measured at different resolutions would be necessary, which may become possible after technological advancements. Until then, the agreement of XRCT and MPF

fabric orientations in two thirds of the samples investigated here highlight the potential of the MPF method, and suggest that it could be useful to characterize the fabric of pores with sizes below the XRCT-resolution on standard-sized cores. Previously published empirical relationships between average pore shape and MPF, or the average pore elongation direction and the maximum principal susceptibility of the MPF (Hrouda et al., 2000; Jones et al., 2006; Pfliegerer & Halls, 1993) are partly confirmed, and the concept of the total shape ellipsoid further expands these relationships, as it allows quantitative comparison.

The magnetic anisotropy degree is lower than the anisotropy degree of the total shape ellipsoid. This is expected, given the physics of self-demagnetization and shape anisotropy, and the low susceptibility of the ferrofluid and high measurement frequency (Biedermann, 2019; Biedermann et al., 2021; Jones et al., 2006). The relationship between pore axial ratio and MPF has been described by the equivalent pore concept (Hrouda et al., 2000), and corrections thereof (Jones et al., 2006). However, because not only the geometry of individual pores, but also their orientation and spatial arrangement influence the MPF, there is no unique and straightforward relationship and predicting MPFs for a given pore space needs numerical modeling (Biedermann, 2020). Here, no clear correlation was observed, partly because measured susceptibility decreases with increasing frequency (Biedermann et al., 2021). Therefore, higher fluid susceptibilities and measurement frequency of 1 kHz are recommended for MPF studies (Biedermann et al., 2021). Half of the samples display similar anisotropy shapes for both fabric measures within measurement uncertainty, while the others displayed discrepancies in anisotropy shape. This may be related to the different parts of the pore space captured, or an inherent difference between methods, and needs to be investigated further.

It remains to be established whether or not the MPF and total shape ellipsoid do relate to permeability. There are empirical correlations of MPF, pore fabrics and permeability anisotropy (Almqvist et al., 2011; Benson et al., 2003; Hailwood et al., 1999; Nabawy et al., 2009; Pfliegerer & Halls, 1994). Permeability anisotropy is also a second order tensor property, and essential for reservoir characterization, but the measurement method should be improved to obtain a full tensor with estimating uncertainty and heterogeneity. Future work will need to investigate whether the total shape ellipsoids and MPFs defined here correlate clearly with laboratory-measured permeability anisotropy. This study lays the foundation for the quantitative comparison between a variety of fabric measures and second-order properties. More types of reservoir rocks and fabrics need to be analyzed for a detailed and thorough understanding of MPFs and their ability to predict pore fabrics and permeability anisotropy in the future, following the procedure outlined here.

### **3.5. Conclusions**

The main goals of the study were (1) to establish quantitative relationships between XRCT-derived pore fabric data and MPFs, and (2) to investigate how the methods can complement each other in order to improve 3D pore space description for reservoir characterization. The comparison of pore fabrics calculated from XRCT and MPF data was accomplished by defining the total shape ellipsoid, an average measure of the pore fabric, integrating information on the pore shapes and orientation density derived from the XRCT data. The total shape ellipsoid is mathematically represented by a second order symmetric tensor, and can thus be directly compared to second order tensor properties such as susceptibility or permeability. It is therefore useful not only in MPF studies, but also a wide range of fluid flow applications, or when predicting other physical rock properties relevant for reservoir evaluation and hydrocarbon exploitation.

Generally, a good agreement was observed between the total shape ellipsoid and MPFs in terms of fabric orientation, and partly in terms of anisotropy shape. This confirms and expands previous empirical relationships between average pore shape or preferred pore orientation with MPFs.

Anisotropy degrees cannot be compared directly, because the susceptibility of the ferrofluid plays an important role in controlling the MPF anisotropy degree. Some open questions remain, including whether MPFs really are able to capture micropores (> 10 nm of magnetic nanoparticle) as suggested in previous studies, and how the total shape ellipsoid is affected by resolution-artefacts and segmentation uncertainties. Nevertheless, the ability to quantitatively correlate MPF and total shape ellipsoid data will make the MPF method more useful in future applications.

### **Acknowledgments**

We are very thankful for the support from technician Sandro Bula. We would like to thank R. Castellanza from the Università degli Studi Milano Bicocca (Milano, Italy) for providing the calcarenites. Bjarne Almqvist, Philippe Robion and one anonymous reviewer are gratefully acknowledged for their thoughtful reviews which helped to improve the manuscript. The XRCT analysis in Bern was supported by the European Research Council (ERC) under the European Union's Horizon 2020 research and innovation program (grant agreement No 850530 to PL). The Bruker Skyscan 2211 at the University of Fribourg has been funded through R'Equip Swiss National Science Foundation grant 206021\_150731. This study was funded by the Swiss National Science Foundation, project 176917 (to ARB).

## **4. Article II: Quantitative assessment of direct and indirect measures of 3D pore fabrics and permeability anisotropy in sedimentary rocks**

**(Potentially for future publication)**

**Y. Zhou<sup>1</sup>, A. Foubert<sup>2</sup>, P. Lanari<sup>1</sup>, & A. R. Biedermann<sup>1,3</sup>**

<sup>1</sup>Institute of Geological Sciences, University of Bern, Baltzerstrasse 1+3, CH-3012 Bern, Switzerland.

<sup>2</sup>Department of Geosciences, University of Fribourg, Chemin du Musée 6, CH-1700 Fribourg, Switzerland.

<sup>3</sup>Now at Paul Scherrer Institute, Forschungsstrasse 111, 5232 Villigen PSI, Switzerland.

Corresponding author: Yi Zhou (zy930com@gmail.com)

### **Key Points:**

- 3D pore fabrics derived from 2D thin-section, X-ray computed tomography, permeability anisotropy, and magnetic pore fabric are compared
- Magnetic pore fabric quantitatively reveals pore fabric and fluid flow direction
- Integrating methods to predict flow direction benefit geothermal energy exploitation, CO<sub>2</sub> sequestration and groundwater management

### **Abstract**

Reliable characterization of pore fabrics is essential for understanding fluid flow directionality in porous media, with important implications for geothermal energy production, CO<sub>2</sub> sequestration, and groundwater flow. Thin-section analysis provides detailed pore fabric visualization but is limited to two-dimensional representations. XRCT can non-destructively determine 3D pore fabrics, but data processing is time consuming, and voxel resolution depends on density and sample size. Permeability anisotropy can be measured directly, but can be affected by heterogeneity, potentially leading to over- or underestimation of the degree of anisotropy. MPF serves as an alternative method for estimating pore fabrics and preferred flow directions, with the advantage of obtaining the full tensor from a single core. This study compared 2D thin-section-derived 3D pore fabrics, X-ray computed tomography (XRCT)-derived data (pore fabrics, permeability, and magnetic pore fabric (MPF)), permeability anisotropy from different numbers of measurements, and MPF analyses. The study used sandstone and carbonate samples, along with a synthetic quartz sample. Comparisons of all tensors show the agreement in the maximum and minimum principal directions of pore fabrics, permeability anisotropy, and MPF for most samples (eight out of eleven), although the degree and shape of anisotropy vary. Simulated and laboratory-measured permeability anisotropy differ, likely due to undetected micropores. This study suggests MPFs as an efficient way to evaluate between-sample heterogeneity, determine principal pore fabric directions and predict permeability anisotropy for cross-calibration. The results contribute to the advancement of techniques for reliable pore fabric characterization and understanding fluid flow directionality, with implications for renewables and hydrocarbon exploitation, and groundwater management.

### **Plain Language Summary**

In this study, a comprehensive understanding of porous rock structures and fluid flow within them is pursued, which is essential during the energy transition phase when it comes to resource extraction and management, such as geothermal energy, but also groundwater management. The

study compares four distinct techniques: thin-section analysis, which provides a 2D view of pores; X-ray computed tomography (CT scan), which provides a 3D view of pores and allow computing permeability; permeability anisotropy measurements, which directly indicate the direction of fluid flow but require multiple cores; and magnetic pore fabric (MPF), a rapid method for estimating overall pore structure of the rock. Using a variety of rock samples, the study analyzes the advantages and limitations of each method. The results show that MPF is a highly efficient approach for evaluating differences between rock samples and determining the primary directions of fluid flow. By integrating these techniques, researchers can achieve a more thorough characterization of pore structure and flow directionality in porous rocks. This deeper understanding ultimately benefits the efficiency of resource extraction and management, leading to better decision and practices in hydrocarbon, geothermal and groundwater industries.

#### **4.1. Introduction**

Accurately understanding and characterizing pore fabrics and permeability anisotropy is essential for the exploitation of resources such as geothermal energy but also traditional hydrocarbons and groundwater (Aliyu & Chen, 2018; Gao & Hu, 2018; Kibria et al., 2018; Yang et al., 2018). Pore fabrics, including pore shape, alignment, connectivity, and distribution, directly influence fluid flow in the subsurface. Additionally, permeability anisotropy, which represents the variability of permeability in different directions, is critical for determining preferred fluid flow directions.

The typical methods for pore fabric determinations include thin section analysis and X-ray computed micro-tomography (XRCT). Thin sections injected with fluorescent resin allow for direct observation of luminescent pore networks under a UV light microscope. This method only provides 2D images, limiting comprehensive pore fabric analysis (Prévosteau et al., 1970; Přikryl, 2015).

Using XRCT data sets, digital rock models can be constructed to analyze three-dimensional pore size, shape, and orientation distributions, and to calculate physical properties such as permeability and MPF (Andrä et al., 2013; Biedermann, 2020; Holzer et al., 2011; Madadi & Varslot, 2009; Pini & Madonna, 2016). The total shape ellipsoid, using a second-order tensor to represent the pore fabrics of the sample, facilitates the correlation of XRCT results with tensorial physical properties, such as permeability anisotropy and magnetic pore fabric (MPF) (Zhou et al., 2022). To achieve representative 3D pore characterization, a balance must be struck between sample volume and suitable resolution for micropore detection (Lai et al., 2018; Sun et al., 2021).

Permeability anisotropy can directly evaluate the preferred flow directions, and it is a second-order tensor, requiring the measurement of at least six independent directions (Coulson & Nye, 1958). The selected literature (64 papers) on permeability anisotropy measurements (Figure 4.1) reveal that most studies (56 out of 64 papers) measured 2-3 directions, including one perpendicular to the bedding and the others parallel to the bedding (Adams et al., 2013, 2016; Al-Azani et al., 2019, 2021; Al-Dujaili et al., 2021; Armitage et al., 2011; Auradou et al., 2005; Ayan et al., 1994; Benson et al., 2003, 2005; Bhandari et al., 2015; Cheng et al., 2012; Clennell et al., 1999; Dai et al., 2019; Dautriat et al., 2009; Dewhurst et al., 1996; Farquharson et al., 2016; Farrell et al., 2014; Gehne & Benson, 2017; Georgi et al., 2002; Goupil et al., 2022; Hong et al., 2019; Ismail et al., 2014; Iverson et al., 1996; Jia et al., 2022; Jiang et al., 2021; Kawano et al., 2011; Khan & Teufel, 2000; Leroueil et al., 1990; Li et al., 2021; Lou et al., 2021; Louis et al., 2005; Lu et al., 2019; Malkovsky et al., 2009; Metwally & Sondergeld, 2011; Meyer, 2002; Meyer & Krause, 2006; Nabawy, 2018; Nordquist, 2015; O’Kelly, 2007; Pan et al., 2015; Panja et al., 2021; Peffer et al., 1997; Pei et al., 2023; Prasad & Nur, 2003; Prats, 1972; Sato et al., 2018; Scholes et al., 2007; Tan et al., 2023; Wang & Pan, 2017; Witt & Brauns, 1983; Youssef et al., 2021; Yu et al., 2020; Zhang et al., 1999; Zhang & Tullis, 1998; Zhang & Wang, 2018). Some studies measured other directions, such as

30, 45, 60-degree angles between the measured directions and fabric orientation (Baas et al., 2007; Cabrera & Samaniego, 2021; Mokhtari et al., 2013; Okazaki et al., 2013; Zhang et al., 2021). However, all of the above measurements require a priori information about the fabric orientation, such as bedding, fault or paleoflow. Otherwise, the permeability anisotropy may be under- or overestimated. Pfeleiderer & Halls (1994) measured six directions to compute the full tensor of permeability anisotropy. Clavaud et al. (2008) and Rasolofosaon & Zinszner (2002) also presented full-tensor data, but only one principal direction was measured, and the tensor was calculated based on the three-dimensional shape of the fluid invasion front. Furthermore, when seven or more directions are measured, the confidence angle can be calculated (Jelinek, 1977), which allows an assessment of the significance level of the permeability anisotropy.

Note that the selected literature focuses on permeability anisotropy measurements of natural rocks, identified primarily through a Google Scholar search using keywords related to "permeability anisotropy measurements of natural rocks" and sorted by relevance (publication year up to 2024). Initial search results were filtered based on title and abstract relevance, prioritizing papers clearly demonstrating multi-directional permeability anisotropy measurements. This relevance-based approach was adopted due to the inefficiency of chronological review given the large and often irrelevant search result pool. This process yielded 64 highly relevant papers out of 210 reviewed, primarily concerning sedimentary rocks, especially sandstones, and to a lesser extent carbonates, shales, and coal. More detailed selection criteria and the filtering process are described in the caption of Figure 4.1.

A promising alternative approach is the analysis of magnetic pore fabrics (MPFs) using ferrofluid-impregnated samples, which provides an indirect method for determining pore fabrics and permeability anisotropy (Pfleiderer & Halls, 1990, 1994). Since the single sample can be rotated in a magnetic field to measure different directional susceptibilities, avoiding the prior information on fabric. Given that the size of magnetic particles in ferrofluid ranges from 10 to 20 nm, the MPF method can detect pores of similar size (Robion et al., 2014). Most studies consistently conclude that MPFs align with principal pore fabric directions (Louis et al., 2005; Pfeleiderer & Halls, 1990) and with the permeability anisotropy orientations (Benson et al., 2003; Louis et al., 2005; Pfeleiderer & Halls, 1994). MPFs exhibit a lower degree of anisotropy than pore fabrics and permeability anisotropy (Benson et al., 2003; Jones et al., 2006; Louis et al., 2005; Nabawy et al., 2009; Pfeleiderer & Halls, 1994). MPF-derived porosity is lower than Helium porosity (Nabawy et al., 2009), but not always lower than water porosity (Robion et al., 2014). Nevertheless, there are inconsistencies between the principal directions of permeability anisotropy and MPF (Baas et al., 2007; Nabawy et al., 2009) (Figure 4.2). Potential reasons include residual ferrofluid on the sample surface, limited direction measurements for absolute permeability, and the influence of pore distributions, intrinsic susceptibility of ferrofluid, and even measurement frequency on MPF (Biedermann, 2019; Biedermann et al., 2021). An additional challenge is that MPFs are dominated by large interconnected pores impregnated with substantial amounts of ferrofluid, whereas permeability anisotropy is more related to the preferred orientation of all connected pores (Pfleiderer & Halls, 1994). Simplified samples with strong anisotropy, which are commonly used in many MPF studies (Biedermann, 2019, 2020; Jones et al., 2006; Pfeleiderer & Halls, 1990), may not accurately represent intricate natural pore fabrics

This study aims to address these challenges by providing a detailed and thorough understanding of the relationships between pore fabric properties, permeability anisotropy, and MPFs in natural and synthetic samples. The research question examines the effectiveness of MPFs in assessing sample heterogeneity and determining preferred directions for pore fabrics and fluid flow, with the results being cross-validated by thin section, XRCT, and permeability measurements, and ultimately contributing to fluid resource exploitation and management.

Readers can expect 3D pore fabrics calculated from three perpendicular thin sections and XRCT data. Permeability anisotropy and MPF are simulated using XRCT data and measured in the laboratory, including full-tensor calculations that evaluate variability and heterogeneity.

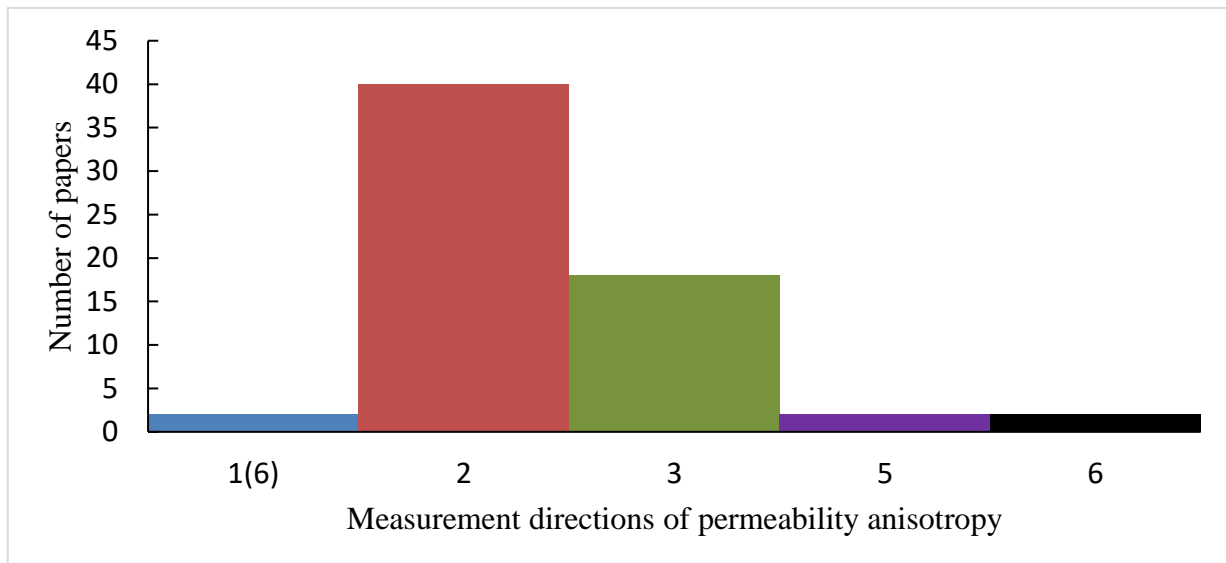


**Figure 4.1.** Measurement directions of permeability anisotropy reported in published studies. The selected literature primarily focuses on permeability anisotropy measurements of natural rocks. Applying Darcy's law, steady-state gas pressure is applied at the end of the sample plug to measure the sample's permeability. Using the Google Scholar search engine, academic articles related to permeability anisotropy measurements of natural rocks were searched, with the publication date up to 2024 and the results sorted by relevance. It is important to note that although the search engine shows tens of thousands of results, not all of these papers are useful for our study. Due to the nature of the search algorithm, it presents all relevant results, even those with minimal relevance, such as papers that mention the keywords only in the reference or introduction sections but do not focus on them in the main content. For some results, keywords appear separately throughout the text, deviating significantly from their original meaning. Additionally, some papers mention permeability but do not cover measurements, anisotropy, or use natural samples, and some use simulations instead of physical measurements. The academic terminology used by different research communities is not entirely consistent, and authors' writing habits vary. Based on these characteristics, reviewing the search results in chronological order becomes highly inefficient, as even searching for a single year yields over ten thousand results, most of which are irrelevant to our study. Therefore, all results were sorted by relevance, and the papers were reviewed sequentially. Only papers whose titles or abstracts clearly indicated the presence of all key information were further examined to determine if they measured permeability anisotropy in multiple directions. By following this approach, by the 21th page of search results, the probability of finding relevant articles had significantly decreased. In total, 210 papers were reviewed, of which 64 are highly relevant to our needs, focusing on permeability anisotropy measurements of natural rocks. The literature dealt with sedimentary rocks, primarily sandstones, with a smaller portion covering carbonates, shales, and coal. It is important to note that although the literature spans from 1972 to 2023, this does not represent a comprehensive review of all papers from 1972 to 2023. Due to the nature of the search engine and our strategy, the search results are sorted and presented by relevance for review, not in chronological order. Among 64 academic articles, two papers measured one direction to infer permeability anisotropy (Clavaud et al., 2008; Rasolofosaon and Zinszner, 2002), 40 papers measured two directions (Al-Dujaili et al., 2021; Armitage et al., 2011; Ayan et al., 1994; Bhandari et al., 2015; Cheng et al., 2012; Clennell et al., 1999; Dai et al., 2019; Dewhurst et al., 1996; Farquharson et al., 2016; Gehne & Benson, 2017;

Georgi et al., 2002; Goupil et al., 2022; Hong et al., 2019; Ismail et al., 2014; Iverson et al., 1996; Jia et al., 2022; Kawano et al., 2011; Khan & Teufel, 2000; Leroueil et al., 1990; Louis et al., 2005; Lu et al., 2019; Malkovsky et al., 2009; Metwally & Sondergeld, 2011; Meyer, 2002; Meyer & Krause, 2006; Nabawy, 2018; Nordquist, 2015; O’Kelly, 2007; Panja et al., 2021; Peffer et al., 1997; Prasad & Nur, 2003; Prats, 1972; Scholes et al., 2007; Wang & Pan, 2017; Witt & Brauns, 1983; Youssef et al., 2021; Yu et al., 2020; Zhang et al., 1999; Zhang & Tullis, 1998; Zhang & Wang, 2018), 18 papers measured three directions (Adams et al., 2013, 2016; Al-Azani et al., 2019, 2021; Auradou et al., 2005; Benson et al., 2003, 2005; Dautriat et al., 2009; Farrell et al., 2014; Jiang et al., 2021; Li et al., 2021; Lou et al., 2021; Mokhtari et al., 2013; Okazaki et al., 2013; Pan et al., 2015; Pei et al., 2023; Sato et al., 2018; Tan et al., 2023), two papers measured five directions (Cabrera & Samaniego, 2021; Zhang et al., 2021), and two papers measured six directions (Baas et al., 2007; Pfeleiderer & Halls, 1994).

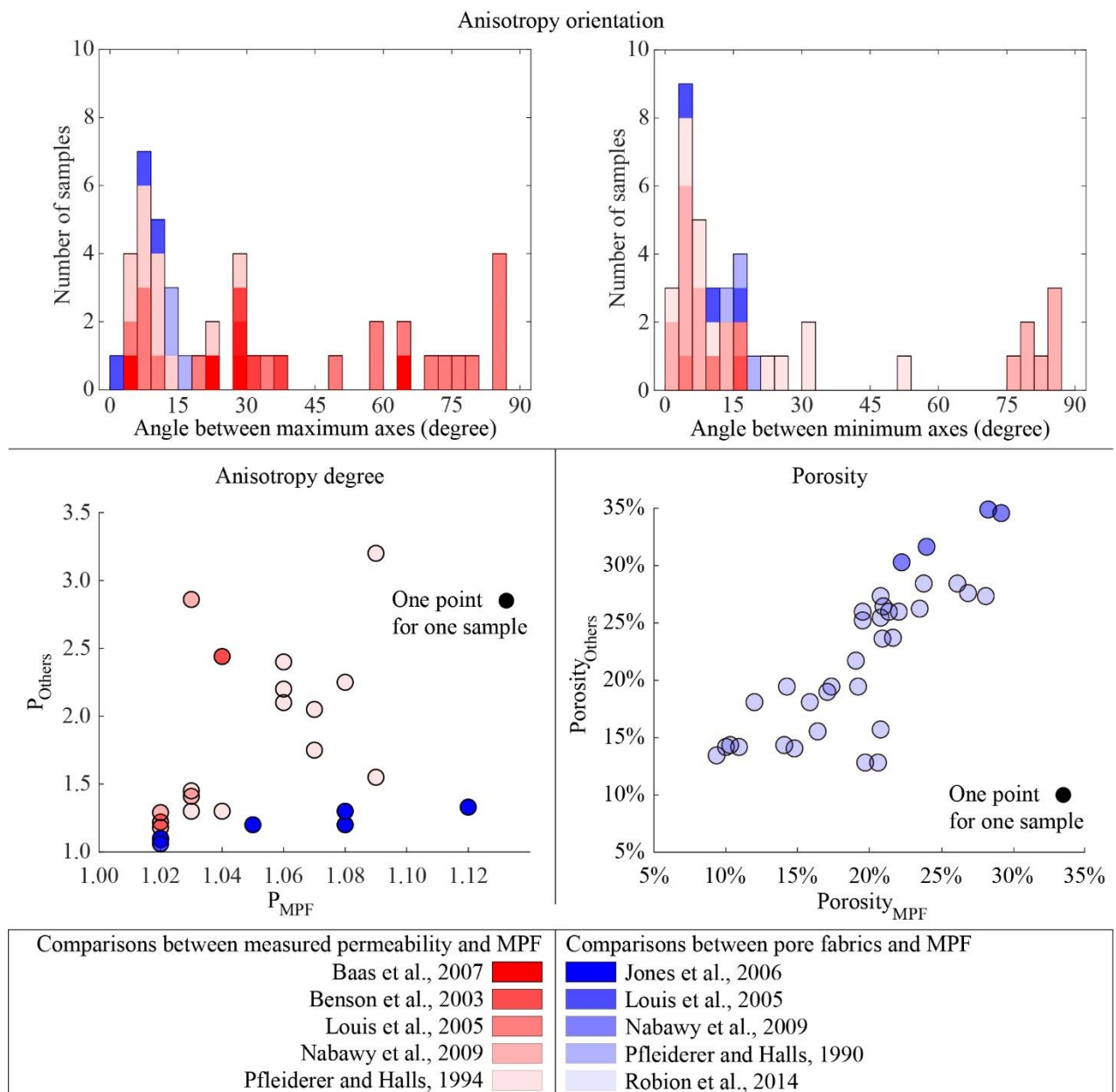


**Figure 4.2.** Published MPF studies reporting on pore fabric, permeability and MPF anisotropy. The upper panel compares the anisotropy orientation of pore fabric, permeability and MPF. The lower left panel compares the anisotropy degree between pore fabric, permeability and MPF. The lower right panel compares the porosity measured by helium with the porosity inferred by MPF.

## 4.2. Materials and Methods

### 4.2.1 Sample description and characterization

Eight sedimentary rocks with different pore characteristics are investigated, including sandstones (Berea (B25, B350, B660), Berea Spider (BS), Bentheimer (BT), Castlegate (CG), Molasse (D12), Salt Wash North (SWN)) and carbonates (Calcarenite (MI6), and Indiana limestone (I)). Additionally, one synthetic quartz sandstone (S3) was made. For sample preparation, the Molasse, Calcarenite and synthetic quartz samples were each prepared as 8 cm×8 cm×8 cm cubes. To test samples commonly used in industrial applications and to investigate the heterogeneity of dm-scale blocks, the benchmark samples (14 cm×14 cm×9 cm blocks) were ordered and analyzed. Berea sandstones are from Cleveland Quarries, and others are from Kocurek Industries, Inc.

The Berea sandstone is one of “Benchmark samples”, which has been used by the hydrocarbon industry for many years as a standard in core-flood experiments. It is known to be a well-sorted, medium-grained, homogeneous Mississippian sandstone. Berea Sandstone has a fabric with cross-bedded loose and tight layers. The strength and other properties vary depending on whether they are measured parallel or perpendicular to the layers, and hence the strength anisotropy is evident. Berea sandstone is primarily composed of quartz grains (~150 μm grain size) with a uniform grain size distribution. Other secondary minerals total less than 20%, including feldspar, kaolinite, dolomite, calcite, rutile, and zircon. The porosity is about 19% and permeability ranges from 15 to  $80 \times 10^{-15} \text{ m}^2$  (Bernabe & Brace, 1985; Churcher et al., 1991; Hart & Wang, 1995; Øren & Bakke, 2003; Simmons et al., 1982).

The Berea Spider sandstone is homogeneous and transversely isotropic at macro-scale. Berea Spider Sandstone, a variant, likely shares the layered fabric of Berea Sandstone, and its anisotropy is expected to be similar, influenced by these layers (Kocurek Industries). It is known to be an Upper Devonian sandstone with ~82% quartz and microcline, clay and albite (<18%) (Gamal et al., 2020, 2021). Porosity is 19-21% and permeability is 120-300 mD ( $\approx 1.18\text{-}2.96 \times 10^{-13} \text{ m}^2$ ) (Kocurek, 2022c).

The Bentheimer sandstone belongs to the Early Cretaceous (Valanginian) deposited in the Lower Saxony Basin in a shallow marine environment. It is generally homogeneous and isotropic at small scales, however, it can show slight anisotropy due to pore shape. It consists of well-sorted sand with medium grain sizes (180-300 μm). Quartz is the dominant mineral (>90%) with accessory feldspar and clay. The homogeneous samples show 21-27% porosity and 520-3500 mD ( $\approx 5.13\text{-}34.5 \times 10^{-13} \text{ m}^2$ ) permeability (Dubelaar & Nijland, 2015; Kemper, 1976; Kocurek, 2022a; Louis et al., 2005; Peksa et al., 2015; Vos, 1990).

The Castlegate sandstone is a Late Cretaceous fluvial sediment of the Castlegate Formation outcropping in the Book Cliffs of Utah. It has a fabric from fluvial environments with structures like cross-bedding. This leads to anisotropy, where properties like permeability or wave velocity vary depending on the direction relative to these structures. It has a fine to medium grain size (~0.2 mm). Quartz as the primary phase (70-80%) is combined with 5-10% clay. The sample is relatively homogeneous and moderately anisotropic with a porosity of 26-29% and a permeability of  $2\text{-}4 \times 10^{-13} \text{ m}^2$  (Adams & Bhattacharya, 2005; Digiovanni et al., 2007; Ingraham et al., 2013; Kocurek, 2022b; McLaurin & Steel, 2007).

The Molasse sandstone was collected in Rüeggisberg, BE from the Upper Marine Molasse (OMM) of the Swiss molasse basin (SMB) and characterized by cross bedding and parallel bedding (Zhou et al., 2022). The fabric of OMM is characterized by shallow marine and tidal-influenced sedimentary structures like cross-bedding and lamination, and these structures cause anisotropy for mechanical properties and permeability. It has ~20% porosity and up to 650 mD ( $\approx 6.42 \times 10^{-13} \text{ m}^2$ ) permeability.

<sup>13</sup> m<sup>2</sup>) horizontal permeability and low vertical permeability due to thinning upward beds. Therefore, it can be an important reserve and transfer space for CO<sub>2</sub> and fluids (Chelle-Michou et al., 2017; Chevalier et al., 2010; Garefalakis & Schlunegger, 2019; Kohl et al., 2010; Rybach, 2019; Schegg et al., 1997).

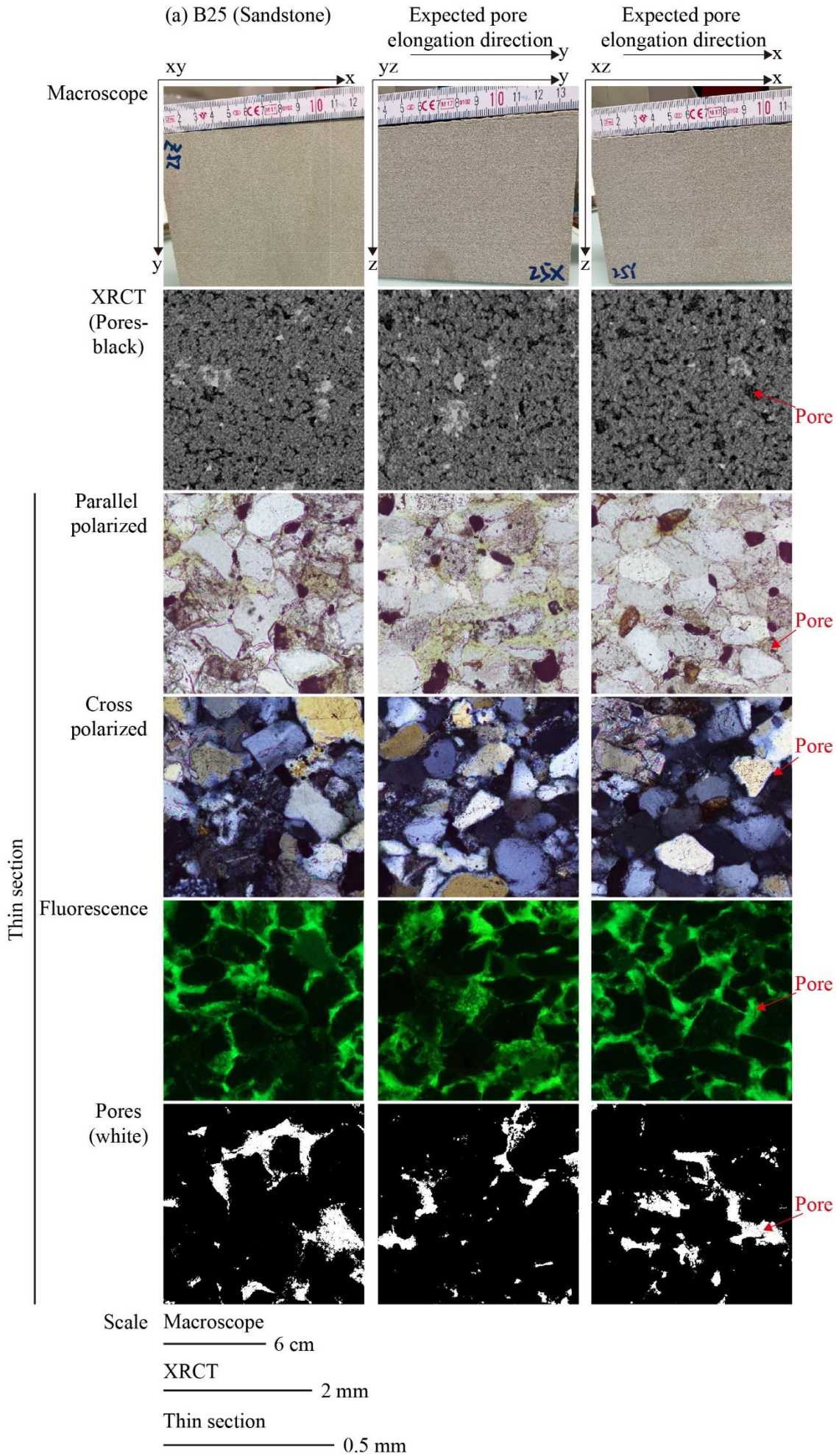
The Salt Wash North sandstone represents the fluvial sediment of the Salt Wash Member of the Upper Jurassic Morrison Formation, with sedimentary structures leading to some degree of anisotropy, affecting how it behaves in different directions. The porosity is about 20% and the permeability is 400-1344 mD ( $\approx 3.95\text{-}13.3 \times 10^{-13}$  m<sup>2</sup>) (Chesley & Leier, 2018; Owen et al., 2015, 2017; Robinson & McCabe, 1997; Tyler & Frank, 1983).

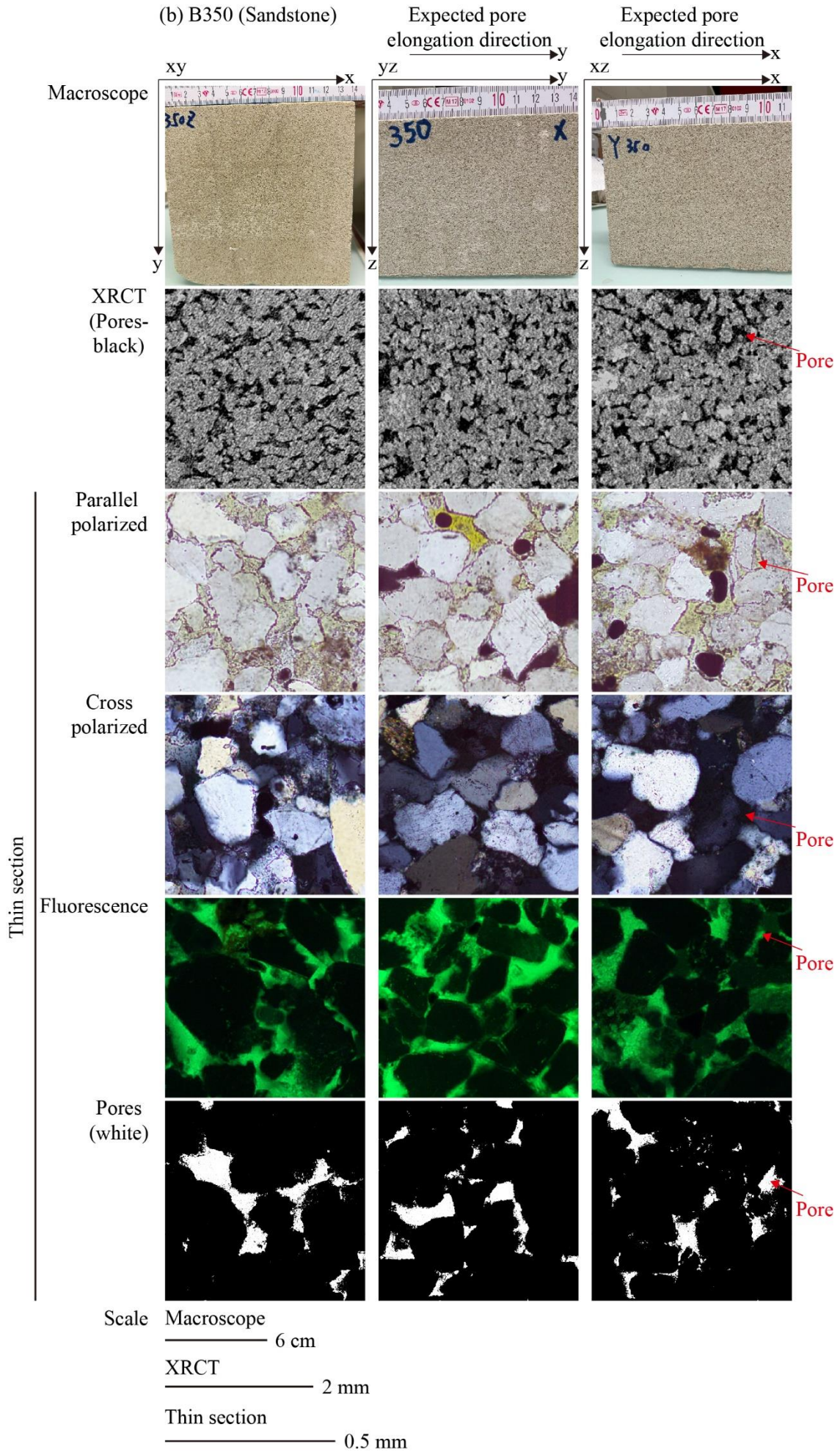
The Calcarenite belongs to the Plio-Pleistocene units of Apulia, Italy. Apulian calcarenite is a soft porous rock formed by the cementation of calcareous grains accumulated in a shallow marine environment. It can exhibit anisotropy with thermal conductivity and P-wave velocity showing directional variations. It is characterized by a porosity between 16% and 60% with more than 99.5% of the pore space interconnected. It includes different pore types, such as intergranular pores, moldic pores, etc. (Andriani & Walsh, 2002; Ciantia et al., 2015; Zhou et al., 2022).

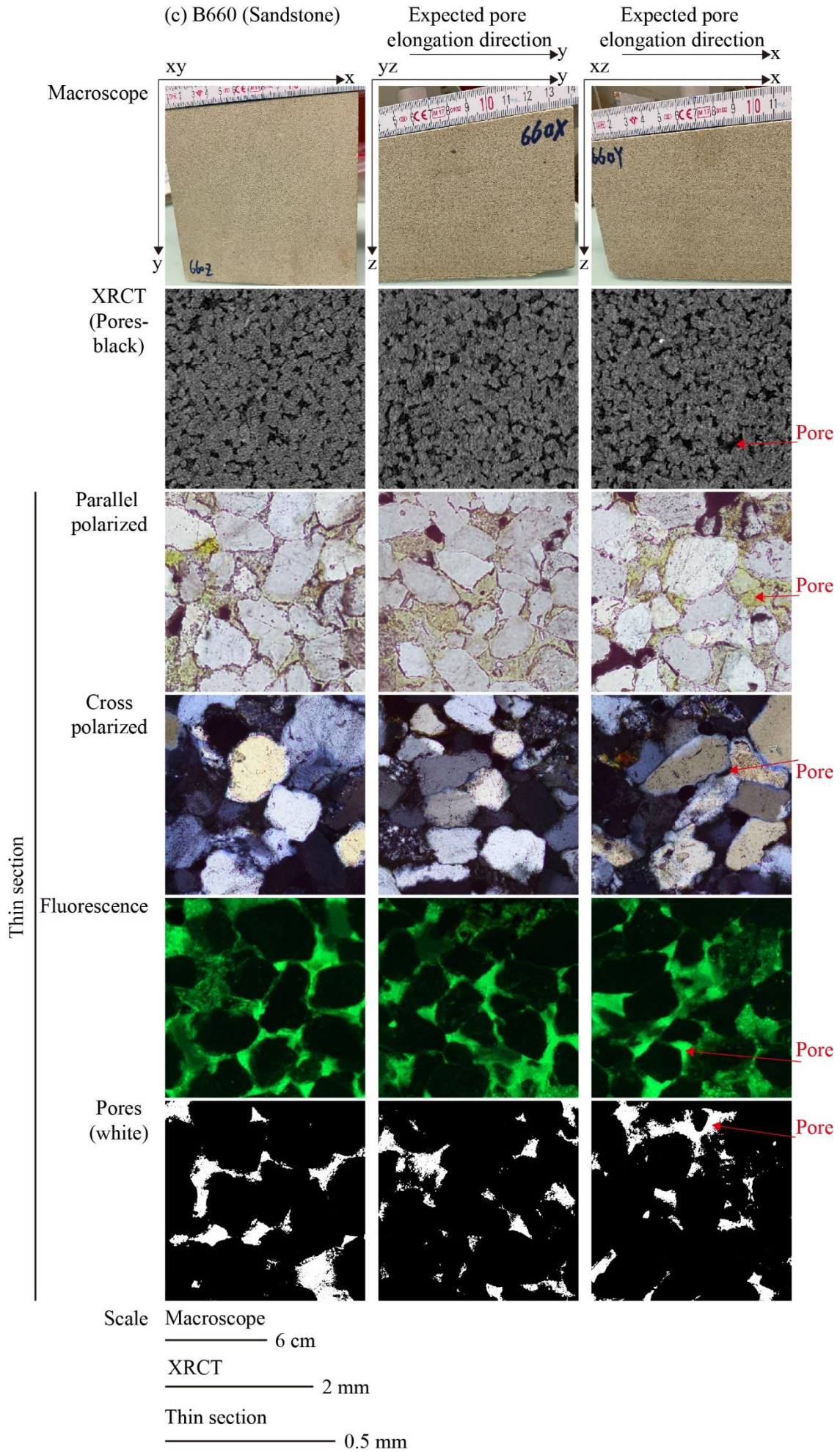
The Indiana limestone is from the Mississippian Salem Formation. The primary composition is calcium carbonate (~98%). It is highly homogeneous and weakly bedded with medium-sized grains, consisting of oolites and fossil debris cemented by calcite. Its uniform fabric makes it less anisotropy. The porosity is 10-21% and permeability is 4-244 mD ( $\approx 0.04\text{-}2.41 \times 10^{-13}$  m<sup>2</sup>) (Churcher et al., 1991; El-maghraby & Blunt, 2013; Hart & Wang, 1995; Schmidt & Huddle, 1977).

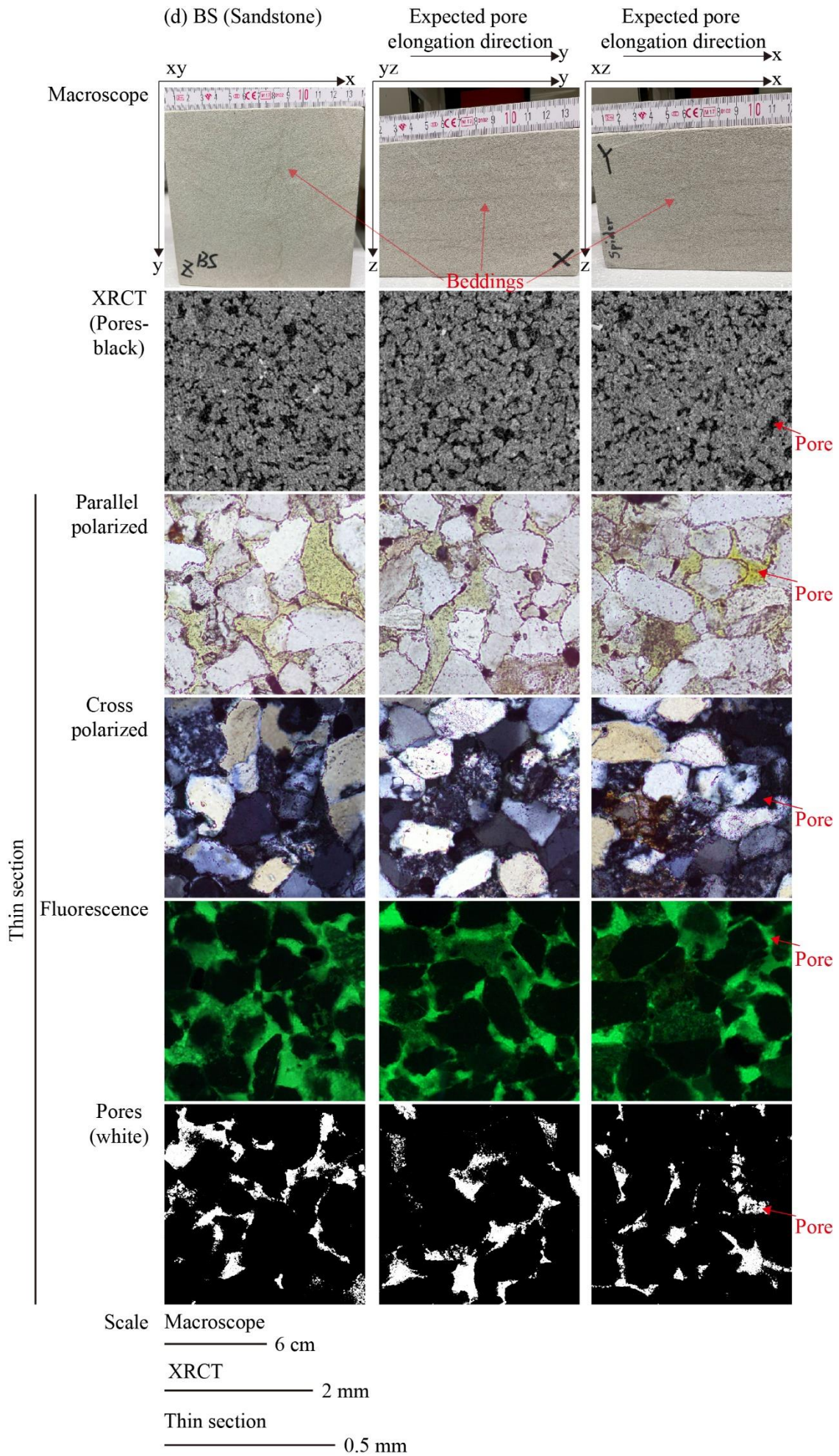
To simply and quickly prepare an anisotropic artificial sample, quartz sand with a grain size of 80-150  $\mu\text{m}$ , similar to that of common molasse samples, was selected to simulate a quartz sandstone texture. The liquid glass as the adhesive was mixed with the quartz sand. The mixture was placed in a cube holder and pressed with a hammer (<5 MPa) before drying in a 100 °C oven for 72 hours. The preparation process does not aim to replicate an actual diagenetic environment but rather seeks to rapidly and simply create an anisotropic structure through the pressing action of a hammer.

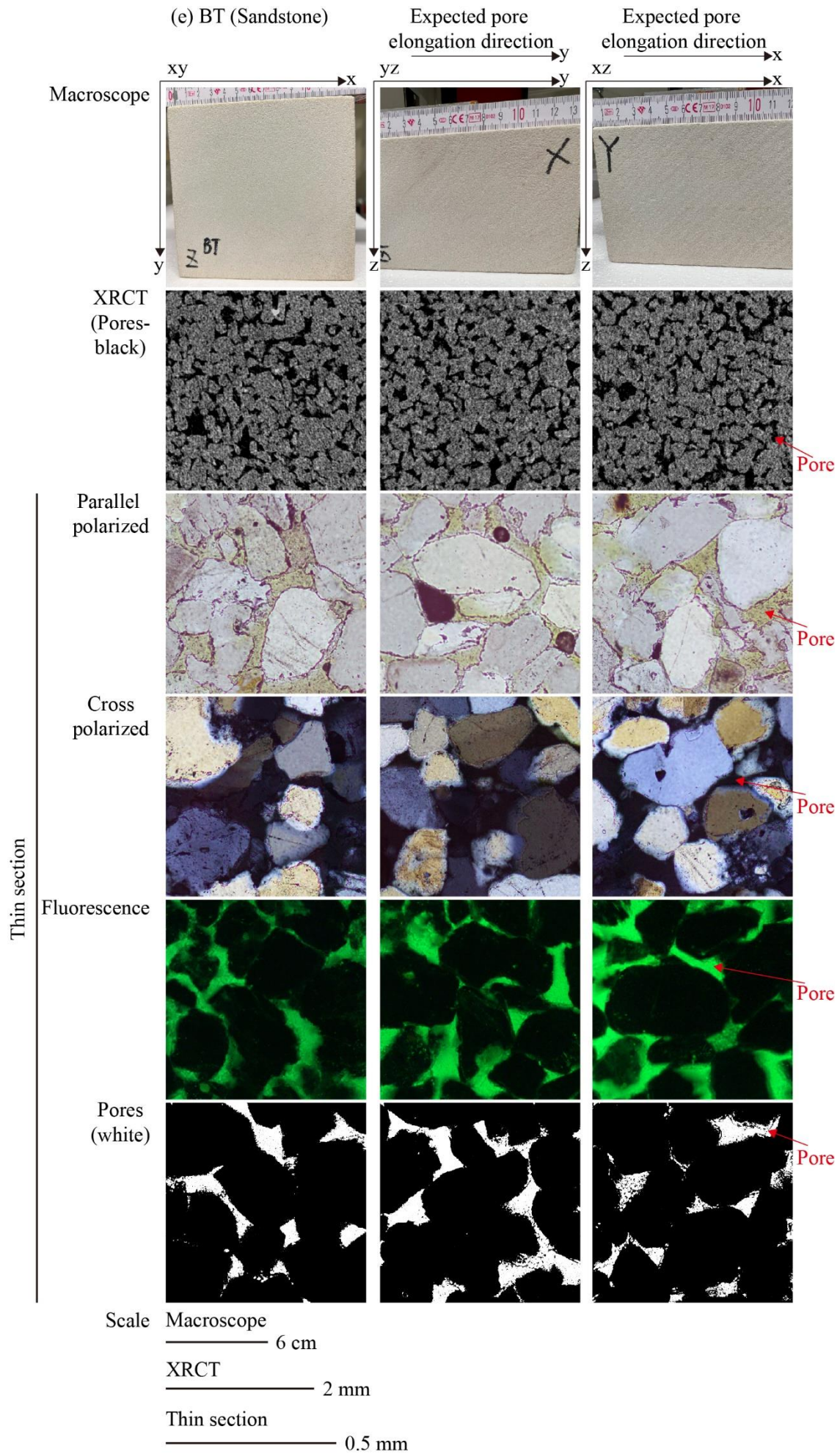
The photographs of three orthogonal surfaces ( $xy$ ,  $yz$ ,  $xz$ ) were taken for each benchmark sample using an iPhone 13 Pro Max. Then the samples were cut for three perpendicular thin sections ( $xy$ ,  $yz$ ,  $xz$ ) and cores. According to the directions of the sedimentary layers provided by the rock supplier, the  $xy$ -direction of the sample block was defined as along the sedimentary layers, i.e., horizontal, while the  $z$ -direction is perpendicular to the layers, i.e., vertical. Therefore, the  $z$ -direction corresponds to the compaction direction experienced during sediment deposition. Due to the influence of compaction, the elongation direction of grains and pores was expected to align along the  $xy$ -direction. In Figure 4.3, the pore fabrics and grain fabrics at the microscopic scale were presented through thin section and XRCT images (methods introduced later) and qualitatively compared with the macroscopic fabrics of the sample as observed in photographs. Through simple visual inspection of the images, an initial attempt was made to empirically validate the directional relationship between the microscopic pore fabrics and the macroscopic sample fabrics. However, it can be observed that only Sample BS shows slightly visible bedding at the macroscopic scale, while the other samples exhibit relatively homogeneous structures with no clear bedding. At the microscopic scale, there are also no significant directional features in the pore fabrics and grain fabrics. However, the following sections presented quantitative analysis of pore fabrics to establish a quantitative relationship between the macroscopic fabrics and the microscopic pore fabrics.

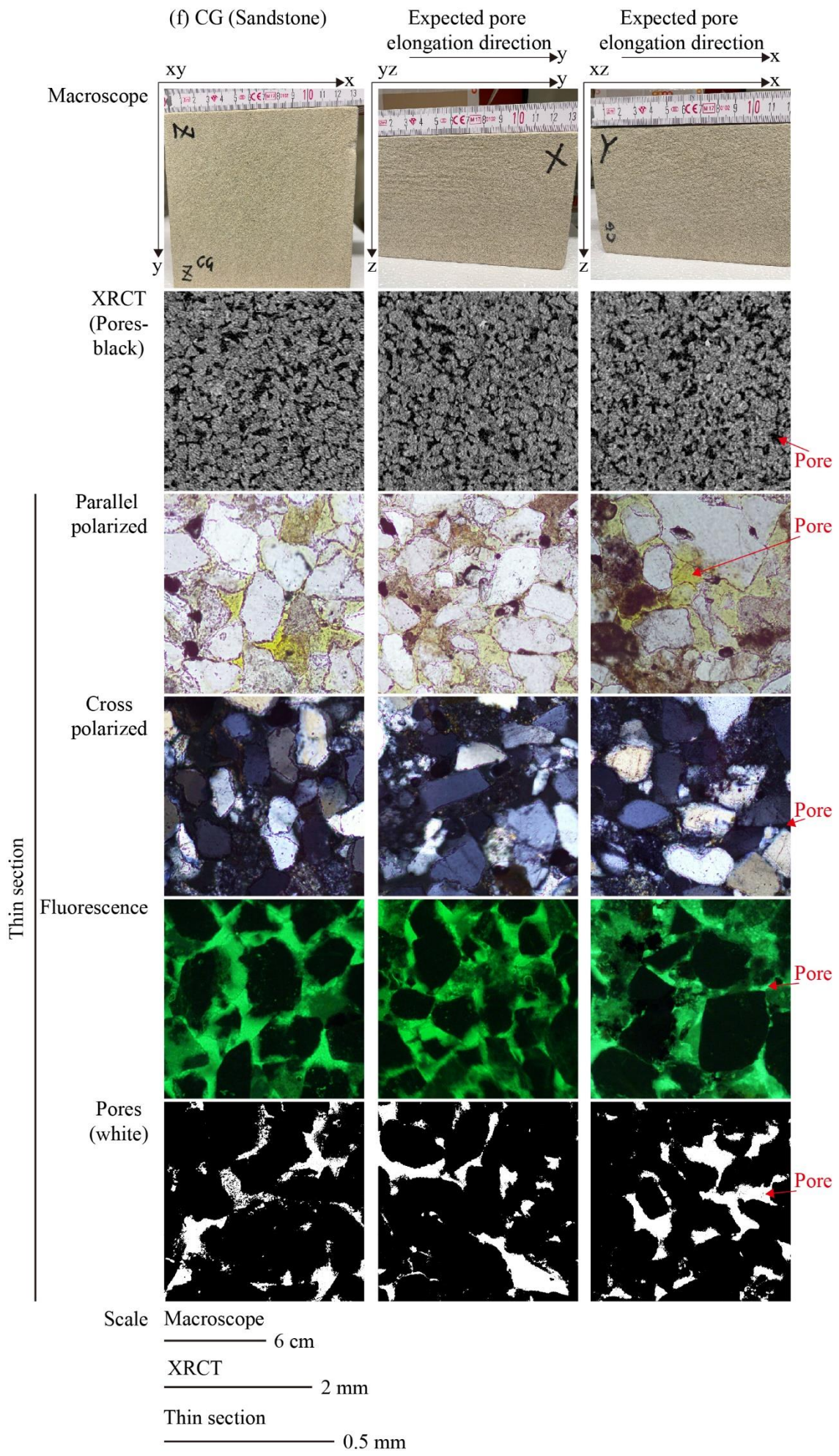


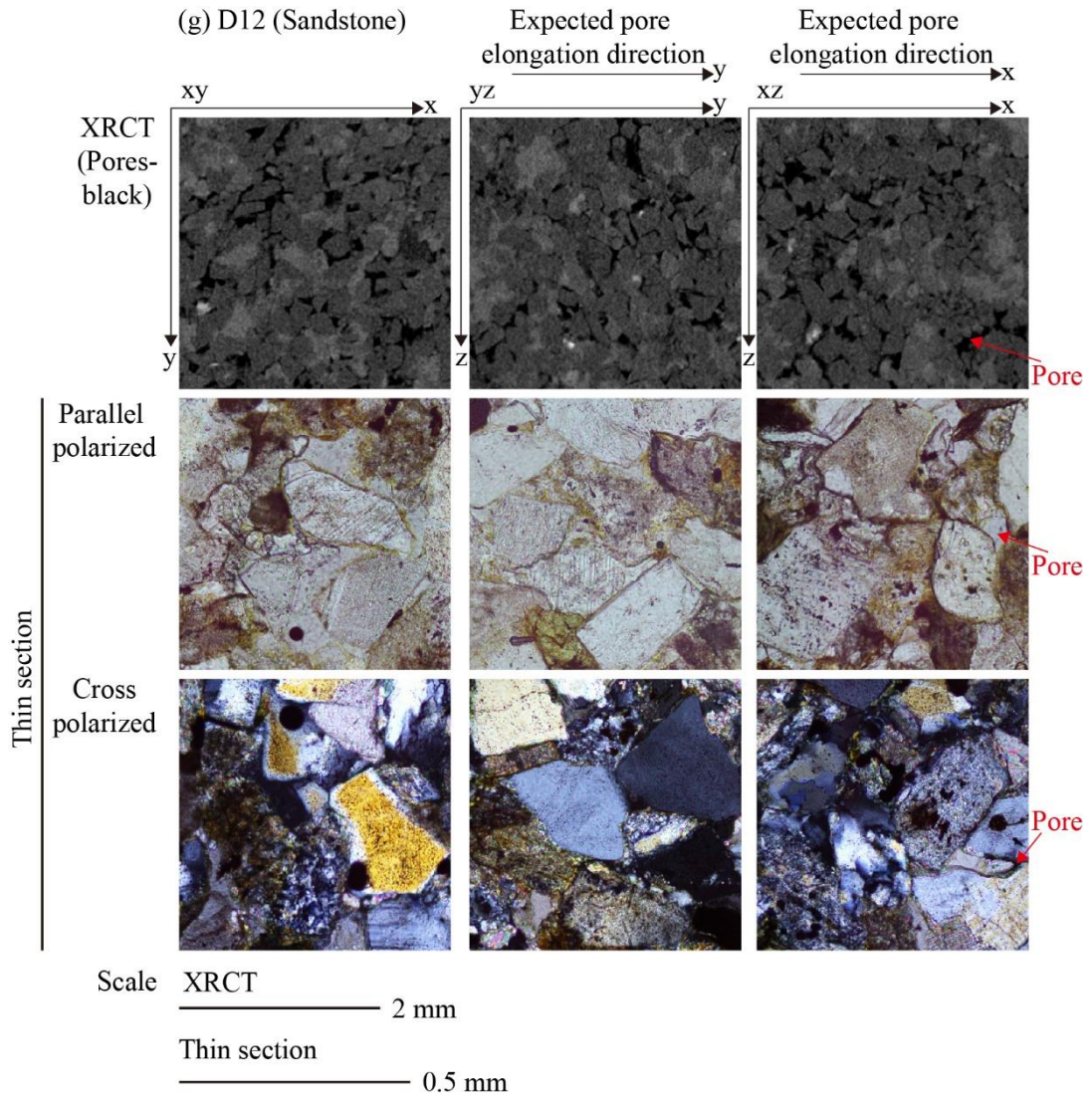


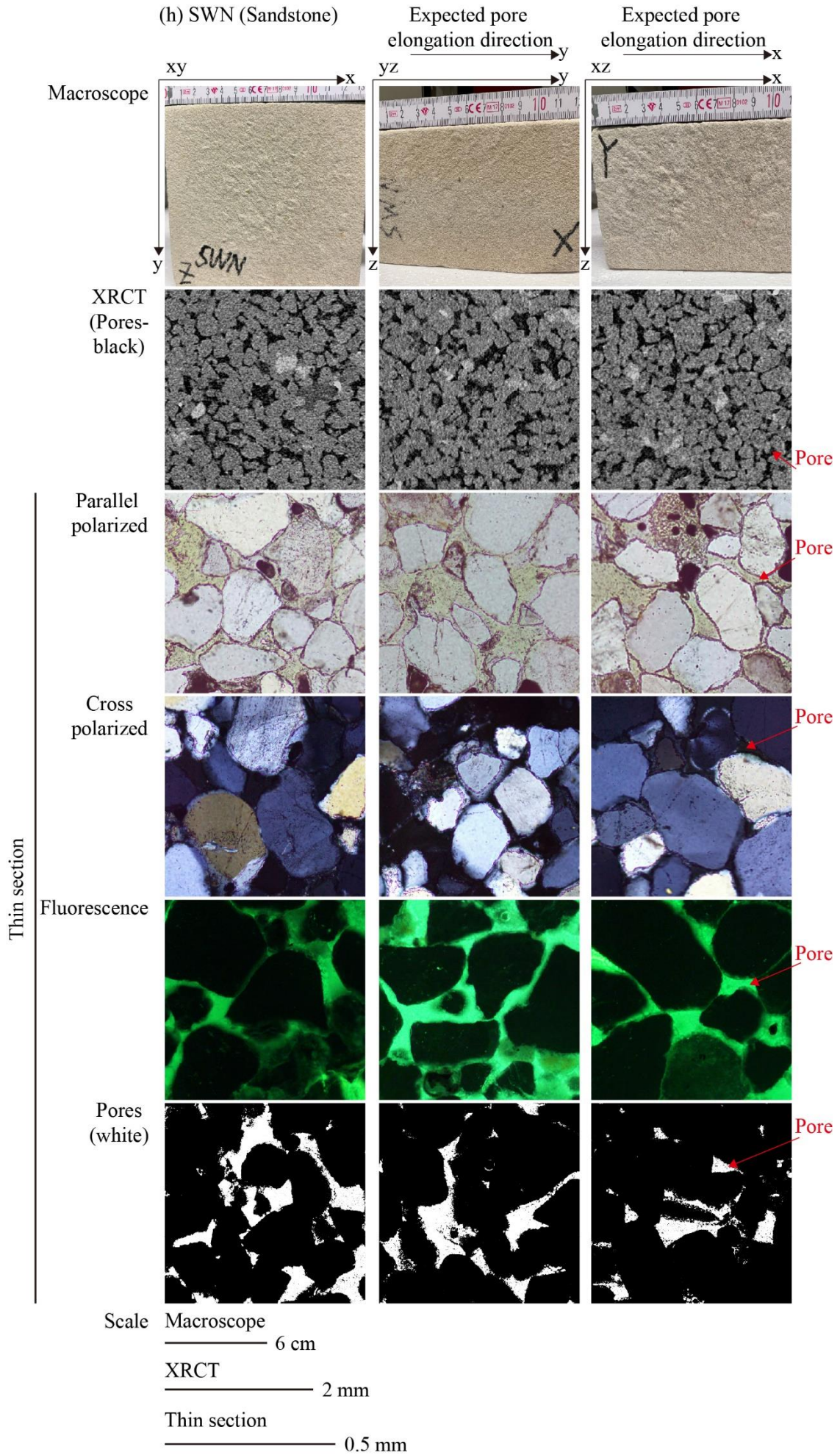


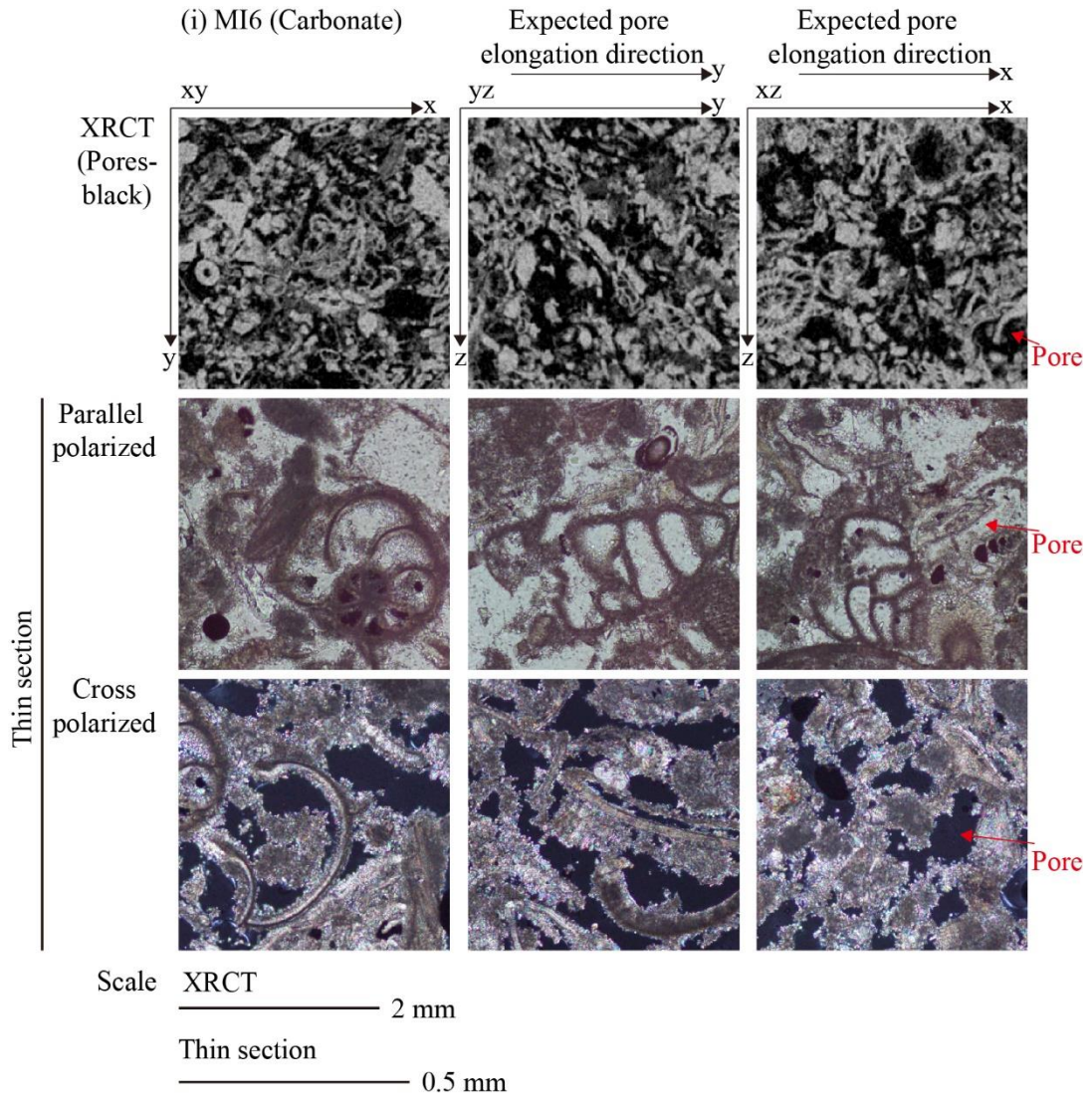


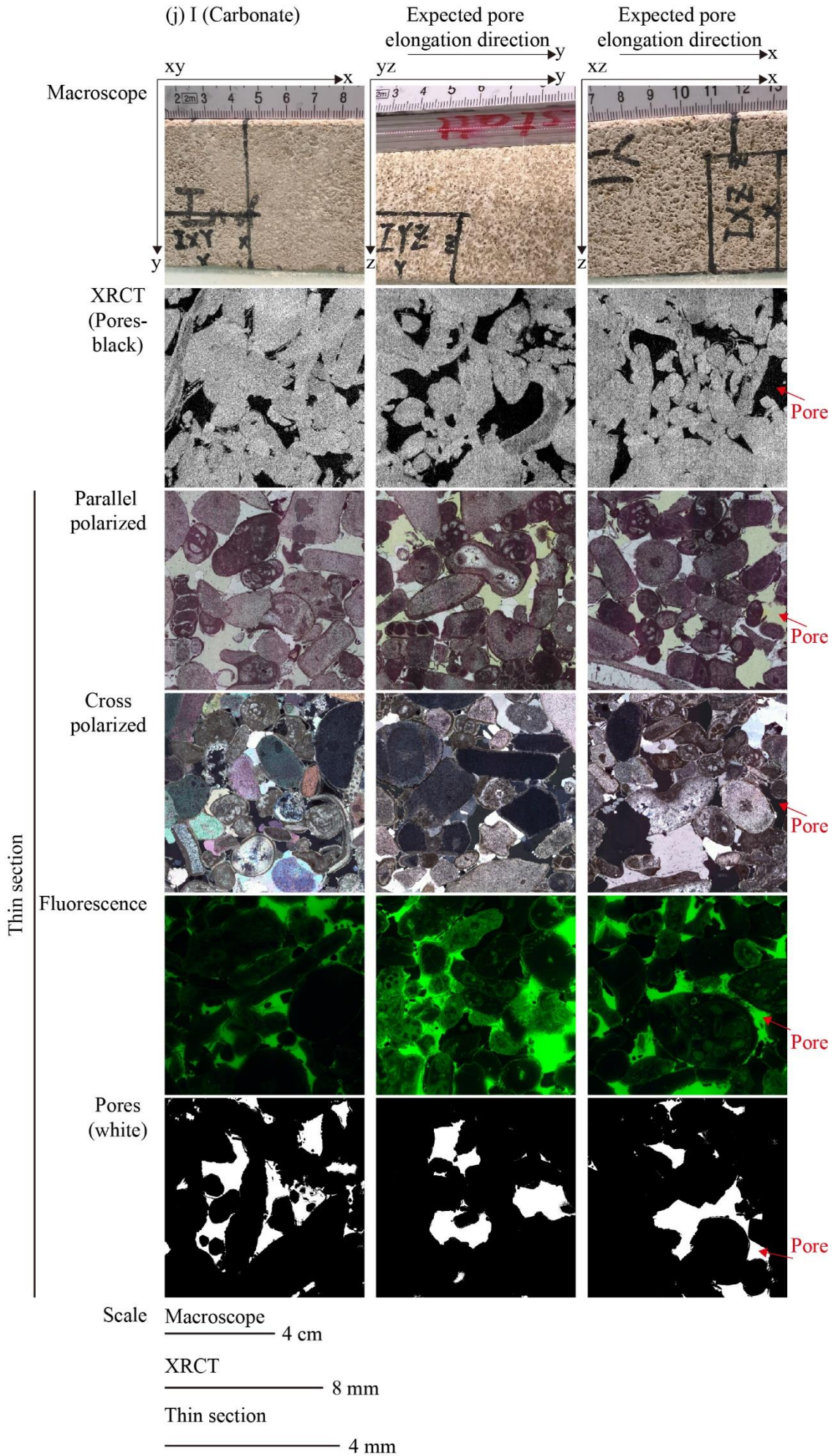


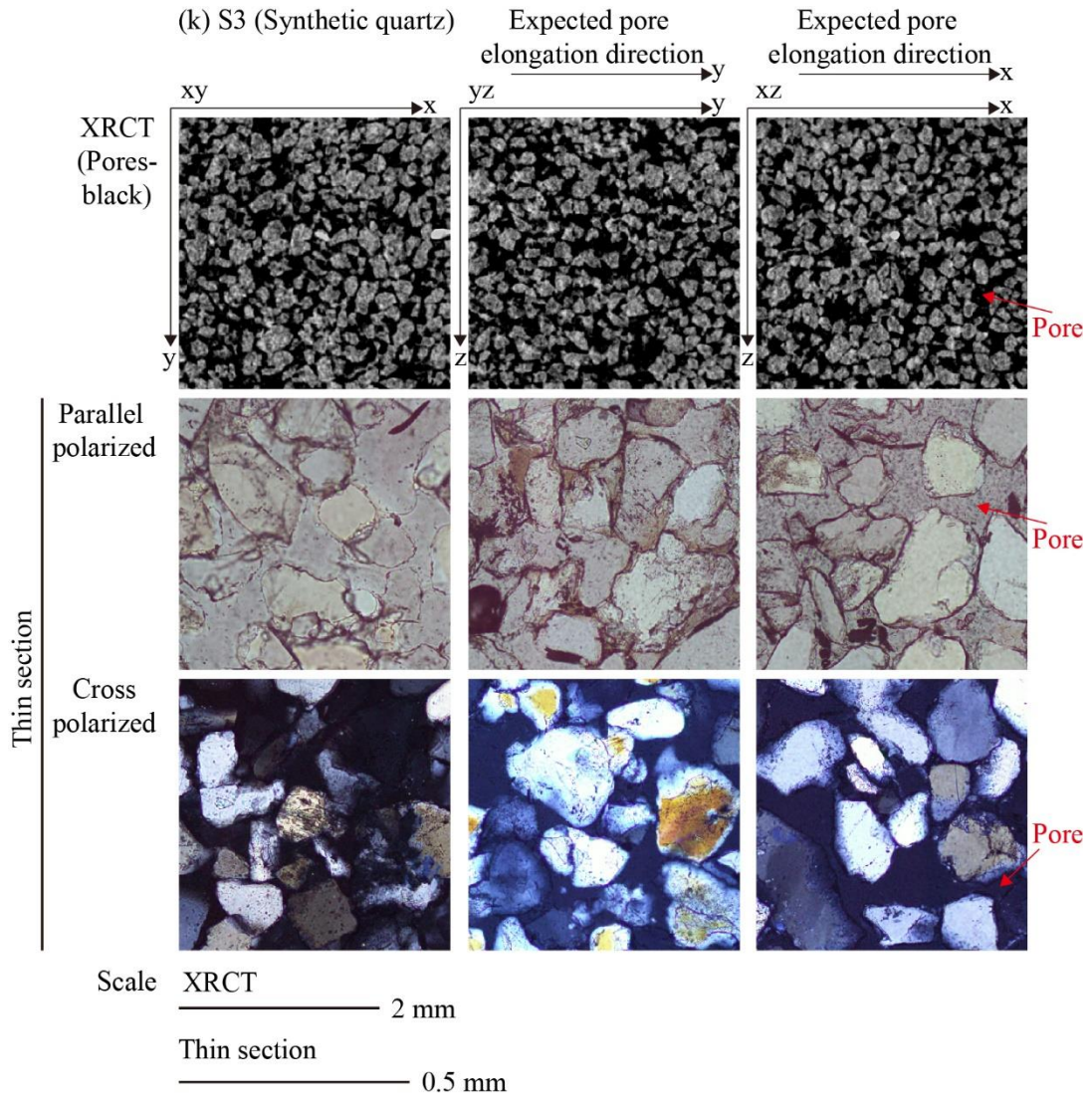






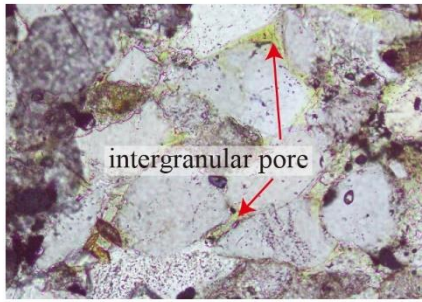




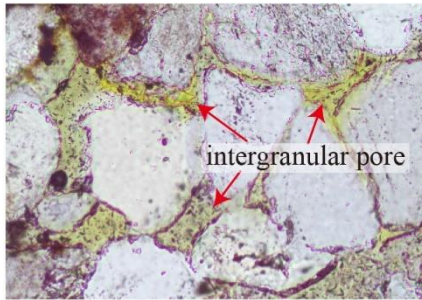


(I) Thin sections for types of pores  
Sandstone

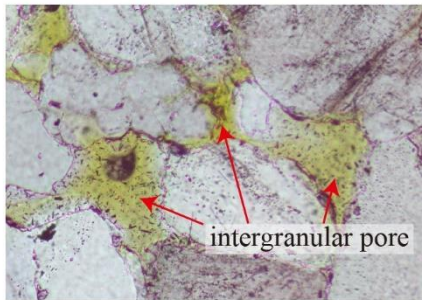
B25



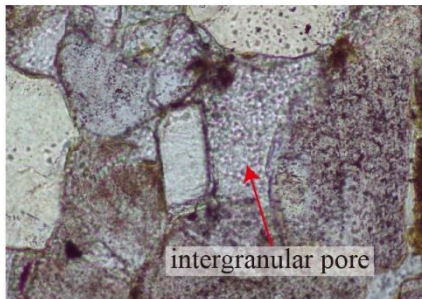
B660



BT

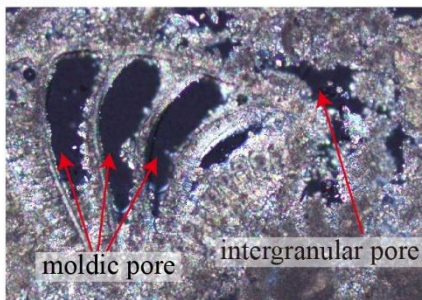


D12

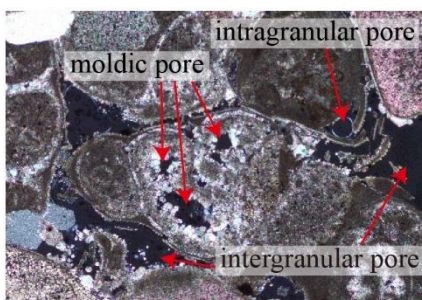


Carbonate stone

MI6 (1)

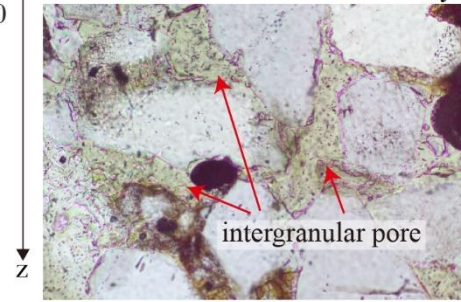


I

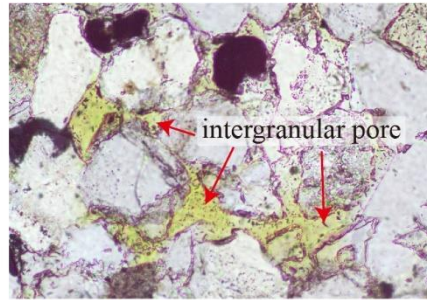


Expected pore elongation direction → y

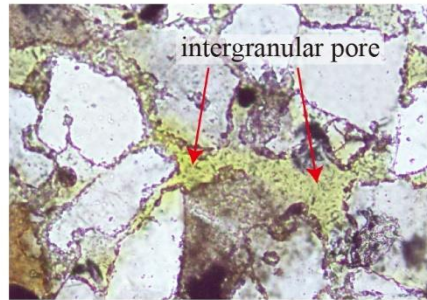
B350



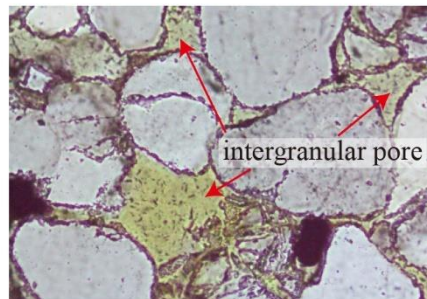
BS



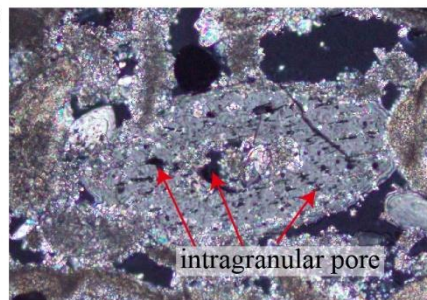
CG



SWN

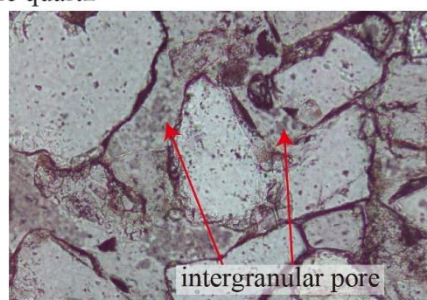


MI6 (2)



Synthetic quartz

S3



0.8 mm  
(I)

0.2 mm  
(others)

**Figure 4.3.** (a-k) Macroscopic fabrics of the sample blocks examined from photographs on three perpendicular surfaces ( $xy$ ,  $yz$ ,  $xz$ ) (see text) and pore fabrics on XRCT images of cores and thin sections in three orthogonal orientations ( $xy$ ,  $yz$ ,  $xz$ ). The first column shows the macroscopic fabrics from photographs of blocks. The surface of block BS has slight bedding structures, while the other blocks are relatively homogeneous without any clear structures. The second column shows the pore fabrics on XRCT images of cores. Columns three to six sequentially show the characteristics for pore fabrics and grain fabrics on the thin sections that were impregnated with fluorescent resin. These include images under parallel-polarized light, cross-polarized light, green UV light, and pore fabrics (shown in white) extracted using the ImageJ software. Samples D12, MI6, and S3, being part of an early experimental group, lack external photographs and consideration of fluorescent resin during thin section preparation. Some thin sections have a weak fluorescence due to the sparse presence of fluorescent resin on the minerals. Therefore, only the brightest luminescent parts were extracted for pore fabrics analysis. (l) Identification of pore types in thin sections ( $yz$ ). These images are magnifications of the thin section images in part (a-k), aimed at providing a clearer view of the microscopic pore fabrics, with a particular focus on highlighting the pore types. All sandstone and synthetic quartz samples display images under plane-polarized light, with pore areas injected with yellow resin clearly visible. The primary pore type is intergranular pores. In contrast, calcarenite MI6 and limestone I display images under cross-polarized light, where black pore areas are more easily identified. These samples contain inter- and intragranular pores and moldic pores. Note that molasse D12, calcarenite MI6, and synthetic quartz S3 are early samples that were not injected with colored resin. Consequently, pore areas in samples D12 and S3 can only be identified with difficulty under plane-polarized light through repeated comparison and careful observation, while in cross-polarized light, quartz grains exhibit undulatory extinction, making pore area identification even more challenging.

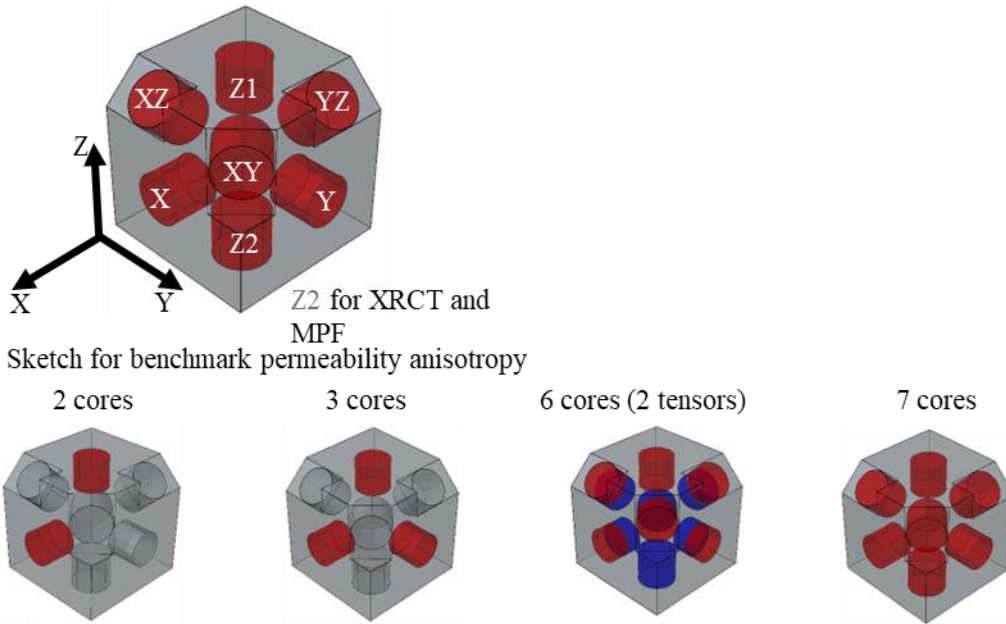
All sandstones show quartz as the primary mineral and intergranular pores as the main pore type. Samples B350 and D12 show more secondary minerals with the presence of clays. MI6 and I have bioclastic fragments and oolites as the main grains cemented by calcite, with various pore types including inter- and intragranular pores, and moldic pores (Figure 4.3).

After macroscopic visualization of the blocks, for the first group of samples (Molasse, Calcarenite and synthetic quartz), one standard size core of 25 mm diameter and 22 mm length was drilled from each of six directions, X, Y, Z, XY, YZ, XZ. An additional core from each block was drilled along the Z direction for the Molasse and Calcarenite and along the X direction for the synthetic quartz sandstone (Table 4.1 and Figure 4.4a). Benchmark sample blocks were first subjected to a simple XRCT scan to check for sample heterogeneity. Then, 18 cores were drilled from the six directions for each benchmark sample to check the variability of the blocks (Table 4.1 and Figure 4.4b). All sample cores were dried in an oven at 100 °C for 48 h. The grain volume was measured by a Micromeritics AccuPyc 1340 Automatic Gas (He) Pycnometer system at the University of Bern, and the bulk volume was calculated by the diameter and height of cores, which were repeatedly measured using a caliper. The porosity was then determined by comparing the grain volume with the bulk volume.

**Table 4.1.** Sample list for directional cores

Sample name	Directional core
D12, MI6	X, Y, Z1, Z2, XY, YZ, XZ
S3	X1, X2, Y, Z, XY, YZ, XZ
B25, B350, B660, BS, BT, CG, SWN, I	X1, X2, Y11, Y12, Y21, Y22, Z11, Z12, Z13, Z21, Z22, Z23, XY1, XY2, YZ1, YZ2, XZ1, XZ2

(a) Sketch for directional cores of sample D12, MI6 and S3



(b) Sketch for directional cores of benchmarks (B25, B350, B660, BS, BT, CG, SWN, I)

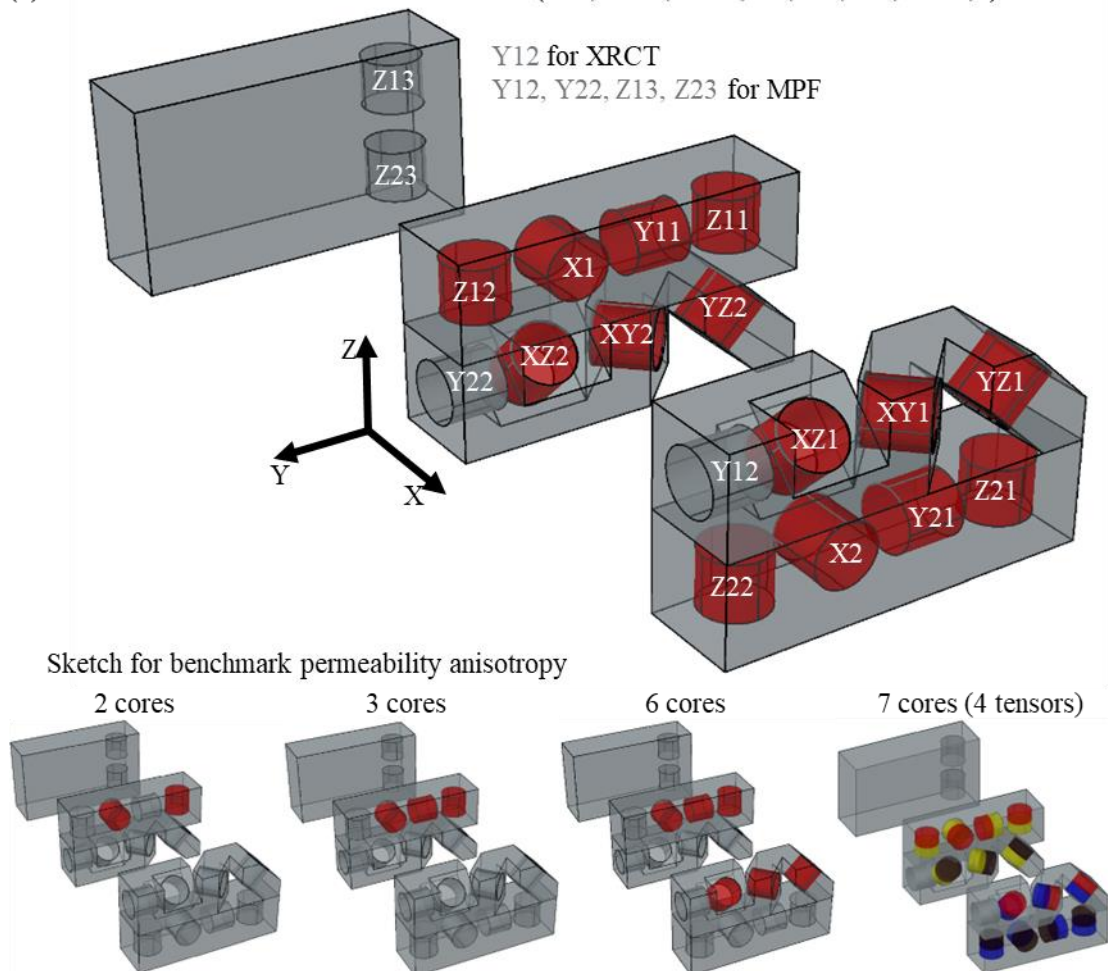


**Figure 4.4.** Sketch for directional cores. (a) Directional cores of samples D12, MI6 and S3 and cores for permeability anisotropy, (b) directional cores of benchmark samples B25, B350, B660, BS, BT, CG, SWN, I, and cores for permeability anisotropy of benchmarks.

## 4.2.2 Direct and indirect pore fabric determination

### 4.2.2.1 Thin section analysis

Pore characterization was first performed on thin sections. In the case of the first group of samples D12, MI6 and S3, standard resin impregnation was used to prepare thin sections; thus, no additional pore analysis was performed beyond the examination under plane- and cross-polarized light. In contrast, the thin sections of the benchmark samples were impregnated with the fluorescent resin, which facilitates the identification of pores using fluorescence microscopy. However, by covering of these sections with glass slides prior to polishing, an overflow of colored resin was observed on the mineral surfaces. Therefore, only the brightest fluorescent areas were identified as pores (Figure 4.3). High-resolution imaging was achieved using a microscope at 10× magnification. For sample I, both the grains and pores are significantly larger than those in other samples. A 5x magnification was sufficient, and the sampling area was larger than others to ensure the collection of representative data. Pore analysis was carried out using ImageJ software with the Threshold function for pore segmentation and the Analyze Particles function to determine the area and principal axis of the best-fitting ellipse for each pore. The pore size was determined by the equivalent diameter of a circle with an area equal to that of the pore, referred to as the EqDiameter. The Representative Elementary Area (REA) was defined by evaluating the distribution of porosity and pore size as a function of the included area, with an 8 mm × 8 mm section selected for analysis (Zhou et al., 2022). The aggregate shape of the ellipses in each thin section was calculated by summing the tensors of the best-fit ellipses of the pores (Zhou et al., 2022). By aggregating the tensors from total shape ellipses in the  $xy$ ,  $yz$ , and  $xz$  thin sections, the second-order tensors were derived to represent the average three-dimensional pore structure, i.e., total shape ellipsoid (Shimamoto & Ikeda, 1976). For further analysis, only pores with a minimum size of 4×4 pixels (2.3×2.3 μm<sup>2</sup>) were considered, as they were large enough to be reliably detected (Zhou et al., 2022).

The anisotropy degree ( $P = a/c$ , [1, ∞]) and shape ( $U = (2*b-a-c)/(a-c)$ , [-1,1]) can be calculated by using the lengths of the principal axes of the total shape ellipsoid ( $a ≥ b ≥ c$ ) (Jelinek, 1981).

### 4.2.2.2 XRCT data acquisition and processing

One core from each sample (B25Y12, B350Y12, B660Y12, BSY12, BTY12, CGY12, D12X, SWNY12, MI6Z2, IY12, S3Z) was scanned with a Bruker SkyScan 1273 at the University of Bern, with a resolution of 5.5 μm pixel size, using a 1 mm Al+0.038 mm Cu filter, with operating parameters set at 100 kV and 80 μA to achieve an exposure time of 275 ms.

Image reconstruction including the correction of misalignments, as well as ring and beam hardening artifacts, were performed using NRecon (Skyscan, 2011). Subsequently, the XRCT data were processed using Avizo (ThermoFisher Scientific, version 2021.2), applying an Unsharp masking filter for noise reduction (Polesel et al., 2000; Strobel, 1996) and a watershed algorithm for pore segmentation (Bieniek & Moga, 2000). The representative elementary volume (REV) was constructed analogously to the representative elementary area (REA) method (Zhou et al., 2022). A volume of 600×600×600 voxels (3.3×3.3×3.3 mm<sup>3</sup>) was designated as the REV for subsequent pore analysis, permeability simulation, and MPF modeling. All pores larger than 4×4×4 voxels (22×22×22 μm<sup>3</sup>) were classified as detectable in shape for further analysis (Zhou et al., 2022).

The total shape ellipsoid was used to represent pore fabrics, incorporating bootstrap methods (Constable & Tauxe, 1990; Tauxe et al., 1998; Zhou et al., 2022) and calculating 95% confidence ellipses (Hext, 1963; Jelínek & Kropáček, 1978; Owens, 2000; Zhou et al., 2022). The degree of anisotropy  $P$  and shape  $U$  of the pore fabrics were derived similarly to the thin section analysis approach.

XRCT-derived pore network models were reconstructed using Avizo software and facilitated the calculation of the permeability tensor via simulated fluid flow from various orientations, using a standard input pressure of 0.13 MPa and a default fluid viscosity of 0.001 Pa·s. Increasing the pressure and fluid viscosity significantly increased the simulation computation time but did not notably alter the simulated permeability anisotropy orientation, degree, or shape—the parameters of primary interest in this study. Therefore, the default settings were used to reduce simulation computation time. The permeability anisotropy was determined by analyzing the eigenvectors and eigenvalues of the tensor. The degree and shape of anisotropy can also be calculated from the eigenvalues corresponding to maximum, intermediate and minimum permeability.

The MPF was modeled for each sample based on the XRCT data using FinIrrSDA software (Biedermann, 2020) to assess total anisotropy and shape anisotropy.

#### 4.2.2.3 Permeability anisotropy measurements

Permeability anisotropy, a second-order tensor, requires a minimum of six directional measurements, with additional cores in identical orientations to evaluate variability. Samples were analyzed by CoreLab ((UK) for air permeability testing at a confining pressure of 800 psig ( $\approx 5.52$  MPa). Preliminary full tensor permeability anisotropy measurements focused on D12, MI6, and S3 samples, considering inherent variability. Six directional cores (X, Y, Z, XY, YZ, XZ) with one additional core were obtained for full tensor permeability estimation with 95% confidence ellipse. Six different cores (X, Y, Z1, XY, YZ, XZ or X, Y, Z2, XY, YZ, XZ) were selected for the full tensor calculation without confidence intervals. A trio (X, Y, Z) or a pair (X, Z) of cores was chosen to derive the vertical and horizontal directional permeability anisotropy of the fabric, in accordance with common practices in the literature (Figure 4.1, 4.4). Consequently, the permeability anisotropy results derived from seven, six, three, and two cores were compared, to identify potential discrepancies due to under- or over-estimation when examining limited cores. Eight benchmark blocks of larger dimensions were prepared for further analysis. For these, 14 cores were drilled in six directions to compute four tensors including confidence ellipses (X1, Y11, Z11, Z12, XY1, YZ1, XZ1 and X2, Y21, Z21, Z22, XY2, YZ2, XZ2 and X1, Y11, Z11, Z12, XY2, YZ2, XZ2 and X2, Y21, Z21, Z22, XY1, YZ1, XZ1). Similar to previous procedures, six, three, and two directional cores were also evaluated for comparison purposes (Figure 4.4). Second-order permeability tensors were quantified analogously to the total shape ellipsoid calculations, considering the eigenvectors  $V1, V2, V3$ , the anisotropy degree  $P = k1/k3$ , and the shape  $U = (2*k2 - k1 - k3)/(k1 - k3)$ , where  $k1 \geq k2 \geq k3$  represent the principal permeabilities.

#### 4.2.2.4 Magnetic pore fabric measurements

The anisotropic magnetic susceptibility (AMS) of each dry sample was determined by 15 directional measurements taken while the sample was rotated to elucidate the inherent anisotropy of the rock (Jelinek, 1996). The instrumentation included a MFK1-FA susceptibility bridge from AGICO (Czech Republic), operating at approximately 1 kHz and applying a standard magnetic field of 200 A/m. The AMS data comparison for either seven cores per sample (D12, MI6, S3) or 18 cores from benchmark samples ensured evaluations within a consistent coordinate framework, and verified the homogeneity of each sample. Initially characterized cores from the first group (D12, MI6, S3) were impregnated with a diluted, oil-based ferrofluid (FerroTec EMG 909 with an intrinsic susceptibility of 1.38 SI) under a 100 kPa vacuum for one hour. This procedure was similar to that used in previous studies (Zhou et al., 2022). This ferrofluid was diluted at a volume ratio of 1:30 with hardener to resin at a ratio of 1:4. After impregnation, the MPFs were measured to determine the magnetic anisotropy, following to the same protocol as the AMS measurement (Table 4.2).

The susceptibility-based impregnation efficiency ( $I.E._{susc}$ ) and the MPF-inferred porosity ( $\phi_{MPF}$ )

were determined by comparing the sample susceptibility to that of the impregnation fluid (Pugnetti et al., 2022):

$$I.E._{susc} = \frac{\Delta k_{mean}}{\varphi k_{fluid}} * 100\%$$

$$\varphi_{MPF} = \frac{\Delta k_{mean}}{k_{fluid}} * 100\%$$

where  $k_{fluid}$  is the ferrofluid susceptibility, while  $\varphi$  is the sample porosity, ranging from 0 to 1.  $\Delta k_{mean}$  is the change in the mean susceptibility of the sample during impregnation. Given the insignificance of the magnetic susceptibility of the pre-impregnation sample compared to the post-impregnation sample,  $\Delta k_{mean}$  can be replaced by the mean susceptibility of the impregnated sample  $k_{mean}$ . Note that both  $k_{fluid}$  and  $k_{mean}$  are normalized to the volume of the measured ferrofluid or sample and can then be compared.

**Table 4.2.** AMS and MPF measurement settings. “\” means no data. The diluted ferrofluids' susceptibilities were measured and adjusted for self-demagnetization, yielding susceptibility values of 0.17 SI for EMG 705 (1:10), 0.19 SI for EMG 905 (1:10), and 0.012 SI for EMG 909 (1:30).

	Volume ratio of ferrofluid and dilution	Impregnation method	Frequency (kHz)	Field (A/m)
<b>AMS</b>				
All cores	\	\	~1	200
<b>MPF</b>				
D12, MI6, S3	1:30 EMG 909 : hardener and resin	100 kPa vacuum for 1 hours	~1	200
B25, B350, B660, BS, BT, CG, SWN	1:10 EMG 705 : distilled water	100 kPa vacuum for 24 hours	~1	200
I	1:10 EMG 905 : oil EMG 900	100 kPa vacuum for 24 hours	~1	200

In addition, dissolution that occurs at the sample surfaces during ferrofluid impregnation resulted in a reduction in sample mass after impregnation. This phenomenon was relatively more pronounced in samples with weak cementation, where dissolution was more pronounced. As a result, it was not possible to determine the mass of ferrofluid in the impregnated sample by measuring the difference in mass, making it impossible to calculate the mass-based impregnation efficiency ( $I.E._{mass}$ ).

The relatively lower intrinsic susceptibility and higher viscosity of the resin mixture resulted in reduced impregnation efficiency. Water-wet quartz sandstone (Zhang et al., 2020) and oil-wet carbonate surfaces (Zhang et al., 2006; Zhang & Austad, 2006) influenced the choice of impregnation media. To improve impregnation efficiency, water-based EMG 705 (4.04 SI intrinsic susceptibility and <5 mPa•s viscosity) was selected for sandstones, and oil-based EMG 905 (3.52 SI intrinsic susceptibility and <5 mPa•s viscosity) was selected for limestones. The ferrofluids were diluted with distilled water or exclusive oil (EMG 900 from FerroTec) in a volume ratio of 1:10 (Table 4.2).

Although the initial susceptibility of the ferrofluid is specified by the Ferrotec company, susceptibility of the ferrofluid is frequency dependent, being higher than the initial susceptibility for oil-based fluid, but lower for water-based fluid (Biedermann et al., 2021). Furthermore, due to the self-demagnetization (Clark, 2014; Osborn, 1945; Sato & Ishii, 1989; Stoner, 1945), the susceptibility must be measured under standard conditions and corrected to obtain the true intrinsic susceptibility of the ferrofluid ( $k_{int}$ )

$$k_{int} = \frac{k_m}{1 - Nk_m}$$

Where,  $N$  is the self-demagnetization factor, which depends on the shape of the magnetic material, and  $k_m$  is the measured susceptibility of the ferrofluid. The ferrofluid, consisting of strongly magnetic nanoparticles suspended in a carrier liquid, is macroscopically treated as a homogeneous strongly magnetic liquid. Here, the self-demagnetization factor is determined by the shape of the fluid during the measurement process. Therefore, the susceptibilities of diluted ferrofluids stored in cylinders (1.63-cm diameter by 0.95-cm height) were measured and adjusted for self-demagnetization, yielding susceptibility values of 0.17 SI for EMG 705 (1:10), 0.19 SI for EMG 905 (1:10), and 0.012 SI for EMG 909 (1:30).

The statistical reliability of anisotropy against instrument noise for the MPF, was determined by confidence angles  $E13$  ( $=E31$ ),  $E12$  ( $=E21$ ) and  $E23$  ( $=E32$ ), derived from average directional susceptibilities (Hext, 1963; Jelinek, 1977, 1981). Narrow confidence angles indicate pronounced anisotropy with precise orientations.  $P$  and  $U$ , which characterize magnetic anisotropy, were calculated as  $k1/k3$  and  $(2*k2-k1-k3)/(k1-k3)$ , respectively, where  $k1 \geq k2 \geq k3$  are the primary susceptibilities (Jelinek, 1981).

#### 4.2.3 Correlation of thin section, XRCT, permeability anisotropy and MPF data

Porosity measurements obtained from the Helium pycnometer were directly compared to porosities calculated from thin section, XRCT, and MPF data. Similarly, measured permeability values were directly compared with those calculated from XRCT data. Permeability anisotropy measurements in 7, 6, 3, and 2 directions were compared to determine the need for seven-direction measurements for accurate data quality assessment and to avoid underestimation of anisotropy. Comparisons were made between pore fabrics derived from thin section analysis, XRCT data (total shape ellipsoid, simulated permeability anisotropy, MPF model), measured permeability anisotropy, AMS, and MPF. These comparisons focused on the orientation, represented by the angle between the principal axes of different properties relative to the confidence angle, and also considered the degree and shape of anisotropy. In addition, the total tensors derived from these different methods were calculated to allow a direct comparison of anisotropy orientations between them.

#### 4.3. Results

Porosity measurements of the sampled collection range from 17.43% to 55.58%, while permeabilities range from 3.4 to 14180.3 mD (approximately  $33.56-139948.68 \times 10^{-16} \text{ m}^2$ ). The data generally follow the expected porosity-permeability relationship. Sample B25 has the lowest porosity at 17.43%, while sample MI6 has the highest at 55.58%. Most samples show the same trend of increasing porosity values with helium pycnometer-derived porosity values being greater than XRCT-derived porosity values, followed by MPF-derived and thin-section-derived porosity values. Thin section and MPF data provide comparable porosity values for all samples. In the case of sample SWN, the MPF data shows a slightly lower porosity than the thin section; however, their respective porosities are similar within uncertainty. Sample S3 shows a unique ordering where the MPF-derived porosity is greater than XRCT-derived porosity which is greater than the helium-derived porosity (Table 4.3 and Figure 4.5).

**Table 4.3.** Porosity comparison of laboratory measurements by He pycnometer, numerical calculations based on thin sections and XRCT data, and estimation from MPF.  $I.E._{susc}$  is also presented. The susceptibility-based impregnation efficiency ( $I.E._{susc}$ ) and the MPF-inferred porosity were determined by comparing the sample susceptibility to that of the impregnation fluid. “\” means no data. For samples D12, MI6 and S3, only one core of each sample was impregnated by ferrofluid, so error estimates of their MPF-porosity and  $I.E._{susc}$  based on multiple measurements for one core.

Sample	Porosity (He pycnometer, AccuPyc 1340) (%)	Porosity (thin sections / magnification: 10x) (%) (threshold, (solid-void) 0-255)	Porosity (Skyscan 1273 / resolution: 5.5 $\mu$ m) (%) (threshold, (void-solid) 0-255)	Porosity (MPF) (%)	$I.E._{susc}$ (%)
<b>Sandstone</b>					
B25	18.05 $\pm$ 0.62	4.7 $\pm$ 0.4 (83)	14 $\pm$ 1 (51)	7.8 $\pm$ 0.6	42.9 $\pm$ 5.0
B350	24.11 $\pm$ 0.64	7.6 $\pm$ 0.5 (87)	19 $\pm$ 2 (44)	9.4 $\pm$ 0.4	38.8 $\pm$ 2.3
B660	23.85 $\pm$ 0.62	7.8 $\pm$ 0.9 (83)	19 $\pm$ 2 (55)	11.4 $\pm$ 3.0	48.4 $\pm$ 12.1
BS	23.83 $\pm$ 0.46	7.6 $\pm$ 0.4 (83)	18 $\pm$ 1 (48)	10.2 $\pm$ 0.9	42.2 $\pm$ 4.1
BT	26.62 $\pm$ 0.56	11 $\pm$ 0 (81)	22 $\pm$ 2 (43)	10.7 $\pm$ 0.7	40.2 $\pm$ 2.8
CG	32.60 $\pm$ 0.64	11 $\pm$ 1 (90)	23 $\pm$ 1 (50)	10.7 $\pm$ 2.1	32.9 $\pm$ 6.5
D12	21.53 $\pm$ 0.71	\	12 $\pm$ 2 (35)	9.2 $\pm$ 0.1	42.6 $\pm$ 0.1
SWN	32.92 $\pm$ 1.01	10 $\pm$ 1 (102)	17 $\pm$ 2 (44)	8.3 $\pm$ 1.5	25.3 $\pm$ 4.3
<b>Carbonate stone</b>					
MI6	54.01 $\pm$ 1.57	\	37 $\pm$ 3 (40)	32.4 $\pm$ 0.1	60.1 $\pm$ 0.1
I	20.97 $\pm$ 1.07	9.1 $\pm$ 1.9 (68)	12 $\pm$ 1 (42)	9.5 $\pm$ 1.1	46.3 $\pm$ 6.3
<b>Synthetic quartz</b>					
S3	40.97 $\pm$ 0.94	\	42 $\pm$ 2 (45)	44.7 $\pm$ 0.1	109 $\pm$ 0.1

For the pore size distribution, data from thin sections indicate a decreasing trend in the proportion of pores as their size increases, with larger pores showing lower relative quantities. Conversely, XRCT data show a bimodal distribution, with peaks at  $\sim$ 30 and  $\sim$ 100  $\mu$ m. Thin section data show a wider pore size range (2-400  $\mu$ m) compared to XRCT data (20-400  $\mu$ m) (Figure 4.6).

#### 4.3.1 Thin section

Examining the degree of anisotropy  $P$  and shape  $U$ , sample BS has the lowest range of 1.02-1.03 among all samples, while sample CG has the highest  $P$  values, between 1.07-1.08. Samples B25, B350, BT, CG, and SWN show a relatively prolate anisotropy shape with mean  $U$  values ranging from -0.14 to -0.38. Conversely, samples B660, BS, and I have a relatively oblate shape with mean  $U$  values ranging from 0.02 to 0.18. However, all samples show considerable variation in  $U$  across different total shape ellipsoids, indicating inconsistent anisotropy shapes for each sample (Figure 4.7).

Samples B25, B350, BT, CG, and SWN have the minimum axes ( $V_3$ ) of pore fabrics closely aligned with the  $z$ -direction, while the maximum and intermediate axes ( $V_1$ ,  $V_2$ ) lay within the  $xy$ -plane. Samples B660 and BS have an angle of about  $35^\circ$  between the  $V_3$  and  $z$ -axis, and between the  $V_1$  and the  $xy$ -plane. For sample I, the anisotropy orientations of pore fabrics show inconsistent distributions between different tensors (Figure 4.8).

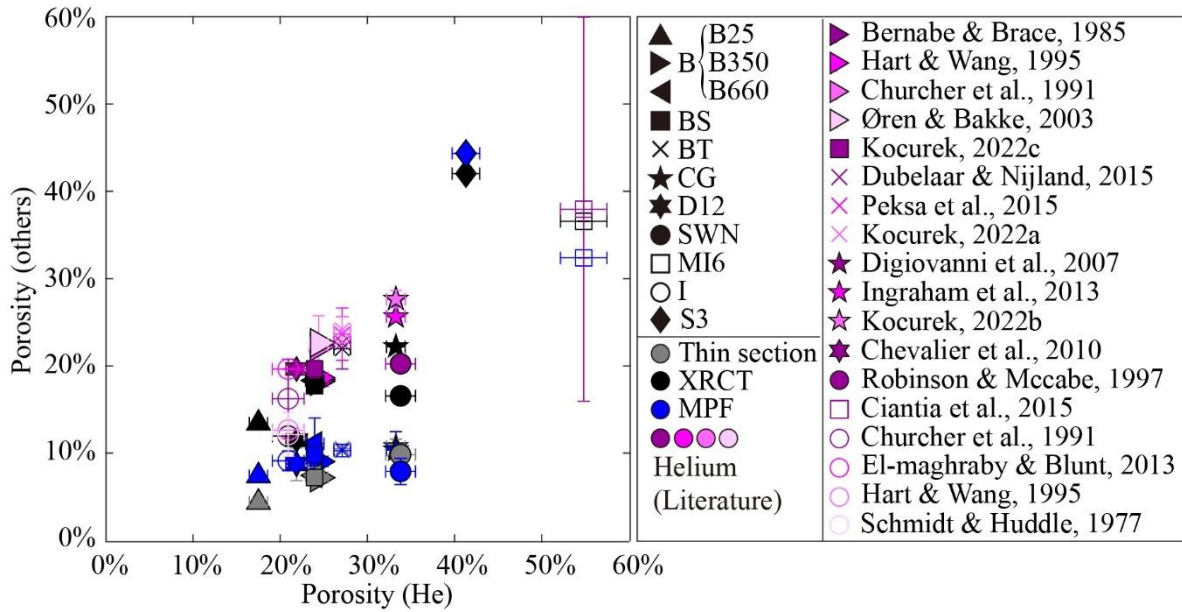


**Figure 4.5.** Porosity for different samples from Helium pycnometer, thin section analysis, XRCT, MPF-derived data, and Helium pycnometer (literature). Different shapes of symbols represent the different samples. The samples B25, B350, and B660 are all Berea sandstone with different permeabilities, and thus, they are represented by similar symbols, specifically triangles oriented in different directions. All sandstone samples (B25, B350, B660, BS, BT, CG, D12, SWN, S3) are represented with solid symbols, while carbonate samples (MI6, I) are represented with open symbols. Helium porosity, obtained using the standard measurement method, is used as the  $x$ -axis, while porosity obtained from other methods is represented by different colors as the  $y$ -axis. Note that symbols of the same shape (regardless of color differences) correspond to the same sample, so they share the same value on the  $x$ -axis, all representing He porosity. However, their different colors correspond to porosity from other methods or literature, showing their values on the  $y$ -axis. Gray represents thin section-derived porosity, black represents XRCT-derived porosity, blue represents MPF-derived porosity, and purple also represents He porosity, but these are not measured in this study (the He porosity measured in this study is shown on the  $x$ -axis) and are instead sourced from the literature, with different shades of purple indicating different references.

#### 4.3.2 XRCT data

Regarding the degree of anisotropy for XRCT-derived pore fabrics in different sandstones, sample D12 has the highest  $P$  value of 1.34, while sample BS has the lowest value of 1.09. For carbonates, the degrees of anisotropy area at 1.31 for sample I and 1.27 for sample MI6. The synthetic sample S3 has an average  $P$  of 1.07. In terms of anisotropy shapes for XRCT-derived pore fabrics, samples BS, CG, and SWN have prolate shapes, while samples B350, B660, D12, and I are oblate. Samples B25, BT, MI6, and S3 show inconsistent anisotropy shapes (Figure 4.7).

For XRCT-derived pore fabrics, expect for MI6, all samples have the  $V1$  axes of total shape ellipsoids and Orientation Distribution Functions (ODFs) within the  $xy$ -plane. Samples B25, B350, B660, BT, D12, I, and S3 have  $V3$  axes that are subparallel to the  $z$ -axis. Samples BS, CG, and SWN have their  $V2$  and  $V3$  axes aligned with the  $xz$ -plane. Sample MI6's  $V1$  and  $V2$  axes show a broad distribution along the  $xz$ -plane, with the  $V3$  axis trending subparallel to the  $y$ -axis (Figure 4.8).

In terms of simulated permeability anisotropy, sample D12 has the highest degree of anisotropy at 2.53, and sample BS has the lowest at 1.07 compared to other samples. Samples B25, B660, BS, and S3 are characterized by their oblate anisotropy shapes, with  $U$  values ranging from 0.03 to 0.61. The remaining samples have prolate shapes, with  $U$  values ranging from -0.04 to -0.55

(Figure 4.7). For sandstones and synthetic sample S3, the  $VI$  axes of the simulated permeability anisotropy are nearly parallel to the  $xy$ -plane. The  $VI$  of Sample MI6 is closely aligned with the  $z$ -axis, while that of Indiana limestone I is oriented at about  $30^\circ$  to the  $xy$ -plane (Figure 4.8).

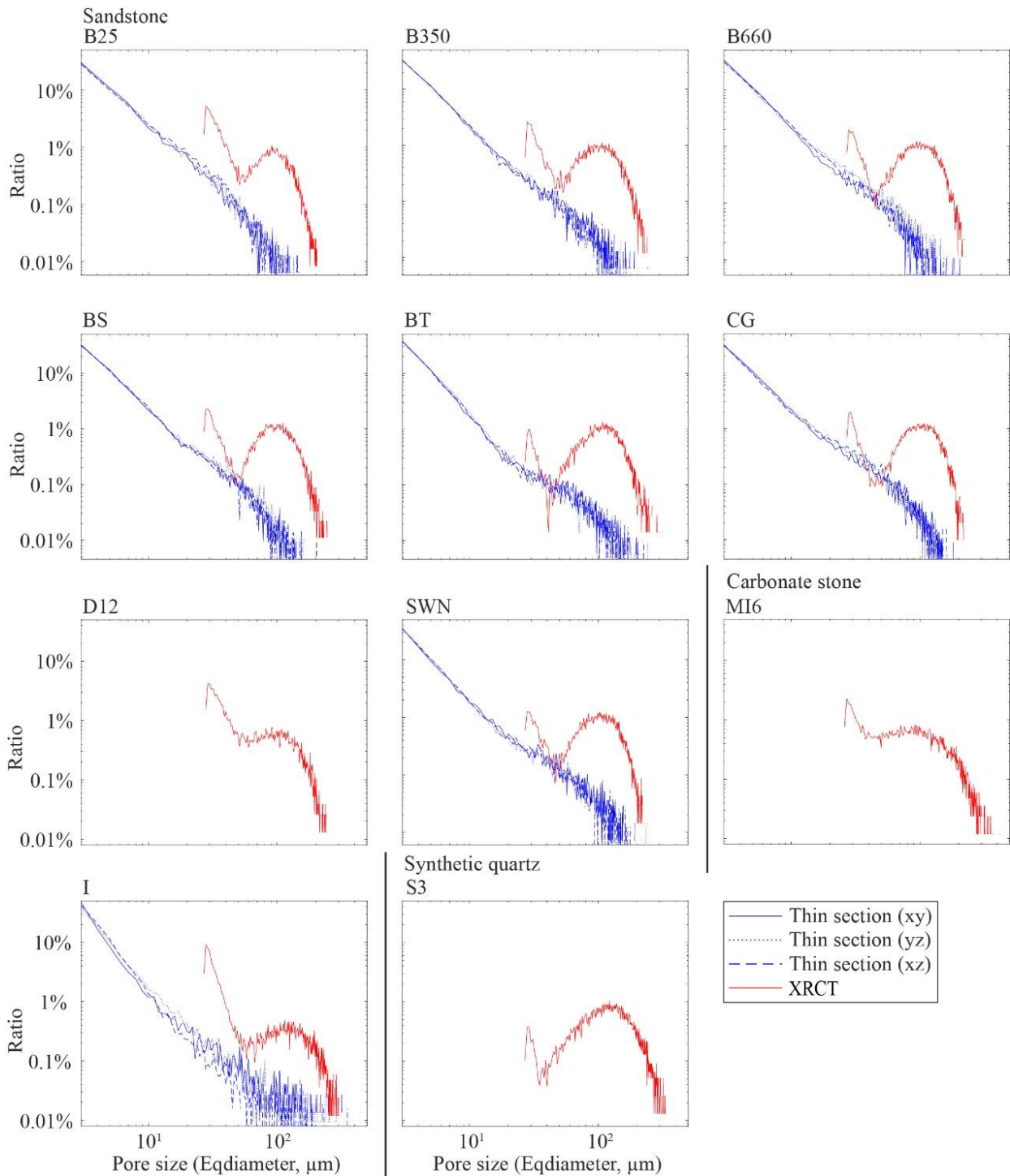


**Figure 4.6.** Pore size distribution for all samples. Pore size is presented by EqDiameter which is the diameter of a circle or sphere with the same area or volume as a single pore. The distribution is presented as percent of pores, comparing the number of pores for each size with the total number of pores.

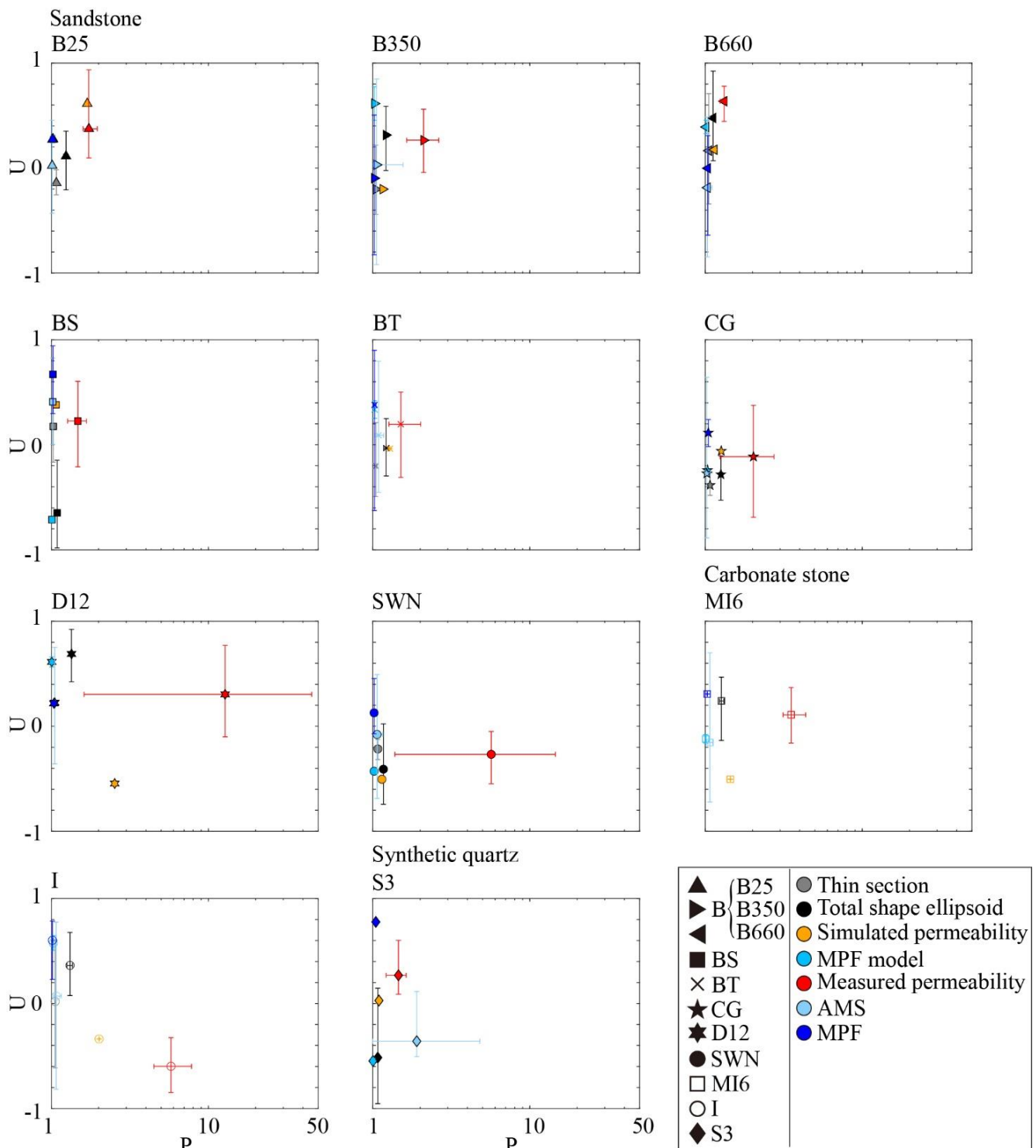


**Figure 4.7.** Anisotropy degree ( $P$ ) and shape ( $U$ ) of all samples from pore fabrics of thin section analysis, XRCT-derived data (total shape ellipsoids, simulated permeability anisotropy, and MPF model), measured permeability anisotropy, AMS and MPF.

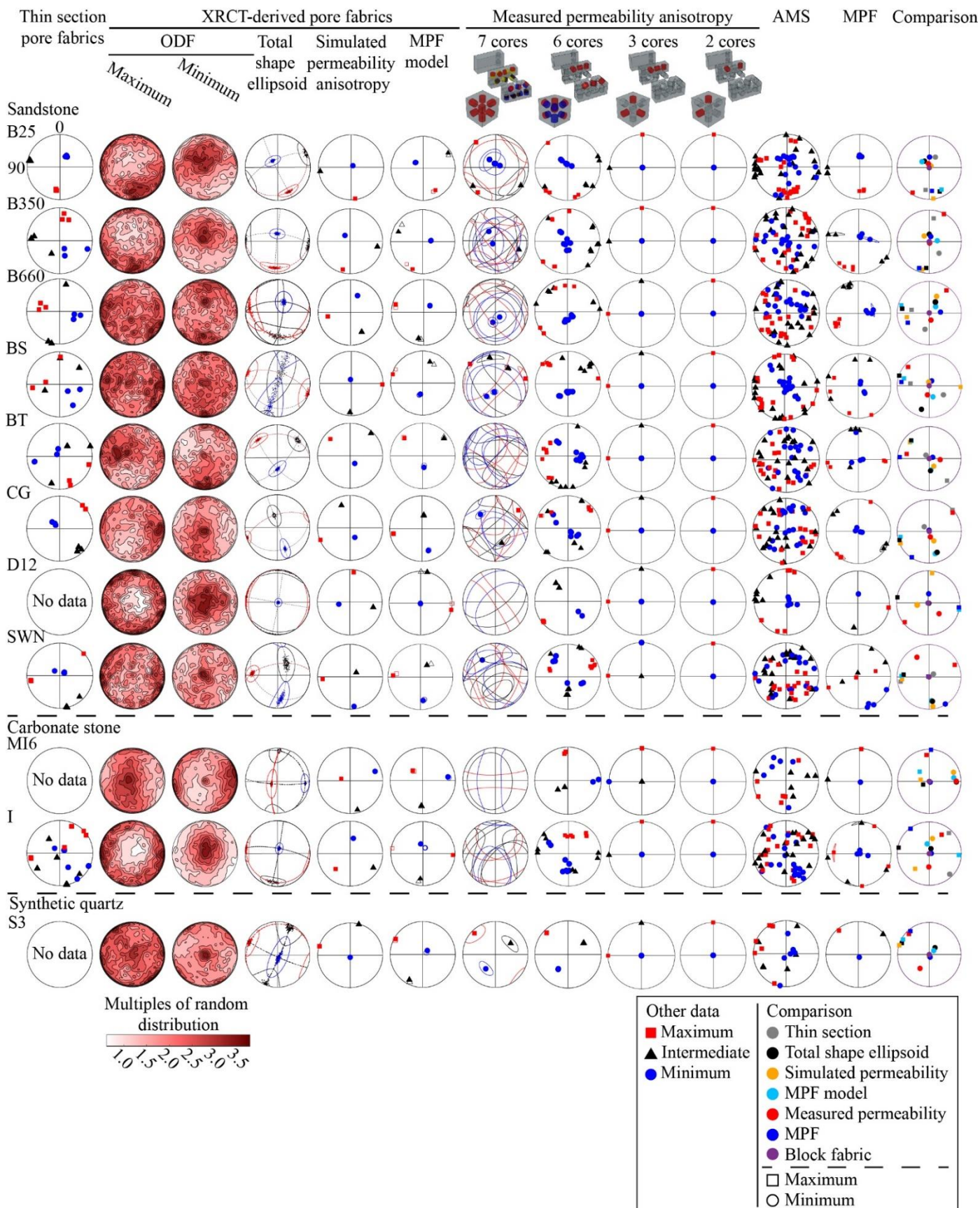


**Figure 4.8.** Comparison of orientation of pore fabrics from thin section analysis, XRCT-derived data (orientation density functions of pore axes, bootstrapped total shape ellipsoids, simulated permeability anisotropy, and MPF model), measured permeability anisotropy (7, 6, 3, 2 cores), AMS and MPF. In the last column, the block fabric was added. During sedimentation, vertical compaction occurs, the maximum axis of the block fabric is considered to be along the  $xy$ -direction, while the minimum axis is along the  $z$ -direction, i.e., the compaction direction.

In the MPF models, the degree of anisotropy of sample CG is the highest at 1.03 compared to other samples, while the  $P$  of sample S3 is the lowest at 1.00. Berea sandstone B25, B350, B660, sandstone BT, D12, and limestone I have oblate anisotropy shapes with  $U$  values ranging from 0.28 to 0.61, while other samples have prolate shapes ranging from -0.12 to -0.71 (Figure 4.7). The  $V1$  axes of all samples are nearly parallel to the  $xy$ -plane, except for calcarenite sample MI6 which is parallel to the  $z$ -axis. The  $V3$  axes of samples B25, B350, B660, I, and S3 are closely aligned with the  $z$ -axis, and samples BS and BT have their  $V3$  axes at approximately  $30^\circ$  to the  $z$ -axis. Samples CG and SWN have their  $V3$  axes nearly aligned with the  $x$ -axis, and sample MI6 has its  $V3$  axes along the  $y$ -axis (Figure 4.8).

### 4.3.3 Permeability anisotropy

Permeability exhibits significant variability both between and within samples. Sample B25 has a significantly lower permeability, ranging from 43 to 71 millidarcies (mD), while synthetic quartz S3 has the highest, ranging between 10355 and 14180 mD. Within individual samples, directional core permeabilities also vary; for example, sample B350 has a permeability ranging from 225 mD to 555 mD, and sample B660 has a narrower range of 334 mD to 438 mD. Variations are also evident in other samples, with sample BS ranging from 360 mD to 598 mD, sample BT from 2038 mD to 3066 mD, and sample CG from 631 mD to 937 mD. Sample D12 shows more important fluctuations with permeabilities as low as 3.4 mD and as high as 27 mD. The remaining samples show heterogeneity: sample SWN ranges from 1206 mD to 3463 mD, sample MI6 from 678 mD to 2128 mD, and sample I exhibits a range from 673 mD to 2137 mD (Figure 4.9). The degree of permeability anisotropy is significantly greater than that of other measured or simulated data (Figure 4.7). The lowest anisotropy value is 1.32 from Berea sandstone B660, and the highest is 12.78 from molasse D12. Most samples exhibit oblate anisotropy shapes with  $U$  values between 0.11 and 0.64, except for samples CG, SWN, and I, which exhibit relatively prolate shapes with  $U$  values between -0.11 and -0.60 (Figure 4.7).

Analysis of the anisotropy directions of the permeability, derived from seven cores equipped with confidence ellipses, shows that the groups of seven cores  $X1, Y11, Z11, Z12, XY1, YZ1, XZ1$ , and  $X1, Y11, Z11, Z12, XY1, YZ1, XZ1$ , show subtle anisotropy directions across all benchmark samples. In contrast, the group of  $X2, Y21, Z21, Z22, XY2, YZ2, XZ2$ , as well as the group of  $X2, Y21, Z21, Z22, XY1, YZ1, XZ1$ , show the tendency of more pronounced anisotropy in all benchmarks except for sample SWN. Specifically, benchmark samples B25, B350, B660, and BS exhibit significant  $V3$  axes nearly parallel to the  $z$ -axis, while the  $V1$  and  $V2$  axes are broadly oriented in the  $xy$ -plane. For sample CG, the  $V2$  and  $V3$  axes are approximately at 45 degrees to the  $z$ -axis, and the  $V1$  axes are in the  $xy$ -plane. For Sample SWN, one  $V3$  axis is oriented at about 50 degrees to the  $z$ -axis, and other directions are much less significant. In cases where only a single tensor measurement is available, samples D12 and MI6 show insignificant anisotropy. However, sample S3 shows pronounced anisotropy with a significant  $V1$  axis in the  $xy$ -plane and  $V2$  and  $V3$  axes positioned at  $\sim 45^\circ$  to the  $z$  direction (Figure 4.8).

Measurements taken from six cores show that the  $V3$  axes of samples B25, B350, B660, and BS are close to the  $z$ -axis and the  $V1$  and  $V2$  axes are distributed in the  $xy$ -plane. The principal directions in samples BT and CG have similar but inconsistent distributions. Samples D12 and S3 have the  $V1$  axes in the  $xy$ -plane and the  $V2$  and  $V3$  axes at  $\sim 45^\circ$  to the  $z$ -axis. Sample MI6 has the  $V1, V2$ , and  $V3$  axes aligned in the  $x, z$ , and  $y$  directions, respectively. Samples SWN and I show inconsistent anisotropy in permeability (Figure 4.8).

For three-core measurements, all samples have the  $V3$  axes aligned in the  $z$  direction, and the  $V1$  and  $V2$  axes in the  $xy$ -plane, except samples SWN and MI6, which have  $V1$  and  $V3$  axes in the  $xy$ -plane and the  $V2$  axes in the  $z$  direction. For two-core measurements ( $X, Z$ ), all samples have the

$V1$  axes in the  $x$  direction and the  $V3$  axes at the  $z$  direction (Figure 4.8).

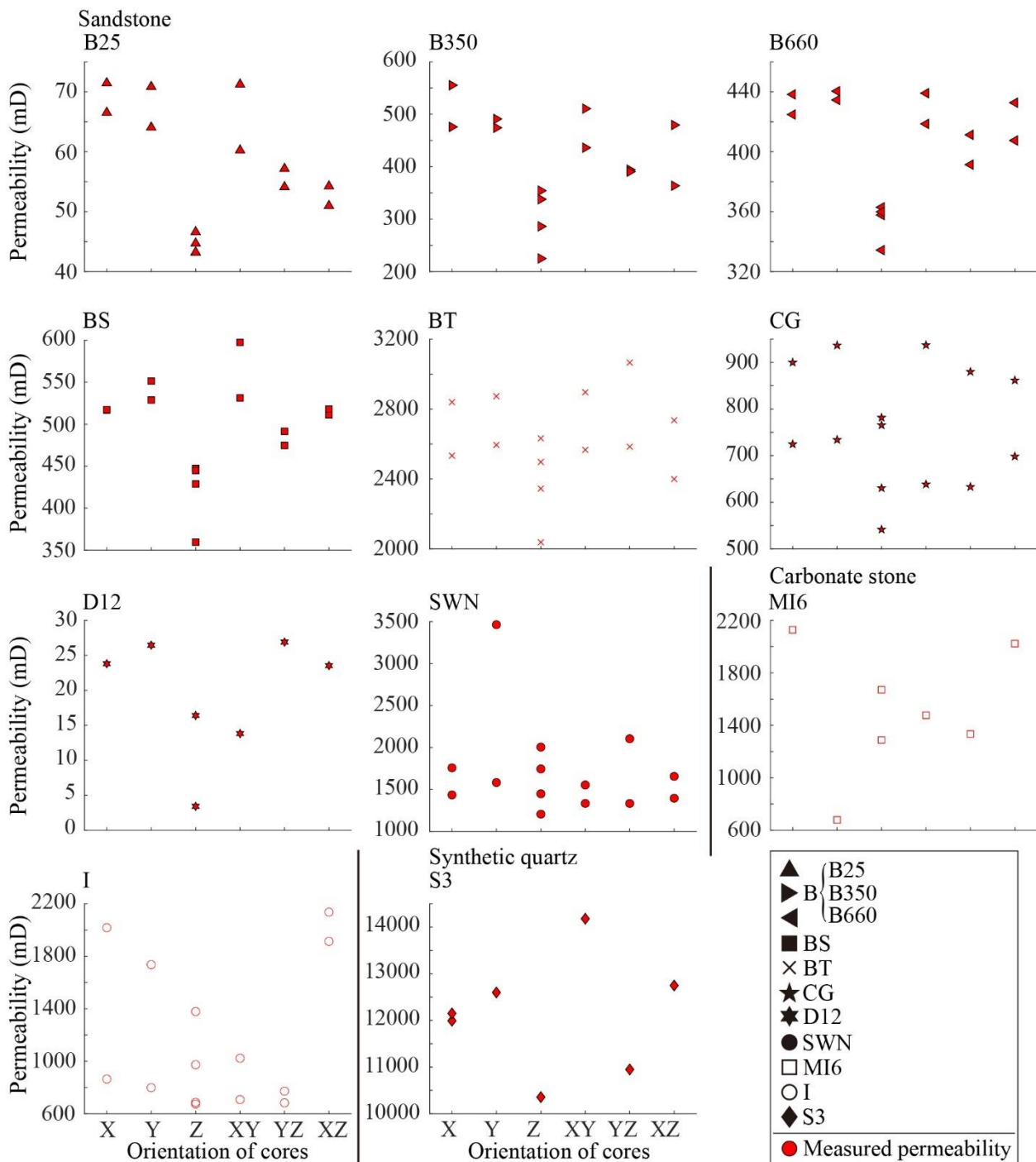


**Figure 4.9.** Permeability of different directional cores from each sample.

#### 4.3.4 AMS and MPF

The AMS of dry samples over all 7 or 18 directional cores shows the highest and lowest anisotropy degrees of 1.90 from sample S3 and 1.01 from sample B25, respectively. Sample BS has a relatively oblate anisotropy shape with a range of 0 to 0.83, while the anisotropy shapes of the other samples vary between cores (Figure 4.7).

The AMS orientations are consistent for the molasse sample D12, with the  $V3$  axes subparallel to the  $z$ -axis, and  $V1$  and  $V2$  in the  $xy$ -plane. Sample BS shows a similar but less consistent distribution of principal directions among different cores. All other samples exhibit inconsistencies

in the anisotropy orientations (Figure 4.8).

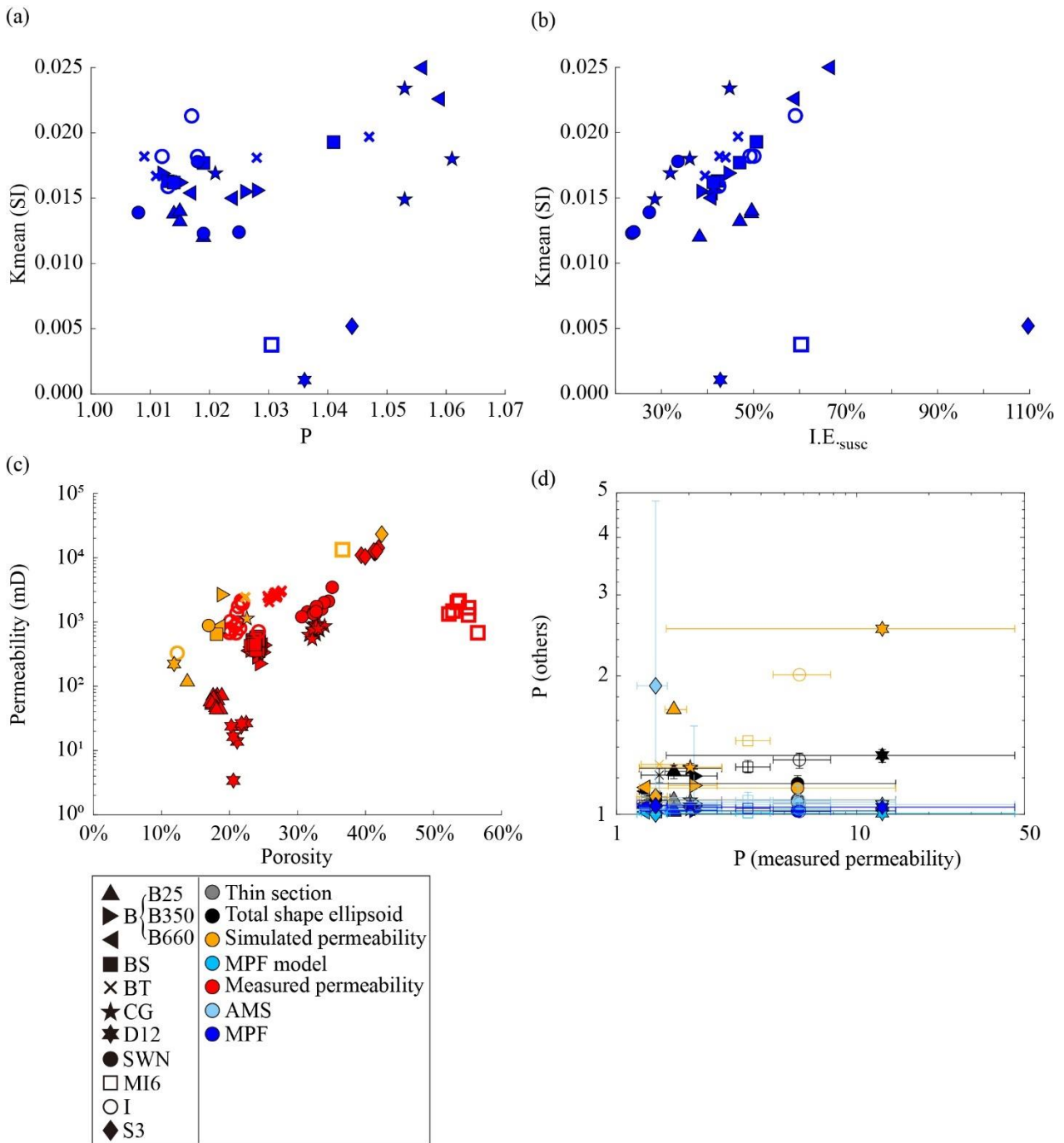


**Figure 4.10.** (a) Degree of anisotropy of MPF ( $P$ ) vs mean susceptibility of MPF ( $k_{mean}$ ), and (b) susceptibility-based impregnation efficiency ( $I.E._{susc}$ ) vs mean susceptibility of MPF ( $k_{mean}$ ). (c) Porosity VS permeability from laboratory measurements and simulation from XRCT data. (d) Comparison of anisotropy degree of measured permeability with pore fabrics derived by thin section, XRCT-derived data (total shape ellipsoids, simulated permeability anisotropy, and MPF model), AMS and MPF.

According to the MPF data, the highest and lowest degrees of anisotropy,  $P$ , are 1.05 for sample CG and 1.02 for sample I. Samples B350, B660, and BT show inconsistent anisotropy shapes across different cores, while the other samples have consistent oblate shapes (Figure 4.7).

In terms of MPF principal directions, all samples generally show the  $V3$  axes near the  $z$ -axis and  $V1$  and  $V2$  in the  $xy$ -plane. However, sample SWN has  $V1$  and  $V2$  axes with a band distribution nearly parallel to the  $yz$ -plane, and  $V3$  in the  $xy$ -plane (Figure 4.8).

Comparing the mean magnetic susceptibility with the degree of anisotropy for each sample shows no significant trend. However, there is a significant positive correlation between susceptibility-based impregnation efficiency and the mean susceptibility for all samples (Figure 4.10a, 4.10b).

#### 4.3.5 Comparison

Overall, there is a relatively positive correlation between measured porosity and permeability, and between simulated porosity and permeability. However, samples D12 and MI6 show relatively lower measured permeability than the general trend. For all samples except S3, measured porosities (18.05-54.01%) exceed simulated porosities (12-37%). Samples B25, B350, B660, BS, CG, D12, MI6, and S3 show higher simulated permeabilities (117.17-23246.9 mD) than measured (43.18-14180.3 mD), while samples BT, SWN, and I show the opposite, with measured permeabilities (673.03-3065.81 mD) exceeding simulated values (328.47-2436.69 mD) (Figure 4.10c).

Anisotropy shapes derived from different methods, including thin section, total shape ellipsoids, simulated permeability, MPF model, measured permeability, AMS, and MPF, consistently show inconsistencies for each sample (Figure 4.7). The degrees of anisotropy from XRCT ( $P$  values ranging from 1.07 to 1.34) are generally higher than those from thin sections ( $P$  values from 1.03 to 1.07). The MPF model ( $P$  values from 1.00 to 1.03), AMS ( $P$  values from 1.01 to 1.90), and MPF ( $P$  values from 1.02 to 1.05) show relatively lower degrees of anisotropy. Measured permeability, with the highest anisotropy degrees (from 1.32 to 12.78), surpasses all other methods, including those from simulated permeability ( $P$  values from 1.07 to 2.53) (Figure 4.7, 4.10d).

When comparing anisotropy orientations from different methods, samples B25, B350, B660, BS, BT, CG, and S3 consistently show  $V1$  axes in the  $xy$ -plane and  $V3$  axes subparallel to the  $z$ -axis. Sample D12 shows similar distributions, yet with inconsistent  $V1$  axes in the  $xy$ -plane between methods. Samples SWN, MI6, and I have inconsistent principal direction distributions across methods (Figure 4.8).

#### 4.4. Discussion

Comparative porosity analysis shows that for most samples, helium-derived porosity exceeds XRCT, MPF, and thin-section-derived porosity in descending order (Table 4.3 and Figure 4.5). Clearly, helium pycnometer, thin section and XRCT analysis can detect pores of different sizes (Alabi et al., 2014; Chitale et al., 2014; Cnudde & Boone, 2013; Silva, 2018; Landis & Keane, 2010; Nishiyama & Kusuda, 1994; Přikryl, 2015; Soete et al., 2022). The influence of sedimentary facies can also amplify the differences in various porosity determinations. For example, among Berea sandstones, sample B25 is more compacted than B350 and B660, with tighter grain contacts and narrower pores and throats. Therefore, liquid injection methods are less capable of detecting a large number of micropores compared to gas methods. Similarly, for sandstone samples, compaction and intergranular cementation lead to narrower throats between pores, making it difficult for liquids to impregnate. In contrast, carbonate rock samples with extensive dissolution result in more connected intragranular and moldic pores, facilitating fluid injection (Figure 4.3).

For liquid impregnation methods, MPF can typically detect more pores than thin section analysis, due to its lower fluid viscosity. However, one exception exists, and this is probably because MPF requires to impregnate fluid into the entire sample, whereas thin sections only require fluid injection on the sample surface to cut and prepare thin sections. When impregnation efficiency is

poor, MPF-derived porosity will be smaller. An exception is observed for  $MPF > XRCT > He$  porosity, possibly due to residual ferrofluid on the sample surface causing overestimation in the MPF-derived method, and an increased threshold for pore segmentation in XRCT resulting in higher XRCT porosity values.

The pore size distribution trends and distribution ranges between thin sections and XRCT are different (Figure 4.6), due to the different resolutions (De Boever et al., 2016; Bosak et al., 2004; Ronchi & Cruciani, 2015). The better resolution of thin sections images compared to XRCT data results in the identification of more micropores with random shapes, which reduces the degree of anisotropy in the total shape ellipsoids from thin section data (Figure 4.7, 4.10d). The use of unnormalized tensors in the calculation of total shape ellipsoids favors larger and more defined pores, resulting in consistent anisotropy orientations for six of the eight samples using both thin section and XRCT measurements (Figure 4.8). However, the two outliers both have weak anisotropy structures, resulting in incongruent anisotropy between the different methods (Figure 4.8).

Simulated permeabilities are higher relative to measured values in eight out of eleven samples (Figure 4.10c), possibly due to smoother grain surfaces and more open pores for the XRCT-derived data. The significantly higher anisotropy degree in the permeability values compared to other methods can be attributed to increased fluid flow in specific directions under high-pressure air determination, and pressure air can access to smaller micropores and throats with significant anisotropy (Figure 4.7, 4.10d). Insignificant anisotropy orientations determined from seven core measurements may be due to the heterogeneity of the block and the limited number of directional cores available for determination. Increasing the number of directional cores used to compute a tensor could potentially narrow the confidence angles, thereby increasing the significance of the orientations. Despite these differences, the measured and simulated permeabilities generally agree in having the  $V1$  axes in the  $xy$ -plane and the  $V3$  axes close to the  $z$ -axis for most samples (seven out of eleven samples) (Figure 4.8). Discrepancies between the two methods may be due to the less significant anisotropy in XRCT pore fabrics (as in sample B660) or the insignificant anisotropy (as in samples SWN, MI6, and I).

Magnetic susceptibility data, including the MPF model, AMS, and MPF, have lower degrees of anisotropy compared to other methods. Variables affecting the MPF data include fluid susceptibility during impregnation, pore geometry, orientation, and distribution (Biedermann, 2019, 2020; Biedermann et al., 2021; Jones et al., 2006). There appears to be no trend between the degree of anisotropy and susceptibility, but there is a clear positive correlation exists between impregnation efficiency and susceptibility (Figure 4.10a, 4.10b), suggesting that higher contents of ferrofluid in the samples directly result in higher magnetic susceptibility. Complex factors influence the degree of anisotropy beyond the ferrofluid content as discussed above. Anomalous samples with greater than 100% impregnation efficiency may have excess ferrofluid on their surface, overestimating the magnetic susceptibility of the sample. The orientation of the MPF data is consistent with other methods for the majority of samples (eight out of eleven samples) (Figure 4.8), with discrepancies involving samples with insignificant anisotropy structures potentially driving the inconsistency with other methods.

Quantitative comparisons from different resolutions and scales, including thin sections, XRCT, permeability anisotropy, MPF, and block, exhibit consistent orientations in eight out of eleven samples (see last column in Figure 4.8). This demonstrates that in these samples with significant anisotropic structures, the fabric's orientation is consistent across both macroscopic and microscopic scales.

#### **4.5. Conclusions**

This study presents a method for deriving three-dimensional total shape ellipsoids from two-dimensional shape ellipses obtained from three orthogonal thin sections. While pore fabric analysis using thin section microscopy is widely used because of its simplicity, it is inherently limited by its two-dimensional nature, which can distort the understanding of pore structures. By incorporating total shape ellipsoids from three perpendicular thin sections, the calculation of total shape ellipsoids now captures the true spatial distribution of pore structures. In addition, this research has implemented a four-tensor measurement of permeability anisotropy to comprehensively evaluate variability and heterogeneity within one single sample.

The anisotropy orientations of permeability generally correlate well with pore fabrics derived from thin sections, XRCT data (including pore fabrics, simulated permeability and MPF model), and MPF. However, anisotropy shapes show discrepancies between different determination methods. For the degree of anisotropy, the typical order is: measured permeability > simulated permeability > XRCT-derived total shape ellipsoids > thin-section-derived total shape ellipsoids > AMS > MPF > MPF model. This hierarchy confirms previous empirical correlations between these properties (Benson et al., 2003; Jones et al., 2006; Louis et al., 2005; Nabawy et al., 2009; Pflaiderer & Halls, 1994). In summary, given the simplicity and efficiency of the MPF method, it is recommended to initially use MPF to obtain indicative information on pore fabrics and the optimal direction of fluid flow. Subsequently, measuring permeability in the corresponding optimal direction and its perpendicular direction will suffice to calculate more accurate permeability anisotropy. This approach reduces the need for time-consuming and expensive full-tensor measurements of permeability and provides more accurate prior information on fabrics compared to observations on hand specimens and microscopic observations, thus minimizing under- and overestimation of anisotropy.

However, several questions remain unanswered. It is unclear how the insignificant anisotropy within a sample fabric affects different determination methods, potentially leading to discrepancies in anisotropy between them. It is also uncertain whether samples with higher homogeneity and anisotropy will show more consistent agreement between pore fabric, permeability anisotropy, and MPF.

#### **Acknowledgment**

We would like to thank R. Castellanza from the Università degli Studi Milano Bicocca (Milano, Italy) for providing the calcarenites. The XRCT analysis in Bern was supported by the European Research Council (ERC) under the European Union's Horizon 2020 research and innovation program (grant agreement No. 850530 to PL). The Bruker Skyscan 2211 at the University of Fribourg was funded by R'Equip Swiss National Science Foundation grant 206021\_150731. This study was funded by the Swiss National Science Foundation, project 176917 (to ARB).

## 5. Article III: Comparing thin-section-derived and X-ray tomography-derived pore fabrics, permeability anisotropy and magnetic pore fabrics in hot isostatically pressed calcite-muscovite rocks

(Potentially for future publication)

Y. Zhou<sup>1</sup>, A. Foubert<sup>2</sup>, P. Lanari<sup>1</sup>, C. Madonna<sup>3</sup>, & A. R. Biedermann<sup>1,4</sup>

<sup>1</sup>Institute of Geological Sciences, University of Bern, Baltzerstrasse 1+3, CH-3012 Bern, Switzerland.

<sup>2</sup>Department of Geosciences, University of Fribourg, Chemin du Musée 6, CH-1700 Fribourg, Switzerland.

<sup>3</sup>Department of Earth Sciences, ETH Zurich, Sonneggstrasse 5, CH-8092 Zürich, Switzerland.

<sup>4</sup>Now at Paul Scherrer Institute, Forschungsstrasse 111, 5232 Villigen PSI, Switzerland.

Corresponding author: Yi Zhou (zy930com@gmail.com)

### Key Points:

- Calcite-muscovite samples produced by hot isostatic pressing exhibit varying anisotropy through different mixing ratios
- Pore fabrics derived by thin section and X-ray microtomography analysis, permeability anisotropy, and magnetic pore fabric are compared
- Magnetic pore fabric method can effectively predict the fabric anisotropy change and the preferred flow direction

### Abstract

Investigating the pore structure and permeability of rocks is crucial for the understanding, exploitation and exploration of fluid resources in the subsurface. Natural rock samples often exhibit significant heterogeneity, posing challenges for controlled experiments. In this study, calcite-muscovite composites are used to simulate the texture of impure carbonate rocks. Homogeneous structures with varying anisotropies are produced by uniformly mixing irregular calcite and sheet-like muscovite grains in ratios of 3:7, 5:5, and 7:3. These mixtures are then subjected to 20 MPa cold pressing, followed by 160 MPa and 670 °C hot isostatic pressing for three hours, generating uniaxial vertical compressive stress ( $z$ ) and lateral tensile strain ( $xy$ ). This study provides a cross-comparison of the pore structure and permeability anisotropy of synthetic samples, employing three-dimensional pore fabric determinations based on thin section and XRCT analysis, permeability simulation and magnetic pore fabric (MPF) modelling based on XRCT digital rock, as well as permeability measurements, and magnetic pore fabrics based on samples injected with ferrofluid. Thin section data, permeability, and MPF consistently indicate anisotropy orientations with the maximum axes along the lateral tensile direction ( $xy$ ) and the minimum axes along the vertical compression direction ( $z$ ), whereas XRCT data differ, showing discrepancies in anisotropy orientations for four out of ten samples. The degree of anisotropy in permeability and MPF increases with the proportion of muscovite. Thus, the MPF method serves as an effective prior tool for predicting the optimal flow direction, thereby aiding in the exploration of subsurface fluid resources such as water resources, fluid flow related to geothermal energy exploitation and hydrocarbons.

## Plain Language Summary

Hot water but also hydrocarbons, among other fluid resources, are significant energy resources. These fluids mainly move and collect in the pores of underground rocks. Thus, understanding the direction these pores extend and how fluids flow is essential. However, many natural rocks have significant internal differences, making effective comparative studies difficult. To overcome this challenge, using high-temperature and high-pressure conditions can simulate natural formation and synthetic rocks can be created using common minerals like calcite and muscovite. These synthetic samples have evenly distributed characteristics and show differences between lateral and axial directions. Thin-section microscopy and X-ray scanning allow to observe the rock's pore structure. Fluid flow rates in various directions can be directly measured and simulated. Magnetic fluids are injected into the pores to measure changes in magnetic properties in different directions for pore structure analysis. Ultimately, a good match can be found between magnetic fluid measurements and the optimal direction of fluid flow in rocks. Therefore, this method can effectively improve the assessment of how fluid resources move underground.

## 5.1. Introduction

The complex pore fabrics in rocks affect fluid flow patterns. Permeability anisotropy measurements can directly indicate the preferred flow orientation. Therefore, accurately characterizing pore geometry and permeability anisotropy in reservoir rocks is critical for geothermal energy and hydrocarbon exploration, and underground water management (Aliyu & Chen, 2018; Frosch et al., 2000; Gao & Hu, 2018; Kibria et al., 2018; Wagner et al., 2005; Yang et al., 2017, 2018; Zhang et al., 2020).

Thin-section analysis has been used for studying pore fabrics, usually integrated with fluorescent microscopy. However, this technique has its limitations that restrict their scope and accuracy due to its two-dimensional nature (Anselmetti et al., 1998; Chen et al., 2000; Nishiyama & Kusuda, 1994, 1996; Přikryl, 2015). X-ray computed micro-tomography (XRCT) is another method that has been increasingly popular for three-dimensional characterization of pore structures. XRCT datasets can help to build digitized models of rocks that can subsequently be utilized for analyzing pore fabrics, and even calculating permeability anisotropy and MPF (Andrä et al., 2013b; Biedermann, 2020; Holzer et al., 2011; Madadi & Varslot, 2009; Pini & Madonna, 2016). However, higher resolutions are required for micropore detection, but this leads to a reduction in sample size, thus necessitating a trade-off between sample size and resolution (Chen et al., 2020; Cnudde & Boone, 2013; Lai et al., 2018; Landis & Keane, 2010; da Silva, 2018). Permeability anisotropy measurements offer a direct way to evaluate preferred fluid migration directions. A priori information on the fabric orientation, such as paleo-flow directions, bedding or faults, is required to predict the approximate preferred flow direction, thereby aiding in the selection of the permeability measurement direction to calculate anisotropy (Adams et al., 2013, 2016; Armitage et al., 2011; Baas et al., 2007; Mokhtari et al., 2013; Okazaki et al., 2013; Zhang & Wang, 2018). Otherwise, measurements in at least six directions are the minimum conditions for calculating a full tensor of permeability anisotropy (Clavaud et al., 2008; Coulson & Nye, 1958; Pflaiderer & Halls, 1994; Rasolofosaon & Zinszner, 2002). The investigation of magnetic pore fabrics (MPFs) using ferrofluid-impregnated samples offers an indirect method for assessing pore fabrics and permeability anisotropy. This approach is based on the empirical relationships among MPFs, pore fabrics, and permeability anisotropy, which demonstrate that the principal directions of MPFs, pore fabrics, and permeability are aligned (Benson et al., 2003; Louis et al., 2005; Pflaiderer & Halls, 1990, 1994). Since the sample can be rotated in a magnetic field to measure the full-tensor anisotropy, the extensive information about fabric orientation is not required upfront, making this methodology quick and adaptive. Theoretically, the magnetic particles with 10-20 nm size indicate the potential of MPF method to assess micropores with similar size (Robion et al., 2014). However, factors, such as complex fabric, fracture network in rocks, ferrofluid susceptibility and

measurement frequency, will affect the correlations between MPFs, pore fabrics and permeability anisotropy. For instance, localized fracture development or significant tortuosity in flow paths may lead to notable changes in flow direction and permeability, but their impact on pore fabrics and MPFs is not substantial. The susceptibility of ferrofluid and measurement frequency can affect the measurement of MPFs, but they do not influence pore fabrics or permeability anisotropy (Baas et al., 2007; Benson et al., 2003; Biedermann, 2019; Biedermann et al., 2021; Jones et al., 2006; Louis et al., 2005; Nabawy et al., 2009; Pfleiderer & Halls, 1990, 1994).

Sedimentary rocks in nature exhibit heterogeneities in composition, texture, and pore structure. This intrinsic variability poses significant challenges for developing fundamental understandings of rock properties related to composition and microstructure. Synthetic rock samples produced through hot isostatic pressing (HIP) allow researchers to control the sample composition, grain size distribution, and fabric to obtain relatively homogeneous and anisotropy samples for studying rock properties. Homogeneity reduces the differences between different samples during sampling, while significant anisotropy forms the basis for comparing the thin section data, XRCT data, permeability anisotropy, and MPF in this study, as they all exhibit anisotropic features. If the samples do not have significant anisotropy, these methods would not be effective for comparison. Meanwhile, this methodology simulates the high-temperature and high-pressure environment of natural rock formation. Heilbronner & Bruhn (1998) and Misra & Burg (2012) utilized some common mineral components, such as hemihydrate and calcite, or muscovite with quartz and feldspar, in the preparation of HIP samples, but the porosity was not reported. Some studies presented remarkably small porosities (< 2%) (Post & Tullis, 1999; Rutter & Brodie, 2004b, 2004a; Rybacki & Dresen, 2000; Rybacki et al., 2008, 2010). Other studies have presented significant porosities, such as ~10% (Caristan et al., 1981) and up to 19.5% (Bernabe et al., 1982), but the correlation between the experimental conditions and the sample porosity has not been elucidated. Although Pec & Al Nasser (2021) produced HIP samples made of quartz and feldspar with porosity as high as 14%, the porosity was influenced by a significant amount of cracks generated during the load experiment. Zhang et al. (1994) used calcite powder obtained by crushing and sieving Wombeyan marble to manufacture HIP samples with a maximum porosity of 16.7%. Schmidt et al. (2008) utilized mixtures of calcite and muscovite powders to produce HIP samples with porosities up to 25.2% (Table 5.1). Given the necessity for sufficient porosity to conduct pore structure investigations, attention must be paid to grain growth as a primary factor reducing porosity during the HIPing process. Typically, grain growth can be suppressed by shortening the HIPing duration and preparing samples with porosities exceeding 20% (Olgaard & Evans, 1988; Schmidt et al., 2008). For samples containing calcite components, the addition of Al<sub>2</sub>O<sub>3</sub> or muscovite can also effectively inhibit calcite growth (Berger & Herwegh, 2004; Olgaard & Evans, 1986; Schmidt et al., 2008).

The aim of this study is to prepare relatively homogeneous artificial rock samples by using common rock mineral components through the HIP method simulating formation processes occurring in natural rocks. Meanwhile, the samples need to have a high porosity and varying anisotropy to facilitate the relevant experiments on pore structure and permeability. The research question lies in utilizing artificial rocks to retain the relatively complex and diverse fabrics of natural rocks while reducing their significant heterogeneity. Based on these samples, various pore fabric determination methods were conducted, including three-dimensional pore structure characterization established by three perpendicular thin sections and XRCT data, as well as permeability anisotropy measurements and MPF. The quantitative relationship between pore fabrics, permeability anisotropy and MPF was further elucidated, promoting MPF as a priori method for rapid and effective detection of pore structure and fluid flow direction, thereby facilitating the exploration and development of subsurface flow resources.

**Table 5.1.** Public studies using synthetic samples prepared by the hot isostatic pressing method, including the used raw materials, experimental parameters and the achieved sample properties.

Study	Raw material details			Experiment parameters				Achieved sample properties			Comments
	Composition	Grain size	Pretreatment	Cold pressing pressure	Hot pressing temperature	Hot pressing pressure	Hot pressing time	Grain size	Porosity	Pore size	
Heilbronner & Bruhn, 1998	Mixed hemihydrate and calcite powders (reagent grade)	Not specified	500 °C for 24 h	Not specified	550 °C	200 MPa	4 h	2.3 µm for anhydrite, 2.6 and 3.1 µm for calcite	Not specified	Not specified	The porosities were not specified
Misra & Burg, 2012	Muscovite with quartz and feldspar crystals (8–10 vol.%)	30–60 µm	Not specified	200±4 MPa	590 °C	170 MPa	30 h	Not specified	Not specified	Not specified	The porosities were not specified
Post & Tullis, 1999	Fine-grained albitic feldspar	1–10 µm	Not specified	Not specified	900 °C	1500 MPa	10 h	Not specified	< 1 %	Not specified	Remarkably small porosities
Rybacki & Dresen, 2000	Anorthite aggregates fabricated from crushed CaAl <sub>2</sub> Si <sub>2</sub> O <sub>8</sub> glass	< 60 µm	800 °C in air for 60 h and then 120 °C for several days	300 MPa	900 °C for 1 h, and then 1050 °C for 2 h, and finally 1200 °C for 2 h	300 MPa	5 h	Not specified	~30 % after cold pressing but <1 % after HIP	Not specified	Remarkably small porosities
Rutter & Brodie, 2004a	Clear Brazilian quartz crystals	0.4, 1.3 and 4.5 µm	Not specified	Not specified	1000–1200 °C	300 MPa	23–27 h	Not specified	< 2 %	Not specified	Remarkably small porosities

Rutter & Brodie, 2004b	Clear Brazilian quartz crystals	0.4 $\mu\text{m}$	Not specified	Not specified	1000-1200 $^{\circ}\text{C}$	300 MPa	27 h	Not specified	< 2 %	Not specified	Remarkably small porosities
Rybacki et al., 2008	>97% Fine-grained anorthite glass powder	Not specified	Not specified	Not specified	1100 $^{\circ}\text{C}$	300 MPa	24 h	3.7 $\pm$ 0.7 $\mu\text{m}$ , aspect ratio ~2.5	~1 %	Not specified	Remarkably small porosities
Rybacki et al., 2010	>99% Fine-grained anorthite glass powder	< 11 $\mu\text{m}$	(1) First group, dried for 60 h at 800 $^{\circ}\text{C}$ in air (2) Second group, dried for 60 h at 800 $^{\circ}\text{C}$ in argon	170 MPa	(1) 880 $^{\circ}\text{C}$ for 0.5 h and subsequently 1100 $^{\circ}\text{C}$ for 24 h. (2) 900 $^{\circ}\text{C}$ for 2 h, followed by 20 h at 1150 $^{\circ}\text{C}$	300 MPa	(1) 24.5 h (2) 22 h	3.7 $\pm$ 0.7 $\mu\text{m}$ , aspect ratio ~2.5	~1 %	Not specified	Remarkably small porosities
Caristan et al., 1981	Quartz powder from commercially available crushed quartz sand, and calcite powder from reagent-grade chemical	~5 $\mu\text{m}$ for quartz, and 3-4 $\mu\text{m}$ for calcite	Not specified	160 MPa	980 or 1250 $^{\circ}\text{C}$ for quartz, and 200-770 $^{\circ}\text{C}$ for calcite	208-500 MPa for quartz, and 500 MPa for calcite	0.08-4.0 h for quartz, and 0.5, 2 and 3 h for calcite	Not specified	~10 %	Not specified	The factors leading to the high porosity (~10 %) were not specified
Bernabe et al., 1982	Calcite powder	2-20 $\mu\text{m}$	Not specified	160 MPa	200-770 $^{\circ}\text{C}$	500 MPa	0.5-3 h	Not specified	1.6-19.5 % (permeability 0.052-70*10 <sup>-18</sup> m <sup>2</sup> )	Not specified	The factors leading to the high porosity (19.5 %) were not specified

Zhang et al., 1994	Calcite powder by crushing and sieving Wombeyan marble, containing 96 % CaCO <sub>3</sub> , 2.5 % MgCO <sub>3</sub> , and less than 0.2 % SiO <sub>2</sub>	38-53 μm (>80 %)	100 °C for at least 1 day	300 MPa	360-560 °C	200-300 MPa	1.5-37.5 h	1-30 μm	3.7-16.7 %	19-224 nm	The compositions leading to high porosity (16.7 %) could be useful for our purposes
Schmidt et al., 2008	Mixed calcite and muscovite powders	<100 μm	120 °C for 24 h	<5, 20,40,100, 200,400 MPa	670 °C	150-170 MPa	3 h	2.1-7.8 μm for calcite	10.1-69.4 % after cold pressing but 3.0-25.2 % after hot pressing	Not specified	The compositions leading to high porosity (25.2 %) could be useful for our purposes
Pec & Al Nasser, 2021	Quartz and potassium feldspar powders mixed in a 7:3, 1:1, or 3:7 ratio by weight	10-20 μm	Not specified	Not specified	750 °C	750-900 MPa	4.6-20 h	Not specified	2-14 %	Not specified	The load experiments created a lot of cracks, affecting the porosities

## 5.2. Materials and Methods

### 5.2.1 Sample description

For the HIP sample preparation, the primary requirement for manufacturing artificial rock samples is to ensure sufficient porosity as this study aims to investigate pore fabrics using these samples. Following a review of public literature (Table 5.1), samples with unspecified porosity were excluded, due to limited resources and uncertainty regarding whether the experimental materials and conditions used can yield the high porosity required. Additionally, samples with excessively low porosity (<2%) were also disregarded. While some studies have produced samples with high porosity, the reasons for this high porosity are either not clearly stated or the porosity measurements are influenced by subsequent experiments. Finally, the studies of Zhang et al. (1994) and Schmidt et al. (2008) were identified as the most suitable options. Zhang et al. (1994) only employed calcite powder as the raw material, with more stringent grain size requirements (38-53  $\mu\text{m}$ ), whereas Schmidt et al. (2008) utilized various mixtures of calcite and muscovite to prepare samples, with experimental requirements that are easier to operate.

This study adopted the preparation method of Schmidt et al. (2008) to fabricate HIP rock samples. The calcite powder, provided by Alberto Luisoni AG with the name of calcite M 60/10, was crushed from a metamorphic marble from Carrara with high chemical purity. Its chemical composition mainly consists of 98.50 wt%  $\text{CaCO}_3$ , 1.20 wt%  $\text{MgCO}_3$ , 0.08 wt%  $\text{SiO}_2$ , 0.06 wt%  $\text{Al}_2\text{O}_3$ , and 0.02 wt%  $\text{Fe}_2\text{O}_3$  by mass percentage. The particle size is less than 100  $\mu\text{m}$  (>99.8%). The muscovite powder was sourced from mica MU 101 by Alberto Luisoni AG. By mass percentage, its typical properties include 51 wt%  $\text{SiO}_2$ , 32 wt%  $\text{Al}_2\text{O}_3$ , and 8.5 wt%  $\text{K}_2\text{O}$ . Only 0.07 % of its particle size is larger than 100  $\mu\text{m}$ . The above data was provided by the supplier Alberto Luisoni AG. This experiment mainly considers the influence of grain sizes, component ratios, and magnetic properties. Both calcite and muscovite powders were further sieved into two grain size ranges, <50  $\mu\text{m}$  and 50-100  $\mu\text{m}$ . The two components were mixed in three ratios: 3:7, 5:5, and 7:3. Additionally, samples with mixtures of 3:7 and 7:3 were prepared with both particle size ranges (<50  $\mu\text{m}$  and 50-100  $\mu\text{m}$ ), while mixtures of 5:5 only have grain size with 50-100  $\mu\text{m}$ . For all groups of samples, 1 % magnetite or 1 %  $\text{Al}_2\text{O}_3$  was added to the samples with same other properties, assessing the influence of magnetic properties on the subsequent MPF experiments. Furthermore, the addition of  $\text{Al}_2\text{O}_3$  and muscovite can prevent growth of calcite (Berger & Herwegh, 2004; Olgaard & Evans, 1986; Schmidt et al., 2008). Due to limited resources, ten samples were prepared with the mixed powders in different ratios, grain sizes, and magnetic properties for mutual comparison (Table 5.2).

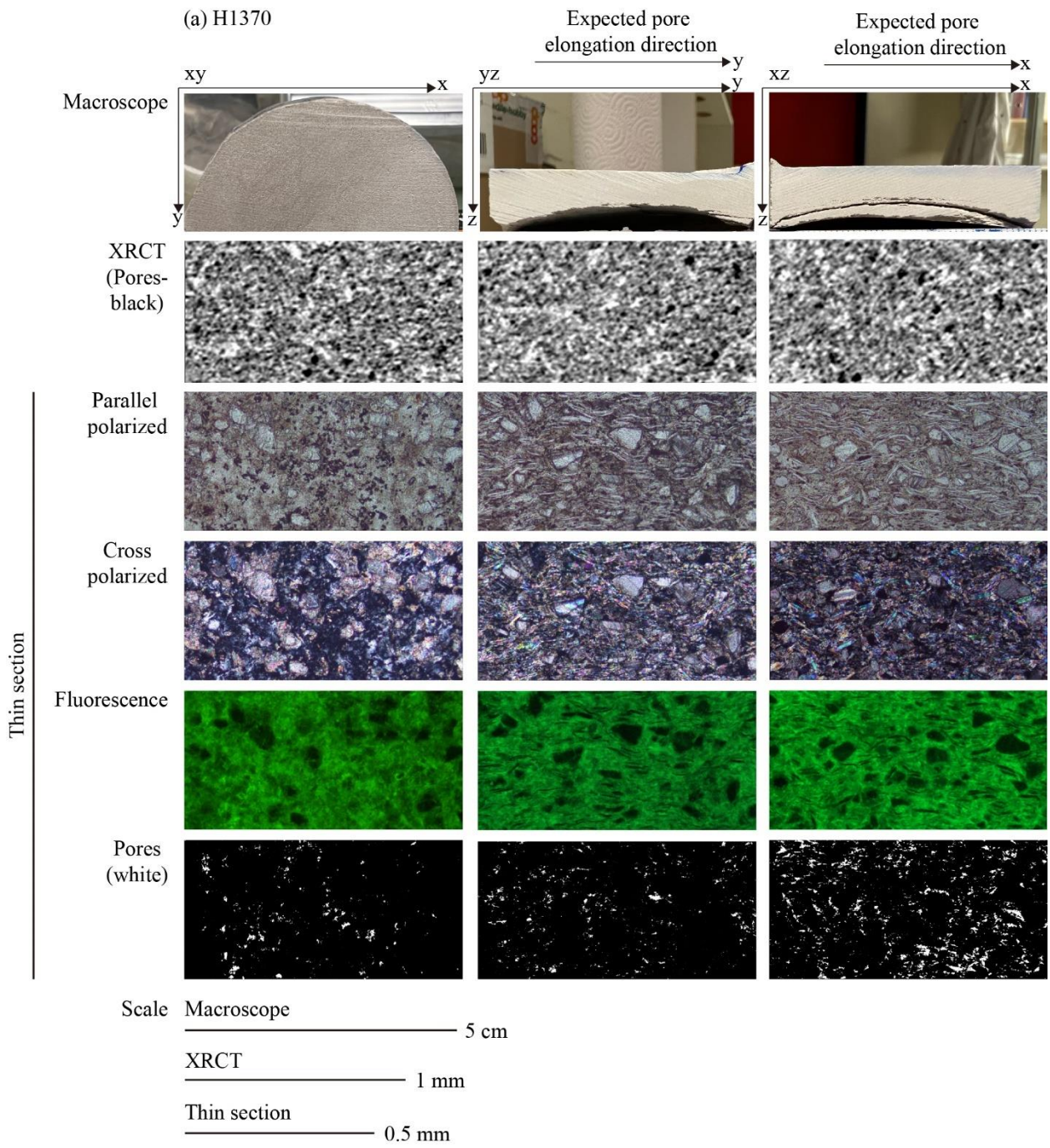
All mixed powders were dried in an oven at 120 °C for over 24 hours. The dried powders were placed into stainless steel cylindrical jackets for cold pressing. The jackets were lined with nickel foils to isolate the samples from the magnetic properties of iron materials. The jackets are 20.4 cm high with an inner diameter of 5.1 cm. The powders were filled into the jackets in small batches and compacted manually to ensure homogeneity. The manual cold pressing pressure is approximately 20 MPa. The powders were filled to about 1 cm below the jacket's opening, resulting in an original sample volume of approximately 400  $\text{cm}^3$ . The top of the powders was wrapped with nickel foils and covered with a stainless-steel lid. All ten jackets were transported to the Rock Physics and Mechanics Laboratory (RPMLab) at ETH Zurich for subsequent procedures. After welding and sealing the samples, they were hot isostatically pressed for 3 hours at 670 °C under a pressure of 160 MPa.

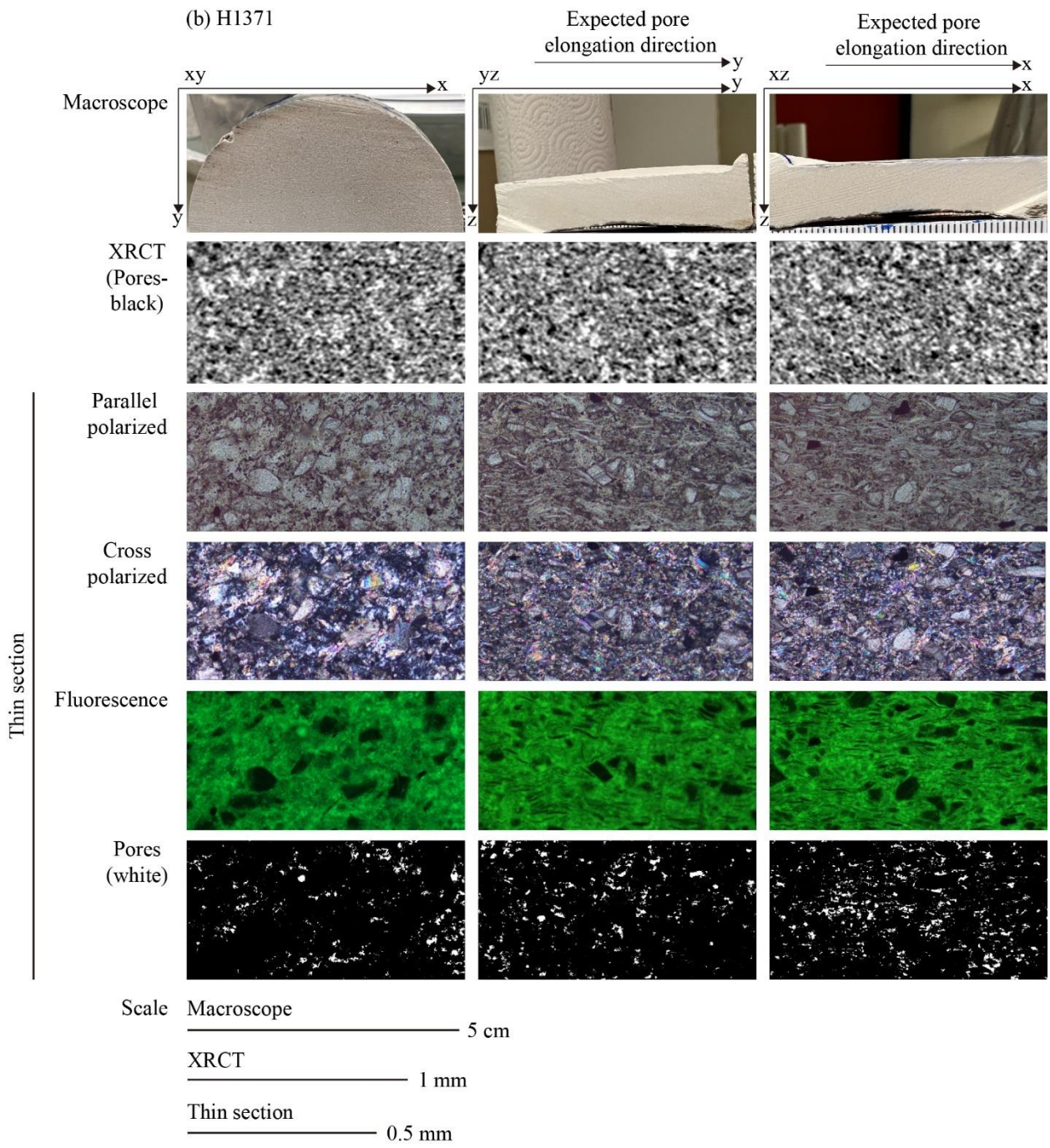
The prepared HIP samples were removed from the jackets for structure observations. To avoid contamination from the containers and nickel foils, the outer edges of the samples were trimmed. Firstly, cylindrical samples were cut to prepare thin sections and cores, and their longitudinal ( $xz$ ) and transverse ( $xy$ ) cut surfaces were photographed using an iPhone 13 pro max. The  $z$ -direction

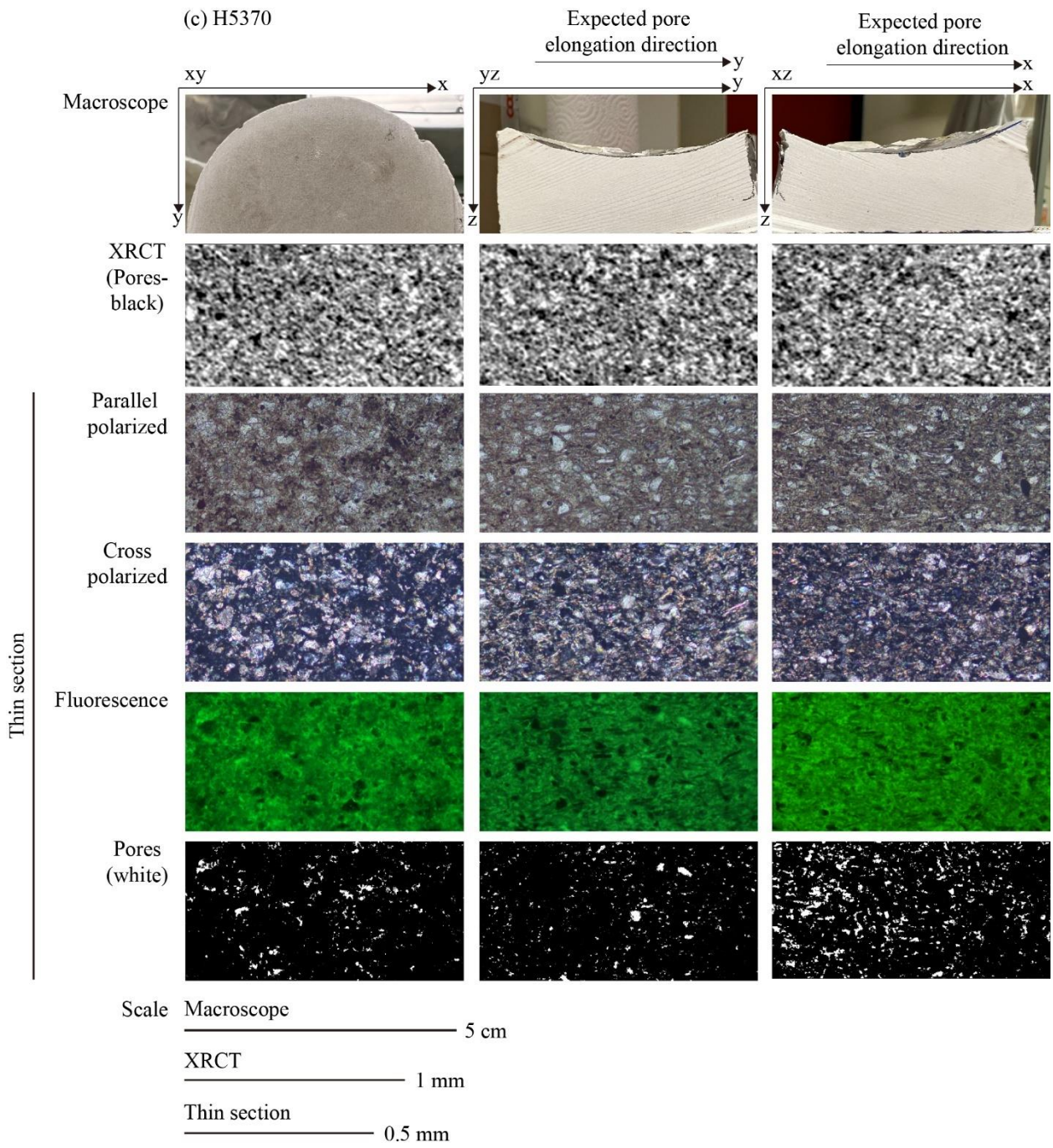
corresponds to the compaction direction. Due to the influence of compaction, the elongation direction of grains and pores was expected to align along the  $xy$ -direction. In Figure 5.1, the pore fabrics and grain fabrics at the microscopic scale were presented through thin section and XRCT images (methods introduced later) and compared with the macroscopic fabrics of the sample as observed in photographs. Through simple visual inspection of the images, an initial attempt was made to empirically validate the directional relationship between the microscopic pore fabrics, grain fabrics and the macroscopic sample fabrics. The macroscopic fabrics from iPhone photographs and microscopic pore fabrics and grain fabrics from XRCT image of cores reveal that all HIP samples exhibit highly homogeneous fabrics due to uniform powder mixing and high-pressure compaction. At the same time, pores are very small in both iPhone photographs and XRCT image.

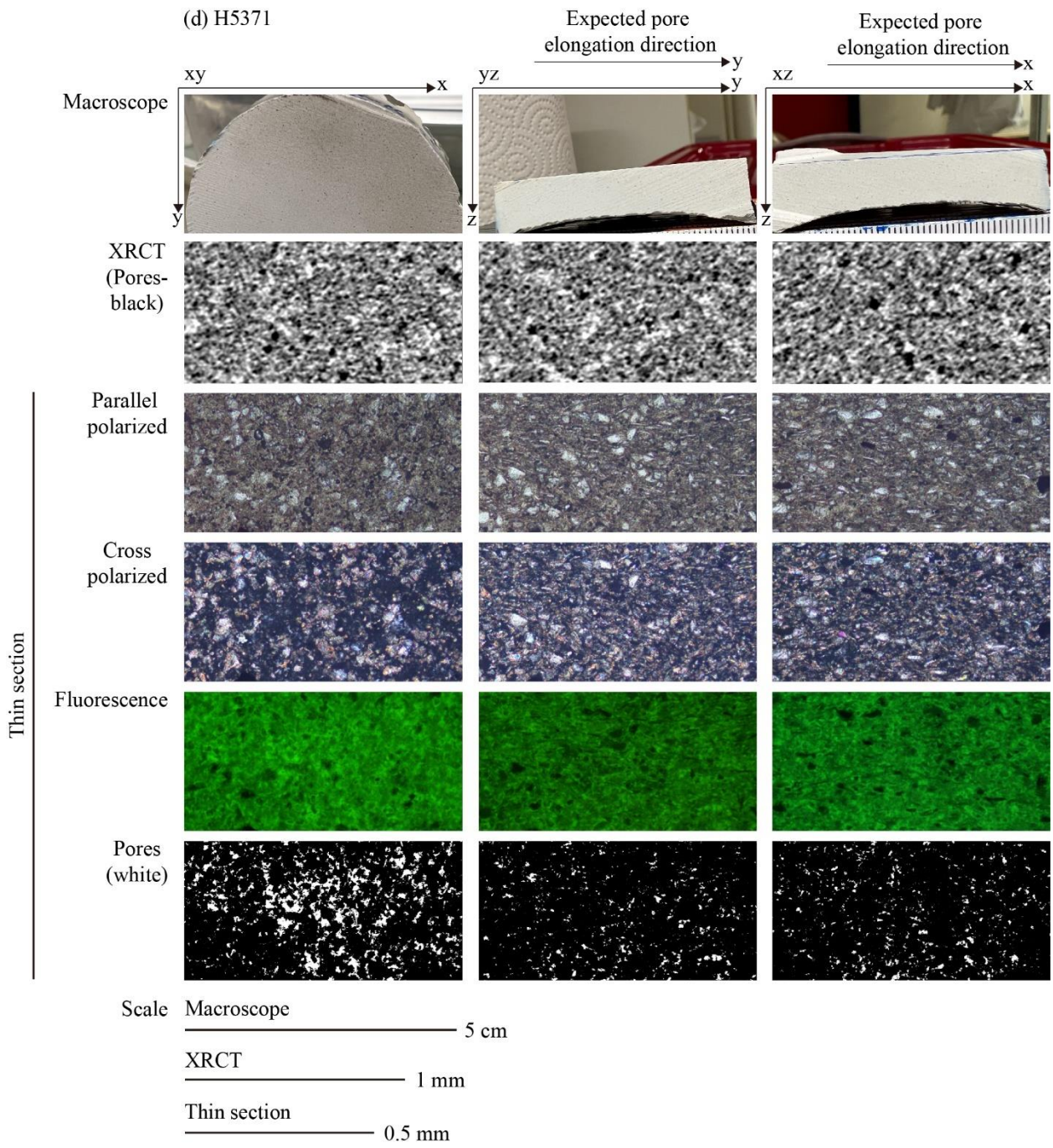
**Table 5.2.** Sample list.

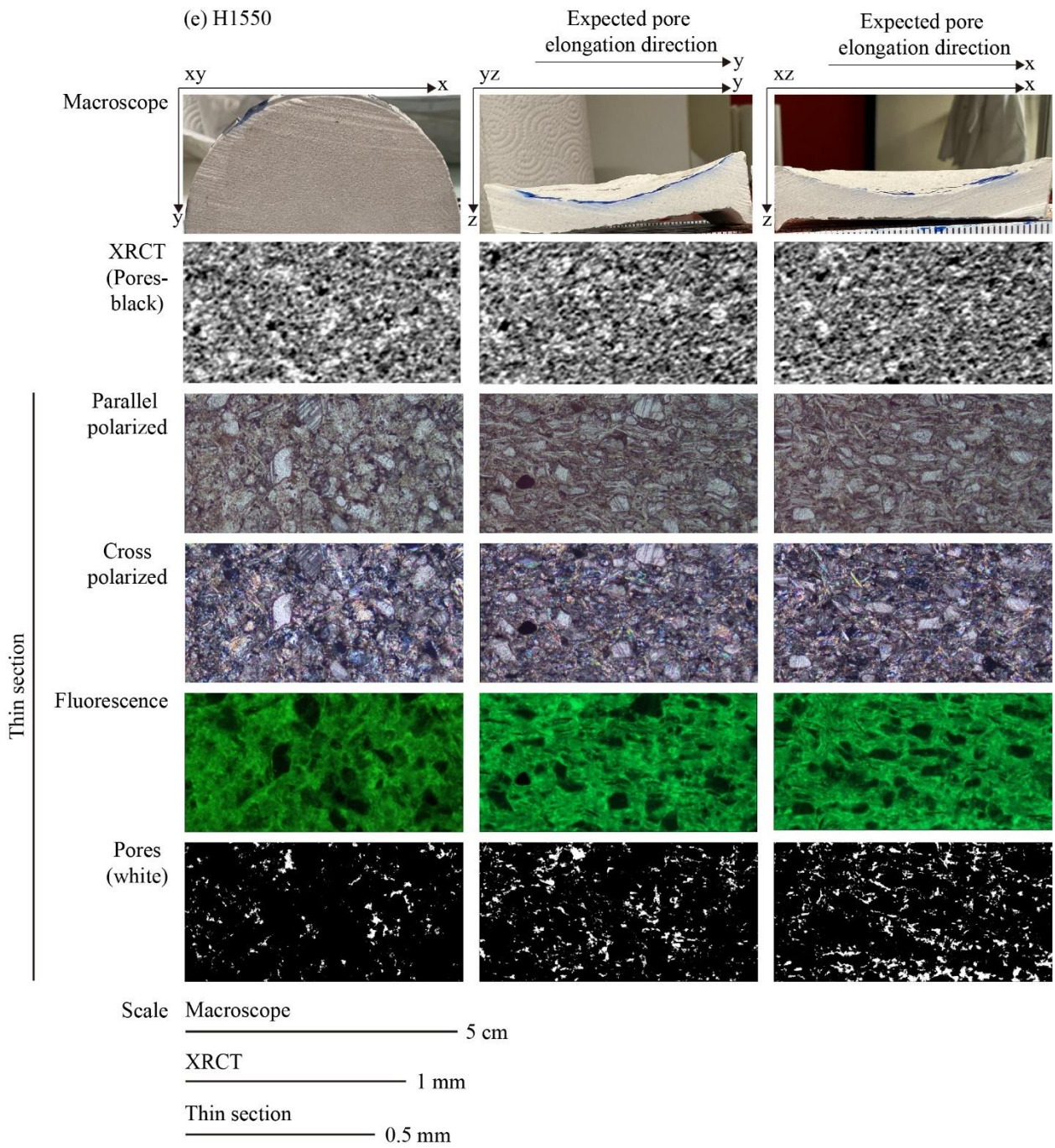
Sample name	Calcite	Muscovite	Magnetite	Uniaxial cold-pressing	Hot isostatic pressing	Temperature	Duration
H1370	30 %, 50<100 $\mu\text{m}$	70 %, 50<100 $\mu\text{m}$	none (replace by $\text{Al}_2\text{O}_3$ 1 %)	20 MPa	160 MPa	670 °C	3 h
H1371	30 %, 50<100 $\mu\text{m}$	70 %, 50<100 $\mu\text{m}$	1 %	20 MPa	160 MPa	670 °C	3 h
H5370	30 %, <50 $\mu\text{m}$	70 %, <50 $\mu\text{m}$	none (replace by $\text{Al}_2\text{O}_3$ 1 %)	20 MPa	160 MPa	670 °C	3 h
H5371	30 %, <50 $\mu\text{m}$	70 %, <50 $\mu\text{m}$	1 %	20 MPa	160 MPa	670 °C	3 h
H1550	50 %, 50<100 $\mu\text{m}$	50 %, 50<100 $\mu\text{m}$	none (replace by $\text{Al}_2\text{O}_3$ 1 %)	20 MPa	160 MPa	670 °C	3 h
H1551	50 %, 50<100 $\mu\text{m}$	50 %, 50<100 $\mu\text{m}$	1 %	20 MPa	160 MPa	670 °C	3 h
H1730	70 %, 50<100 $\mu\text{m}$	30 %, 50<100 $\mu\text{m}$	none (replace by $\text{Al}_2\text{O}_3$ 1 %)	20 MPa	160 MPa	670 °C	3 h
H1731	70 %, 50<100 $\mu\text{m}$	30 %, 50<100 $\mu\text{m}$	1 %	20 MPa	160 MPa	670 °C	3 h
H5730	70 %, <50 $\mu\text{m}$	30 %, <50 $\mu\text{m}$	none (replace by $\text{Al}_2\text{O}_3$ 1 %)	20 MPa	160 MPa	670 °C	3 h
H5731	70 %, <50 $\mu\text{m}$	30 %, <50 $\mu\text{m}$	1 %	20 MPa	160 MPa	670 °C	3 h

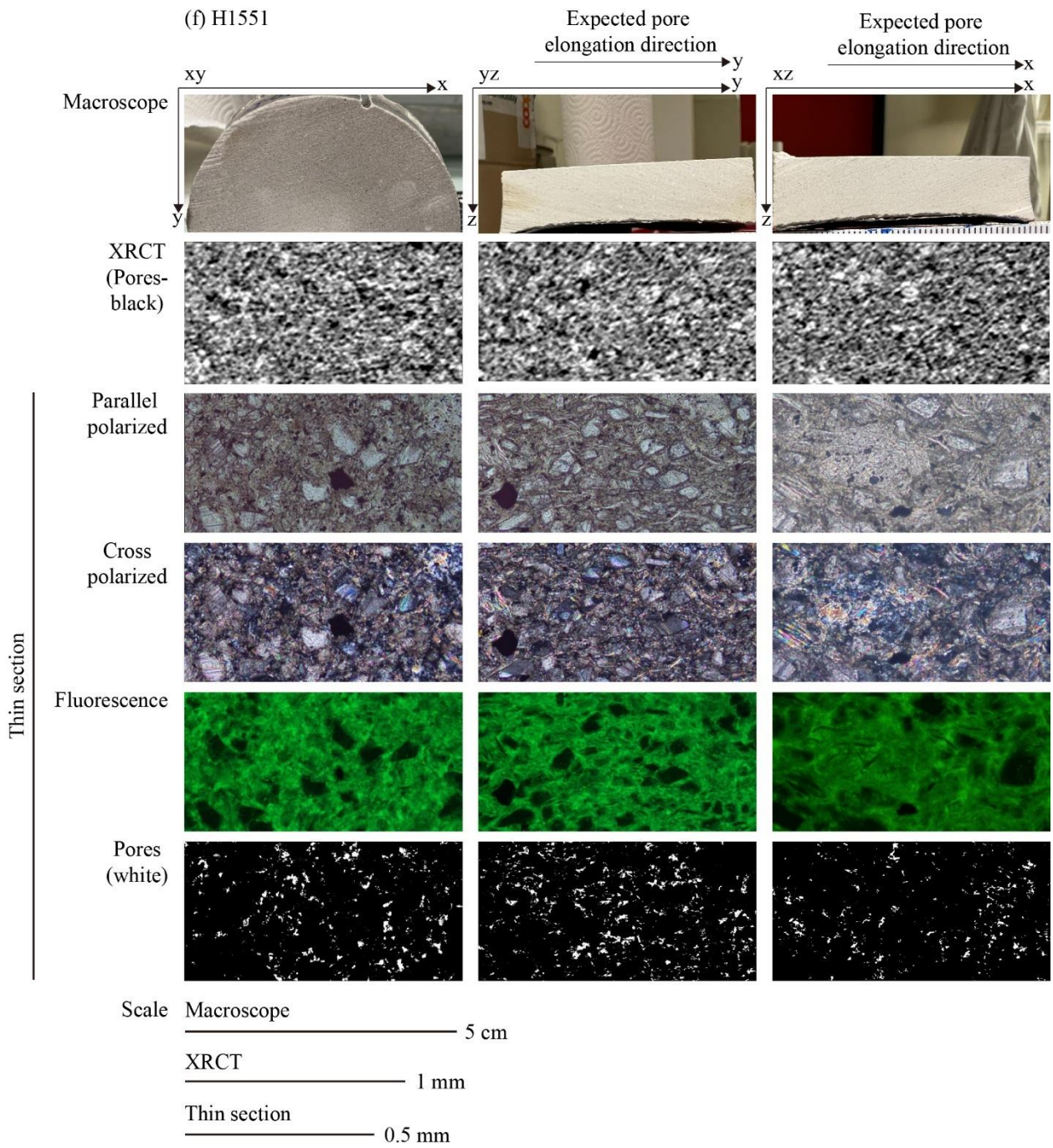


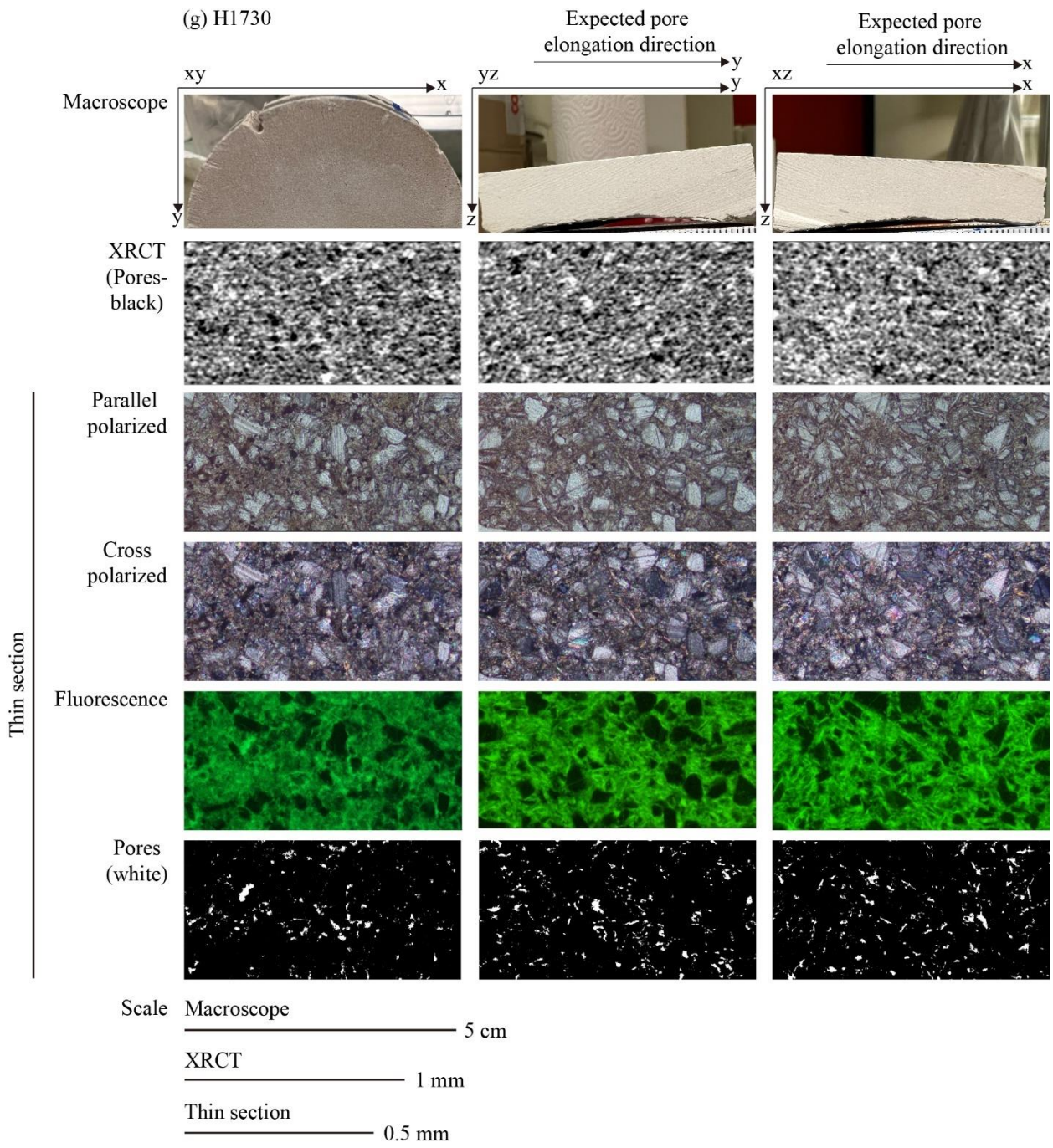


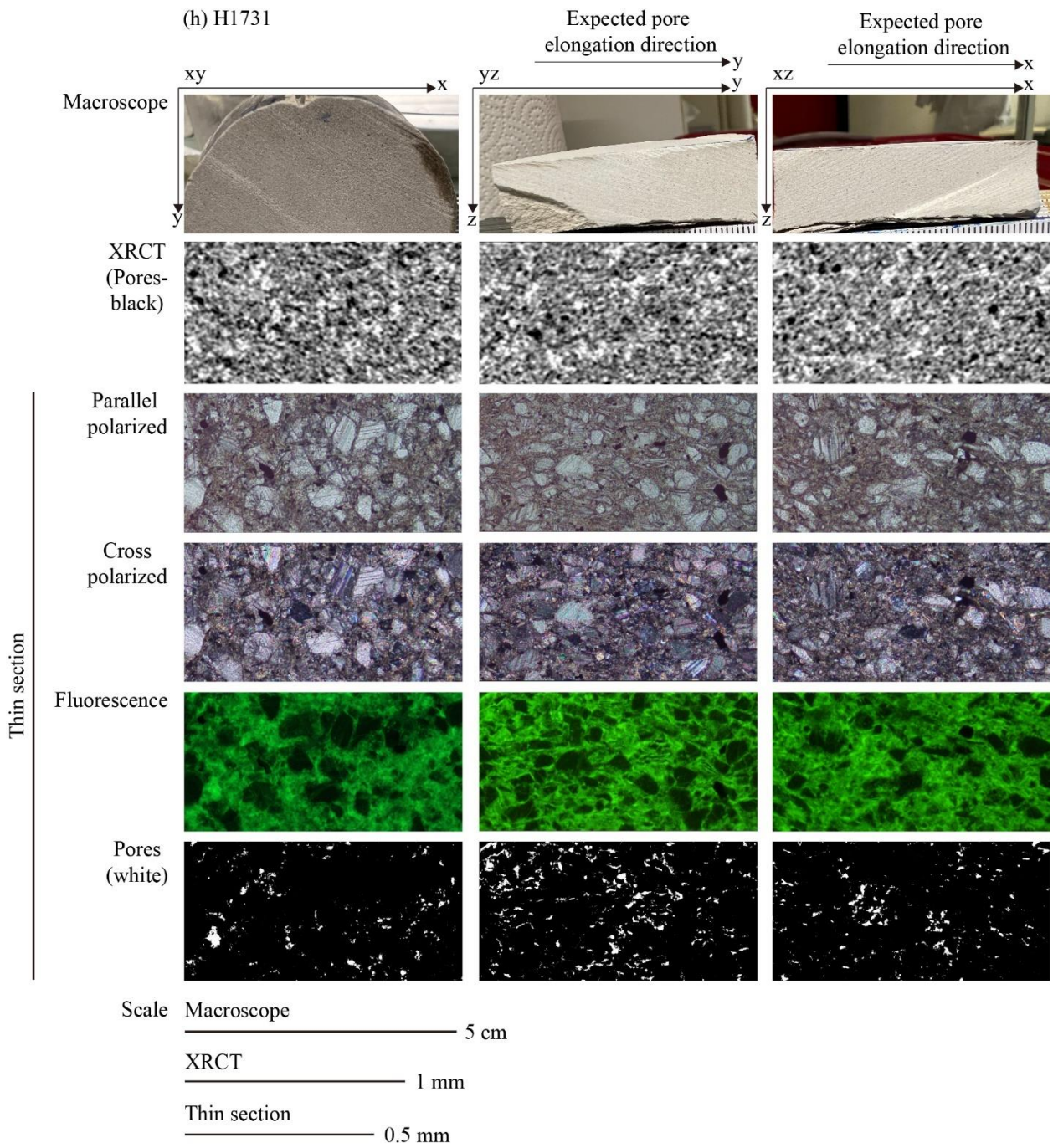


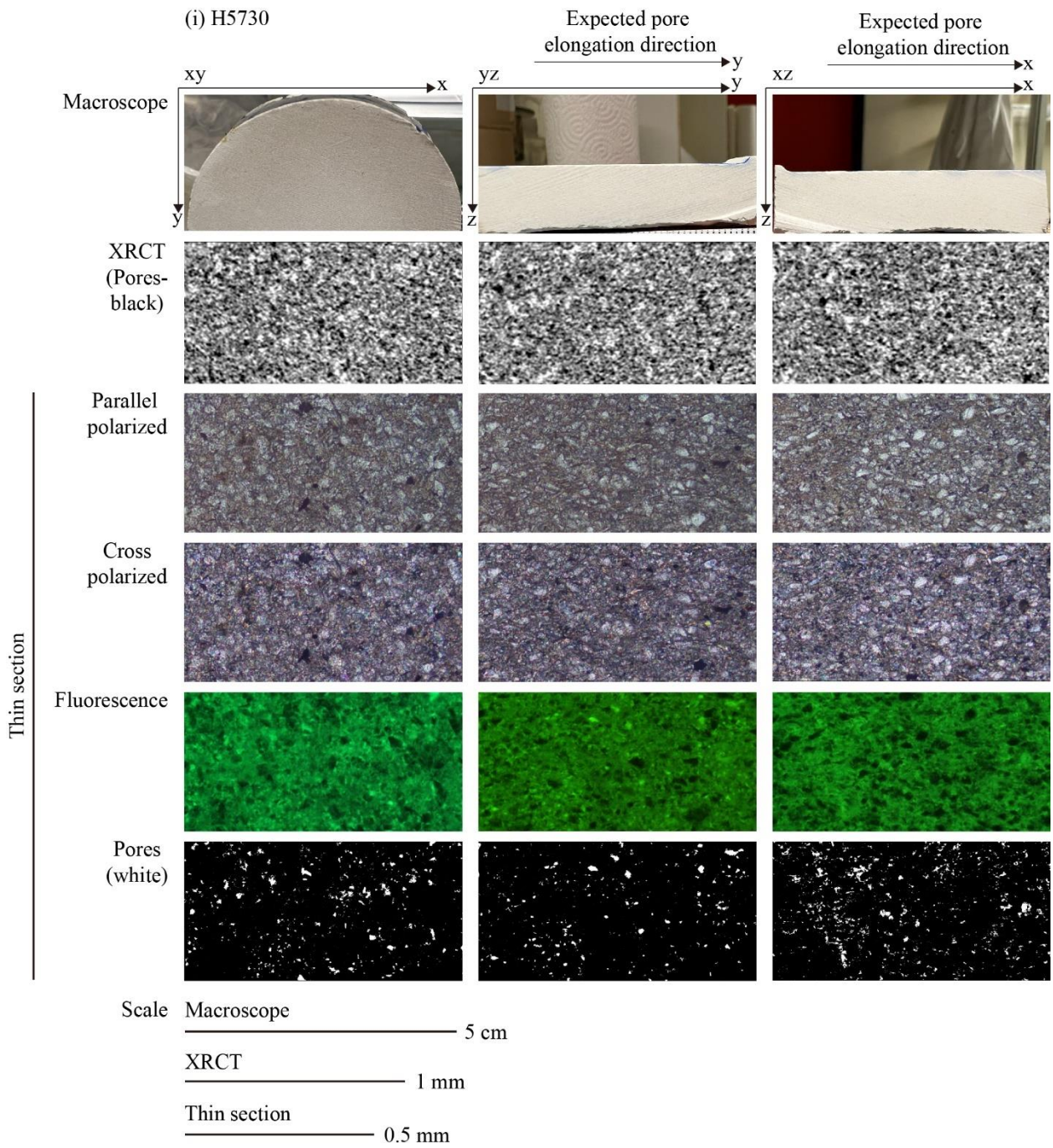


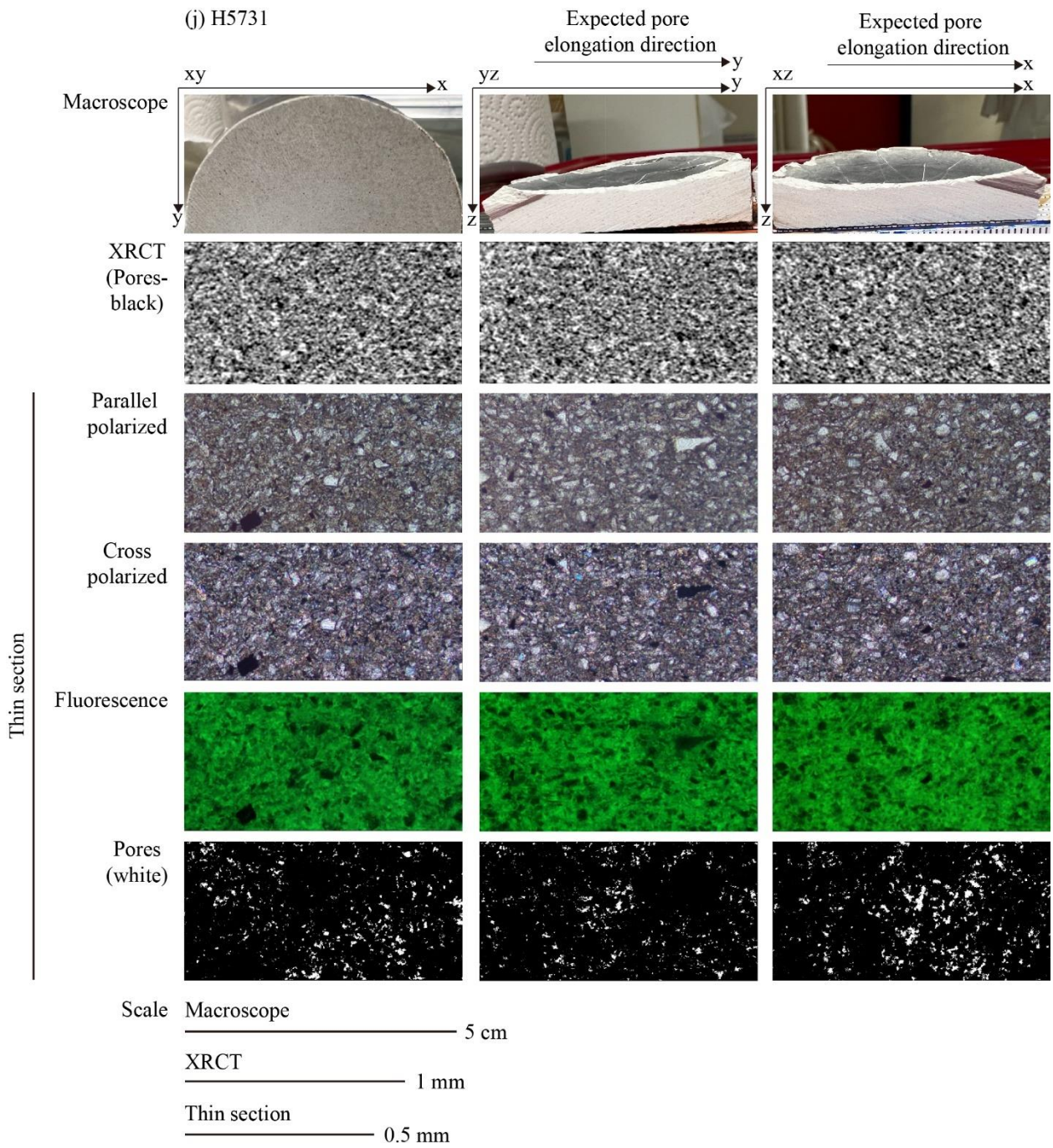












(k)

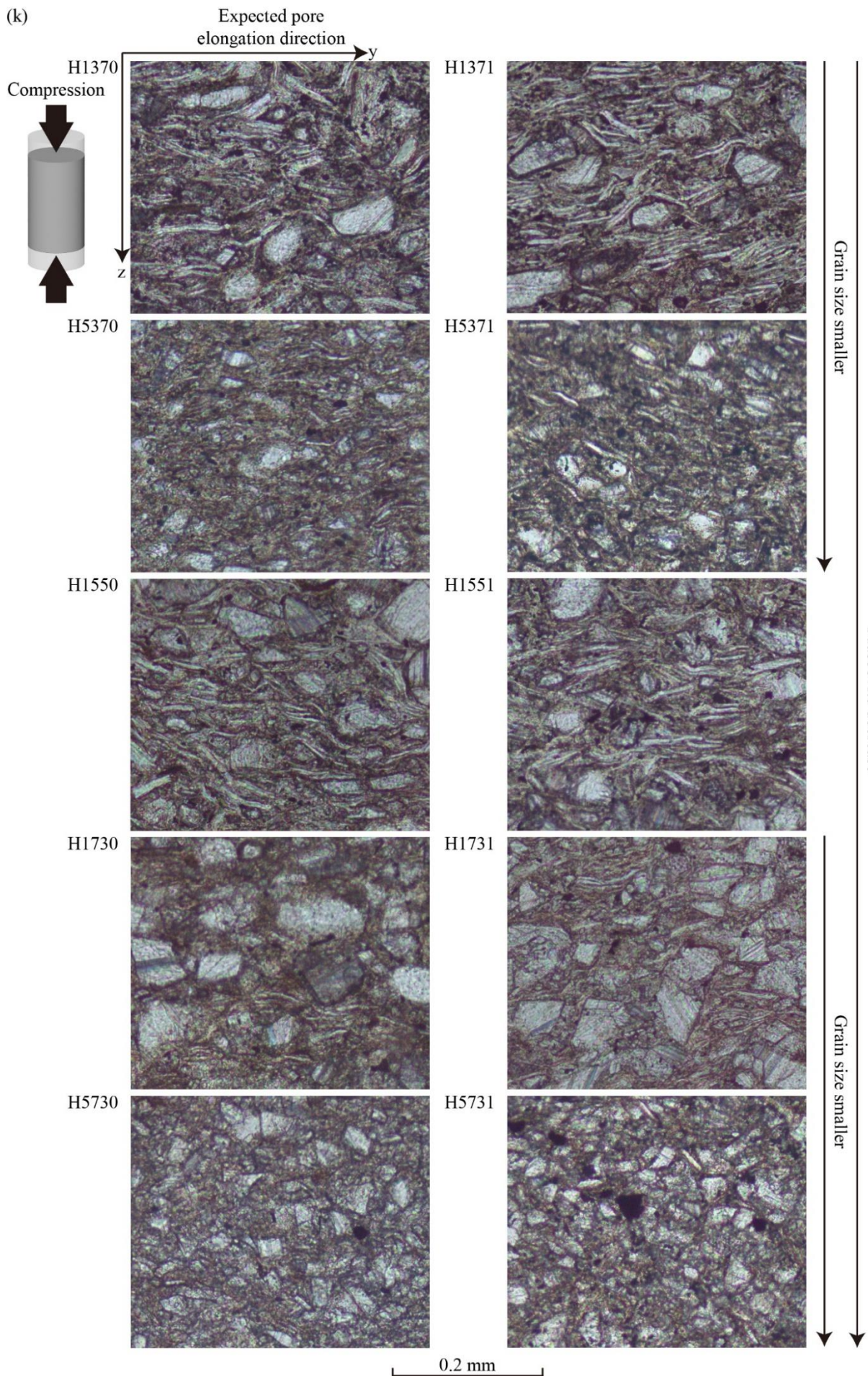


**Figure 5.1.** (a-j) Macroscopic fabrics of the sample blocks on the three mutually perpendicular surfaces ( $xy$ ,  $yz$ ,  $xz$ ) examined from photographs (see text), structure features on XRCT images of cores and thin sections in three orthogonal orientations ( $xy$ ,  $yz$ ,  $xz$ ). The first column displays the macroscopic fabrics of the three perpendicular surfaces ( $xy$ ,  $yz$ ,  $xz$ ) of each sample block, as directly photographed using an iPhone 13 Pro Max camera. All blocks are very homogeneous without any clear structures. The second column presents the structural characteristics from the XRCT images of cores in three orthogonal directions ( $xy$ ,  $yz$ ,  $xz$ ). Columns three to six sequentially exhibit the structural and mineral characteristics on the thin sections in the three orthogonal directions ( $xy$ ,  $yz$ ,  $xz$ ) that have been infused with fluorescent resin. These include images under parallel-polarized light, cross-polarized light, green UV light, and pore fabrics (shown in white) extracted using the ImageJ software. Some thin sections have a weak fluorescence due to a sparse application of fluorescent resin on the minerals. Therefore, only the brightest luminescent parts were extracted for pore fabrics analysis. (k) Magnified thin-section images in  $yz$  plane. All images are under plane-polarized light, with pore areas injected by yellow resin. The primary pore type is intergranular pores. However, the samples are highly compacted and possess small grains with tight grain-to-grain contact, resulting in very small pores. Significant anisotropic features can be observed due to the strip-like distribution of muscovite grains along the lateral direction. However, this anisotropy gradually weakens as the muscovite content decreases or as the grain size becomes smaller.

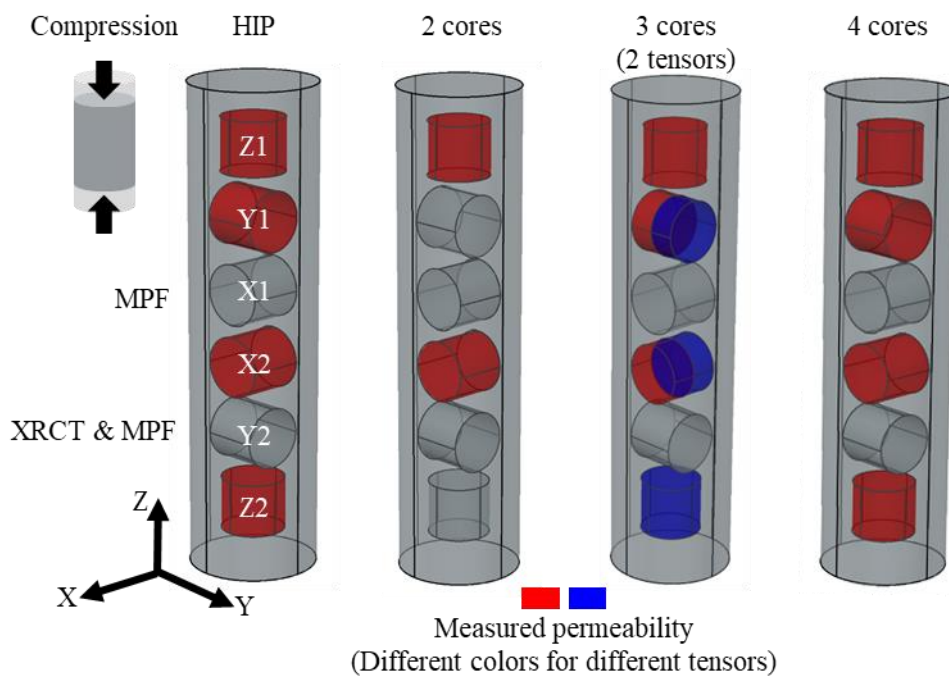


**Figure 5.2.** Sketch for directional cores of HIP sample and permeability anisotropy.

Three thin sections in mutually perpendicular directions ( $xy$ ,  $yz$ , and  $xz$ ) were prepared and impregnated by fluorescent resin for subsequent pore structure observation. Mineral analysis using parallel polarized light and crossed polarized light microscopy reveals that the vertical thin sections ( $yz$  and  $xz$ ) exhibit grain distribution along transverse direction ( $xy$ ). Muscovite grains, due to their laminar nature, appear as fine stripes distributed transversely on the vertical thin sections, while calcite grains, which have irregular shapes, exhibit uncertain distributions. On the transverse thin sections ( $xy$ ), calcite and muscovite grains present random distribution. Certainly, the anisotropy characteristic tends to decrease as the proportion of muscovite components decreases. The predominant porosity consists of intergranular pores. The pore structure constrained by grain boundaries are expected to exhibit lateral distribution in vertical thin sections

and random distribution in the transverse thin sections (Figure 5.1). However, due to the extremely small pore sizes, it is difficult to identify a large number of pore fabrics through visual observation in thin sections. However, the following sections will introduce using image processing software to segment the pores (the brightest parts) from fluorescence images, enabling a quantitative analysis of pore fabrics, and hence establishing a quantitative relationship between the macroscopic fabrics and the microscopic pore fabrics.

The remaining samples were cut into cores with a height of 22 mm and a diameter of 25 mm. Each sample was cut into cores in the  $X$ ,  $Y$ , and  $Z$  directions, with two cores in each direction, for a total of six ( $X1$ ,  $X2$ ,  $Y1$ ,  $Y2$ ,  $Z1$ ,  $Z2$ ) (Figure 5.2). Because HIP samples were formed by uniaxially pressing uniformly mixed mineral powder at high temperatures, they exhibited strong homogeneity for whole sample and anisotropy between the lateral and axial directions. The lateral characteristics could be approximated as uniform ( $X = Y$ ), so measurements in at least two directions (transverse and longitudinal) are needed to calculate any tensor properties, such as permeability anisotropy. Additional core measurements in more directions could be used to assess errors and reliability. All cores were dried in an oven at 100 °C for 48 hours, and then porosity measurements were performed using a Micromeritics AccuPyc 1340 Automatic Gas (He) Pycnometer system in the Petrophysics Laboratory at the University of Bern.

## 5.2.2 Direct and indirect pore fabric determination

### 5.2.2.1 Thin section analysis

Thin section analysis were performed using conventional microscopic observations under parallel-polarized and cross-polarized light. The fabric of the main mineral components, calcite and muscovite, were qualitatively observed and interpreted. Due to the prior injection of fluorescent resin into the pores during preparation, the pore fabrics under UV light irradiation could be highlighted for later segmentation and analysis. It should be noted that, as the fluorescent resin was injected into the thin section without further meticulous polishing and subsequently covered with a coverslip, some resin may have overflowed onto the surface of mineral particles, resulting in a weak fluorescence signal. Therefore, during the pore structure analysis, only regions exhibiting significant fluorescence emission were identified as pores.

For the fluorescent two-dimensional images of the thin sections, ImageJ software was utilized for pore analysis to obtain the area of each pore, as well as the two principal directions and lengths of its best fit ellipse. The size of each pore was represented by the circular diameter of its equivalent area. The tensor sum of each pore shape yielded a total shape ellipse to represent the overall pore shape (Zhou et al., 2022). Each sample was prepared with three thin sections in mutually perpendicular directions ( $xy$ ,  $yz$ ,  $xz$ ), and the combination of the total shape ellipses from the three thin sections provided the total shape ellipsoid, i.e., the three-dimensional pore structure of the sample (Shimamoto & Ikeda, 1976). The lengths of the three principal axes ( $a$ ,  $b$ ,  $c$ ) of the total shape ellipsoid could be used to calculate the anisotropy degree ( $P = a/c$ ,  $[1, \infty]$ ) and shape ( $U = (2*b-a-c)/(a-c)$ ,  $[-1,1]$ ) of the pore shape (Jelinek, 1981).

To improve efficiency and conserve resources, the minimum area that maintains the representative properties of the study, known as the Representative Elementary Area (REA), was selected for further research. By calculating the function relationship between the variables of interest (in this study, porosity and pore size) and the area of the study region, a REA that maintains the relatively stable variation of the research variables could be obtained (Zhou et al., 2022). For this study, the REA was  $5 \times 5 \text{ mm}^2$  (10 times magnification). Pores smaller than  $4 \times 4$  pixels ( $2.3 \times 2.3 \text{ }\mu\text{m}^2$ ) were excluded from the shape analysis as they could not provide effective shape characteristics (Zhou et al., 2022).

#### 5.2.2.2 XRCT data acquisition and processing

The Y2 core of each HIP sample (Figure 5.2) was scanned for its three-dimensional structure using a Bruker SkyScan 1273 at the University of Bern. The scanning parameters were set to 5.5  $\mu\text{m}$  pixel size, with 1 mm Al+0.038 mm Cu filter, 100 kV voltage, 80  $\mu\text{A}$  current, and 275 ms exposure time. Subsequently, NRecon was employed to reconstruct and correct the images (Skyscan, 2011). Post-processing was conducted using Avizo (version 2021.2), beginning with noise reduction (utilizing the Unsharp masking filter) and pore segmentation (employing the watershed algorithm) (Bieniek & Moga, 2000; Polesel et al., 2000; Strobel, 1996). Following these preprocessing steps, digital pore fabrics of the samples were obtained. For subsequent pore structure analysis, the representative elementary volume (REV) was selected as 600×600×600 voxels (3.3×3.3×3.3  $\text{mm}^3$ ), and pores smaller than 4×4×4 voxels (22×22×22  $\mu\text{m}^3$ ) were excluded (Zhou et al., 2022). For pore fabric analysis, the total shape ellipsoids of the samples were computed, and the anisotropy orientation, degree, and shape of the pores were determined. Additionally, the bootstrap method was employed to generate more ellipsoids for computing 95% confidence ellipses to assess data quality (Constable & Tauxe, 1990; Hext, 1963; Jelínek & Kropáček, 1978; Owens, 2000; Tauxe et al., 1998; Zhou et al., 2022). Based on the digital pore fabrics, the full tensor of permeability anisotropy was simulated using the built-in toolkit in Avizo. The default standard settings of the software Avizo were a pressure of 0.13 MPa and a fluid viscosity of 0.001 Pa·s. Increasing the pressure and fluid viscosity significantly increased the simulation computation time but did not notably alter the simulated permeability anisotropy orientation, degree, or shape—the parameters of primary interest in this study. Therefore, the default settings were used to reduce simulation computation time. The simulated permeability anisotropy was further analyzed for anisotropy orientation, degree, and shape. Similarly, utilizing the pore network derived from XRCT, MPF was simulated using the FinIrrSDA software (Biedermann, 2020).

#### 5.2.2.3 Permeability anisotropy measurements

The X2, Y1, Z1, and Z2 cores were sent to CoreLab in the UK for gas permeability measurements, with a confining pressure of 800 psig ( $\approx 5.52$  MPa). Additional cores can be used to compute more tensors for comparison or to calculate 95% confidence ellipses to assess sample heterogeneity. The results obtained from two directional cores (X2, Z1 or X2, Z2 or Y1, Z1 or Y1, Z2), three directional cores (X2, Y1, Z1, or X2, Y1, Z2), and four directional cores (all) were compared to illustrate the impact of the number of directional cores used for calculating the permeability anisotropy (Figure 5.2). Permeability anisotropy can be characterized by computing its anisotropy orientation, degree, and shape through its three principal axes. The calculation method remains consistent with the formulas in the thin section to use three principal axes (a, b, c) to calculate the anisotropy degree ( $P = a/c$ , [1,  $\infty$ ]) and shape ( $U = (2*b-a-c)/(a-c)$ , [-1,1]).

#### 5.2.2.4 Magnetic pore fabric measurements

The measurements of magnetic anisotropy in cores are divided into two parts: the anisotropic magnetic susceptibility (AMS) of the original rock samples and the magnetic susceptibility of the samples after the injection of ferrofluid (i.e., MPF). Both methods involve measuring the samples in 15 directions to calculate their magnetic anisotropy (Jelinek, 1996). The measurements were conducted using an MFK1-FA susceptibility bridge (AGICO, Czech Republic) in the Laboratory of Natural Magnetism (LNM) at ETH Zurich. Measurements were performed at a frequency of approximately 1 kHz and a magnetic field of 200 A/m. For each sample, X1 and Y2 cores were selected. Initially, AMS measurements were conducted, followed by complete immersion of the samples in ferrofluid and then subjected to a 24-hour impregnation experiment under a vacuum of 100 kPa. Subsequently, the samples were dried at room temperature for 24 hours before MPF measurements.

Regarding the selection of ferrofluid, the physical properties of the magnetic particles and mineral

grains need to be considered to enhance the impregnation efficiency and ensure proper wetting of muscovite and calcite during the injection process. Muscovite grains exhibit a distinct negative charge on their surfaces and possess some hydrophilicity (Liu & Buckley, 1999), while calcite grains exhibit either positive or negative charges and generally tend to be more oleophilic (Hassan et al., 2019; Taheriotaghsara et al., 2021). Therefore, a water-based magnetic fluid EMG 705 (FerroTec), containing anionic surfactants, was chosen for the study to ensure smooth wetting of muscovite grains during impregnation and to allow the magnetic particles to flow freely in the pores without being adsorbed by the muscovite grains. Additionally, EMG 705 has a high intrinsic magnetic susceptibility of 4.04 SI and low viscosity, less than 5 mPa•s. The magnetic fluid was diluted with distilled water at a volume ratio of 1:10 before injection.

The impregnation efficiency based on susceptibility ( $I.E.susc$ ) and porosity derived by MPF ( $\varphi_{MPF}$ ) were calculated using the following formulas (Pugnetti et al., 2022):

$$I.E.susc = \frac{\Delta k_{mean}}{\varphi k_{fluid}} * 100\%$$

$$\varphi_{MPF} = \frac{\Delta k_{mean}}{k_{fluid}} * 100\%$$

Where  $\Delta k_{mean}$  is the difference in mean magnetic susceptibility of the sample before and after injection,  $\varphi$  is the porosity measured by the Pycnometer system, and  $k_{fluid}$  is the susceptibility of the ferrofluid.

Due to the frequency-dependent (Biedermann et al., 2021) and self-demagnetization (Clark, 2014; Osborn, 1945; Sato & Ishii, 1989; Stoner, 1945) issues, the susceptibility of the ferrofluid needs to be measured under experimental conditions, and corrected using the following formula:

$$k_{int} = \frac{k_m}{1 - Nk_m}$$

Where  $k_{int}$  is the true intrinsic susceptibility of the ferrofluid,  $k_m$  is the measured susceptibility, and  $N$  is the self-demagnetization factor, which depends on the shape of the measured object. For the ferrofluid measured here, which is a cylinder with a height of 0.95 cm and a diameter of 1.63 cm,  $N$  is 0.43 (Clark, 2014; Osborn, 1945; Sato & Ishii, 1989; Stoner, 1945). The final corrected ferrofluid susceptibility is 0.17 SI.

The significance of magnetic anisotropy directionality was assessed by calculating confidence angles  $E13$  ( $=E31$ ),  $E12$  ( $=E21$ ) and  $E23$  ( $=E32$ ) (Hext, 1963; Jelinek, 1977, 1981). Anisotropy degree and shape were determined using the same method above based on susceptibilities along the three principal axes (Jelinek, 1981). The mean susceptibility of impregnated samples was compared with anisotropy degree, anisotropy shape, and susceptibility-based impregnation efficiency to observe their correlation.

### 5.2.3 Correlation of thin section, XRCT, permeability anisotropy and MPF data

First, the porosity directly measured by a Helium pycnometer was compared with that obtained through thin section and XRCT image analysis, as well as MPF-derived porosity. Then, the pore size distribution from thin section analysis was compared with that from XRCT digital rock analysis. Porosity was compared with permeability, including both measured and XRCT-derived values. Anisotropy orientation, degree, and shape data from the analysis of thin section-derived pore structures, XRCT-derived pore fabrics (i.e., Total shape ellipsoid), XRCT data-simulated permeability anisotropy and MPF, along with measured permeability anisotropy, AMS of original samples, and MPF of impregnated samples were compared. Anisotropy degree was additionally integrated into a single figure to compare permeability anisotropy with other forms of anisotropy.

### 5.3. Results

The porosity measured directly by Helium pycnometer ranges from 12.16 % to 26.79 % across all HIP samples. Samples with smaller grain sizes and higher muscovite content tend to exhibit greater porosity, with H5370 showing the highest porosity at  $24.35 \pm 2.44$  % and H1730 exhibiting the lowest at  $16.26 \pm 4.10$  %. The impact of magnetite inclusion on porosity is inconclusive. For groups H5370 and H5371, as well as H5730 and H5731, the average porosity tends to decrease after magnetite inclusion, while the difference is less significant for other control groups. However, it's worth noting that the variation in porosity among different cores within each sample is significant. Porosity obtained through other methods shows relatively small differences within each sample. The trends in porosity variation among samples obtained from other methods are similar to those measured by Helium, though porosity derived from thin section and MPF analysis is smaller, ranging from 2.1 % to 6.2 % and 1.51 % to 2.75 %, respectively. The relatively low impregnation efficiency of the ferrofluid (7.03 % to 12.3 %) contributes to this. Porosity derived from XRCT data closely approximates that measured by pycnometer, ranging from 12 % to 22 %. The three samples (H1370, H1550, H1730) prepared under the reference (Schmidt et al., 2008) experimental conditions show Helium porosities consistent with those reported in the literature (Figure 5.3 and Table 5.3).

**Table 5.3.** Porosity comparison of laboratory measurements by He pycnometry, numerical calculations based on thin sections and XRCT data, and estimation from MPF. I.E.<sub>susc</sub> was also presented.

Sample	Porosity (He pycnometry, AccuPyc 1340) (%)	Porosity (thin sections / magnification: 10x) (%) (threshold, (solid-void) 0-255)	Porosity (Skyscan 1273 / resolution: 5.5 $\mu$ m) (%) (threshold, (void-solid) 0-255)	Porosity (MPF) (%)	I.E. <sub>susc</sub> (%)
H1370	20.98 $\pm$ 2.52	4.6 $\pm$ 1.3 (65)	18 $\pm$ 1 (43)	1.6 $\pm$ 0.1	7.0 $\pm$ 0.1
H1371	21.03 $\pm$ 3.11	3.6 $\pm$ 0.9 (68)	15 $\pm$ 1 (57)	1.8 $\pm$ 0.1	9.1 $\pm$ 0.1
H5370	24.35 $\pm$ 2.44	4.9 $\pm$ 0.6 (61)	21 $\pm$ 1 (55)	2.6 $\pm$ 0.1	11.4 $\pm$ 0.5
H5371	22.29 $\pm$ 1.57	4.7 $\pm$ 1.5 (55)	20 $\pm$ 1 (53)	2.6 $\pm$ 0.2	11.6 $\pm$ 0.7
H1550	18.03 $\pm$ 2.46	3.8 $\pm$ 0.5 (73)	16 $\pm$ 1 (53)	1.8 $\pm$ 0.2	10.2 $\pm$ 1.0
H1551	18.08 $\pm$ 0.85	3.7 $\pm$ 0.8 (65)	15 $\pm$ 1 (51)	2.0 $\pm$ 0.1	11.1 $\pm$ 0.5
H1730	16.26 $\pm$ 4.10	3.7 $\pm$ 0.4 (71)	15 $\pm$ 1 (57)	1.7 $\pm$ 0.1	10.5 $\pm$ 0.6
H1731	16.56 $\pm$ 3.20	3.5 $\pm$ 0.6 (73)	13 $\pm$ 1 (57)	1.7 $\pm$ 0.1	10.4 $\pm$ 0.6
H5730	18.79 $\pm$ 2.79	2.7 $\pm$ 0.6 (64)	15 $\pm$ 1 (50)	1.9 $\pm$ 0.1	9.3 $\pm$ 0.9
H5731	17.85 $\pm$ 0.42	2.4 $\pm$ 0.3 (68)	17 $\pm$ 1 (56)	1.9 $\pm$ 0.1	10.4 $\pm$ 0.2

Regarding pore size distribution, there is high overlap in distribution characteristics among different orientation thin sections ( $xy$ ,  $yz$ ,  $xz$ ), all exhibiting a linear decreasing trend where larger pores constitute a smaller proportion, ranging from 3 to 200  $\mu$ m. In contrast, pore size distribution obtained from XRCT analysis for most samples shows a linear decrease within the 25-100  $\mu$ m range. However, samples H1370, H5370, and H5371 exhibit a bimodal distribution with peaks around 25-60  $\mu$ m and 150-400  $\mu$ m, with peaks approximately at 30  $\mu$ m and 280  $\mu$ m, respectively. Although H5730 also shows pore size in the 200-400  $\mu$ m range, it accounts for a minimal proportion (approximately 0.01 %), and its overall distribution trend aligns with other samples (Figure 5.4).

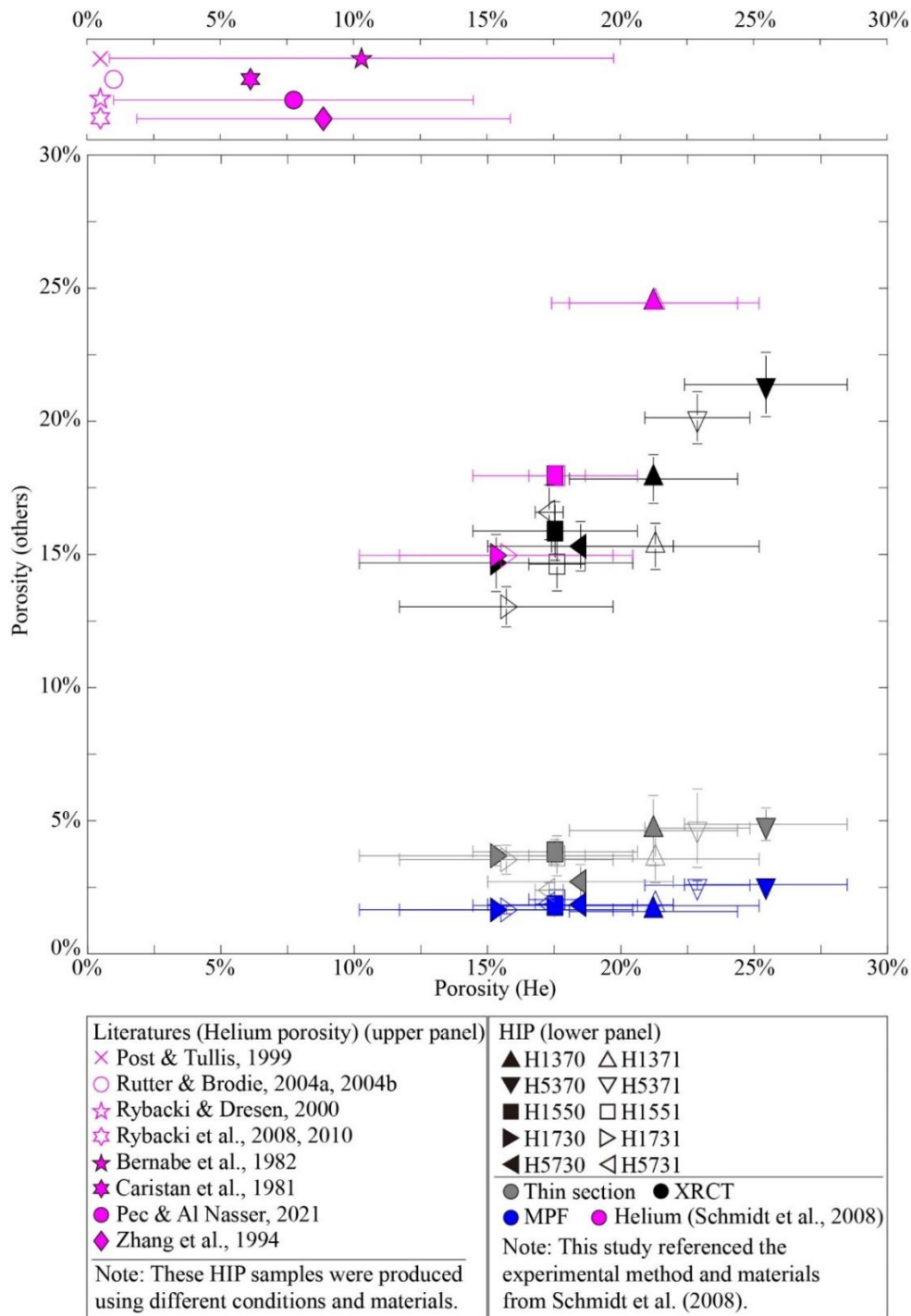


**Figure 5.3.** Porosity for different samples from Helium pycnometer, thin section, XRCT, MPF-derived data, and Helium pycnometer (literatures). For the lower panel, the symbols of the same shape (regardless of color differences) correspond to the same sample, so they share the same value on the x-axis, all representing He porosity measured in this study. However, their different colors correspond to porosity from other methods or literature, showing their values on the y-axis. Gray represents thin section-derived porosity, black represents XRCT-derived porosity, blue represents MPF-derived porosity, and purple represents He porosity sourced from Schmidt et al. (2008). Note that since Schmidt et al. (2008) used the same method to produce samples, their Helium porosity can be compared directly with the porosity in our study (lower panel). In contrast, other studies used different methods and materials to create HIP samples, so their Helium porosities are only used for reference (upper panel).

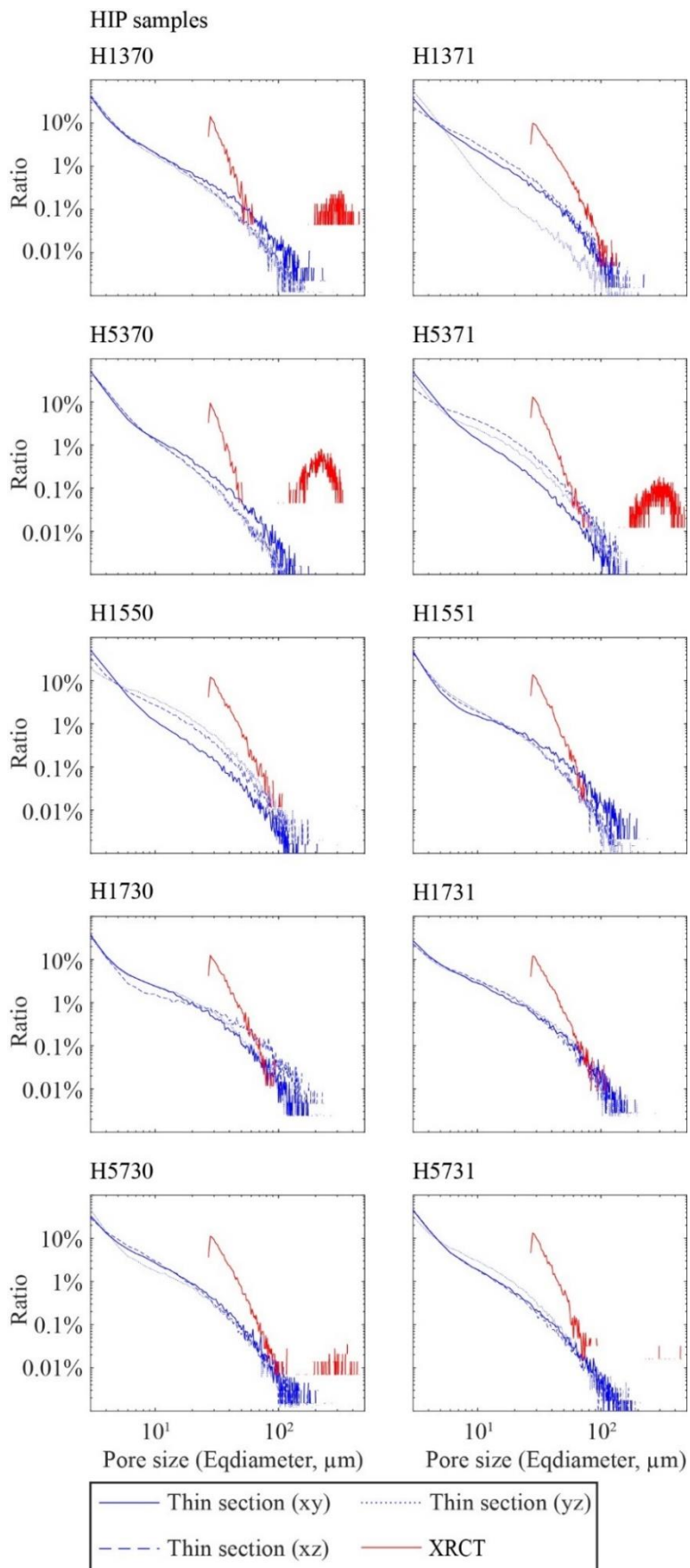


**Figure 5.4.** Pore size distribution analysis from three perpendicular thin sections and XRCT data for all samples. Pore size is presented by EqDiameter which is the diameter of a circle or sphere with the same area or volume as a single pore. The distribution is presented by percent of pores, comparing the number of pores in each size with the total number of pores. Due to differences in resolution, XRCT did not detect some small grains between pores, causing these pores to merge into larger ones. As a result, XRCT data exhibits a steeper and even multimodal pore size distribution compared to thin section data.

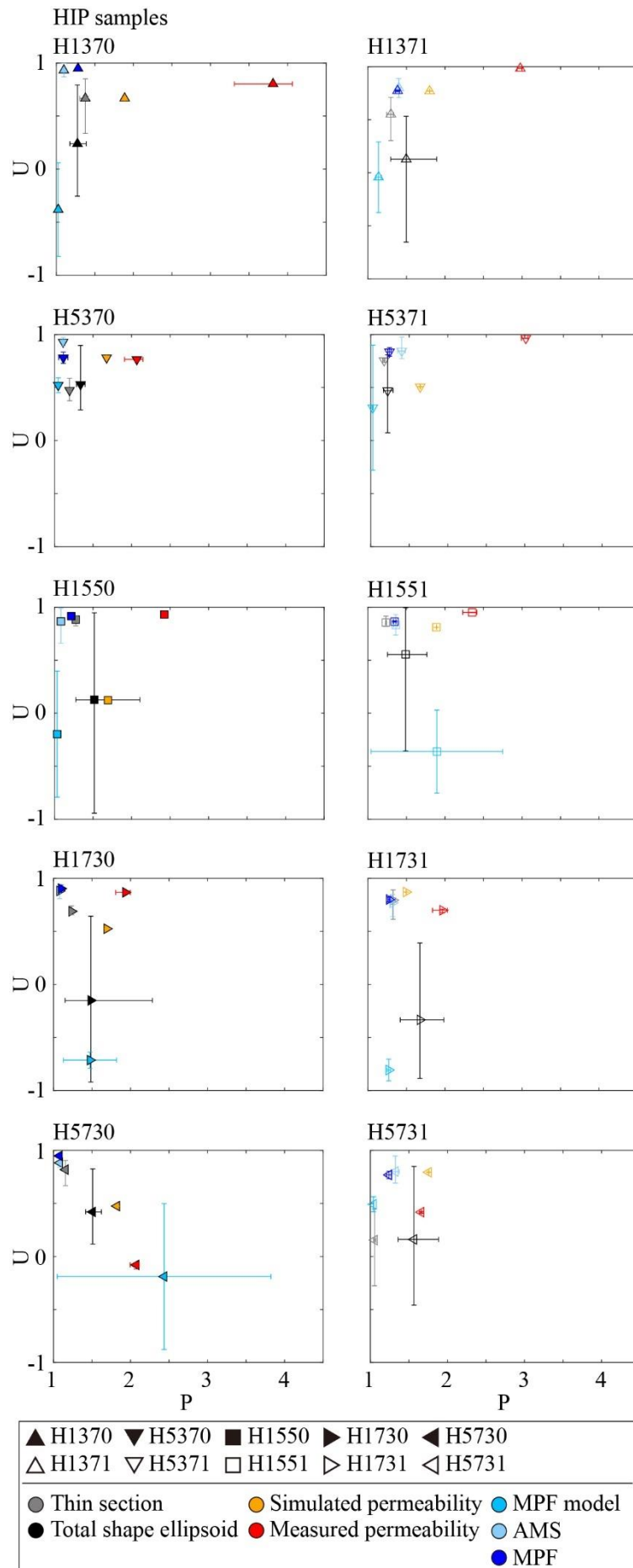


**Figure 5.5.** Anisotropy degree ( $P$ ) and shape ( $U$ ) of all samples from pore fabrics of thin section analysis, XRCT-derived data (total shape ellipsoids, simulated permeability anisotropy, and MPF model), measured permeability anisotropy, AMS and MPF.

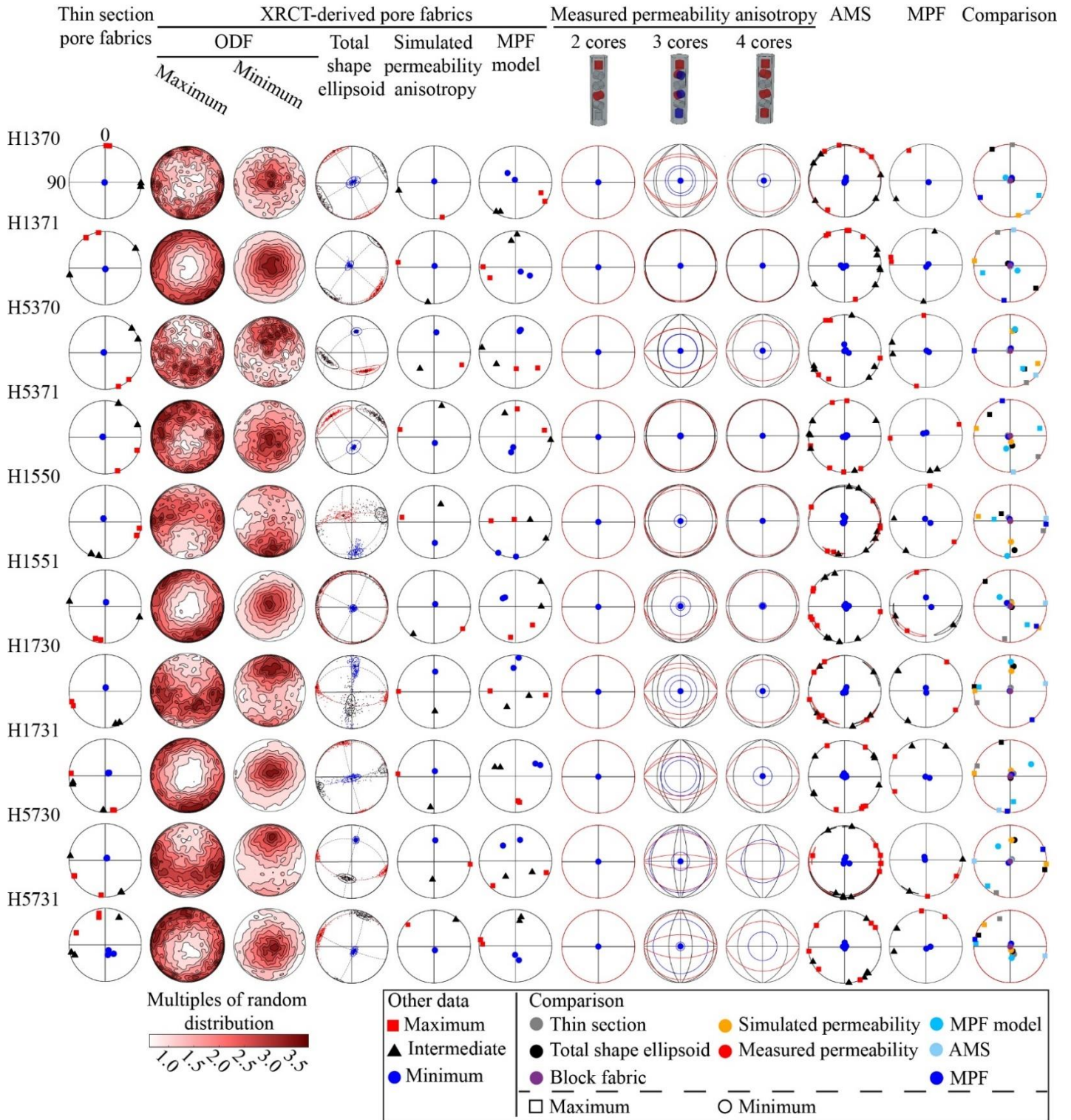


**Figure 5.6.** Comparison of orientation of pore fabrics from thin section analysis, XRCT-derived data (orientation density functions of pore axes, bootstrapped total shape ellipsoids, simulated permeability anisotropy, and MPF model), measured permeability anisotropy (2, 3, 4 cores), AMS and MPF. In the last column, the block fabric was added. Due to the vertical compaction, the maximum axis of the block fabric is considered to be along the  $xy$ -direction, while the minimum axis is along the  $z$ -direction, i.e., the compaction direction.

### 5.3.1 Thin section

For the pore structure analyzed from thin sections, sample H1370 exhibits the highest anisotropy degree  $P$ , ranging from 1.30 to 1.41, while sample H5731 shows the lowest anisotropy degree, ranging from 1.04 to 1.07. The influence of adding magnetite and varying component proportions on the anisotropy degree is not significant. However, samples with smaller grains ( $<50\ \mu\text{m}$ ) tend to have lower anisotropy degrees. Regarding anisotropy shape  $U$ , sample H1550 has the highest value, ranging from 0.82 to 0.91, while H5731 has the lowest value, ranging from -0.28 to 0.45. Except for H5731, which lacks consistent anisotropy shape, the rest of the samples exhibit an oblate ellipsoid shape, i.e.,  $U > 0$  (Figure 5.5). The anisotropy orientations of all samples show that the minimum principal axes  $V3$  align along the  $z$ -axis direction, while the intermediate and maximum principal axes, i.e.,  $V2$  and  $V1$ , are distributed in the  $xy$  plane. Sample H5731 exhibits slight differences again, with  $V3$  showing an angle of approximately  $10^\circ$  with the  $z$ -axis, and  $V2$  and  $V1$  showing an angle of approximately  $10^\circ$  with the  $xy$  plane (Figure 5.6).

### 5.3.2 XRCT data

For XRCT-derived pore fabrics, sample H1730 exhibits both the highest and lowest anisotropy degree values (ranging from 1.15 to 2.29). Sample H1551 has the maximum anisotropy shape value of 0.99, while sample H1550 has the minimum value of -0.94. Samples H5370, H5371, and H5730 display an oblate ellipsoid shape, while the remaining samples show inconsistent anisotropy shapes. Simulated permeability anisotropy results indicate that sample H1551 has the highest anisotropy degree of 1.89, whereas H1731 has the lowest at 1.49. All samples exhibit an oblate anisotropy shape, with sample H1731 having the maximum  $U$  value of 0.87 and sample H1550 having the minimum at 0.12. The simulated MPF model reveals that among all samples, H5730 exhibits the maximum anisotropy degree at 3.82, while sample H5371 has the minimum at 1.02. Samples H1730 and H1731 show prolate anisotropy shapes, while H5370 and H5731 exhibit oblate anisotropy shapes, and the remaining samples do not demonstrate consistent anisotropy shape. Sample H5371 has the maximum  $U$  value at 0.90, whereas sample H1731 has the minimum at -0.91. There is no significant influence from component proportion, magnetite, grain size on the anisotropy degree and shape of the samples (Figure 5.5).

The orientation density functions (ODF) projection images for the maximum and minimum principal axes of each pore shape in the samples, as well as the three-axis directional projection images of the total shape ellipsoid, are analyzed. Only H1370, H1371, H1551, H1731, and H5731 show the characteristic distribution of  $V3$  parallel to the  $z$ -axis, with  $V1$  and  $V2$  distributed along the  $xy$  plane. For samples H5370, H5371, H1550, and H5730, there is an angle between  $V3$  and the  $z$ -axis, resulting in an angle between  $V1$ ,  $V2$ , and the  $xy$  plane, with deviation angles of approximately  $50^\circ$ ,  $18^\circ$ ,  $80^\circ$ , and  $60^\circ$ , respectively. For sample H1730, its ODF image shows the minima near the  $x$ -axis direction, while the maxima were distributed along a plane approximately  $30^\circ$  from the  $yz$  plane. However, its total shape ellipsoid image shows insignificant  $V2$  and  $V3$  directions, both appearing as bands distributed along the  $xz$  plane, with  $V1$  parallel to the  $y$ -axis direction. Using the same software, Avizo, the permeability anisotropy simulation based on the same digital pore structure also approximately matches the direction distributions of the total shape ellipsoids for all samples. The results of MPF simulated using FinIrrSDA software show that, compared to the total shape ellipsoid, samples H1370, H1371, H1551, H1731, and H5731 have larger angles between  $V3$  and the  $z$ -axis, as well as between  $V2$ ,  $V1$ , and the  $xy$  plane, with deviation angles of approximately  $10^\circ$ ,  $15^\circ$ ,  $32^\circ$ ,  $61^\circ$ , and  $24^\circ$ , respectively. The remaining samples show similar characteristics to the total shape ellipsoid and simulated permeability anisotropy (Figure 5.6).

### 5.3.3 Measured permeability anisotropy

The measured permeability data indicate that the  $X$  directional core of sample H5371 exhibits the

highest permeability of 0.49 mD, whereas the Z directional core of sample H1370 demonstrates the lowest permeability of 0.04 mD. Due to the anisotropic structure induced by axial compaction, the transverse (X, Y core) permeability of all samples is higher than their axial (Z core) permeability. For samples with a 5:5 ratio of calcite to muscovite (H1550, H1551), the addition of magnetite (H1551) results in lower permeability. For samples with other component ratios, those with added magnetite exhibit higher permeability. There is no clear relationship between component ratio and sample permeability, as well as between grain size and sample permeability (Figure 5.7).

Although the permeabilities of HIP samples are very low, their anisotropy degrees are high. They reach as high as 3.81 (H1370), and as low as 1.66 (H5731). The proportion of mineral components significantly influences the degree of permeability anisotropy. A higher proportion of muscovite leads to a higher *P*-value in the samples. However, the effects of grain size and magnetite on the anisotropy degree are not significant. Except for sample H5730, which exhibits weak prolate anisotropy shape ( $U = -0.08$ ), all other samples show significant oblate anisotropy shape, with *U* values reaching up to 0.98 (H1371) (Figure 5.5).

Using two directional cores ( $X_2, Z_1$  or  $X_2, Z_2$  or  $Y_1, Z_1$  or  $Y_1, Z_2$ ) to calculate permeability anisotropy, all samples exhibit  $V_3$  aligned along the  $z$ -axis, with the other principal axes parallel to the  $xy$  plane. Two tensors with 95% confidence ellipses can be calculated using three cores ( $X_2, Y_1, Z_1$ , or  $X_2, Y_1, Z_2$ ). Samples H1371, H5371, H1550, and H1551 all show significant anisotropy directional characteristics, with the minimum permeability direction  $V_3$  parallel to the  $z$ -axis, and  $V_1$  and  $V_2$  parallel to the  $xy$  plane. Samples H1370, H5370, H1730, H5730, and H5731 exhibit one tensor with similar directional characteristics to the aforementioned samples, while another tensor shows nonsignificant directions for the three principal axes of permeability anisotropy. Both tensors for sample H1731 show nonsignificant principal axes directions. Permeability anisotropy calculated using four cores ( $X_2, Y_1, Z_1, Z_2$ ) demonstrates significant anisotropy directions for all samples except H5730 and H5731, with  $V_3$  aligned along the  $z$ -axis and  $V_1, V_2$  distributed on the  $xy$  plane (Figure 5.6).

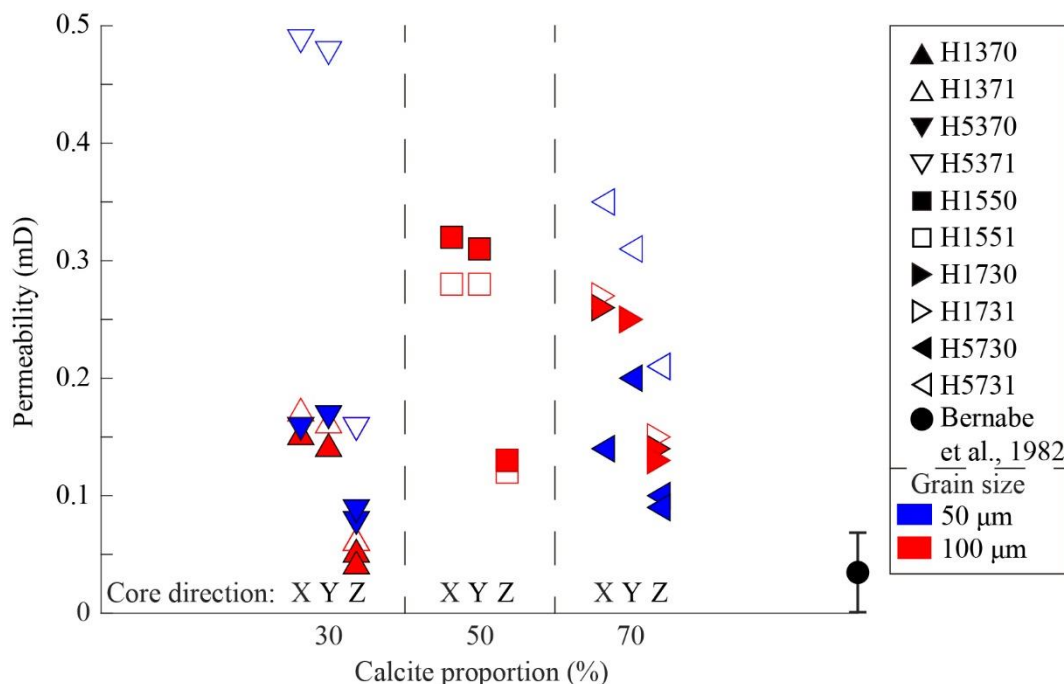


**Figure 5.7.** Permeability of different directional cores from each sample. Data from publication has also been added, specifically from Bernabe et al., 1982, using calcite powder, with permeability ranging from  $0.050$  to  $70 \times 10^{-3}$  mD.

### 5.3.4 AMS and MPF

The anisotropy degree of the AMS of original samples ranges from 1.07 to 1.45. Sample H5371 exhibits the highest  $P$ -value, while sample H1730 displays the lowest. Sample H1370 presents the maximum  $U$  value for AMS at 1.00, whereas sample H1731 records the minimum at 0.64. All samples exhibit an oblate anisotropy shape in their AMS. Introducing magnetite, higher proportions of muscovite, and smaller grain sizes correspond to higher anisotropy degrees of AMS. The inclusion of magnetite in the samples leads to a reduction in their  $U$  values (Figure 5.5).

The  $k_{mean}$  of MPF in the injected samples ranges from  $2.58 \times 10^{-3}$  to  $4.70 \times 10^{-3}$  SI, with sample H5371 having the highest value and H1731 having the lowest. It's noteworthy that the  $k_{mean}$  of MPF refers to  $\Delta k_{mean}$ , indicating the change in mean magnetic susceptibility of the samples before and after ferrofluid injection. The maximum impregnation efficiency  $I.E._{susc}$  for the samples is 12.34 % (H5371), while the minimum is 7.04 % (H1370) (Table 5.3). Grain size, magnetite content, and composition ratio of the samples show no significant influence on  $k_{mean}$  and  $I.E._{susc}$  (Figure 5.8c). The anisotropy degree of MPF in the samples ranges from 1.01 to 1.41, with sample H1730 exhibiting the smallest  $P$  value, while H1371 shows the largest  $P$  value. Regarding anisotropy shape, sample H5730 has the maximum value of 0.97, whereas sample H5370 has the minimum value of 0.73. All samples demonstrate significant oblate anisotropy shape. The inclusion of magnetite, higher proportions of muscovite, and larger grain sizes result in a larger anisotropy degree, but they do not significantly affect the anisotropy shape (Figure 5.5). There is no significant correlation between  $k_{mean}$  and anisotropy degree, as well as between  $k_{mean}$  and anisotropy shape of the MPF (Figure 5.8a, 5.8b). As for both AMS and MPF anisotropy orientations, all samples exhibit significant anisotropic characteristics, with the minimum principal axes  $V3$  aligning parallel to the  $z$ -axis, and the  $V1$  and  $V3$  principal axes distributing along to the  $xy$  plane (Figure 5.6).

### 5.3.5 Comparison

The aforementioned comparisons have been made regarding the porosity and pore size calculated using different methods. Contrasting the relationship between porosity and permeability from direct measurements and XRCT digital rock calculation reveals that the simulation results from XRCT demonstrate higher permeability and lower porosity comparing to direct measurements. The positive correlation between porosity and permeability is significant in the XRCT data, but the directly measured porosity and permeability do not exhibit a clear linear relationship. For the direct measurement date, regardless of whether porosity increases or decreases, the sample permeability remains relatively low (Figure 5.8d). For anisotropy degree, measured permeability consistently exhibits the highest  $P$ -values. The AMS and MPF show a significant correlation with measured permeability, with all three demonstrating anisotropy degree increasing as the proportion of muscovite component in the sample increases (Figure 5.8e). Comparative images of anisotropy orientations also reveal significant similarities among thin-sections-derived pore fabrics, AMS, MPF, and measured permeability anisotropy, all showing the characteristic of the minimum principal axes  $V3$  aligning along the  $z$ -axis and the maximum principal axes  $V1$  aligning along the  $xy$  plane. However, pore fabrics derived from XRCT digital rock, simulated permeability anisotropy, and simulated MPF model exhibit significant differences from the aforementioned four data sources (thin section, measured permeability, AMS, MPF) in some samples, including samples H5370, H1550, H1730, and H5730. Additionally, the simulated MPF model shows directional differences from other data in samples H1371, H1551, H1731, and H5731 (Figure 5.6).

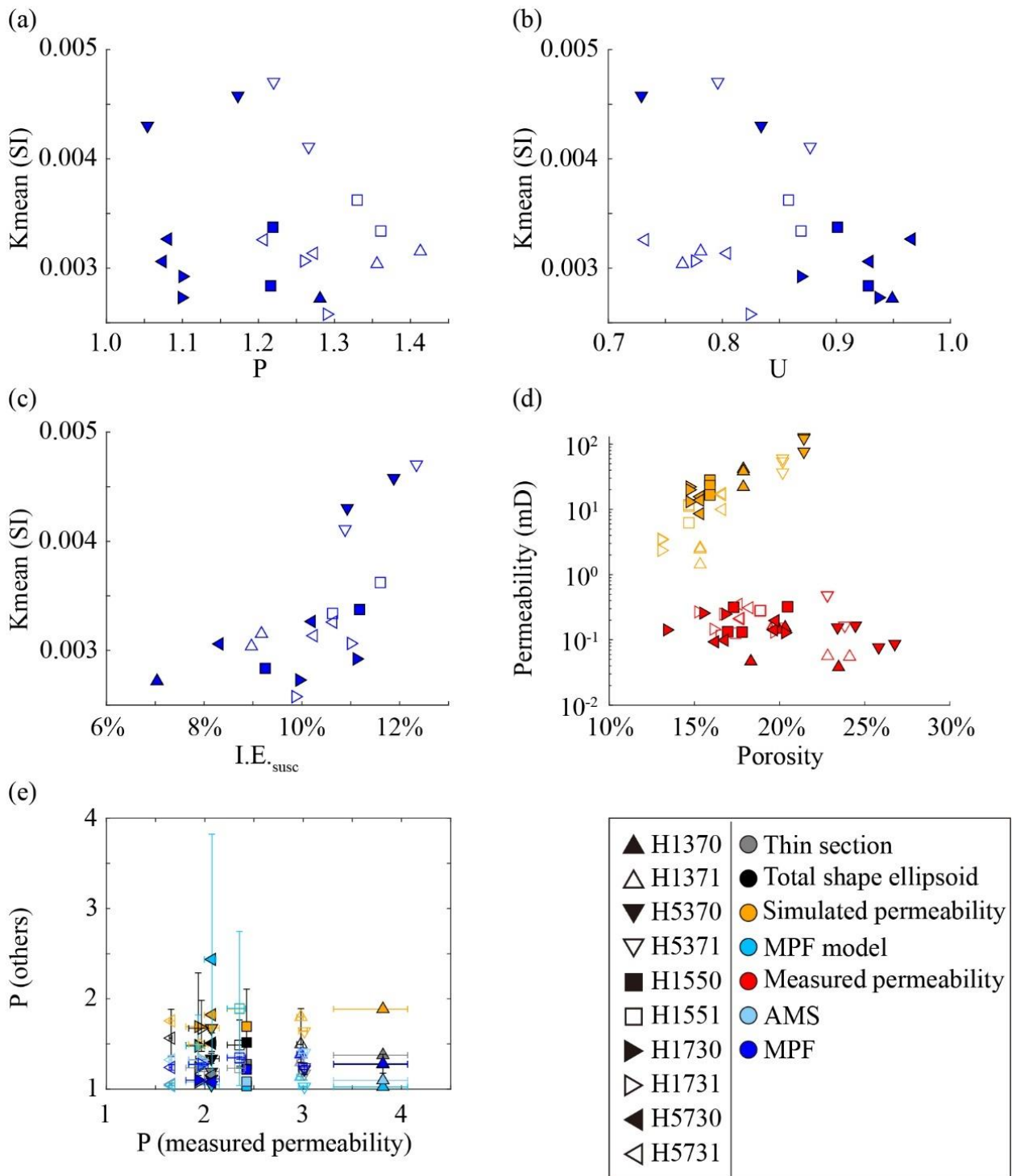


**Figure 5.8.** (a) Anisotropy degree of MPF ( $P$ ) vs mean susceptibility of MPF ( $k_{mean}$ ), (b) Anisotropy shape of MPF ( $U$ ) vs mean susceptibility of MPF ( $k_{mean}$ ), and (c) susceptibility-based impregnation efficiency ( $I.E._{susc}$ ) vs mean susceptibility of MPF ( $k_{mean}$ ). (d) Porosity VS permeability from laboratory measurements and simulation from XRCT data. (e) Comparison of anisotropy degree of measured permeability with pore fabrics derived by thin section, XRCT-derived data (total shape ellipsoids, simulated permeability, and MPF model), AMS and MPF.

#### 5.4. Discussion

Significant differences were observed in the measured porosity of different sampling cores for each sample (Figure 5.3). This may be due to the heterogeneous nature of the samples caused by uneven mixing of mineral powders with different grain sizes and shapes during the mixing process. It is also possible that cores taken near the ends of the cylinder sample ( $Z1$ ,  $Z2$  cores) are more

affected by high temperature and high pressure from the boundary, resulting in differences in porosity. To avoid boundary effects and large variations in porosity, cores for thin section, XRCT, and MPF analysis were taken near the central region of each sample.

It is observed that smaller grain sizes result in higher porosity (Figure 5.3). Microscopic observation of thin sections reveals that smaller grains exhibit greater roundness and smaller size variations, leading to more pore space between grains. In samples with larger grains, the presence of more irregular grains and greater size variations, along with tight contact and interstitial filling between grains, reduces the pore space (Figure 5.1). Additionally, higher muscovite content results in higher porosity because muscovite has a flaky grain shape, enlarging the interconnected pore space. XRCT-derived porosity approximates the measured porosity and porosity provided in literature for samples prepared using the same method (Schmidt et al., 2008), while porosities derived from thin sections and MPF are significantly smaller (Figure 5.3). This is primarily because the former uses air measurement, while the latter ones use more viscous fluids such as resin or ferrofluid for sample injection, making it more difficult for the fluid to penetrate into smaller pores, naturally resulting in the non-detection of a large number of micropores.

In the analysis of pore size distribution, XRCT data exhibits a narrower and steeper range compared to thin section data, primarily due to differences in resolution. Consequently, XRCT fails to detect numerous smaller pores. Moreover, whereas the majority of samples demonstrate linear distribution characteristics, samples H1370, H5370, and H5371 exhibit bimodal features. This occurrence is possibly attributed to some pores not resolved by XRCT resolution.

Simulated permeability exceeds measured permeability, which may be attributed to the limited ability of XRCT digital rock structures to fully replicate the physical properties of real rocks. For instance, the completely smooth surfaces of digital rock grains and the resolution limitations leading to only detection of numerous large pores rather than micro-pores and throats can collectively result in an overestimation of the simulated permeability. Moreover, compared to the conditions used for measuring permeability, the simulation used lower pressure and higher fluid viscosity, which would typically result in lower permeability values. Therefore, the difference in settings is not the primary reason for the simulated permeability being higher than the measured ones. Furthermore, the lack of a significant relationship between measured porosity and permeability may stem from the fact that, unlike porosity which is primarily influenced by pore space size, permeability is influenced by various factors including pore geometry, connectivity, distribution, and even pressure sensitivity (Bernabe et al., 2003; Hu et al., 2020; Šperl & Trčková, 2008; H. Wang et al., 2019; Wenlian et al., 2016; Worthington, 2008; Zheng et al., 2015; Zhong et al., 2020). Therefore, there isn't a universally applicable relationship between porosity and permeability.

The linear growth relationship between the mean susceptibility ( $k_{mean}$ ) of injected samples and their impregnation efficiency ( $I.E._{susc}$ ) primarily arises from the increased injection of ferrofluid, naturally resulting in greater magnetic susceptibility of the samples. However, the anisotropy degree and shape of the MPF are significantly influenced by pore fabrics, thereby rendering their relationship with  $k_{mean}$  less significant.

When comparing the anisotropy of various datasets, only the AMS and MPF of the samples are affected by the addition of magnetite. The strong magnetism of magnetite affects the measurement of the magnetic anisotropy. Therefore, the AMS and MPF of samples with added magnetite exhibit a higher anisotropy degree and slightly weakened oblate anisotropy shape (reduced  $U$  value).

Regarding mineral composition, muscovite with its sheet-like structure is more prone to forming

preferred direction of fluid flow along maximum direction of muscovite grain shape, compared to the irregularly shaped calcite particles (Figure 5.1). Consequently, measured permeability and MPF, obtained by injecting samples with argon or water-based ferrofluid, show a significant increase in anisotropy degree with increasing muscovite content. However, thin section analysis using more viscous resin and simulated permeability based on digital rock both present insignificant changes with varying muscovite content, probably due to the limitation by the viscosity of the injected fluid or the XRCT image resolution. Therefore, thin section and XRCT images can only capture relatively larger pores. When changes in the proportion of muscovite lead to variations in micro-pores, these changes are not reflected in the thin section and XRCT images. Nevertheless, all four datasets related to fluid flow characteristics exhibit a pronounced oblate anisotropy shape. XRCT-derived pore fabrics and MPF model solely based on XRCT-derived pore fabrics are not significantly affected by muscovite and do not exhibit consistent anisotropy shape. Meanwhile, the AMS of original sample shows a slight increase in anisotropy degree with increasing muscovite content, maintaining a consistent oblate anisotropy shape. This may be due to the presence of a small amount of magnetic impurities with muscovite, possibly like hematite. However, the magnetic susceptibility of the original sample is much smaller than those of the samples impregnated with ferrofluid, so magnetic impurities do not affect the MPF results. As the amount of sheet-like muscovite increases, the anisotropy degree of the grain fabrics and pore fabrics increases. Both the measured permeability and MPF significantly follow this trend for anisotropy degree because they can detect more micropores, whereas thin section and XRCT cannot due to fluid viscosity or resolution limitations.

Measured permeability exhibits the highest anisotropy degree, followed by simulated permeability, while the anisotropy degree of MPF model, AMS, and MPF are significantly lower than that of measured permeability (Figure 5.5e). This discrepancy may stem from the fact that magnetic anisotropy measurement and calculation are influenced by various factors such as the magnetic susceptibility of the ferrofluid used, pore shape, size, etc. (Biedermann, 2019, 2020; Biedermann et al., 2021; Jones et al., 2006).

Regarding anisotropy orientations, thin-section-derived pore fabrics, measured permeability anisotropy, MPF and block show significant directional consistency. This demonstrates that the fabric orientation is consistent across both macroscopic and microscopic scales. However, in four out of ten samples, XRCT-based pore fabrics, simulated permeability anisotropy, and MPF model are inconsistent with the former. This is because the preferred direction of connected pore fabrics does not always represent the optimal direction of fluid flow. Factors, such as pore tortuosity, pore and throat size distribution, can affect fluid flow direction (Cai et al., 2019; Geffen et al., 1951; Zhang, 2013). Also, resolution limitation for XRCT data may be another reason, resulting in undetected micropores. Therefore, thin section analysis, measured permeability, and MPF using fluid (i.e., resin, argon, ferrofluid) impregnation methods will produce relatively consistent anisotropy orientation, differing from digital pore fabrics and related simulation data. As grain size decreases and the proportion of muscovite decreases, more irregular calcite particles are present in the samples, leading to a significant reduction in the directional significance of permeability anisotropy. However, thin section analysis and MPF still exhibit significant anisotropic characteristics. This indicates that compared to gas (argon), which has lower viscosity and better flowability to access more micropores, more viscous resin and water will preferentially choose the dominant flow direction in large pores during sample injection, hence still displaying strong anisotropic features. The anisotropy orientation characteristics of AMS are similar to thin section analysis, measured permeability, and MPF, but AMS is mainly influenced by the magnetic susceptibility of grains, resulting in significant anisotropy orientation due to the oriented arrangement of mineral grains.

## **5.5. Conclusions**

The study uses hot isostatic pressing (HIP) to simulate the high-temperature, high-pressure conditions encountered during natural rock formation. Samples comprise common mineral components, calcite and muscovite. Irregular calcite grains exhibit insignificant anisotropy, whereas muscovite, with its sheet morphology, display anisotropy. Various proportions and grain sizes of muscovite and calcite were mixed to prepare rock samples with different anisotropic pore fabrics. The samples achieve a maximum connected porosity of 26.79 %, with porosity increasing as the proportion of muscovite increased. Addition of 1% magnetite to the samples significantly influences their AMS and MPF, resulting in increased anisotropy degree. However, magnetite has no effect on other pore fabric data and permeability anisotropy. The presence of sheet-like muscovite inhibits fluid flow perpendicular to its planes, creating enhanced anisotropic flow paths. Increasing muscovite ratio, anisotropy degree also increases notably in experiments involving measured permeability and MPF with low-viscosity fluids. Results from experiments injecting fluids, specifically thin-section-derived pore fabrics, measured permeability and MPF, show similar directional characteristics, with the minimum principal axes aligning along the sample compression axis and the maximum principal axes perpendicular to the sample compression axis. However, pore fabrics, simulated permeability, and MPF models based on XRCT digital rock show directional disparities in anisotropy among certain samples. Consequently, mineral grain shape and orientation, as well as stress direction, significantly influence the anisotropy of fluid flow in sample pores, while their impacts on pore structure anisotropy are not always consistent. Pore structure anisotropy does not always correlate with permeability anisotropy. Notably, there are significant quantitative correlations between sample MPF and permeability anisotropy in terms of anisotropy degree and orientation, consistently influenced by grain shape and stress direction. MPF effectively reflects anisotropy orientations and anisotropy degree changes of the sample fabrics. Therefore, MPF serves as a prerequisite experiment for measuring permeability anisotropy, allowing preliminary assessment of the fabric anisotropy and preferred flow direction, reducing the time and effort required for actual measurements, and enhancing experimental efficiency.

## **Acknowledgment**

Sandro Bula, University of Bern, are gratefully acknowledged for his assistance in sample preparation. Thank you to my colleague Philip Hartmeier for the discussions on XRCT image processing, and to my colleague Alejandro Prieto for his help with the experiments. The XRCT analysis in Bern was supported by the European Research Council (ERC) under the European Union's Horizon 2020 research and innovation program (grant agreement No. 850530 to PL). The Bruker Skyscan 2211 at the University of Fribourg was funded by R'Equip Swiss National Science Foundation grant 206021\_150731. This study was funded by the Swiss National Science Foundation, project 176917 (to ARB).

## 6. Conclusion and outlook

This thesis investigated anisotropy in porous media by cross-comparing thin section-derived pore fabrics, X-ray computed tomography (XRCT)-derived pore fabrics, simulated permeability and magnetic pore fabrics (MPF) based on XRCT data, permeability anisotropy, anisotropy of magnetic susceptibility (AMS), and MPF across a variety of sandstone, carbonate, and artificial samples. The study established quantitative relationships among these methods, utilizing six typical sandstones (Berea, Berea Spider, Bentheimer, Castlegate, Molasse, Salt Wash North), two carbonates (Calcarenite and Indiana Limestone), one artificial quartz sandstone bonded with liquid glass and manually compacted, and ten hot isostatic pressing (HIP) artificial rocks composed of irregular calcite and sheet-like muscovite mixtures. These HIP samples enabled testing the influence of mineral composition, grain size, and magnetism on anisotropy.

Key findings include consistent anisotropy orientations across most methods—Thin section-derived pore fabrics, XRCT-derived pore fabrics, simulated permeability and MPF based on XRCT data, permeability anisotropy, MPF and block fabrics—demonstrating unified anisotropy from macroscopic to microscopic scales. The maximum axes of these properties are perpendicular to the compaction direction, while the minimum axes align parallel to it. Exceptions occur in samples with the resolution limitations of XRCT or overly complex pore fabrics, leading to inconsistencies in XRCT-based data. However, MPF and permeability anisotropy maintain robustness, with MPF proving effective in predicting optimal fluid flow directions. Adding strongly magnetic minerals (e.g., 1% magnetite) increases the anisotropy degree of AMS and MPF without affecting other properties, while higher proportions of minerals with significantly anisotropic grain shapes (e.g., sheet-like muscovite) enhance the anisotropy degree of permeability and MPF. The degree of anisotropy typically follows the order: measured permeability > simulated permeability > XRCT-derived total shape ellipsoids > thin-section-derived total shape ellipsoids > AMS > MPF > MPF model. Anisotropy shapes show discrepancies between different determination methods.

This research provides a comprehensive framework for studying anisotropy in porous media, integrating multiple methods to enhance understanding of pore fabrics and fluid flow behavior. This framework is particularly valuable for applications in petroleum reservoir evaluation, geothermal system development, and groundwater management, where accurate anisotropy assessment can optimize resource extraction and management strategies. The MPF method stands out as a simple, efficient tool for rapidly assessing pore fabrics and optimal fluid flow directions, offering practical benefits in industrial settings by reducing measurement time and costs compared to traditional full-tensor permeability analyses. Additionally, the study's cross-comparison approach establishes a reference for future rock physics research, providing a methodological foundation that can be adapted to diverse geological contexts beyond the sandstones and carbonates tested here.

Despite its contributions, the study has several limitations and unresolved issues:

- Thin Section Analysis: Limited resolution may fail to detect micro-pores, and converting 2D data to 3D introduces potential errors, affecting the accuracy of pore fabric representation.
- XRCT Analysis: The trade-off between resolution and sample size restricts its ability to capture overall sample characteristics fully. Uncertainties in image segmentation, often due to manually selected thresholds, may further skew pore fabric and permeability predictions.
- MPF Method: Its effectiveness depends on ferrofluid selection (e.g., compatibility with rock wettability and mineral charge properties), which can influence impregnation efficiency. The impact of minerals with varying wettability and charge properties on ferrofluid behavior remains underexplored.

- **Cross-Calibration:** Discrepancies in anisotropy degree across methods may arise from inherent methodological limitations or sample heterogeneity, complicating direct comparisons.

The study's focus on relatively homogeneous, anisotropic sandstones and carbonates limits its generalizability. The applicability of MPF to rocks with low permeability (e.g., shales, tight carbonates), vesicular textures (e.g., volcanic rocks), or minimal anisotropy remains untested.

To address these limitations, future research should focus on the following:

- **Expanding Rock Types:** Test MPF's effectiveness across a broader range of rocks, including volcanic rocks, shales, tight carbonates, and samples with diverse mineral wettability and charge properties, to assess its versatility.
- **Improving XRCT Analysis:** Investigate the effects of resolution and segmentation uncertainties on total shape ellipsoids, potentially integrating advanced imaging techniques to enhance accuracy.
- **Leveraging AI Technology:** Utilize AI-based image processing to improve the recognition, segmentation and classification for pores and minerals in geological images, reducing manual errors and refining pore fabric characterization.

A recommended best-practice workflow for future anisotropy studies is as follows:

- **Initial MPF Assessment:** Use MPF to quickly evaluate pore fabrics and identify optimal fluid flow directions, leveraging its simplicity and efficiency.
- **Targeted Permeability Measurement:** Measure permeability along the identified optimal flow direction and its perpendicular direction to calculate accurate permeability anisotropy, minimizing the need for full-tensor measurements in six directions.

This workflow reduces time and cost compared to comprehensive permeability tensor analyses while providing more precise fabric information than visual observations on hand-sample or outcrop scale, mitigating risks of under- or overestimating anisotropy. By combining MPF's rapid assessment with selective permeability measurements, researchers can streamline anisotropy studies while maintaining accuracy, offering a practical approach for both academic and industrial applications.

## 7. Supplementary material

**Supplementary material for Article I: Quantitative comparison of 3D pore space properties with magnetic pore fabrics—testing the ability of magnetic methods to predict pore fabrics in rocks**

### Contents of this file

Text S3.1

Figures S3.1 to S3.2

Tables S3.1 to S3.4

### Additional Supporting Information (Files uploaded separately)

Captions for Tables S3.4

### Introduction

The supporting information is about mathematic description for calculating pore shape (Text S3.1), an example for segmentation of pore and solid fraction by watershed algorithm (Figure S3.1), comparisons of XRCT-derived pore fabrics in three perpendicular samples from the same block (Figure S3.2), initial settings for XRCT and MPF measurements (Table S3.1, S3.2), definition of subscripts (Table S3.3), and initial data for MPF (Table S3.4). They are mainly about principles and settings for experiments and data analysis to supply the manuscript.

In table S4, sample D1121Z has anomalies with >100% impregnation efficiency and higher MPF-derived porosity than He-porosity, probably because the magnetic fluid on the sample surface was not entirely eliminated. This anomaly may also result from inhomogeneous fluid, and the uncertainty in the determination of fluid susceptibility/frequency dependence, because of the time-dependent nature of fluid properties.

### Text S3.1.

All texts below are modified from Avizo 2020.1 user's guide.

The first order moments define the centroid or center of mass.

$$M_{1x} = \frac{1}{A(X)} \int_X x dx dy dz, M_{1y} = \frac{1}{A(X)} \int_X y dx dy dz \text{ and } M_{1z} = \frac{1}{A(X)} \int_X z dx dy dz$$

$A(X)$  is the area and  $(x, y, z)$  is a point in the object.

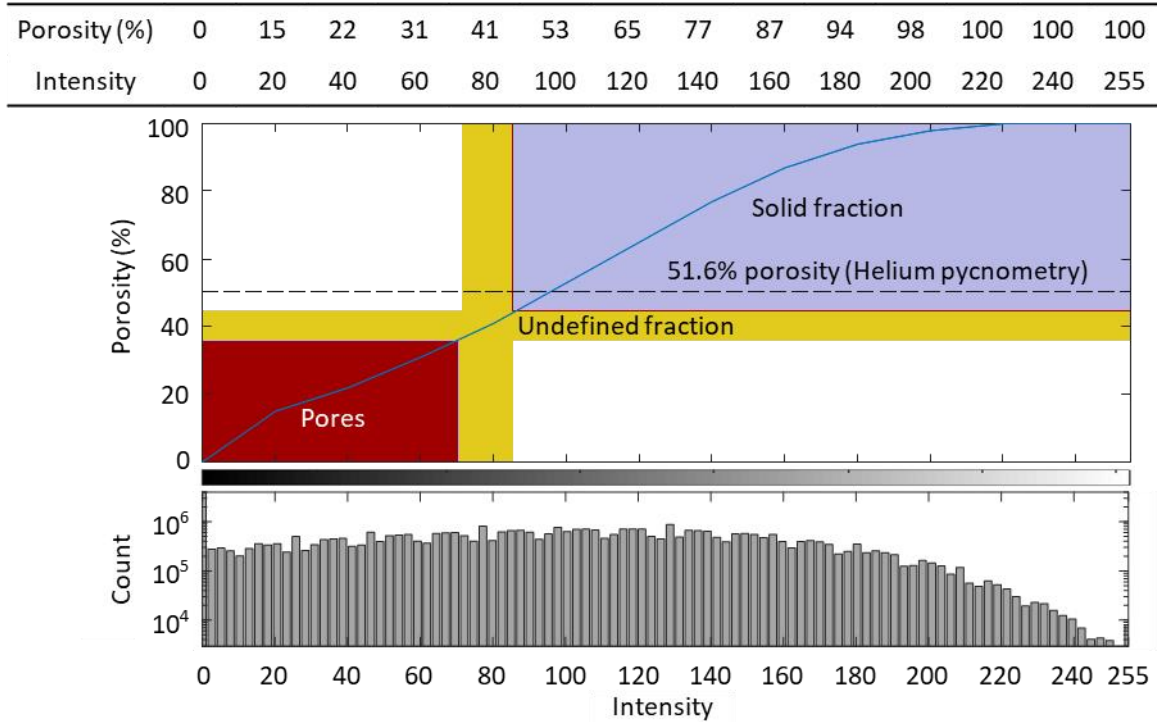
The second order moments are defined as:

$$\begin{aligned} M_{2x} &= \frac{1}{A(X)} \int_X (x - M_{1x})^2 dx dy dz \\ M_{2y} &= \frac{1}{A(X)} \int_X (y - M_{1y})^2 dx dy dz \\ M_{2z} &= \frac{1}{A(X)} \int_X (z - M_{1z})^2 dx dy dz \\ M_{2xy} &= \frac{1}{A(X)} \int_X (x - M_{1x})(y - M_{1y}) dx dy dz \\ M_{2xz} &= \frac{1}{A(X)} \int_X (x - M_{1x})(z - M_{1z}) dx dy dz \\ M_{2yz} &= \frac{1}{A(X)} \int_X (y - M_{1y})(z - M_{1z}) dx dy dz \end{aligned}$$

The orientations are given as the eigenvectors of the inertia matrix:

$$M = \begin{bmatrix} M_{2x} & M_{2xy} & M_{2xz} \\ M_{2xy} & M_{2y} & M_{2yz} \\ M_{2xz} & M_{2yz} & M_{2z} \end{bmatrix}$$

(a)



(b)

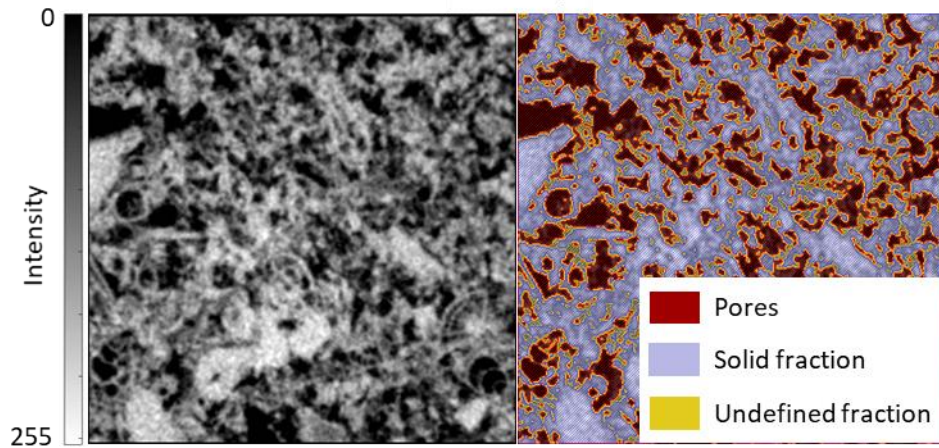


**Figure S3.1.** (a) Single thresholding-related variability of XRCT-derived porosity of sample MI-2-Y3. The blue curve is a cumulative curve for porosity. (b) Segmentation of pores versus solid fraction based on XRCT data of sample MI-2-Y3. 0-73 of the intensity greyscale value is clearly identified as pores and 85-255 is clearly identified as solid fraction. The remaining part (73-85) is undefined and was assigned to a fraction based on hierarchical watershed segmentation.

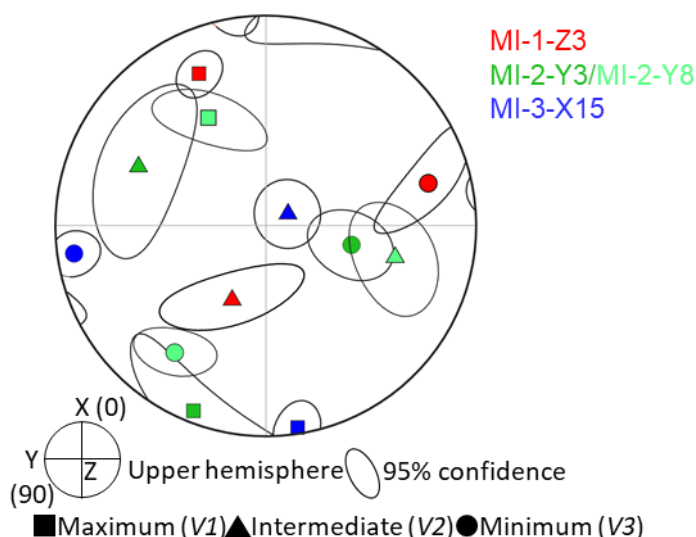


**Figure S3.2.** Comparison of total shape ellipsoids calculated from perpendicularly drilled calcarenite samples, MI-1-Z3, MI-2-Y3, MI-2-Y8 and MI-3-X15. All datasets were rotated to a common coordinate system.

**Table S3.1.** Analytical settings for XRCT scans of all samples. Scans with 15  $\mu\text{m}$  pixel size were conducted with the Bruker Skyscan 2211, those with 9  $\mu\text{m}$  or 5.5  $\mu\text{m}$  pixel size with the Bruker Skyscan 1273.

Sample	Pixel size ( $\mu\text{m}$ )	Filter	Voltage (kV)	Current ( $\mu\text{A}$ )	Exposure time (ms)
Calcarenite					
MI-1-Z3	15	0.5 mm Al	80	230	220
MI-2-Y3	15	0.5 mm Al	80	230	220
MI-2-Y8	9	1 mm Al+0.038 mm Cu	100	80	275
MI-3-X15	15	0.5 mm Al	80	230	220
MI-5-Z21	9	1 mm Al+0.038 mm Cu	100	80	275
MI-5-X22	9	1 mm Al+0.038 mm Cu	100	80	275
Molasse (Rüeggisberg)					
D1121Z	15	0.5mm Ti	100	445	100
D1112Y	15	0.5mm Ti	100	445	100
D1112Y	9	1 mm Al+0.038 mm Cu	100	80	275
D1263Y2	9	1 mm Al+0.038 mm Cu	100	80	275
D1234X	15	0.5mm Mo	110	220	300
Molasse (Entlebuch)					
C43Y	15	0.5mm Cu	150	245	125
C334Y	15	0.5mm Cu	156	200	127
C334Y	9	1 mm Al+0.038 mm Cu	100	80	275
BE42AY	15	0.5mm Cu	156	210	130
Molasse (Düdingen)					
5256X	9	1 mm Al+0.038 mm Cu	100	80	275
Molasse (Tafers)					
F31Z1	5.5	1 mm Al+0.038 mm Cu	100	80	275

**Table S3.2.** Ferrofluid and MPF measurement settings. All samples were impregnated with EMG909 oil-based ferrofluid.

Sample	Volume ratio of ferrofluid and dilution	Impregnation method	Frequency (kHz)	Field (A/m)
Calcarenite				
MI-1-Z3	1:25 with oil	100 kPa vacuum for 24 hours	~4, ~16, ~512	80
MI-2-Y3	1:25 with oil	100 kPa vacuum for 24 hours	~4, ~16, ~512	80
MI-2-Y8	1:30 with hardener and resin	100 kPa vacuum for 1 hour	~1	200
MI-2-Y10	1:50 with hardener and resin	100 kPa vacuum for 1 hour	~1	200
MI-3-X15	1:25 with oil	100 kPa vacuum for 24 hours	Sample broken	
MI-3-X11	1:50 with hardener and resin	100 kPa vacuum for 1 hour	~1, ~4, ~16	200
Mi-5-Z21	1:30 with hardener and resin	100 kPa vacuum for 1 hour	~1	200
MI-5-X22	1:30 with hardener and resin	100 kPa vacuum for 1 hour	~1	200
Molasse (Rüeggisberg)				
D1121Z	1:50 with hardener and resin	100 kPa vacuum for 1 hour	~1, ~4, ~16	200
D1112Y	1:50 with hardener and resin	100 kPa vacuum for 1 hour	~1	200
D1263Y2	1:30 with hardener and resin	100 kPa vacuum for 1 hour	~1	200
D1234X	1:50 with hardener and resin	100 kPa vacuum for 1 hour	~1, ~4, ~16	200
D1221X	1:50 with hardener and resin	100 kPa vacuum for 1 hour	~1	200
D1261X	1:30 with hardener and resin	100 kPa vacuum for 1 hour	~1	200
Molasse (Entlebuch)				
C43Y	1:50 with hardener and resin	100 kPa vacuum for 1 hour	~1, ~4, ~16	200
C334Y	1:30 with hardener and resin	100 kPa vacuum for 1 hour	~1	200
BE42AY	1:50 with hardener and resin	100 kPa vacuum for 1 hour	~1, ~4, ~16	200
Molasse (Düdingen)				
5256X	1:50 with hardener and resin	100 kPa vacuum for 1 hour	Sample broken	
Molasse (Tafers)				
F31Z1	1:50 with hardener and resin	100 kPa vacuum for 1 hour	~1	200

**Table S3.3.** Definition of subscripts used in text and figures.

---

Subscript	Definition
s	variable describing pore shape
s-individual	variable describing individual pore shape
s-total	variable describing total shape ellipsoid
m	variable describing magnetic data
m-MPF	variable describing magnetic pore fabric
susc	variable describing magnetic susceptibility

---

**Additional Supporting Information (Files uploaded separately)**

**Table S3.4.** MPF data for all samples measured in different frequency. There are the mean magnetic susceptibility ( $k_{mean}$ ), the susceptibility of three principle directions ( $k_1, k_2, k_3$ ) with their declinations and inclinations ( $D_1, I_1, D_2, I_2, D_3, I_3$ ), confidence angle ( $E_{13}, E_{12}, E_{23}$ ), anisotropy degree and shape ( $P, U$ ), and He porosity for each sample. For calculating susceptibility-based impregnation efficiency ( $I.E._{susc}$ ) and MPF-derived porosity by comparing susceptibilities between samples and ferrofluid (Parés et al., 2016), the ferrofluid type, dilution ratio and effective susceptibility of diluted ferrofluid ( $k_{fluid}$ ) are added to the table. Due to frequency dependence, there is a correction coefficient used to correct magnetic susceptibility measured in different frequency. The frequency-dependence correction coefficient is cited from Biedermann et al. (2021).

Table is in the separate file Table S3.4.xls. Check <https://doi.org/10.5281/zenodo.12750089>.

## References

- Adams, A. L., Germaine, J. T., Flemings, P. B., & Day-Stirrat, R. J. (2013). Stress induced permeability anisotropy of Resedimented Boston Blue Clay. *Water Resources Research*, 49(10), 6561–6571. <https://doi.org/10.1002/wrcr.20470>
- Adams, A. L., Nordquist, T. J., Germaine, J. T., & Flemings, P. B. (2016). Permeability anisotropy and resistivity anisotropy of mechanically compressed mudrocks. *Canadian Geotechnical Journal*, 53(9), 1474–1482. <https://doi.org/10.1139/cgj-2015-0596>
- Adams, M. M., & Bhattacharya, J. P. (2005). No change in fluvial style across a sequence boundary, Cretaceous Blackhawk and Castlegate Formations of central Utah, USA, 1038–1051. <https://doi.org/10.2110/jsr.2005.080>
- Alabi, G., Kasten, R., Chitale, V., Yadavalli, S., & Piccoli, L. (2014). The Value of Petrophysical Measurements Across Multiple Scales—A Lacustrine Carbonate Example From Campos Basin, Brazil. In *SPWLA Annual Logging Symposium* (p. SPWLA-2014). SPWLA. <https://onepetro.org/SPWLAALS/proceedings-abstract/SPWLA14/All-SPWLA14/28444>
- Al-Azani, K., Al-Yousef, H., & Mahmoud, M. (2019). Effect of Permeability Anisotropy on Probe Permeameter Measurements. In *SPE Middle East Oil and Gas Show and Conference*. <https://doi.org/10.2118/194769-MS>
- Al-Azani, K., El-Husseiny, A., Mahmoud, M., Al-Yousef, H., & Elsayed, M. (2021). Numerical and Experimental Study to Determine the Permeability Anisotropy in Porous Rocks from Probe Permeameter Measurements. *Arabian Journal for Science and Engineering*, 46(7), 7019–7030. <https://doi.org/10.1007/s13369-021-05433-w>
- Al-Dujaili, A. N., Shabani, M., & AL-Jawad, M. S. (2021). Identification of the best correlations of permeability anisotropy for Mishrif reservoir in West Qurna/1 oil Field, Southern Iraq. *Egyptian Journal of Petroleum*, 30(3), 27–33. <https://doi.org/10.1016/j.ejpe.2021.06.001>
- Aliyu, M. D., & Chen, H. P. (2018). Enhanced geothermal system modelling with multiple pore media: Thermo-hydraulic coupled processes. *Energy*. <https://doi.org/10.1016/j.energy.2018.09.129>
- Almqvist, B. S. G., Mainprice, D., Madonna, C., Burlini, L., & Hirt, A. M. (2011). Application of differential effective medium, magnetic pore fabric analysis, and X-ray microtomography to calculate elastic properties of porous and anisotropic rock aggregates. *Journal of Geophysical Research: Solid Earth*, 116(1), 1–17. <https://doi.org/10.1029/2010JB007750>
- Andrä, H., Combaret, N., Dvorkin, J., Glatt, E., Han, J., Kabel, M., et al. (2013a). Digital rock physics benchmarks-Part I: Imaging and segmentation. *Computers and Geosciences*, 50, 25–32. <https://doi.org/10.1016/j.cageo.2012.09.005>
- Andrä, H., Combaret, N., Dvorkin, J., Glatt, E., Han, J., Kabel, M., et al. (2013b). Digital rock physics benchmarks-part II: Computing effective properties. *Computers and Geosciences*, 50, 33–43. <https://doi.org/10.1016/j.cageo.2012.09.008>
- Andriani, G. F., & Walsh, N. (2002). Physical properties and textural parameters of calcarenitic rocks: Qualitative and quantitative evaluations. *Engineering Geology*. [https://doi.org/10.1016/S0013-7952\(02\)00106-0](https://doi.org/10.1016/S0013-7952(02)00106-0)
- Anselmetti, F. S., Luthi, S., & Eberli, G. P. (1998). Quantitative Characterization of Carbonate Pore Systems by Digital Image Analysis1. *AAPG Bulletin*, 82(10), 1815–1836. <https://boris.unibe.ch/id/eprint/87075>
- Armitage, P. J., Faulkner, D. R., Worden, R. H., Aplin, A. C., Butcher, A. R., & Iliffe, J. (2011). Experimental measurement of, and controls on, permeability and permeability anisotropy of caprocks from the CO<sub>2</sub> storage project at the Krechba Field, Algeria. *Journal of Geophysical Research: Solid Earth*, 116(12), 1–18. <https://doi.org/10.1029/2011JB008385>
- Auradou, H., Drazer, G., Hulin, J. P., & Koplik, J. (2005). Permeability anisotropy induced by the shear displacement of rough fracture walls. *Water Resources Research*, 41(9), 1–10. <https://doi.org/10.1029/2005WR003938>
- Avizo. (2020). Avizo 2020.1 user's guide.

- Ayan, C., Colley, N., Cowan, G., Ezekwe, E., Wannell, M., Goode, P., et al. (1994). Measuring permeability anisotropy: the latest approach. *Oilfield Review*, 6(4). <https://www.osti.gov/etdeweb/biblio/6780551>
- Baas, J. H., Hailwood, E. A., McCaffrey, W. D., Kay, M., & Jones, R. (2007). Directional petrological characterisation of deep-marine sandstones using grain fabric and permeability anisotropy: Methodologies, theory, application and suggestions for integration. *Earth-Science Reviews*, 82(1–2), 101–142. <https://doi.org/10.1016/j.earscirev.2007.02.003>
- Benson, P. M., Meredith, P. G., & Platzman, E. S. (2003). Relating pore fabric geometry to acoustic and permeability anisotropy in Crab Orchard Sandstone: A laboratory study using magnetic ferrofluid. *Geophysical Research Letters*, 30(19), 1–4. <https://doi.org/10.1029/2003GL017929>
- Benson, P. M., Meredith, P. G., Platzman, E. S., & White, R. E. (2005). Pore fabric shape anisotropy in porous sandstones and its relation to elastic wave velocity and permeability anisotropy under hydrostatic pressure. *International Journal of Rock Mechanics and Mining Sciences*. <https://doi.org/10.1016/j.ijrmms.2005.05.003>
- Berger, A., & Herwegh, M. (2004). Grain coarsening in contact metamorphic carbonates: Effects of second-phase particles, fluid flow and thermal perturbations. *Journal of Metamorphic Geology*, 22(5), 459–474. <https://doi.org/10.1111/j.1525-1314.2004.00526.x>
- Bernabe, Y., & Brace, W. (1985). Deformation and fracture of Berea sandstone. *Geophysical Monograph*, 56. <https://doi.org/10.1029/GM056p0091>
- Bernabe, Y., Mok, U., & Evans, B. (2003). Permeability-porosity relationships in rocks subjected to various evolution processes. *Pure and Applied Geophysics*, 160(5–6), 937–960. <https://doi.org/10.1007/PL00012574>
- Bernabe, Y., Mok, U., & Evans, B. (2006). A note on the oscillating flow method for measuring rock permeability. *International Journal of Rock Mechanics and Mining Sciences*, 43(2), 311–316. <https://doi.org/10.1016/j.ijrmms.2005.04.013>
- Bernabe, Y., Brace, W. F., & Evans, B. (1982). Permeability, porosity and pore geometry of hot-pressed calcite. *Mechanics of Materials*, 1(3), 173–183. [https://doi.org/10.1016/0167-6636\(82\)90010-2](https://doi.org/10.1016/0167-6636(82)90010-2)
- Bernard, S., Brown, L., Wirth, R., Schreiber, A., Schulz, H.-M., Horsfield, B., et al. (2013). FIB-SEM and TEM investigations of an organic-rich shale maturation series from the Lower Toarcian Posidonia Shale, Germany: Nanoscale pore system and fluid-rock interactions. <https://doi.org/10.1306/13391705M1023583>
- Bhandari, A. R., Flemings, P. B., Polito, P. J., Cronin, M. B., & Bryant, S. L. (2015). Anisotropy and Stress Dependence of Permeability in the Barnett Shale. *Transport in Porous Media*, 108(2), 393–411. <https://doi.org/10.1007/s11242-015-0482-0>
- Biedermann, A. R. (2019). Magnetic Pore Fabrics: The Role of Shape and Distribution Anisotropy in Defining the Magnetic Anisotropy of Ferrofluid-Impregnated Samples. *Geochemistry, Geophysics, Geosystems*. <https://doi.org/10.1029/2019GC008563>
- Biedermann, A. R. (2020). FinIrrSDA: A 3-D model for magnetic shape and distribution anisotropy of finite irregular arrangements of particles with different sizes, geometries, and orientations. *Journal of Geophysical Research: Solid Earth*, 125(12), e2020JB020300. <https://doi.org/10.1029/2020JB020300>
- Biedermann, A. R., Lowrie, W., & Hirt, A. M. (2013). A method for improving the measurement of low-field magnetic susceptibility anisotropy in weak samples. *Journal of Applied Geophysics*. <https://doi.org/10.1016/j.jappgeo.2012.10.008>
- Biedermann, A. R., Pugnetti, M., & Zhou, Y. (2021). Explaining the large variability in empirical relationships between magnetic pore fabrics and pore space properties. *Geophysical Journal International*, 227(1), 496–517. <https://doi.org/10.1093/gji/ggab230>
- Bieniek, A., & Moga, A. (2000). An efficient watershed algorithm based on connected components. *Pattern Recognition*. [https://doi.org/10.1016/S0031-3203\(99\)00154-5](https://doi.org/10.1016/S0031-3203(99)00154-5)

- Bosak, T., Souza-Egipsy, V., Corsetti, F. A., & Newman, D. K. (2004). Micrometer-scale porosity as a biosignature in carbonate crusts. *Geology*, 32(9), 781–784. <https://doi.org/10.1130/G20681.1>
- Bultreys, T., De Boever, W., & Cnudde, V. (2016). Imaging and image-based fluid transport modeling at the pore scale in geological materials: A practical introduction to the current state-of-the-art. *Earth-Science Reviews*, 155, 93–128. <https://doi.org/10.1016/j.earscirev.2016.02.001>
- Cabrera, D., & Samaniego, F. (2021). Experimental Permeability Tensor for Fractured Carbonate Rocks. *Rock Mechanics and Rock Engineering*, 54(3), 1171–1191. <https://doi.org/10.1007/s00603-020-02323-9>
- Cai, J., Zhang, Z., Wei, W., Guo, D., Li, S., & Zhao, P. (2019). The critical factors for permeability-formation factor relation in reservoir rocks: Pore-throat ratio, tortuosity and connectivity. *Energy*, 188, 116051. <https://doi.org/10.1016/j.energy.2019.116051>
- Caristan, Y., Harpin, R. J., & Evans, B. (1981). Deformation of porous aggregates of calcite and quartz using the isostatic hot-pressing technique. *Tectonophysics*, 78(1–4), 629–650. [https://doi.org/10.1016/0040-1951\(81\)90033-0](https://doi.org/10.1016/0040-1951(81)90033-0)
- Chelle-Michou, C., Do Couto, D., Moscariello, A., Renard, P., & Rusillon, E. (2017). Geothermal state of the deep Western Alpine Molasse Basin, France-Switzerland. *Geothermics*. <https://doi.org/10.1016/j.geothermics.2017.01.004>
- Chen, F., Zheng, Q., Ding, X., Lu, S., & Zhao, H. (2020). Pore size distributions contributed by OM, clay and other minerals in over-mature marine shale: A case study of the Longmaxi shale from Southeast Chongqing, China. *Marine and Petroleum Geology*. <https://doi.org/10.1016/j.marpetgeo.2020.104679>
- Chen, Y., Nishiyama, T., Kusuda, H., Kita, H., & Sato, T. (1999). Correlation between microcrack distribution patterns and granitic rock splitting planes. *International Journal of Rock Mechanics and Mining Sciences*, 36(4), 535–541. [https://doi.org/https://doi.org/10.1016/S0148-9062\(99\)00014-5](https://doi.org/https://doi.org/10.1016/S0148-9062(99)00014-5)
- Chen, Y., Nishiyama, T., Terada, M., & Iwamoto, Y. (2000). A fluorescent approach to the identification of grout injected into fissures and pore spaces. *Engineering Geology*, 56(3), 395–401. [https://doi.org/https://doi.org/10.1016/S0013-7952\(99\)00100-3](https://doi.org/https://doi.org/10.1016/S0013-7952(99)00100-3)
- Cheng, P., Besthorn, M., & Firoozabadi, A. (2012). Erratum: Effect of permeability anisotropy on buoyancy-driven flow for CO<sub>2</sub> sequestration in saline aquifers (Water Resources Research (2012) 48 (W09539) DOI: 10.1029/2012WR011939). *Water Resources Research*, 48(10), 1–5. <https://doi.org/10.1029/2012WR013094>
- Chesley, J. T., & Leier, A. L. (2018). Sandstone-body variability in the medial–distal part of an ancient distributive fluvial system, salt wash member of the Morrison Formation, Utah, USA, (May), 568–582. <https://doi.org/10.2110/jsr.2018.32>
- Chevalier, G., Diamond, L. W., & Leu, W. (2010). Potential for deep geological sequestration of CO<sub>2</sub> in Switzerland: A first appraisal. *Swiss Journal of Geosciences*, 103(3), 427–455. <https://doi.org/10.1007/s00015-010-0030-4>
- Chitale, V., Alabi, G., Kasten, R., Taylor, A., & Hoenmans, P. (2014). Learning from deployment of a variety of modern petrophysical formation evaluation technologies and techniques for characterization of a Pre-Salt carbonate reservoir: Case study from Campos Basin, Brazil. In *SPWLA Annual Logging Symposium* (p. SPWLA-2014). SPWLA. <https://onepetro.org/SPWLAALS/proceedings-abstract/SPWLA14/All-SPWLA14/28402>
- Churcher, P. L., French, P. R., Shaw, J. C., & Schramm, L. L. (1991). Rock Properties of Berea Sandstone, Baker Dolomite, and Indiana Limestone. *Society of Petroleum Engineers*. <https://doi.org/10.2118/21044-MS>
- Ciantia, M. O., Castellanza, R., Crosta, G. B., & Hueckel, T. (2015). Effects of mineral suspension and dissolution on strength and compressibility of soft carbonate rocks. *Engineering Geology*, 184, 1–18. <https://doi.org/10.1016/j.enggeo.2014.10.024>

- Clark, D. A. (2014). Methods for determining remanent and total magnetisations of magnetic sources - A review. *Exploration Geophysics*, 45(4), 271–304. <https://doi.org/10.1071/EG14013>
- Clavaud, J. B., Maineult, A., Zamora, M., Rasolofosaon, P., & Schlitter, C. (2008). Permeability anisotropy and its relations with porous medium structure. *Journal of Geophysical Research: Solid Earth*, 113(1), 1–10. <https://doi.org/10.1029/2007JB005004>
- Clennell, M. B., Dewhurst, D. N., Brown, K. M., & Westbrook, G. K. (1999). Permeability anisotropy of consolidated clays. *Geological Society Special Publication*, 158, 79–96. <https://doi.org/10.1144/GSL.SP.1999.158.01.07>
- Cnudde, V., Boone, M., Dewanckele, J., Dierick, M., Van Hoorebeke, L., & Jacobs, P. (2011). 3D characterization of sandstone by means of X-ray computed tomography. *Geosphere*, 7(1), 54–61. <https://doi.org/10.1130/GES00563.1>
- Cnudde, V., & Boone, M. N. (2013). High-resolution X-ray computed tomography in geosciences: A review of the current technology and applications. *Earth-Science Reviews*, 123, 1–17. <https://doi.org/10.1016/j.earscirev.2013.04.003>
- Constable, C., & Tauxe, L. (1990). The bootstrap for magnetic susceptibility tensors. *Journal of Geophysical Research*. <https://doi.org/10.1029/JB095iB06p08383>
- Coulson, C. A., & Nye, J. F. (1958). Physical Properties of Crystals. *The Mathematical Gazette*. <https://doi.org/10.2307/3610487>
- Dai, S., Kim, J., Xu, Y., Waite, W. F., Jang, J., Yoneda, J., et al. (2019). Permeability anisotropy and relative permeability in sediments from the National Gas Hydrate Program Expedition 02, offshore India. *Marine and Petroleum Geology*, 108(March 2018), 705–713. <https://doi.org/10.1016/j.marpetgeo.2018.08.016>
- da Silva, Í. B. (2018). X-ray Computed Microtomography technique applied for cementitious materials: A review. *Micron*, 107(January), 1–8. <https://doi.org/10.1016/j.micron.2018.01.006>
- Dautriat, J., Gland, N., Guelard, J., Dimanov, A., & Raphanel, J. L. (2009). Axial and radial permeability evolutions of compressed sandstones: End effects and shear-band induced permeability anisotropy. *Pure and Applied Geophysics*, 166(5–7), 1037–1061. <https://doi.org/10.1007/s00024-009-0495-0>
- David, C., Robion, P., & Louis, L. (2017). A single laboratory setup for investigating the anisotropy of both seismic and electrical properties in core samples. *Geophysical Journal International*, 210(3), 1595–1608. <https://doi.org/10.1093/gji/ggx248>
- De Boever, W., Derluyn, H., Van Loo, D., Van Hoorebeke, L., & Cnudde, V. (2015). Data-fusion of high resolution X-ray CT, SEM and EDS for 3D and pseudo-3D chemical and structural characterization of sandstone. *Micron*. <https://doi.org/10.1016/j.micron.2015.04.003>
- De Boever, E., Foubert, A., Oligschlaeger, D., Claes, S., Soete, J., Bertier, P., et al. (2016). Multiscale approach to (micro) porosity quantification in continental spring carbonate facies: Case study from the Cakmak quarry (Denizli, Turkey). *Geochemistry, Geophysics, Geosystems*, 17(7), 2922–2939. <https://doi.org/10.1002/2016GC006382>
- Devarapalli, R. S., Islam, A., Faisal, T. F., Sassi, M., & Jouiad, M. (2017). Micro-CT and FIB–SEM imaging and pore structure characterization of dolomite rock at multiple scales. *Arabian Journal of Geosciences*, 10, 1–12. <https://doi.org/10.1007/s12517-017-3120-z>
- Dewhurst, D. N., Brown, K. M., Clennell, M. B., & Westbrook, G. K. (1996). A comparison of the fabric and permeability anisotropy of consolidated and sheared silty clay. *Engineering Geology*, 42(4), 253–267. [https://doi.org/10.1016/0013-7952\(95\)00089-5](https://doi.org/10.1016/0013-7952(95)00089-5)
- Dicker, A. I., & Smits, R. M. (1988). A practical approach for determining permeability from laboratory pressure-pulse decay measurements. In *SPE International Oil and Gas Conference and Exhibition in China* (p. SPE-17578). SPE. <https://doi.org/10.2118/17578-MS>
- Digiovanni, A. A., Fredrich, J. T., Holcomb, D. J., & Olsson, W. A. (2007). Microscale damage evolution in compacting sandstone. *Geological Society*, 289, 89–103.

<https://doi.org/10.1144/SP289.6>

- Donnalioia, M., Giachetta, E., Capolongo, D., & Pennetta, L. (2019). Evolution of fluviokarst canyons in response to the Quaternary tectonic uplift of the Apulia Carbonate Platform (southern Italy): Insights from morphometric analysis of drainage basins. *Geomorphology*. <https://doi.org/10.1016/j.geomorph.2019.03.008>
- Dubelaar, C. W., & Nijland, T. (2015). The Bentheim Sandstone: geology, petrophysics, varieties and its use as dimension stone, *8*, 557–563. <https://doi.org/10.1007/978-3-319-09408-3>
- Dullien, F. A. L. (1979). Porous media: fluid transport and pore structure. *Academic press*.
- Elkhoury, J. E., Niemeijer, A., Brodsky, E. E., & Marone, C. (2011). Laboratory observations of permeability enhancement by fluid pressure oscillation of in situ fractured rock. *Journal of Geophysical Research: Solid Earth*, *116*(B2). <https://doi.org/10.1029/2010JB007759>
- El-Maghraby, R. M., & Blunt, M. J. (2013). Residual CO<sub>2</sub> trapping in Indiana limestone. *Environmental Science & Technology*, *47*(1), 227–233. <https://doi.org/10.1021/es304166u>
- Esteban, L., Géraud, Y., & Bouchez, J. L. (2006). Pore network geometry in low permeability argillites from magnetic fabric data and oriented mercury injections. *Geophysical Research Letters*. <https://doi.org/10.1029/2006GL026908>
- Farquharson, J. I., Heap, M. J., Lavallée, Y., Varley, N. R., & Baud, P. (2016). Evidence for the development of permeability anisotropy in lava domes and volcanic conduits. *Journal of Volcanology and Geothermal Research*, *323*, 163–185. <https://doi.org/10.1016/j.jvolgeores.2016.05.007>
- Farrell, N. J. C., Healy, D., & Taylor, C. W. (2014). Anisotropy of permeability in faulted porous sandstones. *Journal of Structural Geology*, *63*, 50–67. <https://doi.org/10.1016/j.jsg.2014.02.008>
- Feser, M., Gelb, J., Chang, H., Cui, H., Duewer, F., Lau, S. H., et al. (2008). Sub-micron resolution CT for failure analysis and process development. *Measurement Science and Technology*, *19*(9). <https://doi.org/10.1088/0957-0233/19/9/094001>
- Frosch, G. P., Tillich, J. E., Haselmeier, R., Holz, M., & Althaus, E. (2000). Probing the pore space of geothermal reservoir sandstones by Nuclear Magnetic Resonance. *Geothermics*. [https://doi.org/10.1016/S0375-6505\(00\)00031-6](https://doi.org/10.1016/S0375-6505(00)00031-6)
- Gamal, H., Elkatatny, S., & Abdulraheem, A. (2020). Effect of the Filtrate Fluid of Water-Based Mud on Sandstone Rock Strength and Elastic Moduli. <https://doi.org/10.1021/acsomega.0c05067>
- Gamal, H., Elkatatny, S., & Adebayo, A. (2021). Influence of mud filtrate on the pore system of different sandstone rocks. *Journal of Petroleum Science and Engineering*, *202*(October 2020), 108595. <https://doi.org/10.1016/j.petrol.2021.108595>
- Gao, Z., & Hu, Q. (2018). Pore structure and spontaneous imbibition characteristics of marine and continental shales in China. *AAPG Bulletin*. <https://doi.org/10.1306/03291817297>
- Garefalakis, P., & Schlunegger, F. (2019). Tectonic processes, variations in sediment flux, and eustatic sea level recorded by the 20 Myr old Burdigalian transgression in the Swiss Molasse basin. *Solid Earth*, *10*(6), 2045–2072. <https://doi.org/10.5194/se-10-2045-2019>
- Garum, M., Glover, P. W. J., Lorinczi, P., Drummond-Brydson, R., & Hassanpour, A. (2020). Micro-and nano-scale pore structure in gas shale using X $\mu$ -CT and FIB-SEM techniques. *Energy & Fuels*, *34*(10), 12340–12353. <https://doi.org/10.1021/acs.energyfuels.0c02025>
- Geffen, T. M., Owens, W. W., Parrish, D. R., & Morse, R. A. (1951). Experimental investigation of factors affecting laboratory relative permeability measurements. *Journal of Petroleum Technology*, *3*(04), 99–110. <https://doi.org/10.2118/951099-G>
- Gehne, S., & Benson, P. M. (2017). Permeability and permeability anisotropy in Crab Orchard sandstone: Experimental insights into spatio-temporal effects. *Tectonophysics*, *712–713*, 589–599. <https://doi.org/10.1016/j.tecto.2017.06.014>
- Gelb, J., Feser, M., Tkachuk, A., Hsu, G., Chen, S., Chang, H., et al. (2009). Sub-micron X-ray computed tomography for non-destructive 3D visualization and analysis. *Microscopy and*

- Microanalysis*, 15(SUPPL. 2), 618–619. <https://doi.org/10.1017/S1431927609093623>
- Georgi, D., Bespalov, A., Tabarovsky, L., & Schoen, J. (2002). On the Relationship between Resistivity and Permeability Anisotropy. *Proceedings - SPE Annual Technical Conference and Exhibition*, 3277–3290. <https://doi.org/10.2523/77715-ms>
- Gostick, J. T. (2017). Versatile and efficient pore network extraction method using marker-based watershed segmentation. *Physical Review E*. <https://doi.org/10.1103/PhysRevE.96.023307>
- Goupil, M., Heap, M. J., & Baud, P. (2022). Permeability anisotropy in sandstones from the Soultz-sous-Forêts geothermal reservoir (France): implications for large-scale fluid flow modelling. *Geothermal Energy*, 10(1), 32. <https://doi.org/10.1186/s40517-022-00243-1>
- Guo, B. (2019). Well Productivity Handbook (Second Edi, pp. 17–51). Gulf Professional Publishing. <https://doi.org/https://doi.org/10.1016/C2018-0-03220-X>
- Gustafsson, M. G. L. (2000). Surpassing the lateral resolution limit by a factor of two using structured illumination microscopy. *Journal of Microscopy*. <https://doi.org/10.1046/j.1365-2818.2000.00710.x>
- Hailwood, E. A., Bowen, D., Ding, F., Corbett, P. W. M., & Whattler, P. (1999). Characterizing pore fabrics in sediments by anisotropy of magnetic susceptibility analyses. *Geological Society, London, Special Publications*, 151(1), 125–126. <https://doi.org/10.1144/GSL.SP.1999.151.01.12>
- Hakami, E. (1995). *Aperture distribution of rock fractures*. Sweden. Retrieved from [http://inis.iaea.org/search/search.aspx?orig\\_q=RN:27020199](http://inis.iaea.org/search/search.aspx?orig_q=RN:27020199)
- Hart, D. J., & Wang, H. F. (1995). Laboratory measurements of a complete set of proelastic moduli for Berea sandstone and Indiana limestone, 100(95), 741–751. <https://doi.org/10.1029/95JB01242>
- Hassan, S. F., Kamireddy, S., Yutkin, M. P., Radke, C. J., & Patzek, T. W. (2019). Adsorption of charged surfactants onto calcium carbonate. In *IOR 2019–20th European Symposium on Improved Oil Recovery* (Vol. 2019, pp. 1–19). European Association of Geoscientists & Engineers. <https://doi.org/10.3997/2214-4609.201900169>
- Heilbronner, R., & Barrett, S. (2013). *Image Analysis in Earth Sciences. Microstructures and Textures of Earth Materials*. <https://doi.org/10.1007/978-3-642-10343-8>
- Heilbronner, R., & Bruhn, D. (1998). The influence of three-dimensional grain size distributions on the rheology of polyphase rocks. *Journal of Structural Geology*, 20(6), 695–705. [https://doi.org/10.1016/S0191-8141\(98\)00010-8](https://doi.org/10.1016/S0191-8141(98)00010-8)
- Heintzmann, R., & Ficz, G. (2013). Breaking the resolution limit in light microscopy. *Methods in Cell Biology*, 114(4), 525–544. <https://doi.org/10.1016/B978-0-12-407761-4.00022-1>
- Hext, G. R. (1963). The Estimation of Second-Order Tensors, with Related Tests and Designs. *Biometrika*. <https://doi.org/10.2307/2333905>
- Holzer, L., Münch, B., Iwanschitz, B., Cantoni, M., Hocker, T., & Graule, T. (2011). Quantitative relationships between composition, particle size, triple phase boundary length and surface area in nickel-cermet anodes for Solid Oxide Fuel Cells. *Journal of Power Sources*, 196(17), 7076–7089. <https://doi.org/10.1016/j.jpowsour.2010.08.006>
- Hong, B., Li, X. an, Wang, L., & Li, L. cui. (2019). Temporal variation in the permeability anisotropy behavior of the Malan loess in northern Shaanxi Province, China: an experimental study. *Environmental Earth Sciences*, 78(15). <https://doi.org/10.1007/s12665-019-8449-z>
- Hrouda, F., Hanak, J., & Terzijski, I. (2000). The magnetic and pore fabrics of extruded and pressed ceramic models. *Geophysical Journal International*. <https://doi.org/10.1046/j.1365-246X.2000.00216.x>
- Humbert, F., Robion, P., Louis, L., Bartier, D., Ledésert, B., & Song, S. R. (2012). Magnetic inference of in situ open microcracks in sandstone samples from the Taiwan Chelungpu Fault Drilling Project (TCDP). *Journal of Asian Earth Sciences*. <https://doi.org/10.1016/j.jseaes.2011.10.009>
- Hu, Z., Klaver, J., Schmatz, J., Dewanckele, J., Littke, R., Krooss, B. M., & Amann-Hildenbrand,

- A. (2020). Stress sensitivity of porosity and permeability of Cobourg limestone. *Engineering Geology*, 273, 105632. <https://doi.org/10.1016/j.enggeo.2020.105632>
- Ingham, J. P. (2010). *Geomaterials Under the Microscope: A Colour Guide*. *Geomaterials Under the Microscope*. <https://doi.org/10.1201/b15140>
- Ingraham, M. D., Issen, K. A., & Holcomb, D. J. (2013). Response of Castlegate sandstone to true triaxial states of stress, 118(November 2012), 536–552. <https://doi.org/10.1002/jgrb.50084>
- Ismail, M. I. Al, Hol, S., Reece, J. S., & Zoback, M. D. (2014). The Effect of CO<sub>2</sub> Adsorption on Permeability Anisotropy in the Eagle Ford Shale. In *SPE/AAPG/SEG Unconventional Resources Technology Conference, Denver, Colorado, USA*. <https://doi.org/10.15530/URTEC-2014-1921520>
- Iverson, W. P., Dunn, T. L., & Ajdari, I. (1996). Relative Permeability Anisotropy Measurements in Tensleep Sandstones. In *SPE/DOE Improved Oil Recovery Symposium*. <https://doi.org/https://doi.org/10.2118/35435-MS>
- Jelinek, V. (1977). The statistical theory of measuring anisotropy of magnetic susceptibility of rocks and its application. *Brno, Czech Republic: Geofyzika*, Vol. 29, pp. 1-87. chrome-extension://efaidnbmnnnibpcajpcgclefindmkaj/http://www.agico.cz/downloads/documents/agicoprints/statistical\_theory.pdf
- Jelinek, V. (1981). Characterization of the magnetic fabric of rocks. *Tectonophysics*. [https://doi.org/10.1016/0040-1951\(81\)90110-4](https://doi.org/10.1016/0040-1951(81)90110-4)
- Jelinek, V. (1996). Measuring Anisotropy of Magnetic Susceptibility on a Slowly Spinning Specimen—Basic Theory. In *AGICO print* (Vol. 10, p. 27). <https://www.agico.cz/text/support/agicoprints/agicoprints.php>
- Jelínek, V., & Kropáček, V. (1978). Statistical processing of anisotropy of magnetic susceptibility measured on groups of specimens. *Studia Geophysica et Geodaetica*. <https://doi.org/10.1007/BF01613632>
- Jezek, J., & Hrouda, F. (2007). A program for magnetic susceptibility-equivalent pore conversion. *Geochemistry, Geophysics, Geosystems*. <https://doi.org/10.1029/2007GC001709>
- Jia, R., Lei, H., Hino, T., & Li, K. (2022). Changes in the Permeability and Permeability Anisotropy of Reconstituted Clays under One-Dimensional Compression and the Corresponding Micromechanisms. *International Journal of Geomechanics*, 22(2). [https://doi.org/10.1061/\(ASCE\)GM.1943-5622.000226](https://doi.org/10.1061/(ASCE)GM.1943-5622.000226)
- Jiang, T., Yao, W., Sun, X., Qi, C., Li, X., Xia, K., et al. (2021). Evolution of anisotropic permeability of fractured sandstones subjected to true-triaxial stresses during reservoir depletion. *Journal of Petroleum Science and Engineering*, 200, 108251. <https://doi.org/https://doi.org/10.1016/j.petrol.2020.108251>
- Jones, S. C. (1997). A technique for faster pulse-decay permeability measurements in tight rocks. *SPE Formation Evaluation*, 12(01), 19–25. <https://doi.org/10.2118/28450-PA>
- Jones, S., Benson, P., & Meredith, P. (2006). Pore fabric anisotropy: Testing the equivalent pore concept using magnetic measurements on synthetic voids of known geometry. *Geophysical Journal International*, 166(1), 485–492. <https://doi.org/10.1111/j.1365-246X.2006.03021.x>
- Karimpouli, S., & Tahmasebi, P. (2019). Segmentation of digital rock images using deep convolutional autoencoder networks. *Computers and Geosciences*. <https://doi.org/10.1016/j.cageo.2019.02.003>
- Kawano, S., Katayama, I., & Okazaki, K. (2011). Permeability anisotropy of serpentinite and fluid pathways in a subduction zone. *Geology*, 39(10), 939–942. <https://doi.org/10.1130/G32173.1>
- Kemper, E. (1976). Geologischer Führer durch die Grafschaft Bentheim und die angrenzenden Gebiete mit einem Abriss der emsländischen Unterkreide. *Bentheim: Verlag Heimatverein Der Grafschaft Bentheim*, 206. <https://library.wur.nl/WebQuery/titel/178883>
- Khan, M. ;, & Teufel, L. W. (2000). The effect of geological and geomechanical parameters on reservoir stress path and its importance in studying permeability anisotropy. *SPE Reservoir Evaluation and Engineering*, 3(5), 394–400. <https://doi.org/10.2118/66184-PA>

- Kibria, M. G., Hu, Q., Liu, H., Zhang, Y., & Kang, J. (2018). Pore structure, wettability, and spontaneous imbibition of Woodford Shale, Permian Basin, West Texas. *Marine and Petroleum Geology*, *91*, 735–748. <https://doi.org/10.1016/j.marpetgeo.2018.02.001>
- Kocurek, Inc. (2022a). Details for Bentheimer Sandstone. Retrieved from <https://kocurekindustries.com/our-products/bentheimer-sandstone>
- Kocurek, Inc. (2022b). Details for Castlegate Sandstone. Retrieved from <https://kocurekindustries.com/our-products/castlegate-sandstone>
- Kocurek, Inc. (2022c). Details for Spider Berea Sandstone. Retrieved from <https://kocurekindustries.com/our-products/berea-spider>
- Kohl, T., Schill, E., & Baujard, C. (2010). *Integrative Geothermal Resource Assessment of the Swiss Molasse Basin. Proceedings World Geothermal Congress*. chrome-extension://efaidnbmnnnibpcajpcglclefindmkaj/<https://www.geothermal-energy.org/pdf/IGAstandard/WGC/2010/1637.pdf>
- Kuila, U., & Prasad, M. (2013). Application of nitrogen gas-adsorption technique for characterization of pore structure of mudrocks. *The Leading Edge*, *32*(12), 1478–1485. <https://doi.org/10.1190/tle32121478.1>
- Lai, J., Wang, G., Wang, Z., Chen, J., Pang, X., Wang, S., et al. (2018). A review on pore structure characterization in tight sandstones. *Earth-Science Reviews*. <https://doi.org/10.1016/j.earscirev.2017.12.003>
- Landis, E. N., & Keane, D. T. (2010). X-ray microtomography. *Materials Characterization*, *61*(12), 1305–1316. <https://doi.org/10.1016/j.matchar.2010.09.012>
- Leroueil, S., Bouclin, G., Tavenas, F., Bergeron, L., & Rochelle, and P. La. (1990). Permeability anisotropy of natural clays as a function of strain. *Canadian Geotechnical Journal*. <https://doi.org/10.1139/t90-072>
- Liang, Y., Wang, S., Feng, Q., Zhang, M., Cao, X., & Wang, X. (2024). Ultrahigh-resolution reconstruction of shale digital rocks from FIB-SEM images using deep learning. *SPE J.*, *29*(3), 1434–1450. <https://doi.org/10.2118/218397-PA>
- Li, C., Wang, S., You, Q., & Yu, C. (2021). A New Measurement of Anisotropic Relative Permeability and Its Application in Numerical Simulation. *Energies*, *14*(16). <https://doi.org/10.3390/en14164731>
- Liu, L., & Buckley, J. S. (1999). Alteration of wetting of mica surfaces. *Journal of Petroleum Science and Engineering*, *24*(2–4), 75–83. [https://doi.org/10.1016/S0920-4105\(99\)00050-9](https://doi.org/10.1016/S0920-4105(99)00050-9)
- Lou, Z., Wang, K., Zang, J., Zhao, W., Qin, B., & Kan, T. (2021). Effects of permeability anisotropy on coal mine methane drainage performance. *Journal of Natural Gas Science and Engineering*, *86*, 103733. <https://doi.org/https://doi.org/10.1016/j.jngse.2020.103733>
- Louis, L., David, C., Metz, V., Robion, P., Menéndez, B., & Kissel, C. (2005). Microstructural control on the anisotropy of elastic and transport properties in undeformed sandstones. *International Journal of Rock Mechanics and Mining Sciences*. <https://doi.org/10.1016/j.ijrmms.2005.05.004>
- Louis, L., Robion, P., & David, C. (2004). A single method for the inversion of anisotropic data sets with application to structural studies. *Journal of Structural Geology*, *26*(11), 2065–2072. <https://doi.org/10.1016/j.jsg.2004.03.005>
- Lu, J., Wang, T., Cheng, W., Yang, T., & Luo, Y. (2019). Permeability Anisotropy of Loess under Influence of Dry Density and Freeze–Thaw Cycles. *International Journal of Geomechanics*, *19*(9). [https://doi.org/10.1061/\(ASCE\)GM.1943-5622.0001485](https://doi.org/10.1061/(ASCE)GM.1943-5622.0001485)
- Madadi, M., & Varslot, T. K. (2009). Digital rock physics: 3D imaging of core material and correlations to acoustic and flow properties, (January). <https://doi.org/10.1190/1.3064143>
- Madonna, C., Almqvist, B. S. G., & Saenger, E. H. (2012). ultrasonic velocities using micro-CT imaging, 1475–1482. <https://doi.org/10.1111/j.1365-246X.2012.05437.x>
- Malkovsky, V. I., Zharikov, A. V., & Shmonov, V. M. (2009). New methods for measuring the permeability of rock samples for a single-phase fluid. *Izvestiya, Physics of the Solid Earth*,

- 45, 89–100. <https://doi.org/10.1134/S1069351309020013>
- Marszałek, M., Alexandrowicz, Z., & Rzepa, G. (2014). Composition of weathering crusts on sandstones from natural outcrops and architectonic elements in an urban environment. *Environmental Science and Pollution Research*. <https://doi.org/10.1007/s11356-014-3312-y>
- Mavris, C., Götze, J., Plötze, M., & Egli, M. (2012). Weathering and mineralogical evolution in a high Alpine soil chronosequence: A combined approach using SEM-EDX, cathodoluminescence and Nomarski DIC microscopy. *Sedimentary Geology*. <https://doi.org/10.1016/j.sedgeo.2012.04.008>
- Mclaurin, B. T., & Steel, R. J. (2007). Architecture and origin of an amalgamated fluvial sheet sand, lower Castlegate Formation, Book Cliffs, Utah, 197, 291–311. <https://doi.org/10.1016/j.sedgeo.2006.10.005>
- Mehmani, A., Verma, R., & Prodanović, M. (2020). Pore-scale modeling of carbonates. *Marine and Petroleum Geology*. Elsevier Ltd. <https://doi.org/10.1016/j.marpetgeo.2019.104141>
- Metwally, Y. M., & Sondergeld, C. H. (2011). Measuring low permeabilities of gas-sands and shales using a pressure transmission technique. *International Journal of Rock Mechanics and Mining Sciences*, 48(7), 1135–1144. <https://doi.org/10.1016/j.ijrmms.2011.08.004>
- Meyer, R. (2002). Anisotropy of sandstone permeability. *CREWES Reaserch Report*, 14, 1–12. <chrome-extension://efaidnbmnnnibpcajpcglclefindmkaj/https://www.crewes.org/Documents/ResearchReports/2002/2002-05.pdf>
- Meyer, R., & Krause, F. F. (2006). Permeability anisotropy and heterogeneity of a sandstone reservoir analogue: An estuarine to shoreface depositional system in the Virgelle Member, Milk River Formation, Writing-on-Stone Provincial Park, southern Alberta. *Bulletin of Canadian Petroleum Geology*, 54(4), 301–318. <https://doi.org/10.2113/gscpgbull.54.4.301>
- Misra, S., & Burg, J. P. (2012). Mechanics of kink-bands during torsion deformation of muscovite aggregate. *Tectonophysics*, 548–549, 22–33. <https://doi.org/10.1016/j.tecto.2012.04.014>
- Mokhtari, M., Alqahtani, A. A., Tutuncu, A. N., & Yin, X. (2013). Stress-dependent permeability anisotropy and wettability of shale resources. *Unconventional Resources Technology Conference 2013, URTC 2013*, 2713–2728. <https://doi.org/10.1190/urtec2013-283>
- Monicard, R. P. (1980). Properties of Reservoir Rocks: Core Analysis (pp. 7–42). Springer, Dordrecht. <https://doi.org/https://doi.org/10.1007/978-94-017-5016-5>
- Montoto, M., Montoto, L., Roshoff, K., & Leijon, B. (1981). MICROFRACTOGRAPHIC STUDY OF HEATED AND NON-HEATED STRIPA GRANITE. In M. BERGMAN (Ed.), *Subsurface Space* (pp. 1357–1368). Pergamon. <https://doi.org/https://doi.org/10.1016/B978-1-4832-8421-7.50204-0>
- Nabawy, B. S. (2018). Impacts of fossil anisotropy on the electric and permeability anisotropy of highly fossiliferous limestone: a case study. *Marine Geophysical Research*, 39(4), 537–550. <https://doi.org/10.1007/s11001-017-9335-2>
- Nabawy, B. S., Rochette, P., & Géraud, Y. (2009). Petrophysical and magnetic pore network anisotropy of some cretaceous sandstone from Tushka Basin, Egypt. *Geophysical Journal International*. <https://doi.org/10.1111/j.1365-246X.2008.04061.x>
- Nishiyama, T., & Kusuda, H. (1994). Identification of pore spaces and microcracks using fluorescent resins. *International Journal of Rock Mechanics and Mining Sciences & Geomechanics Abstracts*, 31(4), 369–375. [https://doi.org/https://doi.org/10.1016/0148-9062\(94\)90904-0](https://doi.org/https://doi.org/10.1016/0148-9062(94)90904-0)
- Nishiyama, T., & Kusuda, H. (1996). Application of a fluorescent technique to the study of the weathering process. *Engineering Geology*, 43(4), 247–253. [https://doi.org/https://doi.org/10.1016/S0013-7952\(96\)00034-8](https://doi.org/https://doi.org/10.1016/S0013-7952(96)00034-8)
- Nordquist, T. J. (2015). *Permeability anisotropy of resedimented mudrocks*. Massachusetts Institute of Technology. <http://hdl.handle.net/1721.1/99578>
- Okazaki, K., Katayama, I., & Noda, H. (2013). Shear-induced permeability anisotropy of simulated serpentinite gouge produced by triaxial deformation experiments. *Geophysical*

- Research Letters*, 40(7), 1290–1294. <https://doi.org/10.1002/grl.50302>
- O’Kelly, B. (2007). Compressibility and Permeability Anisotropy of Some Peat Soils. *Proceedings of the 60th Canadian Geotechnical Conference, Ottawa, Ontario, 21st-23rd October*, 7. <chrome-extension://efaidnbnmnibpcjpcglclefindmkaj/https://citeseerx.ist.psu.edu/document?repid=rep1&type=pdf&doi=18b3b31c03660d76dc613c44fcb4a60cd5a365f0>
- Olgaard, D. L., & Evans, B. (1988). Grain growth in synthetic marbles with added mica and water, 246–260. <https://doi.org/10.1007/BF00373591>
- Olgaard, D. L., & Evans, B. (1986). Effect of Second-Phase Particles on Grain Growth in Calcite. *Journal of the American Ceramic Society*, 69(11), C-272-C-277. <https://doi.org/10.1111/j.1151-2916.1986.tb07374.x>
- Øren, P., & Bakke, S. (2003). Reconstruction of Berea sandstone and pore-scale modelling of wettability effects. *Journal of Petroleum Science and Engineering*. [https://doi.org/10.1016/S0920-4105\(03\)00062-7](https://doi.org/10.1016/S0920-4105(03)00062-7)
- Oryem, M., Castellanza, R., Crosta, G. B., & Hueckel, T. (2015). Effects of mineral suspension and dissolution on strength and compressibility of soft carbonate rocks. *Engineering Geology*, 184, 1–18. <https://doi.org/10.1016/j.enggeo.2014.10.024>
- Osborn, J. A. (1945). Demagnetizing Factors of the General Ellipsoid. *Physical Review*, 67(11-12), 351. <https://doi.org/10.1103/PhysRev.67.351>
- Owen, A., Nichols, G. J., Hartley, A. J., Weissmann, G. S., & Scuderi, L. A. (2015). Quantification of a distributive fluvial system: the Salt Wash DFS of the Morrison Formation, SW USA. *Journal of Sedimentary Research*, 85(5), 544-561. <https://doi.org/10.2110/jsr.2015.35>
- Owen, A., Nichols, G. J., Hartley, A. J., & Weissmann, G. S. (2017). Vertical trends within the prograding Salt Wash distributive fluvial system, SW United States. *Basin Research*, 29(1), 64–80. <https://doi.org/10.1111/bre.12165>
- Owens, W. H. (2000). Statistical applications to second-rank tensors in magnetic fabric analysis. *Geophysical Journal International*. <https://doi.org/10.1046/j.1365-246X.2000.00174.x>
- Pan, Z., Ma, Y., Connell, L. D., Down, D. I., & Camilleri, M. (2015). Measuring anisotropic permeability using a cubic shale sample in a triaxial cell. *Journal of Natural Gas Science and Engineering*, 26, 336–344. <https://doi.org/10.1016/j.jngse.2015.05.036>
- Panja, P., McLennan, J., & Green, S. (2021). Influence of permeability anisotropy and layering on geothermal battery energy storage. *Geothermics*, 90 (July 2020), 101998. <https://doi.org/10.1016/j.geothermics.2020.101998>
- Parés, J. M., Miguens, L., & Saiz, C. (2016). Characterizing pore fabric in sandstones with magnetic anisotropy methods: Initial results. *Journal of Petroleum Science and Engineering*, 143, 113–120. <https://doi.org/10.1016/j.petrol.2016.02.028>
- Pec, M., & Al Nasser, S. (2021). Formation of Nanocrystalline and Amorphous Materials Causes Parallel Brittle-Viscous Flow of Crustal Rocks: Experiments on Quartz-Feldspar Aggregates. *Journal of Geophysical Research: Solid Earth*, 126(5), 1–26. <https://doi.org/10.1029/2020JB021262>
- Peffer, J., O’Callaghan, A., & Pop, J. (1997). In-Situ Determination of Permeability Anisotropy and its Vertical Distribution - A Case Study. In *SPE Annual Technical Conference and Exhibition, San Antonio, Texas*. <https://doi.org/10.2118/38942-MS>
- Pei, X., Liu, Y., Xue, L., Song, L., & Rang, T. (2023). A new determination method for the anisotropic permeability tensor based on the passive differential pressure ratio. *International Communications in Heat and Mass Transfer*, 140, 106544. <https://doi.org/10.1016/j.icheatmasstransfer.2022.106544>
- Peksa, A. E., Wolf, K. A. A., & Zitha, P. L. J. (2015). Bentheimer sandstone revisited for experimental purposes. *Marine and Petroleum Geology*, 67, 701–719. <https://doi.org/10.1016/j.marpetgeo.2015.06.001>
- Persson, A.-L. (1998). Image analysis of shape and size of fine aggregates. *Engineering Geology*, 50(1), 177–186. [https://doi.org/10.1016/S0013-7952\(98\)00009-X](https://doi.org/10.1016/S0013-7952(98)00009-X)

- Petri, B., Almqvist, B. S. G., & Pistone, M. (2020). 3D rock fabric analysis using microtomography: An introduction to the open-source TomoFab MATLAB code. *Computers and Geosciences*, 138. <https://doi.org/10.1016/j.cageo.2020.104444>
- Pfleiderer, S., & Halls, H. C. (1990). Magnetic susceptibility anisotropy of rocks saturated with ferrofluid: a new method to study pore fabric? *Physics of the Earth and Planetary Interiors*, 65(1–2), 158–164. [https://doi.org/10.1016/0031-9201\(90\)90083-A](https://doi.org/10.1016/0031-9201(90)90083-A)
- Pfleiderer, S., & Halls, H. C. (1993). Magnetic pore fabric analysis: verification through image autocorrelation. *Journal of Geophysical Research*, 98(B3), 4311–4316. <https://doi.org/10.1029/92JB01851>
- Pfleiderer, S., & Halls, H. C. (1994). Magnetic pore fabric analysis: a rapid method for estimating permeability anisotropy. *Geophysical Journal International*, 116(1), 39–45. <https://doi.org/10.1111/j.1365-246X.1994.tb02125.x>
- Pini, R., & Madonna, C. (2016). Moving across scales: a quantitative assessment of X-ray CT to measure the porosity of rocks. *Journal of Porous Materials*, 23(2), 325–338. <https://doi.org/10.1007/s10934-015-0085-8>
- Polesel, A., Ramponi, G., & Mathews, V. J. (2000). Image enhancement via adaptive unsharp masking. *IEEE Transactions on Image Processing*. <https://doi.org/10.1109/83.826787>
- Post, A., & Tullis, J. (1999). A recrystallized grain size piezometer for experimentally deformed feldspar aggregates. *Tectonophysics*, 303(1–4), 159–173. [https://doi.org/10.1016/S0040-1951\(98\)00260-1](https://doi.org/10.1016/S0040-1951(98)00260-1)
- Prasad, M., & Nur, A. (2003). Velocity and attenuation anisotropy in reservoir rocks. In *SEG International Exposition and Annual Meeting* (p. SEG-2003). SEG. <https://onepetro.org/SEGAM/proceedings-abstract/SEG03/All-SEG03/90842>
- Prats, M. (1972). The Influence of Oriented Arrays of Thin Impermeable Shale Lenses or of Highly Conductive Natural Fractures on Apparent Permeability Anisotropy. *Journal of Petroleum Technology*. <https://doi.org/https://doi.org/10.2118/4163-PA>
- Prévosteau, J. M., Caye, R., Ragot, J. P., & Pierrot, R. (1970). Méthodes de visualisation des milieux poreux en vue de leur analyse quantitative au microscope. *Bulletin de Minéralogie*, 571–578. Retrieved from [https://www.persee.fr/doc/bulmi\\_0037-9328\\_1970\\_num\\_93\\_5\\_6515](https://www.persee.fr/doc/bulmi_0037-9328_1970_num_93_5_6515)
- Příkryl, R. (2015). Fluorescent microscopy of stained thin sections: A direct tool for the evaluation of pore space characteristics in porous rocks. In *Engineering Geology for Society and Territory - Volume 8: Preservation of Cultural Heritage* (pp. 539–542). Springer International Publishing. [https://doi.org/10.1007/978-3-319-09408-3\\_96](https://doi.org/10.1007/978-3-319-09408-3_96)
- Příkryl, R., & Kou, S. (1996). *Fracture caused by indentation in cracked granitoids. Forskningsrapport / Högskolan i Luleå 1 jan 1974 → 31 dec 1996*. Luleå: Luleå tekniska universitet. Retrieved from <http://urn.kb.se/resolve?urn=urn:nbn:se:ltu:diva-22422>
- Pugnetti, M., Zhou, Y., & Biedermann, A. R. (2021). Experimental improvements for ferrofluid impregnation of rocks using directional forced impregnation methods: results on natural and synthetic samples. Retrieved from <https://doi.org/10.5194/egusphere-egu21-14695>
- Pugnetti, M., Zhou Y., & Biedermann, A. R. (2022). Ferrofluid impregnation efficiency and its spatial variability in natural and synthetic porous media: Implications for magnetic pore fabric studies. *Transport in Porous Media*, 144(2), 367–400. <https://doi.org/10.1007/s11242-022-01809-0>
- Rasolofosaon, P. N. J., & Zinszner, B. E. (2002). Comparison between permeability anisotropy and elasticity anisotropy of reservoir rocks. *Geophysics*, 67(1), 230–240. <https://doi.org/10.1190/1.1451647>
- Reed, S. J. B. (2005). Electron microprobe analysis and scanning electron microscopy in geology. <https://doi.org/10.1017/CBO9780511610561>
- Robinson, J. W., & McCabe, P. J. (1997). Sandstone-Body and Shale-Body Dimensions in a Braided Fluvial System: Salt Wash Sandstone Member (Morrison Formation), Garfield

- County, Utah 1, *AAPG bulletin*, 81(8), 1267-1291. <https://doi.org/10.1306/522B4DD9-1727-11D7-8645000102C1865D>
- Robion, P., David, C., Dautriat, J., Colombier, J. C., Zinsmeister, L., & Collin, P. Y. (2014). Pore fabric geometry inferred from magnetic and acoustic anisotropies in rocks with various mineralogy, permeability and porosity. *Tectonophysics*, 629(C), 109–122. <https://doi.org/10.1109/TITS.2015.2426955>
- Ronchi, P., & Cruciani, F. (2015). Continental carbonates as a hydrocarbon reservoir, an analog case study from the travertine of Saturnia, Italy. *AAPG Bulletin*, 99(4), 711–734. <https://doi.org/10.1306/10021414026>
- Rutter, E. H., & Brodie, K. H. (2004a). Experimental grain size-sensitive flow of hot-pressed Brazilian quartz aggregates. *Journal of Structural Geology*, 26(11), 2011–2023. <https://doi.org/10.1016/j.jsg.2004.04.006>
- Rutter, E. H., & Brodie, K. H. (2004b). Experimental intracrystalline plastic flow in hot-pressed synthetic quartzite prepared from Brazilian quartz crystals. *Journal of Structural Geology*, 26(2), 259–270. [https://doi.org/10.1016/S0191-8141\(03\)00096-8](https://doi.org/10.1016/S0191-8141(03)00096-8)
- Rybach, L. (2019). Geothermal potential of sedimentary basins, especially of the Swiss molasse basin. *Foldtani Kozlony*, 149(3), 401–414. <https://doi.org/10.23928/foldt.kozl.2019.149.4.401>
- Rybacki, E., & Dresen, G. (2000). Dislocation and diffusion creep of synthetic anorthite aggregates. *Journal of Geophysical Research: Solid Earth*, 105(B11), 26017–26036. <https://doi.org/10.1029/2000jb900223>
- Rybacki, E., Wirth, R., & Dresen, G. (2008). High-strain creep of feldspar rocks: Implications for cavitation and ductile failure in the lower crust. *Geophysical Research Letters*, 35(4), 1–5. <https://doi.org/10.1029/2007GL032478>
- Rybacki, E., Wirth, R., & Dresen, G. (2010). Superplasticity and ductile fracture of synthetic feldspar deformed to large strain. *Journal of Geophysical Research: Solid Earth*, 115(8), 1–14. <https://doi.org/10.1029/2009JB007203>
- Sato, M., & Ishii, Y. (1989). Simple and approximate expressions of demagnetizing factors of uniformly magnetized rectangular rod and cylinder. *Journal of Applied Physics*, 66, 983–985. <https://doi.org/10.1063/1.343481>
- Sato, M., Takemura, T., & Takahashi, M. (2018). Development of the permeability anisotropy of submarine sedimentary rocks under true triaxial stresses. *International Journal of Rock Mechanics and Mining Sciences*, 108(May), 118–127. <https://doi.org/10.1016/j.ijrmms.2018.06.010>
- Schegg, R., Leu, W., Cornford, C., & Allen, P. A. (1997). New coalification profiles in the Molasse Basin of Western Switzerland: Implications for the thermal and geodynamic evolution of the Alpine Foreland. *Eclogae Geologicae Helvetiae*, 90(1), 79-96. [https://doi.org/10.1016/0146-6380\(92\)90070-E](https://doi.org/10.1016/0146-6380(92)90070-E)
- Schmitt, M., Fernandes, C. P., da Cunha Neto, J. A. B., Wolf, F. G., & dos Santos, V. S. S. (2013). Characterization of pore systems in seal rocks using nitrogen gas adsorption combined with mercury injection capillary pressure techniques. *Marine and Petroleum Geology*, 39(1), 138–149. <https://doi.org/10.1016/j.marpetgeo.2012.09.001>
- Schmidt, R. A., & Huddle, C. W. (1977). Effect of Confining Pressure on Fracture Toughness of Indiana Limestone, 14(August 1976), 289–293. [https://doi.org/10.1016/0148-9062\(77\)90740-9](https://doi.org/10.1016/0148-9062(77)90740-9)
- Schmidt, V., Burlini, L., Hirt, A. M., & Leiss, B. (2008). Fabrication of synthetic calcite-muscovite rocks with variable texture - An analogue to cataclasite fabrics? *Tectonophysics*, 449(1–4), 105–119. <https://doi.org/10.1016/j.tecto.2007.11.055>
- Scholes, O. N., Clayton, S. A., Hoadley, A. F. A., & Tiu, C. (2007). Permeability anisotropy due to consolidation of compressible porous media. *Transport in Porous Media*, 68(3), 365–387. <https://doi.org/10.1007/s11242-006-9048-5>

- Shimamoto, T., & Ikeda, Y. (1976). A simple algebraic method for strain estimation from deformed ellipsoidal objects. 1. Basic theory. *Tectonophysics*, 36, 315–337. Retrieved from [https://doi.org/10.1016/0040-1951\(76\)90107-4](https://doi.org/10.1016/0040-1951(76)90107-4)
- Simmons, G., Wilkens, R., Caruso, L., Wissler, T., & Miller, F. (1982). *Physical properties and microstructures of a set of sandstones, Annual Report to the Schlumberger-Doll Research Center*. [https://doi.org/10.1016/S1251-8050\(97\)89866-7](https://doi.org/10.1016/S1251-8050(97)89866-7)
- Skyscan. (2011). NRecon User Manual.
- Soete, J., Claes, S., Claes, H., Erthal, M. M., Hamaekers, H., De Boever, E., et al. (2022). Unravelling the pore network and its behaviour: An integrated NMR, MICP, XCT and petrographical study of continental spring carbonates from the Ballık area, SW Turkey. *The Depositional Record*, 8(1), 292–316. <https://doi.org/10.1002/dep2.135>
- Soille, P. (2000). Morphological Image Analysis: Principles and Applications. *Sensor Review*. Retrieved from <https://doi.org/10.1108/sr.2000.08720cae.001>
- Sommaruga, A., Eichenberger, U., & Marillier, F. (2012). Seismic Atlas of the Swiss Molasse Basin, 90.
- Šperl, J., & Trčková, J. (2008). Permeability and porosity of rocks and their relationship based on laboratory testing. *Acta Geodyn Geomater*, 5(149), 41-47. chrome-extension://efaidnbmnribpcajpcglclefindmkaj/[https://www2.irsm.cas.cz/materialy/acta\\_content/2008\\_01/4\\_Trckova.pdf](https://www2.irsm.cas.cz/materialy/acta_content/2008_01/4_Trckova.pdf)
- Stoner, E. C. (1945). XCVII. The demagnetizing factors for ellipsoids. *The London, Edinburgh, and Dublin Philosophical Magazine and Journal of Science*, 36(263), 803–821. <https://doi.org/10.1080/14786444508521510>
- Strang, G. (2022). Introduction to linear algebra. *Wellesley-Cambridge Press*.
- Strobel, N. K. (1996). Nonlinear unsharp masking methods for image contrast enhancement. *Journal of Electronic Imaging*. <https://doi.org/10.1117/12.242618>
- Sun, H., Vega, S., & Tao, G. (2017). Analysis of heterogeneity and permeability anisotropy in carbonate rock samples using digital rock physics. *Journal of Petroleum Science and Engineering*. <https://doi.org/10.1016/j.petrol.2017.06.002>
- Sun, P., Xu, H., Zhu, H., Jia, L., Hu, X., Fang, H., et al. (2021). Investigation of pore-type heterogeneity and its control on microscopic remaining oil distribution in deeply buried marine clastic reservoirs. *Marine and Petroleum Geology*. <https://doi.org/10.1016/j.marpetgeo.2020.104750>
- Taheriotaghsara, M., Bonto, M., Nick, H. M., & Eftekhari, A. A. (2021). Estimation of calcite wettability using surface forces. *Journal of Industrial and Engineering Chemistry*, 98, 444–457. <https://doi.org/10.1016/j.jiec.2021.03.019>
- Tan, F. Q., Li, X. K., Ma, C. M., Lv, J. R., & Liu, W. T. (2023). Genetic mechanism of permeability anisotropy in conglomerate reservoir and its controlling factors. *Bulletin*, 135(3–4), 852–866. <https://doi.org/10.1130/B36403.1>
- Tauxe, L., Gee, J. S., & Staudigel, H. (1998). Flow directions in dikes from anisotropy of magnetic susceptibility data: The bootstrap way. *Journal of Geophysical Research: Solid Earth*. <https://doi.org/10.1029/98jb01077>
- Thomson, P. R., Aituar-Zhakupova, A., & Hier-Majumder, S. (2018). Image segmentation and analysis of pore network geometry in two natural sandstones. *Frontiers in Earth Science*. <https://doi.org/10.3389/feart.2018.00058>
- Thorpe, A. N., Senftle, F. E., Holt, M., & Grant, J. (2016). Electron microscopy studies of low concentrations of nanoscale Fe<sub>3</sub>O<sub>4</sub> particles in epoxy resin. *Journal of Materials Research*, 15(11), 2488-2493. <https://doi.org/10.1557/JMR.2000.0357>
- Tyler, N., & Frank, A. (1983). Depositional Setting of the Salt Wash Member of the Morrison Formation, Southwest Colorado, 53(1), 67–82. <https://doi.org/10.1306/212F8157-2B24-11D7-8648000102C1865D>
- Vázquez, M. A., Galán, E., Ortiz, P., & Ortiz, R. (2013). Digital image analysis and EDX SEM as

- combined techniques to evaluate salt damp on walls. *Construction and Building Materials*. <https://doi.org/10.1016/j.conbuildmat.2013.03.067>
- Vos, M. (1990). Selection of outcrop samples for acoustic measurements on reservoir rock. *Internal Report Delft University of Technology*, 63.
- Wagner, R., Kühn, M., Meyn, V., Pape, H., Vath, U., & Clauser, C. (2005). Numerical simulation of pore space clogging in geothermal reservoirs by precipitation of anhydrite. *International Journal of Rock Mechanics and Mining Sciences*. <https://doi.org/10.1016/j.ijrmms.2005.05.008>
- Wang, F. P., Reed, R. M., John, A., & Katherine, G. (2009). Pore networks and fluid flow in gas shales. In *Proceedings - SPE Annual Technical Conference and Exhibition*. <https://doi.org/10.2118/124253-ms>
- Wang, H., Ji, B., Lv, C., Zhang, L., Li, X., Cui, C., et al. (2019). The stress sensitivity of permeability in tight oil reservoirs. *Energy Exploration & Exploitation*, 37(4), 1364–1376. <https://doi.org/10.1177/0144598719855819>
- Wang, Y., & Pan, B. (2017). Permeability anisotropy measurement and anisotropic evaluation method abstract. *Progress in Geophysics*, 32(6). Retrieved from 10.6038/pg20170636
- Wenlian, X., Tao, L. I., Min, L. I., Jinzhou, Z., Zheng, L., & Ling, L. I. (2016). Evaluation of the stress sensitivity in tight reservoirs. *Petroleum Exploration and Development*, 43(1), 115–123. [https://doi.org/10.1016/S1876-3804\(16\)30013-1](https://doi.org/10.1016/S1876-3804(16)30013-1)
- Wirth, S. B., Carlier, C., Cochand, F., Hunkeler, D., & Brunner, P. (2020). Lithological and tectonic control on groundwater contribution to stream discharge during low-flow conditions. *Water (Switzerland)*. <https://doi.org/10.3390/w12030821>
- Witt, K. J., & Brauns, J. (1983). Permeability-Anisotropy Due to Particle Shape. *Journal of Geotechnical Engineering*, 109(9). [https://doi.org/10.1061/\(ASCE\)0733-9410\(1983\)109:9\(1181\)](https://doi.org/10.1061/(ASCE)0733-9410(1983)109:9(1181))
- Worthington, P. F. (2008). A diagnostic approach to quantifying the stress sensitivity of permeability. *Journal of Petroleum Science and Engineering*, 61(2–4), 49–57. <https://doi.org/10.1016/j.petrol.2008.03.003>
- Yang, R., Hao, F., He, S., He, C., Guo, X., Yi, J., et al. (2017). Experimental investigations on the geometry and connectivity of pore space in organic-rich Wufeng and Longmaxi shales. *Marine and Petroleum Geology*, 84, 225–242. <https://doi.org/10.1016/j.marpetgeo.2017.03.033>
- Yang, R., Hu, Q., He, S., Hao, F., Guo, X., Yi, J., & He, X. (2018). Pore structure, wettability and tracer migration in four leading shale formations in the Middle Yangtze Platform, China. *Marine and Petroleum Geology*. <https://doi.org/10.1016/j.marpetgeo.2017.10.010>
- Yang, Y., Wang, K., Zhang, L., Sun, H., Zhang, K., & Ma, J. (2019). Pore-scale simulation of shale oil flow based on pore network model. *Fuel*. <https://doi.org/10.1016/j.fuel.2019.03.083>
- Youssef, A. A., Alassar, R. S., Mahmoud, M., Elsayed, M., & Al-Dweik, A. Y. (2021). A novel approach for measuring plane anisotropic permeability through steady-state flow between two concentric cylinders. *Advances in Water Resources*, 151, 103884. <https://doi.org/https://doi.org/10.1016/j.advwatres.2021.103884>
- Yu, X., Ahmadiania, M., Shariatipour, S. M., Lawton, D., Osadetz, K., & Saeedfar, A. (2020). Impact of Reservoir Permeability, Permeability Anisotropy and Designed Injection Rate on CO<sub>2</sub> Gas Behavior in the Shallow Saline Aquifer at the CaMI Field Research Station, Brooks, Alberta. *Natural Resources Research*, 29(4), 2735–2752. <https://doi.org/10.1007/s11053-019-09604-3>
- Zeng, J., Feng, X., Feng, S., Zhang, Y., Qiao, J., & Yang, Z. (2017). Influence of tight sandstone micro-nano pore-throat structures on petroleum accumulation: Evidence from experimental simulation combining x-ray tomography. *Journal of Nanoscience and Nanotechnology*. <https://doi.org/10.1166/jnn.2017.14514>
- Zhan, X., Schwartz, L., Smith, W., Toksöz, N., & Morgan, D. (2009). Pore scale modeling of rock

- properties and comparison to laboratory measurements. *79th Society of Exploration Geophysicists International Exposition and Annual Meeting 2009, SEG 2009*, 500, 1935–1939. <https://doi.org/10.1190/1.3255234>
- Zhang, D. L., Liu, S., Puerto, M., Miller, C. A., & Hirasaki, G. J. (2006). Wettability alteration and spontaneous imbibition in oil-wet carbonate formations. *Journal of Petroleum Science and Engineering*, 52(1–4), 213–226. <https://doi.org/10.1016/j.petrol.2006.03.009>
- Zhang, J., Liu, G., Torsaeter, O., Tao, S., Jiang, M., Li, G., & Zhang, S. (2020). Pore-throat structure characteristics and its effect on flow behavior in Gaotaizi tight siltstone reservoir, northern Songliao Basin. *Marine and Petroleum Geology*. <https://doi.org/10.1016/j.marpetgeo.2020.104651>
- Zhang, L. (2013). Aspects of rock permeability. *Frontiers of Structural and Civil Engineering*, 7, 102–116. <https://doi.org/10.1007/s11709-013-0201-2>
- Zhang, N., Zhao, F., Guo, P., Li, J., Gong, W., Guo, Z., & Sun, X. (2018). Nanoscale Pore Structure Characterization and Permeability of Mudrocks and Fine-Grained Sandstones in Coal Reservoirs by Scanning Electron Microscopy, Mercury Intrusion Porosimetry, and Low-Field Nuclear Magnetic Resonance. *Geofluids*, 2018(1), 2905141. <https://doi.org/10.1155/2018/2905141>
- Zhang, P., & Austad, T. (2006). Wettability and oil recovery from carbonates: Effects of temperature and potential determining ions. *Colloids and Surfaces A: Physicochemical and Engineering Aspects*, 279(1–3), 179–187. <https://doi.org/10.1016/j.colsurfa.2006.01.009>
- Zhang, P., Hu, L., Meegoda, J. N., & Gao, S. (2015). Micro/Nano-pore Network Analysis of Gas Flow in Shale Matrix. *Scientific Reports*. <https://doi.org/10.1038/srep13501>
- Zhang, S., & Tullis, T. E. (1998). The effect of fault slip on permeability and permeability anisotropy in quartz gouge. *Tectonophysics*, 295(1–2), 41–52. [https://doi.org/10.1016/S0040-1951\(98\)00114-0](https://doi.org/10.1016/S0040-1951(98)00114-0)
- Zhang, S., Paterson, M. S., & Cox, S. F. (1994). Porosity and permeability evolution during hot isostatic pressing of calcite aggregates. *Journal of Geophysical Research: Solid Earth*, 99(B8), 15741–15760. <https://doi.org/10.1029/94JB00646>
- Zhang, S., Tullis, T. E., & Scruggs, V. J. (1999). Permeability anisotropy and pressure dependency of permeability in experimentally sheared gouge materials. *Journal of Structural Geology*, 21(7), 795–806. [https://doi.org/10.1016/S0191-8141\(99\)00080-2](https://doi.org/10.1016/S0191-8141(99)00080-2)
- Zhang, T., Tao, S., Tang, D., Tang, S., Xu, H., Zhang, A., et al. (2021). Permeability Anisotropy in High Dip Angle Coal Seam: A Case Study of Southern Junggar Basin. *Natural Resources Research*, 30(3), 2273–2286. <https://doi.org/10.1007/s11053-021-09831-7>
- Zhang, W., & Wang, Q. (2018). Permeability anisotropy and gas slippage of shales from the Sichuan Basin in South China. *International Journal of Coal Geology*, 194(February), 22–32. <https://doi.org/10.1016/j.coal.2018.05.004>
- Zhang, X., Ge, J., Kamali, F., Othman, F., Wang, Y., & Le-Hussain, F. (2020). Wettability of sandstone rocks and their mineral components during CO<sub>2</sub> injection in aquifers: Implications for fines migration. *Journal of Natural Gas Science and Engineering*, 73(September 2019), 103050. <https://doi.org/10.1016/j.jngse.2019.103050>
- Zhang, Z., Ma, B., Ranjith, P. G., Yang, S., & Zhou, L. (2020). Indications of risks in geothermal systems caused by changes in pore structure and mechanical properties of granite: an experimental study. *Bulletin of Engineering Geology and the Environment*. <https://doi.org/10.1007/s10064-020-01901-z>
- Zhao, J., Chen, H., Zhang, J., Zhang, W., & Chen, G. (2022). Quantitative characterization of organic and inorganic pores in shale based on FIB-SEM. *Frontiers in Earth Science*, 10, 994312. <https://doi.org/10.3389/feart.2022.994312>
- Zhao, Y., Zhang, K., Wang, C., & Bi, J. (2022). A large pressure pulse decay method to simultaneously measure permeability and compressibility of tight rocks. *Journal of Natural Gas Science and Engineering*, 98, 104395. <https://doi.org/10.1016/j.jngse.2021.104395>

- Zheng, J., Zheng, L., Liu, H.-H., & Ju, Y. (2015). Relationships between permeability, porosity and effective stress for low-permeability sedimentary rock. *International Journal of Rock Mechanics and Mining Sciences*, 78, 304–318. <https://doi.org/10.1016/j.ijrmms.2015.04.025>
- Zhong, X., Zhu, Y., Liu, L., Yang, H., Li, Y., Xie, Y., & Liu, L. (2020). The characteristics and influencing factors of permeability stress sensitivity of tight sandstone reservoirs. *Journal of Petroleum Science and Engineering*, 191, 107221. <https://doi.org/10.1016/j.petrol.2020.107221>
- Zhou, Y., Pagnetti, M., Foubert, A., Lanari, P., Neururer, C., & Biedermann, A. R. (2022). Quantitative comparison of 3D pore space properties with magnetic pore fabrics—testing the ability of magnetic methods to predict pore fabrics in rocks. *Geochemistry, Geophysics, Geosystems*. <https://doi.org/https://doi.org/10.1029/2022GC010403>
- Zubair, M. (2012). Digital Rock Physics for Fast and Accurate Special Core Analysis in Carbonates. In *New Technologies in the Oil and Gas Industry*. <https://doi.org/10.5772/52949>

## **Appendix**

### **Appendix for Article I: Quantitative comparison of 3D pore space properties with magnetic pore fabrics—testing the ability of magnetic methods to predict pore fabrics in rocks**

XRCT particle analyses and MPF data obtained in this article can be obtained from <https://doi.org/10.5281/zenodo.6782552>.

### **Appendix for Article II: Quantitative assessment of direct and indirect measures of 3D pore fabrics and permeability anisotropy in sedimentary rocks**

Thin section analyses, XRCT analyses including pore fabrics, simulated permeability and MPF model, measured permeability anisotropy, AMS and MPF data in this article can be obtained from <https://doi.org/10.5281/zenodo.11216307>.

### **Appendix for Article III: Comparing thin-section-derived and X-ray tomography-derived pore fabrics, permeability anisotropy and magnetic pore fabrics in hot isostatically pressed calcite-muscovite rocks**

Thin section analyses, XRCT analyses including pore fabrics, simulated permeability and MPF model, measured permeability anisotropy, AMS and MPF data in this article can be obtained from <https://doi.org/10.5281/zenodo.11216342>.